Allocation of Dump Load in Islanded Microgrid Using the Mixed-Integer Distributed Ant Colony Optimization with Robust Backward\Forward Sweep Load Flow

By

Maen Zohair Kreishan

A Thesis Submitted to
Brunel University London
for the degree of
Doctor of Philosophy

Department of Electronic and Electrical Engineering,
College of Engineering, Design and Physical Sciences

Brunel University London
London, United Kingdom

September 2022

Abstract

Reliable planning and operation of droop-controlled islanded microgrids (DCIMGs) is fundamental to expand microgrids (MGs) scalability and maximize renewable energy potential. Employing dump loads (DLs) is a promising solution to absorb excess generation during off-peak hours while keeping voltage and frequency within acceptable limits to meet international standards. Considering wind power and demand forecast uncertainties in DCIMG during off-peak hours, the allocation of DL problem was modelled as two problems, viz., deterministic and stochastic. The former problem was tackled using four highly probable deterministic generation and demand mismatch scenarios, while the latter problem was formulated within scenario based stochastic framework for uncertainty modelling. The mixed-integer distributed ant colony optimization (MIDACO) was introduced as a novel application in microgrids to find the optimal location and size of DL as well as the optimal droop setting for distributed generation (DG). Furthermore, to enhance the convergence of the proposed optimization technique, three robust and derivative free load flow methods were developed as novel extensions of the original backward\forward sweep (BFS) for grid-connected MGs. The three load flow methods are called special BFS, improved special BFS, and general BFS. The first two methods rely on one global voltage variable distributed among all DGs, while the latter has more general approach by adopting local voltage at each generating bus. The deterministic multi-objective optimization problem was formulated to minimize voltage and frequency deviation as well as power losses. Inversely, the stochastic multi-objective problem with uncertainty was formulated to minimize total microgrid cost, maximum voltage error, frequency deviation, and total energy loss. The proposed method was applied to the IEEE 33-, 69-, and 118-test systems as modelled in MATLAB environment and further validated against competitive swarm and evolutionary metaheuristics. Various convergence tests were considered to demonstrate the efficacy of the proposed load flow methods with MIDACO's non-dominated solution. Likewise, different optimization parameters were utilized to investigate their impact on the solution. Moreover, the advantage of multi-objective optimization against single objective was provided for the deterministic optimization problem, while the effect of load model and droop response were also investigated. The obtained results in chapter 5 and 6 further demonstrate the fundamental role of DL in voltage and frequency regulation while minimizing costs and energy losses associated with DCIMG operation. Accordingly, an improved voltage and frequency profiles for the system after DL inclusion were attained in Figure 6.9 and Figure 6.10, respectively. To demonstrate the competitiveness of DL-based energy management system (EMS) against storage-based EMS, a brief cost benefit analysis considering hot water demand was also provided.

Acknowledgement

First, praise be to Allah, lord of the worlds, for making this possible.

I would like to express my heartfelt gratitude and appreciation to my supervisor, Dr. Ahmed Zobaa, for his distinguished guidance and generous support all the way. I have been blessed to have him as a true mentor with great wisdom. Also, I would like to thank my supervisory team members, Dr. Mohamed Darwish and Dr. Maysam Abbod for their continued support and dedication during my time at Brunel University London. Furthermore, thanks go to my panel member, Prof. Hamed Al-Raweshidy, for his valuable comments and feedback. I would like to take this opportunity to thank Dr. Martin Schlueter from Hokkaido University, Japan, for his outstanding work on the MIDACO algorithm and offering me the help and support whenever needed.

Finally, I would like to express my gratitude to my mother, my wife, my son, my dear family, and my dear friends for their inspiration, love, and support along the way.

Dedication

This thesis is dedicated to my late father, Zuhair Kreishan (1939-2021), the best man and solicitor advocate I have ever known.

Table of Contents

List of Tables

List of Figures

List of Acronyms

AC	Alternating Current
ACS	Ant Colony System
ACO	Ant Colony Optimization
ACOmi	Mixed-Integer Ant Colony Optimization
AI	Artificial Intelligence
AS	Ant System
BCBV	Branch Current Bus Voltage
BEMS	Battery Energy Management System
BESS	Battery Energy Storage System
BFS	Backward\Forward Sweep
BIBC	Branch Incidence Branch Current
CBA	Cost Benefit Analysis
DBFS	Direct Backward\Forward Sweep
DC	Direct Current
DCIMG	Droop Controlled Islanded Microgrid
DG	Distributed Generation
DL	Dump Load
DLEMS	Dump Load Energy Management System
DPH	Dynamic Population Heuristic
DR	Demand Response
DRB	Droop Bus
EC	Emissions Cost
ELC	Electronic Load Controller
EMS	Energy Management System
ESS	Energy Storage System
EV	Electric Vehicle
FC	Fuel Cost
FSH	Final Stage Heuristic
GA	Genetic Algorithm
GBFS	General Backward\Forward Sweep
G-S	Gauss-Seidel Method
HMI	Human Machine Interface
IBDG	Inverter-Based Distributed Generation
IEA	International Energy Agency
IEC	International Electrotechnical Commission
IEEE	Institute of Electrical and Electronic Engineers

LCOE	Levelized Cost of Energy
LF	Load Flow
Li-ion	Lithium Ion Battery
MATLAB	Matrix Laboratory
MBFS	Modified Backward\Forward Sweep
MC	Maintenance Cost
MCDP	Multi-Criteria Decision Problem
MG	Microgrid
MGCC	Microgrid Central Controller
MIDACO	Mixed-Integer Distributed Ant Colony Optimization
MINLP	Mixed-Integer Nonlinear Programming
MISQP	Mixed-Integer Sequential Quadratic Programming
MMAS	Min-Max Ant System
MOACO	Multi-Objective Ant Colony Optimization
MOGA	Multi-Objective Genetic Algorithm
MOO	Multi-Objective Optimization
MOPSO	Multi-Objective Particle Swarm Optimization
MPPT	Maximum Power Point Tracking
MVE	Maximum Voltage Error
NBFS	Nested Backward\Forward Sweep
NC	Not converged
NDB	Non-Droop Bus
Ni-Cd	Nickel Cadmium Battery
N-R	Newton-Raphson Method
NSGA-II	Non-dominated Sorting Genetic Algorithm
OPM	Oracle Penalty Method
OUP	Optimization with Uncertainty Problem
p.u.	Per Unit System
PDF	Probability Density Function
PF	Power Factor
PSCAD	Power System Computer Aided Design
PSO	Particle Swarm Optimization
PV	Photovoltaic
RES	Renewable Energy Source
RTS	Reliability Test System
RWM	Roulette Wheel Mechanism
SA	Solution Archive
SM	Solution Matrix
SBFS	Special Backward\Forward Sweep

SBFS-II	Improved Special Backward\Forward Sweep
SCADA	Supervisory Control and Data Acquisition
SDT	Single Dimension Tuning
SEIG	Self-Excited Induction Generator
TC	Technical Cost
TEL	Total Energy Loss
TMC	Total Microgrid Cost
VB	Virtual Bus
WABA	Weighted Average Best Ant
WT	Wind Turbine

List of Symbols and Nomenclatures

V-f	Voltage and frequency
PQ	Constant power bus
PV	Constant voltage bus
P-f	Active power and frequency
Q-V	Reactive power and bus voltage
Q-V-f	Reactive power, bus voltage, and frequency
P-V-f	Active power, bus voltage, and frequency
m	Total number of artificial ants in an ant system
a	A single travelling ant
Λ_{ij}^{a}	The transitional probability of ant system
$\mathcal{A}$	Set of all allowed vertices that have not yet been visited by ant a
τ_{ij}	Pheromone information of an ant a between vertices i and j
ξ_{ij}	Heuristic information for ant a walking on the edge between vertices i and j
α_1, α_2	Pheromone and heuristic information weighting parameters, respectively
ϱ	Pheromone evaporation rate
$\Delta\tau_{ij}^{a}$	Amount of pheromone per length of path deposited by ant a walking on the edge between vertices i and j
$\mathcal{L}_a$	Tour length as traversed by an ant a
$\mathcal{Q}$	Constant relates the amount of pheromones dropped by ants
$\phi(x)$	Probability density function for random variable x
$G^i(x)$	Multi-dimensional Gaussian function
$g_\ell^i(x)$	One dimensional PDF of the Gaussian function
$\mathcal{W}_\ell^i$, μ_ℓ^i, σ_ℓ^i	Weight, mean, and standard deviation for the ℓ-th kernel number of the i-th dimension $g_\ell^i(x)$, respectively
k_r	Total number of kernels in the Gaussian function
d	Total number of dimensions in a solution vector
$\mathcal{SA}$	A set representing solution archive
$\mathcal{S}_\ell$	A d-dimensional solution vector
$\breve{\mathcal{F}}(x,y)^{\mathfrak{g}}$, $\breve{\mathcal{F}}(x,y)^{\mathfrak{h}}$	Fitness ranks for solutions at indices $\mathfrak{g}$ and $\mathfrak{h}$ within $\mathcal{SA}$, respectively
$\mathcal{S}_1$	Best overall solution stored in solution archive
$\mathcal{S}_{k_r}$	Worst overall solution stored in solution archive
$\mathcal{E}$	General evolutionary operator within ACOmi framework
$\mathbb{N}^+$	Set of natural numbers without zero

$\mathbb{R}$, $\mathbb{Z}$	Sets of real and integer numbers, respectively
n_{con}, n_{int}	The total number of continuous and integer variable in the MINLP, respectively
$\mathcal{v}$	New generation size within ACOmi framework
$\mathcal{S}_{\ell}^{i}$	Single solution components for all $\ell \in \{1, \cdots, k_r\}$ regarding the corresponding dimension i
$dis_{max}(i)$, $dis_{min}(i)$	Maximum and minimum distance between corresponding single solution components $\mathcal{S}_{\mathfrak{g}}^{i}$ and $\mathcal{S}_{\mathfrak{h}}^{i}$, respectively
$\#generation$	Total number of generations produced within ACOmi framework
$\phi_i^c(x)$, $\phi_j^d(x)$	Continuous and discrete Gaussian PDF's, respectively
$res(z)$	Residual function of the oracle penalty method (OPM)
$\mathcal{F}(z)$	The objective function within OPM framework
Ω	The oracle, a parameter used for constraint handling by OPM.
z	Representation of decision variables within OPM framework.
$\mathcal{g}_i(z)$	Constraint handling function within the residual function of OPM
$\mathcal{P}(z)$	The penalty function within OPM framework.
$\check{\alpha}$	Weight balancing parameter between $res(z)$ and $\mathcal{F}(z)$
$\check{\beta}$	A bias factor for the penalty function
N_{pop}	Actual population size within ACOmi framework.
N_{ants}	Minimum number of ants per population
DP_{max}	Maximum allowed dynamic population of ants
DP_{mean}	The iteration number where DP_{max} is reached
$\#iteration$	Total number of iterations within ACOmi framework
a_{sdt}^{i}	Created single dimension tuning ant
a_u^i, a_l^i	Upper and lower limits for the created ant a_{sdt}^{i} interval
a_{rnd}^{i}	A d-dimensional vector ant with a uniformly distributed random number
a_{waba}^{i}	Created weighted average best ant
da_{max}	Maximum difference in fitness between current and previous best ant
da_{ave}	Average difference in fitness between current and previous best ant
$stage_{final}$	A Boolean constant assigned to the FSH flag
W_{final}	A weight constant that relates da_{ave} with da_{max}
$\mathcal{F}_{ex}$	User desired value for the objective function
ACO_{main}, ACO_{final}	ACOmi implementation binary flags
$\mathcal{F}_{eval}$	Maximal function evaluations within ACOmi framework
$\mathcal{F}_{time}$	Maximal computation time within ACOmi framework
a_i	Ant created for dimension i within ACOmi framework
$\hat{S}$	Total number of decomposed sub-problems

$\mathbb{F}$	Set of all feasible solutions x for a constrained optimization problem
U_i, N_i	The utopia and nadir of an objective function, respectively
$\mathcal{F}_i(x)$	The objective function within MIDACO framework
$\mathcal{g}_i(x)$	The constraints handling function within MIDACO framework
x	Decision variable of the problem within MIDACO framework
x_{min}, x_{max}	Lower and upper limits for the decision variable x, respectively
w_i^j	Matrix of weights for each sub-problem within MIDACO framework
$d_i^j(x)$, $D_j(x)$	Solution x weighted and average distances, respectively
$B_j(x)$	The balance function within MIDACO framework
$T_j(x)$	The target function within MIDACO framework
$\hat{T}_j(x)$	The first target function without utopia-nadir information
$\mathcal{O}$, $\mathcal{C}$	Total number of objectives and constraints of a problem, respectively
$\mathcal{C}_e$	The number of equality constraints of the problem
S_i^c, P_i^c, Q_i^c	The injected apparent, active, and reactive powers in bus i at the c-th iteration, respectively
I_i^c	The injected current into bus i at the c-th iteration
V_i^c	Bus i voltage at the c-th iteration
$[\boldsymbol{B_i^c}]$, $[\boldsymbol{I_i^c}]$	System branch and inject currents at the c-th iteration, respectively
n, m	Distribution system total bus and branch numbers, respectively
$[\boldsymbol{V^s}]$	The slack bus voltage vector
$\left[\boldsymbol{V^{\Delta}}\right]$	The bus voltage mismatch vector
B_b	The current through b branch as defined within BFS framework
Z_b	Line impedance of branch b in a distribution network
f, f_0, f_{ss}	Operational, nominal, and steady state frequency, respectively
V_i, V_0	Operational and nominal voltage at bus i, respectively
P_{Gi0}, P_{Gi}	Bus i's active nominal and generated power, respectively
Q_{Gi0}, Q_{Gi}	Bus i's reactive nominal and generated power, respectively
m_{pi}, n_{qi}	Bus i's droop coefficients for frequency and voltage, respectively
m_{pT}, n_{qT}	Frequency and voltage equivalent droop coefficients, respectively
mn_{DL}	Dump load allocation's optimum droop settings for DGs
P_{Li}, Q_{Li}	Bus i's load active and reactive powers, respectively
P_{Li0}, Q_{Li0}	The active and reactive powers of load at nominal voltage, respectively
nP, nQ	Voltage dependence coefficients for load's active and reactive powers, respectively
F_p , F_q	Frequency dependence coefficients for load's active and reactive powers, respectively
N_{DL}	Dump load bus location

P_{DL}, Q_{DL}	The dump load's consumed active and reactive power, respectively
gk, wk, lk	Total number of dispatchable DGs, WT, and loads in the IMG, respectively
$\mathcal{N}$	A set of all system buses
$\mathcal{GK}$	A subset containing all dispatchable DG buses
P_{loss}, Q_{loss}	Total active and reactive power losses of the MG, respectively
ΔV_i, Δf	Bus i's voltage and frequency deviations, respectively
ε_{Th}	Threshold value for convergence criterion in load flow solution
c_1, c_2	Load flow method iteration counters within SBFS framework
S_i, I_i	Injects of apparent power and current at bus i within SBFS framework, respectively
B_i	The current flowing in the branch between bus i to bus $i+1$
B_{i_max}	Branch current B_i maximum limit
V_{in}	Bus i's new value for voltage at iteration c_1 within SBFS framework
ΔV_{in}	The deviation in voltage error across the system within SBFS framework
Z_i, R_i, X_i	Impedance, resistance, and reactance of branch B_i, respectivey
$[\boldsymbol{Z_i}]$	Row vector of impedance Z_i as seen by branch current B_i
f_{c_2+1}, f_{c_2}	Frequency at the c_2+1 and c_2 iterations within SBFS framework, respectively
$V_{1_{c_2+1}}$, $V_{1_{c_2}}$	Virtual bus voltage at the c_2+1 and c_2 iterations within SBFS framework, respectively
ΔV_1	Virtual bus voltage deviation
E	Voltage error tolerance for SBFS convergence
P_{Gb}, Q_{Gb}	Generated active and reactive powers at virtual bus, respectively
P_{ex}, Q_{ex}	The exchanged active and reactive powers with a pseudo grid, respectively
$[\boldsymbol{B'_i}]$, $[\boldsymbol{I'_i}]$	The inject and branch currents following another backward sweep within SBFS-II framework, respectively
$[\boldsymbol{V'_{in}}]$	The voltage column vector across the system following another sweep within SBFS-II framework
f_{c+1}, f_c	Frequency at the $c+1$ and c iterations within SBFS-II and GBFS framework, respectively
$V_{1_{c+1}}$, V_{1_c}	Virtual bus voltage at the c_2+1 and c_2 iterations within SBFS-II and GBFS framework, respectively
$\Delta V'_{in}$	The deviation in voltage error across the system within SBFS-II and GBFS framework
E′	Voltage error tolerance for SBFS-II convergence

ζ_1, ζ_2	GBFS dynamic damping factors
w_1, w_2	Weights for GBFS objective function
x_1	GBFS optimization problem decision variable
$\mathcal{F}(x_1)$	GBFS optimization problem objective function
$g(x_1)$	GBFS optimization problem constraint handling function
γ_i	Reactive power correction vector within GBFS framework
ΔQ_{Gi}	Reactive power update error at bus i
Q_c	Average reactive power correction factor
Q'_{Gi0}, Q'_{Gi}	Adjusted reference and desired reactive power at bus i, respectively
β	A binary constant to enable or disable reactive power correction within GBFS framework
Q_{min}, Q_{max}	Minimum and maximum reactive power output of DG, respectively
Z_o	Line impedance of the 6-bus system
R_o, X_o	Resistance and reactance of branch having impedance Z_o, respectively
m_{po}, n_{qo}	Active and reactive droops for DGs in the 6-bus system, respectively
sw	Dump load switch
x_2	Deterministic dump load optimization problem's decision variable
$\mathcal{F}_i(x_2)$	Deterministic dump load optimization problem's objective function
$g_i(x_2)$	Deterministic dump load optimization problem's constraint function
S_{Gi}	Generated apparent power by a DG unit at bus i
μ_{L_i}, σ_{L_i}	Mean and standard deviation for load forecast error random variable, respectively
p	Accumulative percentage of load from hourly, daily, and weekly percentages of annual peak system demand
$\phi_{L_i}(p)$	PDF of the random variable defining load forecast error
L_{st}	Specific load level or state of the discretised load PDF
$\Lambda(L_{st})$	Probability of occurrence to the specific load state L_{st}
p^u_{st}, p^l_{st}	Upper and lower limits of load accumulative percentage for state/level L_{st}, respectively
p_{st}	Load's mean accumulative percentage for load state/level L_{st}
$P_{L_i}(p_{st}), Q_{L_i}(p_{st})$	Expected load's active and reactive powers at the average load percentage p_{st} from peak system demand, respectively
$\phi_W(v)$	PDF of the random variable defining wind speed
k_s, c_s	Shape factor and scale index for Weibull distribution PDF, respectively
v	Wind actual velocity
μ_W, σ_W	Mean and standard deviation for wind speed random variable, respectively
$\Gamma(\ )$	The gamma function

W_{st}	Specific wind level or state of the discretised wind PDF
$\Lambda(W_{st})$	Probability of occurrence to the specific wind state W_{st}
v_{st}^{u}, v_{st}^{l}	Upper and lower limits of wind speed for state/level W_{st}, respectively
v_{st}	Wind's mean speed for wind state/level W_{st}
$P_W(v_{st})$	Expected wind turbine active power at the average wind speed v_{st}
v_{ci}, v_{co}	The cut-in and cut-off wind speeds, respectively
v_r	The rated wind speed for the WT
v_μ	The actual average wind speed at the site
P_{Wr}	The rated power of the wind turbine
s	Generation to loading mismatch scenario for the IMG
Ω_s	The set of uncertain variables corresponding to generation/loading mismatch scenario s
Λ_s^i	Probability of occurrence for each random variable at bus i within set of uncertain variables Ω_s
P_{Li}^s, Q_{Li}^s	Load active and reactive powers at bus i during scenario s, respectively
P_{Wi}^s	Wind turbine output power at bus i during scenario s
NV	Total number of uncertain variables during scenario s
NR	Number of reduced highly probable scenarios
Λ_s^N	Normalized convolved probability of scenario s
h, $\mathcal{H}$	Considered off-peak hour and set of off-peak hours, respectively
$\mathcal{F}_i^s(x)$	Objective function value during scenario s
x_3	Stochastic dump load optimization problem's decision variable
$\mathcal{F}_i^{h,s}(x_3)$	The objective function value in scenario s at off-peak hour h
$\mathcal{g}_i^{h,s}(x_3)$	The constraint function value in scenario s at off-peak hour h
$\breve{\mathcal{F}}_i(x_3)$	The expected value for the objective function considering all scenarios in the dump load stochastic optimization problem
H	Total number of off-peak hours
TMC_h^s	Total microgrid costs at the scenario s during the off-peak hour h
FC_h^s, MC_h^s, EC_h^s, TC_h^s	Fuel, maintenance, emissions, and technical costs at the scenario s during the off-peak hour h, respectively
RC_h^s, FRC_h^s	Reactive and frequency costs at the scenario s during the off-peak hour h, respectively
$P_{Gi}^{h,s}$, $Q_{Gi}^{h,s}$	Active and reactive power generated by dispatchable DG unit at the scenario s during the off-peak hour h, respectively
ψ_{fuel}, ψ_{main}, ψ_{emis}	Fuel, maintenance, and emissions cost coefficients, respectively
Ψ_{emis}	Emissions rate by the dispatchable DG
η_P	Fuel consumption efficiency by the dispatchable DG
Ψ_{var}	Reactive power coefficient of the dispatchable DG

ψ_{freq}	Frequency penalty cost coefficient
$f_{ss}^{h,s}$	Steady State frequency during scenario s at off-peak hour h
$V_{in}^{h,s}$	Voltage at bus i considering scenario s during the off-peak hour h
MVE_h^s	Maximum voltage error considering scenario s during the off-peak hour h
$P_{G1}^{h,s}$, $V_1^{h,s}$, $B_1^{h,s}$	Active power, voltage, and branch current at the virtual bus considering scenario s during the off-peak hour h, respectively
Δf_h^s	Frequency deviation considering scenario s during the off-peak hour h
t^h	Off-peak time duration at each s scenario
$P_{loss}^{h,s}$, $Q_{loss}^{h,s}$	Active and reactive power loss considering scenario s during the off-peak hour h, respectively
$B_i^{h,s}$	Branch current at scenario s during the off-peak hour h
V_{hw}	Hot water volume
V_{hw}^{tot}	Total daily demand for hot water volume
P_{hw}	Required power by a water heating boiler to produce hot water of volume V_{hw}
η_{hw}	Efficiency of the water heater
η_{hw}^{ele}, η_{hw}^{gas}	Efficiency for electric and gas boilers, respectively
C_w, ρ_w	Specific heat of water and water density, respectively
$\Delta\mathrm{T}$	Difference in desired hot water temperature
T_{st}, T_{in}	The set-point and the inlet temperatures, respectively
P_{hw}^{ele}, P_{hw}^{gas}	Required power to meet total hot water demand from electric and gas boilers, respectively
ψ_{LCOE}^{eleR}, ψ_{LCOE}^{eleN}	The LCOE coefficients for renewable and non-renewable sourced electric boilers
ψ_{LCOE}^{gas}	The LCOE coefficients for gas boilers
ψ_{LCOE}^{BESS}	Cost coefficient for storage LCOE
ψ_{LCOE}^{Li}, ψ_{LCOE}^{Ni}	The LCOE coefficients for Li-ion and Ni-Cd battery ESS, respectively
HC_{hw}^{e}, HC_{hw}^{g}	Water heating costs for DLEMS and BEMS implementations, respectively
SC_{BESS}	Battery storage costs
HC_{hw}^{tot}	Total costs for running water heating system per calendar year

1 Chapter One: Background

1.1 Problem Statement

Depletion of fossil fuel resources along with tougher legislations on emissions from conventional power generation have caused an unprecedented shift toward renewable-based generation over the last two decades [1]. This major shift is driven by trends to ditch the long-standing centralized structure of the electricity supply industry to become more of distribution focused networks with abundance of distributed generation (DG). Fuelled by governments' incentives, energy conversion efficiency, and reduction in costs; renewable based DG has become the centre of the low carbon and sustainable deregulated electricity supply industry [2]. To facilitate DG growth at the distribution level, microgrids (MGs) have gained an unprecedented attention as a smart solution to accommodate renewable energy expansion projects [3]. A typical MG is defined as a small cluster of dispersed generation in a distribution network framework with flexible loads, which is often linked to utility main grid at the point of common coupling. Moreover, according to MGs' operating purpose, whether it was for economic or technical goals, two modes of operation exist: islanded or grid-connected. Islanded MGs (IMGs), also called autonomous MGs, can have many benefits to consumers in terms of reliability and market participation. Additionally, network operators can alleviate system over loading and enhance customer satisfaction via minimal supply interruptions [4].

It is estimated that over one billion consumers worldwide are still lacking access to green, sustainable, and affordable supply [5]. Therefore, it is imperative to envisage that clustered and adjacent renewable-based IMGs would become fundamental to future projects on rural communities' electrification. Likewise, just before 2020 the energy produced by various renewable technologies was at record high of 26% of global energy production [6]. Therefore, IMG operation is expected to rise considerably in the future to maximize renewable energy utilization and consumer satisfaction. Despite those promising benefits of emerging IMGs, they are often associated with technical and economic challenges. This is attributed to the tendency of IMGs toward high renewable energy sources (RESs) penetration. These high RESs penetration levels would implicate the control strategy implemented by those IMGs and increase their complexity. Moreover, IMGs challenges arise from uncertainties in demand forecast errors and the intermittent nature of RESs along with their impact on cost and quality of those IMGs. Such challenges include: the inability of IMGs to match generation with demand at all times especially during off-peak hours; the inadequate export facilities with main grid or adjacent IMGs facing similar power balancing issues; the high costs of storage-based energy

management systems (EMSs); the need to reduce reliance on conventional forms of energy production for heating and pumping applications in IMGs [2], [7].

On the other hand, successful operation of IMG is dependent on maintaining voltage and frequency (V-f) levels within specific limits set by international standards [8]. This can be achieved by a robust and reliable control scheme which enables the participation of all DG units within an IMG to share the load autonomously. Hence, droop control has been chosen to control the majority of IMGs due to its decentralized philosophy, reliability, and low costs compared to other control schemes [9]–[11]. Consequently, IMGs that implement the droop control strategy are often referred to as droop-controlled IMGs (DCIMGs). However, continuous capacity improvement in renewable energy technologies, mainly wind and solar, will lead to future V-f regulation issues. Likewise, increased grid integration constraints are expected for DCIMGs with over 10% of RESs penetration [12].

To regulate V-f deviations in DCIMG, that is by addressing the expected power mismatch issues, different energy management systems (EMSs) were proposed in literature. Such EMSs include: energy storage systems (ESSs) [13]–[15]; smart charging of electric vehicles (EVs) [16]–[18]; demand response (DR) programs [19], [20]. However, the use of such EMS solutions in IMGs with high share of wind power will often suffer from power balance issues during off-peak hours where the night demand is generally low. Similarly, higher chances of significant wind power generation for two or more consecutive 24-hour cycles will render those EMSs incompetent to handle the excessive power generation. This is because their efficiency and cost effectiveness tend to drop with larger generation to demand mismatches. Furthermore, battery ESSs (BESSs) suffer from idling energy losses, high costs, safety, and environmental concerns [21]. Likewise, EV charging and discharging techniques are often difficult to coordinate and execute [22]. Hence, these EMSs would be more suitable to handle small power deviations during normal operating conditions as a secondary control. Inversely, seeking alternatives to absorb the excess large wind power generation as primary control. Therefore, a viable solution for larger power mismatch would be to dump the extra power at off-peak hours using electronically controlled dump load (DL). Previously, DLs have been used to dissipate excessive power from synchronous and asynchronous generating units via dummy loads controlled by an electronic load controller (ELC) [23]–[26]. Furthermore, DLs have been utilized as V-f regulation solution by dumping power as useful heating and pumping applications [27]–[31].

Despite the economic and technical advantage of DLs over other power management solutions such as BESS and EV, very few studies have addressed DL within DCIMG framework [5]. On the other hand, various DCIMG studies have only addressed the optimal operation and allocation of DG and ESS considering technical, economic, and environmental objectives [32]–[38]. Nonetheless, the issue of V-f regulation as a result of excessive power

mismatch during off-peak hours were seldomly mentioned in these studies [32]–[38]. Additionally, demand and generation uncertainties as well as their impact on off-peak hours of operation were not incorporated adequately in the optimal dispatch studies of droop controlled DGs presented in [39]–[42]. Conversely, studies [43] and [44] were the only ones to address DL allocation as a solution to the large power mismatch problem during off-peak hours within the context of IMG. The aim of the latter studies was to minimize V-f deviations by allocating a single [43] and multiple DLs [44] in a DCIMG as a multi-objective optimization. However, the work presented in [43] and [44] had some limitations in the provided solution due to load flow convergence issues and slow optimization algorithm calculation time. Moreover, no account was given to MG operational costs and emissions. Likewise, no reference was given to losses acquired across the network by the installation of the DL. Additionally, neither study gave a clear indication to the type of renewable generation that was used, nor they accounted for uncertainties in wind generation and demand forecast error as random variables.

The level of randomness in DCIMG operational parameters caused by higher renewable energy penetration and diurnal load fluctuations, has forced the need for more efficient and accurate optimization algorithms. Such algorithms must be able to handle higher degree of randomness in the problem specifications. Actual desired settings for an IMG real-time schedule might differ from the optimized variables due to the probabilistic nature of MG conditions. Hence, deterministic approaches to IMG planning and scheduling which neglect the uncertainties often fall short in providing an accurate and reliable optimal solution in reality [2]. Similarly, the problem of DL allocation into DCIMG is known to be a non-convex mixed-integer nonlinear programming (MINLP). However, when taking uncertainties aboard, the problem is transformed form a deterministic problem with fixed boundaries into a stochastic problem with random parameters. Therefore, it is of great importance that the selected optimization algorithm can provide an adequate solution with an acceptable simulation time. This is especially true if we know that stochastic problems are often solved as multiple number of compounded deterministic problems. On the other hand, many of the previously mentioned studies that addressed uncertainties in DCIMG operation, [39]–[42], had relied upon transforming and approximating the original problem. This was done to comply with classical optimization requirements or to reduce metaheuristics' evaluation time, such as that of particle swarm optimization (PSO) and genetic algorithm (GA). However, those studies had neglected optimization time which has a considerable impact on enabling the optimization cycle in real-time within the shortest durations possible (i.e., less than 15 mins).

Due to the ill-conditioning expected in most DCIMGs, many load flow (LF) methods struggle to reach a converged solution. This often leads to certain assumptions to limit pre-islanding generation levels, reactive droop, line impedance, or power reference points. The

need for having an adaptable LF technique to be applied in DCIMGs is fundamental. This is to expand the boundaries of DCIMG optimization problems that originates from stochastic generation and demand conditions. Consequently, convergence of real-life uncertain MINLPs that addresses DCIMG operation is heavily reliant on LF robustness as well as the speed and accuracy of the utilized optimization technique. According to DCIMG allocation and operation literature [5], ant colony optimization (ACO) and its derivatives were rarely utilized within DCIMG framework and seldomly used for MG allocation studies [45], [46]. Inversely, the mixed-integer ant colony optimization (ACOmi) as extended for multi-objective problems in MIDACO, has proven to be a highly convergent and accurate metaheuristic technique on a variety of benchmark problems [47]. It offered superior serial computation speed for thousands of function evaluations with an intriguing and neat black-box capability for non-convex MINLPs. Nevertheless, it is yet to be applied in MGs as a state-of-the-art high performance optimization algorithm apart from the author's work presented in [48].

In light of the aforementioned problem statement, it can be deduced that storage- and DR-based EMS programs are not efficient or cost-effective solutions to handle large power deviations at off-peak hours. Furthermore, uncertainties in wind power and load forecast greatly influence the operational set points of the system and should not be neglected in future DCIMG planning studies. Previous DL allocation attempts within DCIMG framework, albeit scarce, have overlooked important aspects impacting the solution adequacy for the power mismatch problem during low demand hours. This includes operational costs; emissions; energy losses; convergence of load flow solution; speed and accuracy of the optimization technique; uncertainties modelling. In this thesis, a novel methodology has been proposed based on MIDACO combined with robust LF techniques based on BFS to address limitations of previous studies. Thereafter, formulating a multi-objective optimization problem to optimally size and allocate a DL as well as the optimal droop setting for DG units considering two types of optimization problems, viz., deterministic and stochastic optimization problems. Various optimization objectives were considered in this thesis such as V-f deviations, active and reactive power losses, total microgrid cost, maximum voltage error, and total energy loss.

1.2 Aim and Objectives

The main aim of this thesis is the optimal allocation of dump load in droop-controlled islanded microgrid during off-peak hours of operation using a combination of robust load flow method and state-of-the-art optimization technique called MIDACO. To that end, three efficient load flow methods based on the famous backward\forward sweep technique will be presented to enable the necessary analysis of islanded microgrids. Furthermore, two main optimization problems are presented for the optimal dump load allocation, viz., deterministic and stochastic.

The former considers four highly probable power mismatch scenarios, while the latter considers scenario-based uncertainty modelling for renewable generation and demand prediction. Very few studies have addressed the problem of dump load allocation within DCIMG framework to minimize voltage and frequency deviations. Moreover, many aspects have been neglected such as active and reactive power losses, total MG costs, emissions, maximum voltage error, and total energy loss considering the off-peak operation horizon. Similarly, different convergence issues for load flow solution were approximated, while accuracy and calculation time issues for the metaheuristic techniques used were neglected. In order to achieve the main aim of this research work, several areas were investigated within DCIMG allocation and operation framework. Those include but not limited to: microgrid architecture and decentralized control philosophy; DCIMG optimization problems for the short- and long-term horizon; the various optimization problem components manifested in objective function, constraints, decision variables, and algorithms; dump load application in microgrids; load flow analysis for islanded microgrids. Lastly, to achieve the main aim of this thesis, the following objectives are to be pursued:

1- To develop robust load flow techniques for islanded radial networks with and without communication between the generating units.
2- To obtain a non-dominated solution for DL's optimal location and size as well as dispatchable DGs' optimal droop sets considering a deterministic MINLP with pre-defined mismatch scenarios.
3- To highlight DL allocation efficacy considering single and multi-objective optimization, different load flow techniques, different load models, and different parameters for MIDACO.
4- To obtain a non-dominated solution for DL's optimal location and size as well as dispatchable DGs' optimal droop sets considering a stochastic MINLP with scenario-based uncertainty modelling for wind power and load forecast error.
5- To validate the speed and accuracy advantage of MIDACO against other evolutionary and swarm intelligence techniques considering the DL allocation problem.

1.3 Major Contributions

This research work has contributed to the knowledge by proposing a novel methodology based on the state-of-the-art MIDACO solver as a novel application in microgrids. Furthermore, three load flow methods for islanded systems were developed and proposed to enhance the performance of MIDACO. This was done to find a non-dominated optimal solution for the dump load allocation problem in droop controlled islanded microgrid. The contributions of this thesis are as follows:

1- Development of novel methodology to optimally allocate and size a dump load as well as the optimal droop setting for optimal DG dispatch. The problem was tackled as deterministic optimization problem.
2- Development of three load flow methods that offer better convergence over existing load flow methods with enhanced optimization techniques compatibility.
3- MIDACO was used as a first attempt in load flow analysis to find optimal damping factors to enhance load flow solution convergence.
4- Development of stochastic optimization methodology to account for uncertainty in the problem of dump load allocation and optimal DG dispatch taking wind power and load forecast errors as random uncertain variables.
5- The parallelization strategy of MIDACO was applied for first time in microgrids considering stochastic uncertainty optimization framework. Very promising results were achieved against other metaheuristics with parallelization capabilities.
6- The proposed optimization method herein was compared against other evolutionary and swarm intelligence techniques. This was done to highlight the speed and accuracy advantage in solving the deterministic and stochastic dump load allocation problems.
7- Highlighting dump load as a power management solution with technical and economic advantage over existing energy management systems like BESSs.

1.4 List of Published Work

The following are a list of research work published by the author during his doctoral studies in Brunel University London.

1- M. Z. Kreishan and A. F. Zobaa, “Optimal Allocation and Operation of Droop-Controlled Islanded Microgrids: A Review,” *Energies*, vol. 14, no. 15, Art. no. 15, Jan. 2021, doi: 10.3390/en14154653.
2- M. Z. Kreishan and A. F. Zobaa, “Allocation of Dump Load in Islanded Microgrid Using the Mixed-Integer Distributed Ant Colony Optimization,” *IEEE Systems Journal*, vol. 16, no. 2, pp. 2568–2579, Jun. 2022, doi: 10.1109/JSYST.2021.3100409.
3- M. Z. Kreishan and A. F. Zobaa, “Dump Load Allocation in Islanded Microgrid with Robust Backward\Forward Sweep and MIDACO,” in *Proc. Inter. Uni. Power Eng. Conf. (UPEC)*, Istanbul, Turkey, 2022, pp. 1–6, doi: 10.1109/UPEC55022.2022.9917779.
4- M. Z. Kreishan and A. F. Zobaa, “Mixed-Integer Distributed Ant Colony Optimization of Dump Load Allocation with Improved Islanded Microgrid Load Flow,” *Energies*, vol. 16, no. 1, Art. no. 1, Jan. 2023, doi: 10.3390/en16010213.

Work under review.

- M. Z. Kreishan and A. F. Zobaa, “Scenario Based Uncertainty Modelling for Power Management in Islanded Microgrid Using the Mixed-Integer Distributed Ant Colony Optimization,” *Energies*, under review.

1.5 Thesis Outline

The thesis is organised as follows:

In **Chapter 1**, a background of this research is presented in terms of problem statement along with the main objectives and major contributions of the research work carried out.

In **Chapter 2,** a summary of the detailed literature survey regarding the optimal operation and allocation of DCIMG is provided. Further consideration is given to dump load application in microgrids and load flow analysis in islanded systems. Subsequently, a critical evaluation of DCIMG literature was presented along with the three major identified research gaps.

In **Chapter 3**, introduction to ACO and the mathematical background of the proposed optimization technique, MIDACO, are given. Moreover, details of the multi-objective optimization expansion as well as the hybridization strategy of ACOmi are all elucidated. Accordingly, the main features and parameters of MIDACO are presented in detail.

In **Chapter 4**, a thorough description of load flow analysis in IMG is given. The proposed three load flow methods, viz., special BFS (SBFS), improved SBFS (SBFS-II), and general BFS (GBFS), are explained in detail. More emphasis is given to GBFS in terms of damping factors evaluation and convergence capabilities.

In **Chapter 5,** the DL allocation problem is carefully presented in a deterministic manner. By considering four pre-defined power mismatch scenarios, the allocation problem is handled as a single and multi-objective optimization. Different load models and load flow techniques are used to highlight the efficacy of the non-dominated solution. Similarly, the optimal solution is tested against variations in MIDACO’s parameters, while different acclaimed metaheuristics are considered as basis for comparison with MIDACO.

In **Chapter 6**, the DL allocation problem is tackled in a stochastic framework. That is, depending on uncertainty consideration for renewable generation and demand forecast, problem dimension would evolve from certain to uncertain boundaries. Furthermore, the parallelization strategy of MIDACO is validated against other competitive metaheuristics. Moreover, a brief cost benefit analysis is provided to highlight the advantage of DL allocation as power management solution against energy storage solutions.

Lastly, in **Chapter 7**, conclusions of the thesis findings and contributions are thoroughly elucidated. Also, further recommendations and suggestions for future research work are provided.

2 Chapter Two: Literature Review on Droop Controlled Islanded Microgrids

2.1 Introduction

A considerable movement in research trends toward the optimal operation and design of decentralized distribution networks has taken place over the past ten years. This was made possible by the heavy emphasis given to studies about MGs control, design, and optimal operation in various publications [1], [3], [45], [46], [49]–[67]. The capability of MGs to operate isolated form utility grid and in a decentralized fashion is one of their key distinguishing characteristics. Hence, the utilization of RESs depend on this distinct feature of MGs. An MG is a small-scale network at the distribution level that has many DGs and loads wherein a utility connection may or may not be present at the point of common coupling. Additionally, when DG installation is of RES type; an MG may incorporate an ESS to capture the excess energy for a later use. Hence, there exist different types of DG installations in an MG, such as conventional, renewable, or a combination of both.

Accordingly, when economic and RESs integration goals are desired, a grid-connected mode is sought for in MGs [64]. Additionally, the presence of a huge power grid makes it easier to manage V-f in the MG while utilising available dispersed generation as fixed sources independent of fluctuations in demand [51]. Conversely, IMG operation is often preferred to postpone network's upgrade expenses, carry out regular maintenance, and make up for main grid shortfalls in supply reliability [68]. Additionally, islanding is required to electrify remote communities and isolated locations that are heavily reliant on fossil fuel, where linking such communities to main grids would be expensive or infeasible [60]. In spite of the various environmental and economic advantages that IMG may provide, one important issue arises, which is the way to ensure supply quality.

In accordance with international standards such as IEEE std. 1547.4 for the operation and design of islanded systems [4] as well as IEEE std.1547.7 for DG interconnection with IMGs [69], all or some DGs must stop operating at constant power control and begin responding to demand variations in order to achieve V-f regulation. Decentralized control and centralized control are two different approaches that may be used to implement the aforementioned requirement [57]. The presence of a sophisticated and high-bandwidth infrastructure for communication in the MG is a key factor surrounding the decision to choose the centralized control philosophy. Additionally, for its precise power sharing capability and optimal V-f recovery, the master-slave technique is one of the most relied upon centralized control strategies. However, for the vast majority of IMGs worldwide, this kind of control is

infeasible or at least costly. On the other hand, a reliable control technique is essential to empower MG growth to facilitate the large-scale transition from centralized power generation to decentralized one. Furthermore, the single point of failure associated with the centralized control renders it unworkable and less dependable for large-scale application [1], [57]. Therefore, decentralized control techniques have become increasingly common for running IMGs in situations where investments in extra-high bandwidth communication lines are not required. Droop control, wherein the reactive and active power output of DG units is linearly linked to the voltage and frequency of the MG, respectively, is the decentralized strategy that is most frequently adopted in IMGs. Additionally, droop control's satisfactory power-sharing ability removes the requirement for physical communication between the units. This is because DGs in droop control setup rely on pre-existing infrastructure to collect local readings for V-f. Droop controlled IMGs (DCIMGs) are those islanded MGs that function using any type of decentralized control strategy.

The primary, secondary, and tertiary controls are the common phases in which the DCIMG control technique is implemented. Consequently, it is necessary to have an EMS to oversee those common phases. This will maintain a nearly constant generation/demand balance in the MG while also ensuring that the MG is operating within a pre-defined economic, technical, and environmental limits [61]. A successful implementation of the EMS, which is required to reap the benefits of DG, particularly that of an RES, depends on the effective design and operation of DCIMG. In one hand, DGs are advantageous in terms of improved network voltage support, decreased power losses, generation mix diversity, postponement of grid infrastructure upgrades, and decreased greenhouse gas emissions. Hence, DG is in some ways essential for future smart grids sustainability. On the other hand, because of the unpredictability of RESs operation, the continued growth in renewable energy has given rise to many technical challenges. As a result, DCIMG design and operation undergoes continuous improvement and optimization by numerous researchers using a variety of optimization algorithms of classical and artificial intelligence (AI) type.

With more DGs connected to the distribution network, international standards have strongly necessitated the installation of protective measures [4], [69]. Additionally, to cease energising the system at the event of electric faults. Thus, any control strategy implemented by MGs must interact successfully with existing protection schemes. Those protective measures along with DGs do frequently serve as an uninterrupted power supply (UPS). This is to ensure the continuation and reliability of supply during islanding operation. Conversely, for systems with single point of failure (i.e., master-slave controlled IMG), any permanent fault in the master unit will lead to the collapse of the IMG. Nonetheless, this major disadvantage of IMGs with master-slave control is overcome by DCIMG, wherein several units in DCIMG are functioning in a similar way to the master unit's purpose to increase the reliability.

Based on the detailed analysis of several survey papers [1], [3], [45], [46], [49]–[67] as elucidated in the author's work in [5]. It was determined that little attention was given to the operating mode of MG in some articles that concentrated on the optimal MG planning [49], [66]. Likewise, other articles had optimized the EMS and control strategy of MGs neglecting the other factors in MG design [1], [51], [61], [64]. Additionally, the optimal operation and design of DCIMG received insufficient attention in the MG reviews that tackled optimization methodologies [53], [59]. Thereby, no previously published review study has concentrated fully on DCIMG optimal allocation and operation. That is, by gathering all necessary optimization aspects such as objective functions, constraints, decision variables, and optimization algorithms. Hence, this chapter shall provide an insight to the current state of the art on DCIMG research as well as to pinpoint the main research gaps to be investigated in this thesis.

2.2 Optimal Operation and Allocation of Droop Controlled Islanded Microgrids

The author's DCIMG review presented in [5] as summarised in this chapter herein, gives a critical evaluation of more than 150 optimization focused articles in DCIMG research. The need for DCIMG dedicated optimization research is fundamental in three ways: to pave the way for RESs integration and deployment, to expand the scale of implementation for stable and reliable autonomous MGs, and to contribute in the development of isolated and rural communities' electrification projects. Additionally, IMGs can be broadly classified based on the utilized electric current as AC, DC, and AC/DC microgrids. Whereas the latter MGs are gaining popularity in recent years due to the development in power conversion units, the rise of variable RESs, and the overall reduction in costs.

Conversely, the advantage of decentralized control over centralized control was evident with the vast majority of articles investigating and improving the reliability of autonomous operation and the accuracy of reactive power sharing in emerging DCIMGs [5]. Furthermore, more detailed clarification was given to the three main hierarchal control stages found in most DCIMGs, viz., primary, secondary, and tertiary control. One significant outcome of the literature review in [5], is the classification of optimization problems into six broad categories, viz., allocation, reconfiguration, scheduling and dispatch, EMS and control, multi-criteria decision problem (MCDP), and optimization with uncertainty problem (OUP). Noting that the last two categories often combine the other four categories in a comprehensive EMS and allocation studies [5].

On the other hand, the categorization of the main objectives, constraints, and variables of optimization problems into various distinctive groups. Thereby, classifying objective functions to ten areas as costs minimization, profits maximization, emissions reduction,

voltage improvement, frequency regulation, loadability maximization, losses minimization, power sharing error reduction, stability enhancement, and reliability maximization. Likewise, classifying constraints into nine distinct groups as power flow, DG power, cost, frequency, voltage, thermal, ESS, DR, and radiality limits. As for the sorting of decision variables into six types it was as follows: DG, ESS, DR, RES, controller (i.e., droop and proportional integral), and reconfiguration variables [5].

Lastly, the optimization algorithms adopted in DCIMG studies were categorized as classical, artificial intelligence (AI), and hybrid algorithms [5]. As for classical optimization techniques, these are related to class of deterministic optimization algorithms that uses analytical and derivation methods to guarantee an exact global optimal solution. However, those classical techniques usually require many conditions to be met in the objective and constraint functions such as continuity, convexity, and tractability. Contrariwise, AI techniques belongs to class of stochastic optimization algorithms that uses one or more heuristics to find an approximate solution without a guarantee of global optimality. Most of AI techniques are derived from nature, physical, or social phenomena and does not require any conditions to be met by the objective or constraint functions. Many of the acclaimed metaheuristics are in fact hybrid methods that combine classical (or local solver) techniques with AI techniques. This was done to enhance exploration and exploitation capabilities as well as the overall convergence speed to the optimal non-dominated solution [5].

Based on the equally significant research gaps reported by [5], it is concluded that stability, reliability, and high cost problems are considered as the major barriers standing against DCIMG growth, further RESs expansion, and rural communities' electrification. The importance of tackling such research gaps lies at providing more affordable and reliable electricity supply with greener and more sustainable future smart grids. Therefore, dedicated studies for IMG power flow analysis and efficient optimization techniques are vital for DCIMG expansion. Nonetheless, autonomous DCIMGs are still considered as a not ready application for larger scale implementation. This is attributed mainly to generation/demand uncertainties, ill-conditioning in MGs, and the off-peak hours of operation. Thereby, the following two sections give a focused survey on the main aspects of DL application in MGs and LF analysis in IMG to identify the major barriers standing against reliable and stable DCIMG operation.

2.3 Dump Load Application in Microgrids

The increase in variable renewables integration, predominantly wind power and solar photovoltaics (PVs), was at its highest levels during the past ten years [70]. Nonetheless, two major issues are identified as barriers to renewable energy expansion. Those are the difficulty of meeting constant generation and demand balance as well as the insufficient transmission

capacity to exploit all available renewable generation [7]. Moreover, highly penetrated grids such as those found in the German, Italian and British grids, are expected to face major V-f regulation issues due to the continued growth in renewable energy [70]. Hence, real-time power management is vital for a healthy future of MGs with significant renewable generation.

Various energy management solutions were addressed by [15], [19], [20], [71]–[74] such as BESS to store extra energy at peak times, coordinated EV smart charging, DR programs, and using an electronic load controller (ELC) for smart loads to absorb surplus generation. The use of BESS during low load hours is inefficient due to technical, economic, and environmental reasons [21], whereas coordination problems with EV and DR are often very challenging to handle as a power management solution at low load hours [75]. Therefore, ELC controlled DL was utilized previously to control wind and hydro generation for synchronous and asynchronous units deployed in IMGs [25], [76]–[78]. As suggested by [79], [80], DL has the potential to provide V-f regulation solution if used as heating or pumping applications. Nevertheless, ELC use in IMG is still at the early stages wherein energy losses and generator thermal strain are still seen as barriers to DL expansion in IMGs [25]. Therefore, off-line studies, such as the one presented in this thesis, are necessary to expand the use of DLs in highly penetrated IMGs as V-f regulation solution during off-peak hours.

Employment of DLs to regulate the generator side excess power was utilized previously to provide V-f control for synchronous and asynchronous generating units [23]–[26]. In particular, self-excited induction generator (SEIG) power output has been regulated by means of ELC to dissipate the excess power as heat in DLs in hydro and wind stand-alone power plants [23]–[25], [81]. Similarly, as in [27]–[31], the use of DL was to achieve useful work as heating and pumping application by absorbing excess generation to enhance the power quality of the system and provide V-f control. Moreover, the use of DL was extended in a distributed manner via an experiment to provide V-f regulation to micro-hydro driven SEIG. This was done by installing distributed ELC in each household to provide heating and improve the quality of life [82], [83]. Likewise, a smart load power electronic converter was proposed for nano-grid to enhance PV integration [84].

Furthermore, different studies have addressed the optimal allocation and operation of DCIMG with particular interest to DG and ESS allocation. The location of DG units was optimized to serve different technical and economic objectives such as: minimization of active power losses [32], [33], small signal stability margin [34], and maximization of net energy export [35]. However, studies in [32]–[35] had no account for V-f deviations during off-peak hours nor they considered the uncertainties in generation and demand. Similarly, the allocation of ESS in DCIMG has gained attention to serve technical [36] and economic [37], [38] objectives. Nonetheless, authors in [36]–[38] did not consider off-peak hours of operation,

neither did they incorporate uncertainties in generation and demand. The optimal droop settings for dispatchable DG units have been optimized as an EMS solution considering network reconfiguration in light of uncertainties in wind generation and demand forecast to minimize fuel costs and maximize loadability [39]. Whereas in [40], the total MG cost minimization objective was achieved in a stochastic framework by considering a comprehensive real-time EMS with BESS and DR limits. On the other hand, researchers in [41] have paid particular interest to emissions and costs minimization in DCIMG as independent objectives in stochastic EMS with the availability of BESS to support the IMG. Likewise, authors of [42] have conducted a similar study with the addition of loadability maximization as a third objective. Despite the promising economic and environmental objectives provided by the stochastic EMS solutions presented in [39]–[42], no reference was made in the latter studies to the large generation mismatch expected during off-peak hours in DCIMG. Moreover, none of the studies in [39]–[42] had suggested alternatives for reliance on BESSs as primary power control strategy.

To address issues related to the inherited efficiency problems associated with EMSs reliant on BESS and DR, a novel DL allocation study was presented in [43]. The aim of [43] was to minimize V-f deviations during off-peak hours by consuming excess generation via the DL. The study had used particle swarm optimization (PSO) for the single objective problem and non-dominated sorting GA (NSGA-II) for the multi-objective problem. Moreover, the work in [43] was expanded to allocate multiple number of DL across an IMG to provide the same objectives of V-f deviations [44]. Nonetheless, the use of DL as an EMS solution in DCIMG is still at the early stages since studies addressing the optimal allocation and operation of DL within DCIMG framework are scarce. Moreover, DL allocation as significant over-generation mismatch solution have had limited optimization and load flow analysis tools.

2.4 Load Flow Analysis in Islanded Microgrids

Successful planning and analysis of modern power systems is essential to realise the full potential of smart grids. The significance of smart grids lies in facilitating the shift toward decarbonized and decentralized distribution networks. To that end, power flow studies are fundamental to enable adequate planning, control, and optimization of such modern power systems. Available power flow or LF techniques such as Newton-Raphson (N-R), Gauss-Seidel (G-S), and fast decoupled have been used extensively to study power networks under normal conditions [85]–[89]. However, those latter techniques are prone to convergence and implementation issues when applied to ill-conditioned networks [90], [91]. In addition, many ill-conditioned networks are often referred to as MGs, which resembles networks with DG and controllable loads. This new dimension of distribution networks as brought forward by MGs

often involves bidirectional power flow in radial or weakly meshed topologies [92]. To overcome the problem of ill-conditioned power networks, an LF technique based on Kirchhoff's current and voltage laws was presented in [90]. This derivative free technique is known as backward\forward sweep (BFS) and often applied to radial and weakly meshed distribution networks [90], [93], [94].

Another distinct feature of MG is the ability to work connected or islanded (isolated) from the main utility grid. In grid-connected mode, the V-f across the system are monitored by utility grid control scheme. However, in islanded mode, V-f are controlled by sharing the network loads among DG units. A predominant decentralized control method known as droop control is used to adjust the V-f in IMG as functions of reactive and active power outputs of the DG, respectively. Moreover, in the standard droop control method, the rate of change in the DG's output reactive and active powers is linearly proportional to the voltage and frequency at the DG bus, respectively.

In traditional LF methods, such as N-R, G-S, and BFS, the DG units are treated as negative load buses, while utility grid is considered as slack bus during grid-connected LF analysis. However, in islanded mode, DG units could not be modelled as constant power (PQ), constant voltage (PV), or slack buses. This is attributed to the fact that the system frequency is variable in an IMG. Thus, it will affect line reactance and some loads within the network. Moreover, droop control impacts the power output of DG units due to V-f change. Whereas the absence of slack bus necessitates that DG units must eliminate any power mismatch in the network to maintain stability. Hence, the assumption that DG units are negative constant loads will not hold any longer in an IMG. In that sense, traditional LF techniques mentioned earlier are considered unsuitable to solve the load flow of IMG. Likewise, the IEEE Std. 1547.4 dictates that the load flow analysis for an IMG must adequately account for power imbalance as well as V-f deviations [4].

Recently, researchers have proposed different techniques to solve the LF problem of DCIMG. According to the review of [95], deterministic DCIMG load flow methods are broadly classified as N-R based, G-S based, and BFS based methods. The G-S based methods, also known as fixed point methods, which relay on the original G-S method with modifications to account for droop control by considering a new type of V-f bus was presented in [96]. Despite the simple and accurate approach of [96], it was found that G-S based methods are expected to suffer when applied to larger islanded distribution systems [97]. Another approach for solving LF in small IMGs is based upon branch structure and called forward return algorithm as presented in [98]. The forward return method is solved by employing a system of quadratic voltage equations to obtain powers between adjacent branches. However, the method adaptation to larger system is challenging and requires handling of system buses one by one

[98]. Moreover, an IMG load flow method based on the Z-bus approach was presented in [99] for larger radial systems. However, the method is dependent on the pre-existence of the incidence matrix of the large system, while using compressed column storage format to store all matrices. Moreover, no solution was offered to convergence problems arising from lower reactive droop values. Similarly, formulations of IMG load flow that is based on branch structure was presented in [95], [100], [101]. A distributed slack bus load flow approach was employed with enhanced metaheuristic techniques based on PSO [95], [100] and GA [101] to minimize active and reactive powers mismatch in the network.

On the other hand, the robust Jacobian based methods have also been employed to solve the load flow problem of IMG. As in [102], a Newton trust region technique was adopted to account for the different modes of operation for DG, while a set of nonlinear equations was generated to solve the load flow. Likewise, as in [103], an N-R method was modified to provide an accurate solution for IMG. Nonetheless, according to the notable work of Shirmohammadi et al. [90], Jacobian based methods are not recommended for load flow calculation in distribution networks. This concern is attributed to the high R/X ratio of distribution networks which weakens the Jacobian diagonal predominance and eventually leads to singularity in the matrix [104]. To avoid the convergence issues of Jacobian based methods in distribution networks, BFS was recommended by [90] for distribution systems which are topologically radial or weakly meshed in nature.

Therefore, a BFS load flow method for IMG which are mainly radial in nature needs to account for frequency as a variable and the non-existence of a slack bus. Several variations of the BFS methods were suggested in literature to solve the LF problem of grid connected MG [105]. Those are broadly classified into basic form or quadratic from according to voltage calculation procedure by current injects or power injects, respectively. Nonetheless, the basic and direct form of BFS presented by Teng [106] remains simple, efficient, and memory friendly to solve power flow in radial distribution networks. This was confirmed when compared to other BFS-based methods as analysed by [93]. Subsequently, the novel work by Diaz et al [107], was the first attempt to modify the basic and robust BFS method by [106]. This was done to account for DG units' droop control characteristics and eliminate the need for a slack bus in what was called the direct BFS (DBFS). However, the method relied on having one global voltage variable communicated to all DG buses. This implies that the reactive power update is based on droop values alone, while assuming the existence of communication between DG units. To address that issue, the work in [108] has presented a modified BFS (MBFS) method which relay on local voltage measurements to update the DG reactive power. Nevertheless, the method had convergence issues due to DG units exceeding their permissible limits as a result of local voltage and reactive power updates at lower droop values. Similarly, as in [109], a nested BFS (NBFS) method was proposed to enhance the convergence of MBFS by using

static declaration factors. However, the use of static declaration factors is not suitable for different generation/demand ratios, probabilistic load flow formulations, and lower reactive droop coefficients. Furthermore, the methods presented in [107]–[109] did not account for adequate sharing of the reactive power among all DG units to prevent any unit from exceeding limits or failing. Furthermore, all BFS derived methods require a DG unit to be based at the virtual bus (VB), which might not be the case in practical applications for larger IMG.

The use of swarm and evolutionary computation to enhance the performance of IMG load flow methods is gaining popularity to assist with IMG optimal planning and dispatch. Nevertheless, papers addressing those issues are scarce [95]. As in [110], an IMG load flow method based on PSO was employed to select the optimal modified droop constants to enhance reactive power sharing. Likewise, in [95], [100] bus voltage magnitudes and angles were selected by an improved PSO to minimize active and reactive powers mismatch in an IMG load flow framework. The micro-turbine reference active power was optimized in [111] to minimize total operational cost in an optimal power flow problem. Despite the contributions of [95], [100], [110], [111], they have considered certain system loading conditions. Thus, their load flow solution is problem specific and could not be extended or generalized to other power flow dependent optimization problems. Therefore, any proposed load flow technique for IMG must expand the applicability range to account for the ill-conditioning expected in islanded networks. This includes but not limited to different loading and generation levels, lower droop setting, reactive power sharing errors, and min-max generation limit violations.

2.5 Critical Evaluation of Droop Controlled Islanded Microgrid Literature

Conforming to the subjects and trends for research in the investigated literature heretofore, it is concluded that current research direction should investigate the gaps recognized in this chapter. These gaps include but not limited to:

2.5.1 Dump Load Allocation in Droop Controlled Islanded Microgrids

Significant share of studies has focused on DG and ESS allocation and operation as given in [5], [48]. Nonetheless, they have disregarded critical low demand hours of operation and the expected large power mismatch due to variable renewable generation and demand forecast error. On the other hand, very few studies have addressed the DL allocation problem in DCIMG framework such as [43], [44]. However, the work in [43] suffered from limitations identified as droop impact on solution, active and reactive power losses, and the slow calculation time of the algorithm.

Moreover, few number of steps were given to droop control in [43] by assuming that the load flow converges after the first iteration, signalling convergence issues for the proposed load flow techniques, i.e., DBFS [107]. The convergence issues in DBFS arises from higher voltage error across the system caused by the large number of iterations for the LF method. Those very issues were investigated by [108] as the MBFS method, but without any solutions to the critical reactive power updates at lower droop settings for DGs.

2.5.2 Load Flow Analysis in Droop Controlled Islanded Microgrids

Different variations of the simple and robust BFS method in [106] were put forward to handle IMG by [107]–[109]. However, those methods (i.e., DBFS, MBFS, NBFS) suffer from convergence issues at lower reactive droop values, vulnerability to initial guess of the system generation and demand, challenging set up for DGs droop and power reference points, prone to divergence at high generation/load mismatch, susceptibility to line impedance change, and require the presence of DG unit at the VB. Moreover, no reference was made by any of DBFS [107], MBFS [108], or NBFS [109] on how to handle the min-max generation limits for DG units during the load flow solution. Moreover, they did not provide a suitable approach for load flow analysis in IMG optimization problems.

2.5.3 Uncertainty in Wind Generation and Load Forecast During Off-peak Hours

Despite the promising solution provided by the DL allocation presented in [43], [44], the studies did not account for MG operational costs and emissions. Furthermore, neither study had referred to energy losses acquired across the network considering the operational horizon for off-peak hours. Additionally, neither study in [43], [44] gave a clear indication to the type of renewable generation that was considered, nor they accounted for uncertainties in wind generation and demand forecast error as random variables. Moreover, no differentiation was given to the difference between dispatchable and non-dispatchable DGs in the network. This is necessary as often non-dispatchable units operate according to PQ control, while dispatchable units adopt the V-f control during islanding.

Conversely, many studies that considered uncertainty in their optimization problem such as [39]–[42], did not account for V-f deviations during off-peak hours neither they considered supply quality impact on the total MG costs. Moreover, no clear solution was provided by the latter studies to the inherited efficiency problem of increasing BESSs into IMG as a power management solution. Lastly, the cost benefit analysis (CBA) provided in [44] did not consider uncertainties in demand forecast and renewable generation. Likewise, the costs

considered were not realistic as they did not consider other costs such as capital and running costs. Also, the assumed volume did not consider the total system demand for hot water.

2.5.4 Main Research Gaps

- Load flow analysis for DCIMG is prone to divergence for ill-conditioned systems. Thus, more studies are needed to improve the convergence of load flow solution taking into consideration the role of DGs' local and global voltage measurements. This will be investigated thoroughly in **chapter 4**.
- DL allocation in DCIMG requires further analysis in terms of optimization technique and LF tools to highlight the impact on system losses, voltage, and frequency deviations. That is, by considering highly probable deterministic mismatch scenarios as well as DG optimal droop sets. This will be investigated thoroughly in **chapter 5**.
- Uncertainty in generation and demand is yet to be included in DL allocation studies as a stochastic optimization problem. Therefore, more analysis is required to highlight its impact on costs, emission, V-f deviations, and energy losses of the MG. This will be investigated thoroughly in **chapter 6**.

2.6 Summary

In this chapter, the state of the art on DCIMG research was investigated and analysed. A summary for the most common aspects defining DCIMGs was presented, with more emphasis given to optimization in DCIMG. Various outcomes were reported in terms of DCIMG optimization problem classification into six categories, viz., allocation, reconfiguration, scheduling and dispatch, EMS, OUP, and MCDP. The considered objectives, constraints, and decision variables were sorted into ten, nine, and six distinct groups, respectively. Furthermore, identifying three main optimization algorithm classes in DCIMG, viz., classical, AI, and hybrid, with the latter gaining huge attention in recent studies. On the other hand, a critical evaluation was given to dump load application in MGs as well as current state of research on load flow analysis in IMGs. However, much work is still needed to investigate the effectiveness of new stochastic optimization techniques that are multi-disciplinary in the optimal allocation and operation of DCIMGs. Similarly, there is an urgent need to develop more efficient and robust load flow methods that are capable of dealing with the ill-conditioning expected in IMGs. Finally, the identified research gaps in this chapter, as given in section 2.5.4, will be the focus of this thesis. Those gaps can be summarized as the optimal dump load allocation and operation in DCIMG, convergence of load flow analysis in IMG, and uncertainties in renewable generation and demand forecast during off-peak hours.

3 Chapter Three: Mixed-Integer Distributed Ant Colony Optimization (MIDACO)

3.1 Introduction

In this chapter, the proposed high-performance metaheuristic technique, MIDACO, inspired by the original ACO is described in detail. In the field of stochastic optimization, ACO metaheuristics refer to group of probabilistic algorithms that mimic the food search endeavours of natural ant colonies to solve discrete optimization problems [112]. Ever since ACO emergence, different variations of those algorithms were proposed in literature to tackle other solution domains for MINLP problems such as continuous ACO [113] and multi-objective ACO (MOACO) [114].

Conversely, the proposed algorithm in this thesis, MIDACO, is based on the extended ACO for mixed-integer domains (ACOmi) [115] combined with constraint handling technique known as the oracle penalty method (OPM) [116] to handle multi-and many-objective MINLPs (many-objective problems are those of four or more contradicting objectives). The main difference between MIDACO and other MOACO algorithms, is the introduction of utopia-nadir balance technique that steers the search efforts at the Pareto front towards an area where the best equally traded solution lies (refer to Schlueter et.al [117], [118] for more information).

3.2 Ant Colony Optimization

Proposed in the 1990s by Dorigo [112], the ACO is a class of swarm intelligence techniques wherein the meaningful interaction between agents or boids in a population ultimately attains a certain objective. The inspiration for ACO is based on natural ants foraging behaviour. When real ants go out looking for food, they randomly scout the surrounding areas to their nest. Subsequently, when any ant stumbles with a food source, it examines it for quality and proceeds by carrying what it can back to the nest. In doing so, the ant deposits a certain chemical (pheromone) along the way back to the nest. This pheromone is the way how natural ants signal their achievement by creating a pheromone trail, wherein a closer and higher quality food source would draw more ants along that specific trail. Hence, more pheromones are deposited over time on that trail as the ants are using it repeatedly.

Similarly, any ant that finds a low quality and distant food source, the rate of evaporation to the deposited pheromone will be higher. Hence, that particular low-quality path will be disregarded by the population of ants. This natural instinct behaviour by ants was observed to inadvertently increase the appeal of the best and shortest paths of food from and into the nest [119]. The same behaviour of real ants has been transformed in the form of

artificial ants to find shortest paths on a graph to solve a class of hard combinatorial problems [113]. To visualize the concept of ACO, a two-bridge experiment is illustrated in Figure 3.1 [112], [119].

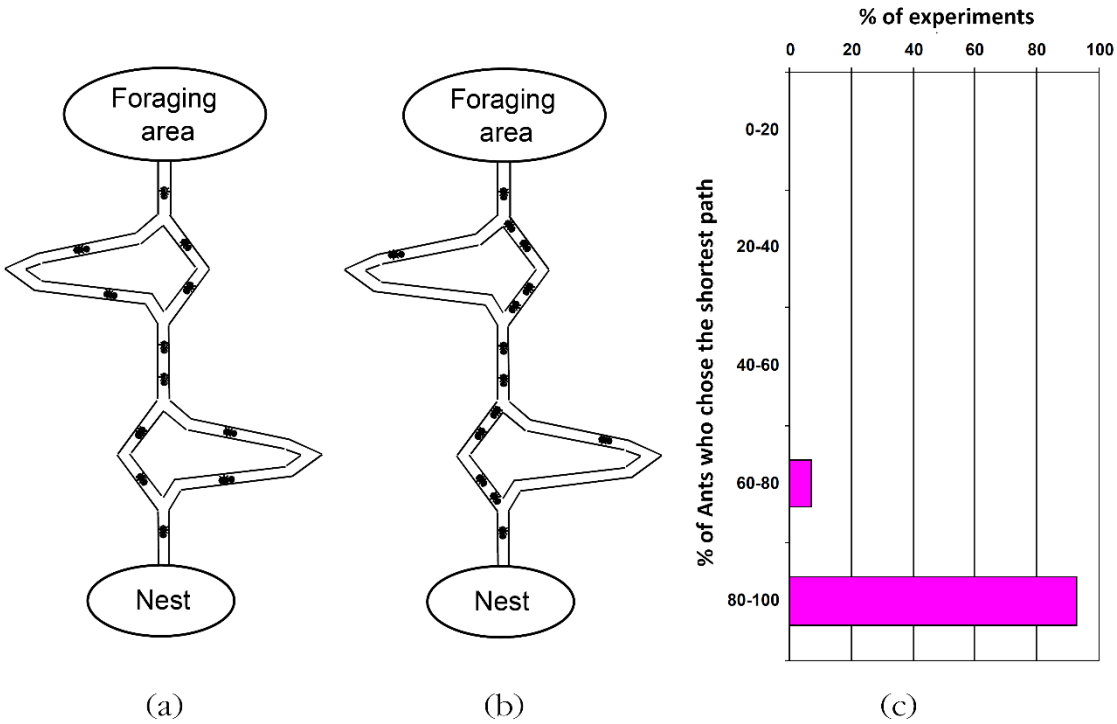

Figure 3.1: Double bridge experiment: (a) ants explore the bridge at first (b) most ants selecting the shortest path eventually (c) percentage relationship between repeated experiments and ants selecting the shortest path [112]

As Figure 3.1 shows, the indirect communication of ants by pheromone dropping of each individual ant will eventually lead to the discovery of the optimal path between the nest and a good quality food source. In other words, a high-quality foraging area is explored by the collective behaviour of the ant colony.

The fundamental principle of ACO metaheuristic lies in obtaining the probabilistic model of the pheromone table wherein a solution search space of combinatorial optimization problem is sampled [113]. The implementation of ACO involves artificial ants' movements on a connected graph (also called construction graph) consisting of vertices and edges. An artificial ant travels the edges of the graph from vertex to vertex without re-visiting any vertex until ultimately the shortest path on the weighted graph is found. The choice of the next allowed vertex to be visited by an ant is based on the probabilistic choice model for solution component building by the chosen ACO metaheuristic.

There are various versions of ACO metaheuristic with different probabilistic model to build the solution, such as ant system (AS) [120], max-min ant system (MMAS) [121], and ant colony system (ACS) [122]. The first, simplest, and most-known model is that of the AS [120],

which was chosen herein as an example. In AS implementation, and for a system with (m) total number of ants, the chance that a single ant (a) will travel across certain edge from vertex i to vertex j, also known as the transitional probability of the ant system (Λ_{ij}^{a}) is given by [113], [120]:

$$\Lambda_{ij}^{a} = \begin{cases} \frac{(\tau_{ij})^{\alpha_1} \cdot (\xi_{ij})^{\alpha_2}}{\sum_{l \in A} (\tau_{il})^{\alpha_1} \cdot (\xi_{il})^{\alpha_2}}, & \forall\, j \in \mathcal{A} \\ 0, & \text{otherwise} \end{cases} \tag{3.1}$$

where $\mathcal{A}$ is a set of all allowed vertices that have not yet been visited by ant a. τ_{ij} is the pheromone information of an ant a between vertices i and j, respectively. ξ_{ij} is the heuristic information for the ant a walking on the edge between vertices i and j, respectively. l is another neighbouring vertex to the vertex j. α_1 and α_2 are positive parameters that dictate the weighting relation between pheromone and heuristic information, respectively. Accordingly, an ant is set to start from a random vertex with a list of tabu vertices not to be visited. Subsequently, an ant will choose the next edge based on the transitional probability described earlier. Once an ant finishes its tour and there are no more allowed vertices to visit, the ant retreats to the starting vertex depositing pheromones τ_{ij} on each visited edge creating a trail. The process is repeated for all m ants until they finish their tours on the constructed graph (i.e., meeting the termination criteria). Similarly, the pheromone droplets τ_{ij} are updated according to the following formula [122]:

$$\tau_{ij} \leftarrow (1 - \varrho) \cdot \tau_{ij} + \sum_{a=1}^{m} \Delta\tau_{ij}^{a} \tag{3.2}$$

where ϱ is the pheromone evaporation rate and is chosen within a small range such that $\varrho \in (0,1]$. This is necessary to avoid trial accumulation by ants and thus reduce rapid convergence issues of the ACO by exploring more areas in the solution search space [113]; $\Delta\tau_{ij}^{a}$ is the amount of pheromone per length of path as deposited by an ant a walking on edge from vertex i to vertex j and is given by [120]:

$$\Delta\tau_{ij}^{a} = \begin{cases} {}^{Q}/_{\mathcal{L}_a}, & \text{if the ant } a \text{ walks on edge } ij \\ 0, & \text{otherwise} \end{cases} \tag{3.3}$$

where $\mathcal{L}_a$ is the path or tour length as traversed by ant a. Q is a constant that relates the amount of pheromones dropped by ants to the path. Different implementations of ACO will have different roles for pheromone update such as those suggested by MMAS [121] and ACS [122] implementations. A general pseudo-code for ACO is illustrated in Algorithm 1.

Algorithm 1. ACO Metaheuristic

```
Initialize ACO Parameters
while termination criterion not met do
    solution construction based on pheromone information
    pheromone intensification and evaporation
    daemon actions (optional)
end while
```

Algorithm 1 is based on three main stages, viz., solution construction, pheromone update, and daemon actions. The first two stages are highly dependent on the ACO implementation adopted, while the latter stage is optional and is user defined. It includes tasks that are not limited to a single ant such as performing a local search by ants or pheromone manipulation [113], [115].

3.3 Ant Colony Optimization Framework in MIDACO

The proposed optimization method in this thesis is based on an ACO framework applicable for mixed-integer domains. As opposed to the original ACO implementation presented in the previous section, the ACO implementation adopted in MIDACO is based on the extended ACO for continuous variables as proposed by [113]. The imitation of real ants as artificial ants walking on a connected graph to solve discrete domain problems is no longer valid for continuous domain problems as the latter corresponds to a different class. Nevertheless, as shown by Socha [123], it is possible to extend ACO to continuous domains without losing the original concept of ACO metaheuristic (i.e., probabilistic construction of solutions based on pheromone information). Thus, the main difference between ACOmi and the original ACO is in building and translating the pheromone information of ants. The internal ACOmi in MIDACO functions by an incremental building of solutions by probabilistic choice using a probability density function (PDF). Generally, a PDF is defined mathematically as any function with all values $\phi(x) \geq 0$ for all x domain that satisfies the property:

$$\int_{-\infty}^{\infty} \phi(x)\, dx = 1 \tag{3.4}$$

Out of all available PDFs, the Gaussian function holds many advantages such as ease of implementation and fast sampling time for random numbers [115]. As for continuous ACO metaheuristic, the Gaussian PDF is adopted contrary to the pheromone table in the original ACO [113]. However, a single PDF is not enough to focus on different promising areas of the search domain. Therefore, the multi-kernel Gaussian function ($G^i(x)$) is divided into several

one-dimensional PDF's ($g_\ell^i(x)$) each having a weight ($\mathcal{W}_\ell^i$), a mean (μ_ℓ^i), and a standard deviation (σ_ℓ^i) for every dimension i of the search domain. This is implemented with k_r number of kernels representing the Gaussian functions inside $G^i(x)$ as follows [115]:

$$G^i(x) = \sum_{\ell=1}^{k_r} \mathcal{W}_\ell^i \cdot g_\ell^i(x) = \sum_{\ell=1}^{k_r} \left(\frac{\mathcal{W}_\ell^i}{\sigma_\ell^i \sqrt{2\pi}}\right) e^{-0.5\left(\frac{x-\mu_\ell^i}{\sigma_\ell^i}\right)^2} \tag{3.5}$$

where i and ℓ refers to the i-th dimension of the decision variable for the MINLP and the ℓ-th kernel number of the individual $g_\ell^i(x)$ of weight $\mathcal{W}_\ell^i$, respectively. Moreover, as the sampled solution candidates are being guided within an individual Gaussian function $g_\ell^i(x)$ by the triplets ($\mathcal{W}_\ell^i$, μ_ℓ^i, σ_ℓ^i), they are characterized as the pheromones that constitute the biological model of the original ACO [115]. Aside from the PDFs' incremental way of solution construction, updating the pheromone information plays a significant part in ACOmi metaheuristic.

Updating pheromones information can be achieved by collecting the most promising solutions found by the search so far and storing them in a solution archive (SA). The SA size is equal to k_r kernels of d-dimensional solution vectors $\mathcal{S}_\ell$ corresponding to k_r objective function values [123]. Moreover, for constrained MINLP, the penalty function value corresponding to the violation of constraints is also stored in the SA, where the attraction of $\mathcal{S}_\ell$ is weighted against the penalty function value rather than the objective function value. More on the penalty function value calculation and the OPM used in MIDACO can be found in [116], while a brief description is given in the following section. The pheromone update process in ACOmi is directly linked to SA update mechanism. That is, the importance of a solution and its corresponding rank in the SA is obtained by calculating its weight $\mathcal{W}_\ell^i$ in a linear fashion according to the total number of kernels k_r [115]:

$$\mathcal{W}_\ell^i = \frac{(k_r - \ell + 1)}{\sum_{u=1}^{k_r} u} \tag{3.6}$$

where u refers to the solution index in the archive SA. Moreover, the sum of all weights is equal to 1 for every dimension i. This specific distribution of weights implies an established ascending linear order of priority for most promising solutions in the SA [115]. In other words, index-1 in SA is having the smallest objective function value (or penalty function value for constraint MILNP) that corresponds to the most important solution so far. While index-k_r, on the other hand, has the largest objective function value hence the least important in the search so far. Therefore, attempting to update the SA directory also implies a direct update of the pheromone information.

Since ACOmi is an evolutionary algorithm, it follows the basic principle for updating solutions based on the role: “Survival of the fittest!”. A solution fitness is ranked based on the value of its objective function (or penalty function for constrained MINLP). Furthermore, ACOmi uses ants (members of a population) to explore the solution search space of a given MINLP. Those individuals might have survived form different generations throughout the iterations process of the algorithm. Therefore, an evolutionary operator is introduced to build the best solutions and save them in the SA. For a set of k_r mixed-integer solutions stored in a solution archive set ($\mathcal{SA}$) such that [124]:

$$\mathcal{SA} = \{(x,y)^1, (x,y)^2, \cdots, (x,y)^{k_r}\} \tag{3.7}$$

In which they are arranged according to their fitness rank [124], that is:

$$\check{\mathcal{F}}(x,y)^{\mathfrak{g}} \geq \check{\mathcal{F}}(x,y)^{\mathfrak{h}}, \forall\, \mathfrak{g}, \mathfrak{h} \in \mathbb{N}^+ : \mathfrak{g} < \mathfrak{h} \leq k_r \tag{3.8}$$

where $\mathfrak{g}$ and $\mathfrak{h}$ are the solution’s $\mathcal{S}_\ell$ indices within a solution archive set $\mathcal{SA}$. Then a general evolutionary operator ($\mathcal{E}$) that creates $\mathcal{v}$ ants form k_r ants, wherein $\mathcal{v}$ and k_r are independent parameters such that $\mathcal{v} > k_r$, can be defined as [124]:

$$\mathcal{E} : (\mathbb{R}^{n_{con}} \times \mathbb{Z}^{n_{int}})^{k_r} \rightarrow (\mathbb{R}^{n_{con}} \times \mathbb{Z}^{n_{int}})^{\mathcal{v}} \tag{3.9}$$

Noting that the PDF is used to sample the very first generation of the algorithm, while the remainder generations of ants are produced by the evolutionary operator $\mathcal{E}$ using the multi-kernel Gaussian PDF utilizing the pheromone triplets ($\mathcal{W}_\ell^i$, μ_ℓ^i, σ_ℓ^i). Detailed explanation of the SA update process and new ant generation roles is covered thoroughly in the next paragraphs.

In constrained MINLP handling by ACOmi, the evaluation of any new promising solution or ant created within a generation will be in the form of comparing its corresponding penalty function value (level of attraction) to the attraction level of every solution stored in the SA directory so far. This is also undertaken in an ascending order from the best overall solution $\mathcal{S}_1$ to the worst overall solution $\mathcal{S}_{k_r}$ as stored in the SA. Based on that, any new solution that has a better attraction than the one already stored in the u-th index of SA will replace it in the u-th index, while solutions formerly saved in the u-th until $k_r - 1$-th indexes will be shifted up one index, implying that the solution $\mathcal{S}_{k_r}$ is discarded. However, if the new generated solution has less attraction than the one stored in the k_r-th index, then no changes will occur to the SA. The introduction of new attractive solutions into the SA translates to a positive pheromone update, while discarding the last solution indicates negative pheromone update. The positive and negative pheromone updates correspond to pheromone intensification and evaporation,

respectively, in the sense of the original ACO. More about pheromone rules for the continuous ACO implementation can be found in [113].

Contrariwise, the calculation of σ_ℓ^i is based on characteristics of the solutions stored in the SA. For every i dimension, the standard deviation is obtained considering all k_r solutions saved in the SA as follows [115]:

$$\sigma_\ell^i = \frac{dis_{max}(i) - dis_{min}(i)}{\#generation} \tag{3.10}$$

$$dis_{max}(i) = max\left\{\left|\mathcal{S}_\mathfrak{g}^i - \mathcal{S}_\mathfrak{h}^i\right| : \mathfrak{g}, \mathfrak{h} \in \{1, \cdots, k_r\}, \mathfrak{g} \neq \mathfrak{h}\right\} \tag{3.11}$$

$$dis_{min}(i) = min\left\{\left|\mathcal{S}_\mathfrak{g}^i - \mathcal{S}_\mathfrak{h}^i\right| : \mathfrak{g}, \mathfrak{h} \in \{1, \cdots, k_r\}, \mathfrak{g} \neq \mathfrak{h}\right\} \tag{3.12}$$

where $dis_{max}(i)$ and $dis_{min}(i)$ are, respectively, the maximum and minimum distance between single solution components $\mathcal{S}_\ell^i$ for all $\ell \in \{1, \cdots, k_r\}$ regarding the corresponding dimension i. $\#generation$ is the total number of generations produced so far. $\mathfrak{g}, \mathfrak{h}$ are solution's $\mathcal{S}_\ell^i$ indices within the set $\mathcal{SA}$. This σ_ℓ^i is used for all k_r Gaussian PDFs relating to a single dimension i of the decision variable. On the other hand, the means μ_ℓ^i are set according to the corresponding solution component (ant) in each dimension i for each kernel ℓ as follows [115]:

$$\mu_\ell^i = \mathcal{S}_\ell^i \tag{3.13}$$

By utilizing the triplets ($\mathcal{W}_\ell^i$, μ_ℓ^i, σ_ℓ^i), the creation process of a new ant based on the incremental construction of solution component is achieved by the following steps. First, for each dimension i, considering the weights $\mathcal{W}_\ell^i$, a mean μ_ℓ^i is selected randomly such that the means at the first index μ_1^i and the last index $\mu_{k_r}^i$ are having, respectively, the highest and lowest choosing probability. Second, using the obtained value of σ_ℓ^i as in (3.10) and sampling around the mean μ_ℓ^i, a random number is generated. Third, once all dimensions are considered, a new ant is generated while its corresponding penalty function values (level of attraction) is evaluated against the solutions stored in the SA. Based on the comparison outcome, the new generated ant will either be stored or discarded.

The main difference between ACOmi implementation proposed by Schlueter et al. [115] and the one proposed by Socha [125], is in the pheromone update rules for the triplets ($\mathcal{W}_\ell^i$, μ_ℓ^i, σ_ℓ^i). In [115], it was as suggested so far in this section (i.e., equations (3.6)-(3.13)), while in [125] those rules were proposed for μ_ℓ^i and σ_ℓ^i only. The other novel extension by Schlueter et al. [115], is the way how the algorithm handles mixed-integers. In particular, the

calculation approach for standard deviations of integer variables which enables better exploration around integer domains avoiding getting stuck in a non-improving situation. To enable the continuous multi-kernel Gaussian PDF to handle mixed integers, a sampling approach must be implemented to the continuous random numbers. Hence, a discretized version of $G^i(x)$ is generated by creating intervals around the integers and calculating the accumulative probability across the interval. For an integer variable d, the period for sampling is defined as $[d-0.5, d+0.5]$ and the probability around the integer d is given as [124]:

$$\phi_i^c(x) = G^i(x), i = \{1, \cdots, n_{con}\} \tag{3.14}$$

$$\phi_j^d(x) = \int_{d-0.5}^{d+0.5} G^{n_{con}+j}(x)\, dx\,, j = \{1, \cdots, n_{int}\} \tag{3.15}$$

where n_{con} and n_{int} are the total number of continuous and integer variable in the MINLP problem, respectively. i and j are subscripts for continuous and integer variables, respectively. $\phi_i^c(x)$ and $\phi_j^d(x)$ are the continuous and discrete Gaussian PDFs, respectively. The continuous multi-kernel Gaussian PDF and its respective discrete multi-kernel Gaussian PDF are illustrated by blue colour in Figure 3.2.

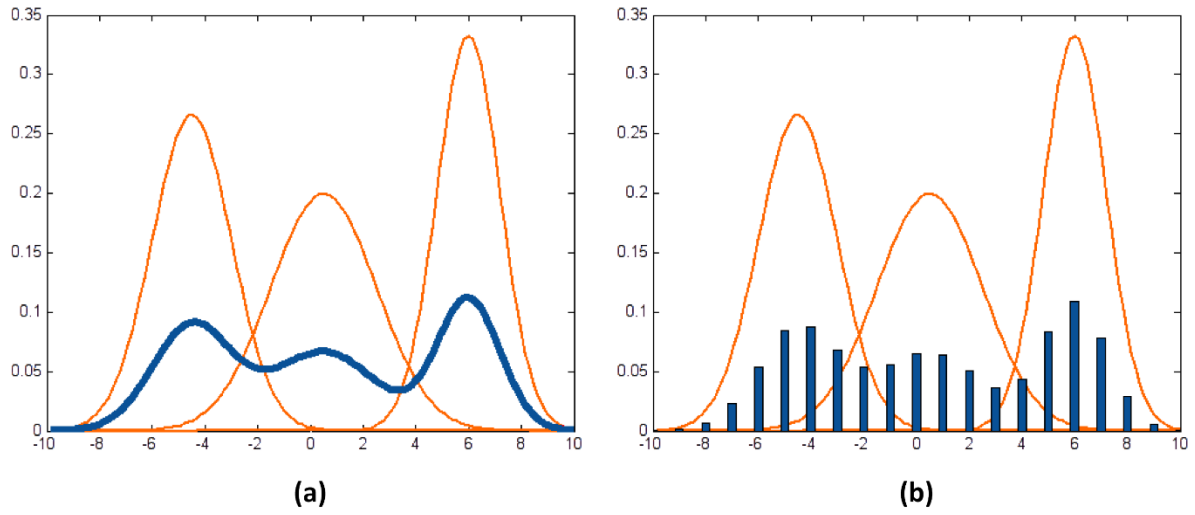

Figure 3.2: Multi-kernel Gaussian PDF: (a) continuous domain (b) discrete domain [126]

The sampling of the continuous PDFs in Figure 3.2 offers an easy extension of the continuous ACO into the discrete domains. However, one issue arises when considering a certain dimension i for a given integer variable where all solution components are of equal values, i.e., $\mathcal{S}_1^i = \mathcal{S}_2^i = \cdots = \mathcal{S}_{k_r}^i$. Then the standard deviation σ_ℓ^i around these components would be zero for that dimension. Consequently, no further improvement is possible to the solution component as the sampling has no deviation from the mean. This drawback of mixed-

integer extension for ACO is alleviated by considering deviations above certain lower limits of the integer variable. This constitutes a major improvement in the way extended ACO is handling integer variables without causing significant change in the ACO framework. Subsequently, the σ_ℓ^i given in equation (3.10) will become for an integer variable in the i-th dimension as [115]:

$$\sigma_\ell^i = max\left\{\frac{dis_{max}(i)-dis_{min}(i)}{\#generation}, \frac{1}{\#generation}, \frac{\left(1-1/\sqrt{n_{int}}\right)}{2}\right\} \tag{3.16}$$

According to this new formula, by the addition of the third term, the deviations based on the Gaussian PDFs for any integer will always be above the lower limit. This lower limit has been fixed by the third term and the number of integer variables n_{int}. In case n_{int} was significantly large, then the third term will converge to 0.5. This implies a deviation exists and it does offer a possibility to navigate further areas for the integer search domain. On the other hand, lower value of n_{int} will lead to smaller lower limits. Moreover, for an MINLP problem with one integer variable, the third term $\left(1-1/\sqrt{n_{int}}\right)/2$ will converge to zero. However, the middle term, $(1/\#generation)$, will ensure slower convergence for the standard deviation, hence more exploration around the mean is still possible. Nonetheless, in some MINLP with lower number of integers, eventually, the chosen integers would be as much close to the optimal value as possible, hence extra wide deviations for more exploration are not required.

3.4 The Oracle Penalty Method

As far as constrained optimization field is concerned, penalty methods are well-known techniques to account for constraint violations in any MINLP. To that end, constraint handling methods work by transforming the optimization problem from constrained type into unconstrained one. This can be attained by having a weighted approach to combine the objective function and the constraint function into one function to be minimized or maximized, this new function is often referred to as the cost function.

According to literature [127], [128], penalty methods can be broadly classified into simple and sophisticated methods. This classification is derived from the nature of how penalty factors are updated or how constraint violations are handled in a population. The most common simple penalty methods include: death and static methods [127], [128]. A general characteristic of simple methods is that they do not require additional parameters, thus making them a popular choice. However, these methods fall short in more complex optimization problems since they tend to be problem specific for static methods, or may require degree of convexity for most part of the search domain in the death methods [128].

Sophisticated penalty methods on the other hand, such as dynamic, adaptive, and annealing methods are more robust in handling challenging optimization problems. Nonetheless, the burden of large number of parameters, the sensitivity of some parameters, and parameters selection difficulty are identified as major drawback of many of those methods [128]. Due to the forgoing, a good penalty method is the one that combines the best of the two categories, i.e., having a broad range of applicability with a minimal number of parameters as possible.

Similarly, a universal penalty method that is applicable to almost every constrained optimization problem is the one adopted by the proposed optimization technique in this thesis. The convenience of the penalty method used in MIDACO, called the OPM, lies in having only one parameter to be tuned and is named as the Oracle or simply Ω [116]. The value of Ω is guessed by the user close to a predicted value for the objective function. This is due to lack of pre-existing knowledge about the global objective function value, which is common in many real-life optimization problems. Hence the name, oracle, was given to this method due to the forecast and predictive nature in the approach to determine the value of the parameter Ω. This implies that the oracle value is usually very similar to the objective function value or slightly larger.

However, to expand this method to real-life applications, it is vital that the OPM performs just as good with wrong or badly chosen oracles. Further details about the derivation and characteristics of the OPM method as well as sufficient numerical tests of its robustness can be found here [116]. For the sake of brevity, only the most essential mathematical formulation, shape of the penalty function, and the oracle update role is described in detail in this section.

The OPM utilizes a residual function which is a Norm-function used to map all constraints ($\mathcal{C}$) violations for an optimization problem [115]. Out of the many available Norm-functions, the l^1-Norm, also known as the Taxicab Norm, was selected to represent the residual function in OPM and is given below [116]:

$$res(z) = \sum_{i=1}^{\mathcal{C}_{eq}} |g_i(z)| - \sum_{i=1+\mathcal{C}_{eq}}^{\mathcal{C}} min\{0, g_i(z)\} \tag{3.17}$$

where the constraints from 1 to $\mathcal{C}_{eq}$ are the equality constraints, while the constraints from $\mathcal{C}_{eq} + 1$ to $\mathcal{C}$ are the non-equality constraints. $g_i(z)$ is the constraints handling function which gives the value of the constraint. z is the vector of all decision variables in the MINLP without explicit reference to the continuous and integer variables of the optimization problem such that $z := (x, y)$ [115]. This definition of the vector z enables the OPM to be generalized to any metaheuristic technique where z represents an iterate. However, in the ACO framework

within MIDACO, z here refers to an ant. Based on the residual and objective function values as well as using the oracle parameter, the penalty function $\mathcal{P}(z)$ can be obtained as [116]:

$$\mathcal{P}(z) = \begin{cases} \breve{\alpha} \cdot |\mathcal{F}(z) - \Omega| + (1-\alpha) \cdot res(z) - \breve{\beta}, & \text{if } \mathcal{F}(z) > \Omega \text{ or } res(z) > 0 \\ -|\mathcal{F}(z) - \Omega|, & \text{if } \mathcal{F}(z) \leq \Omega \text{ and } res(z) = 0 \end{cases} \tag{3.18}$$

where $\breve{\alpha}$ and $\breve{\beta}$ are parameters derived to influence $\mathcal{P}(z)$ and are functions of Ω only. As a result, a representation of the weight balancing between the residual function and the objective function is achieved by $\breve{\alpha}$ parameter. Whereas $\breve{\beta}$ on the other hand, acts as a bias factor for the penalty function and is affected by the number of generations for the penalty function. The values of $\breve{\alpha}$ and $\breve{\beta}$ are calculated, respectively, as follows [116]:

$$\breve{\alpha} = \begin{cases} \frac{|\mathcal{F}(z)-\Omega| \cdot \frac{6\sqrt{3}-2}{6\sqrt{3}} - res(z)}{|\mathcal{F}(z)-\Omega| - res(z)}, & \text{if } \mathcal{F}(z) > \Omega \text{ and } res(z) < \frac{|\mathcal{F}(z)-\Omega|}{3} \\ 1 - \frac{1}{2 \cdot \sqrt{\frac{|\mathcal{F}(z)-\Omega|}{res(z)}}}, & \text{if } \mathcal{F}(z) > \Omega \text{ and } \frac{|\mathcal{F}(z)-\Omega|}{3} \leq res(z) \leq |\mathcal{F}(z) - \Omega| \\ \frac{1}{2} \cdot \sqrt{\frac{|\mathcal{F}(z)-\Omega|}{res(z)}}, & \text{if } \mathcal{F}(z) > \Omega \text{ and } res(z) > |\mathcal{F}(z) - \Omega| \\ 0, & \text{if } \mathcal{F}(z) \leq \Omega \end{cases} \tag{3.19}$$

$$\breve{\beta} = \begin{cases} \left(\frac{|\mathcal{F}(z)-\Omega| \cdot \frac{6\sqrt{3}-2}{6\sqrt{3}}}{1 + \frac{1}{\sqrt{\#generation}}} \right) \cdot \left(1 - \frac{3 \cdot res(z)}{|\mathcal{F}(z)-\Omega|}\right), & \text{if } \mathcal{F}(z) > \Omega \text{ and } res(z) < \frac{|\mathcal{F}(z)-\Omega|}{3} \\ 0, & \text{otherwise} \end{cases} \tag{3.20}$$

According to equation (3.18), the penalty function in OPM has two distinctive cases, one when $\mathcal{F}(z) > \Omega$ and another when $\mathcal{F}(z) \leq \Omega$. As for the former case, and when $res(z)$ function is above zero as well, the $\mathcal{P}(z)$ function acts as a common penalty function type with the calculated values for parameters $\breve{\alpha}$ and $\breve{\beta}$ [115]. Whereas for the latter case when $res(z) = 0$, then $\mathcal{P}(z)$ is equivalent to the negative distance between the oracle and the corresponding objective function value.

Additionally, this situation resembles negative or zero values for the penalty function. A special case of the penalty function is when $\mathcal{F}(z) \leq \Omega$ and $res(z) > 0$, this implies that both parameters $\breve{\alpha}$ and $\breve{\beta}$ are zero which corresponds to an equality between the penalty function and the residual function, i.e., $\mathcal{P}(z) = res(z)$.

The penalty function corresponding to different residual and objective function values is depicted in Figure 3.3 [115].

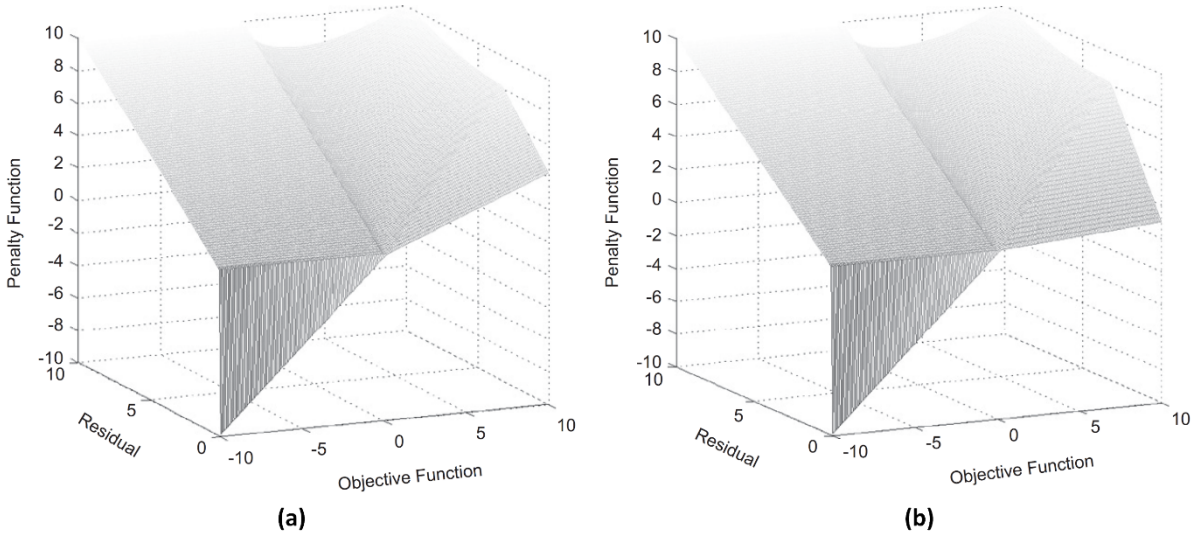

Figure 3.3: The oracle penalty function: (a) $\Omega = 0$ and $\#generation = 1$ (b) $\Omega = 0$ and $\#generation = 100$ [115]

The graphical 3-D shape of Figure 3.3 illustrates the penalty function values considering a given oracle value of zero within the first and hundredth generations. It's worth noting that the impact of Ω value on $\mathcal{P}(z)$ graphical shape is non-existence. This implies that the values above or below zero for Ω will result in movement to the right or to the left across the objective function axis, respectively, for $\mathcal{P}(z)$ values. Moreover, the case when $\mathcal{P}(z) = res(z)$ is illustrated by the upper oblique plane on the left hand-side of both Figure 3.3(a) and Figure 3.3(b). Inversely, the case when $\mathcal{P}(z) \leq 0$ is demonstrated by the orthogonal triangular shape on the left-hand side of Figure 3.3(a) and Figure 3.3(b). As for the upper right-hand side oblique shapes of the 3-D figures in Figure 3.3, these are influenced by the two middle terms of $\breve{\alpha}$ in equation (3.19).

The significance of the two middle terms of $\breve{\alpha}$ plays a vital role in OPM by shifting the balance of weights between the objective function $\mathcal{F}(z)$ and the residual function $res(z)$. Accordingly, more control is exerted on the search efforts toward either one of these functions [115]. For the first middle term of $\breve{\alpha}$, the resultant value is usually in the range of $\breve{\alpha} < 0.5$ and that indicates a balance shift towards the residual function. However, if the prevalent term was the second middle term, then the resultant value would be in the range $\breve{\alpha} \geq 0.5$ and that implies favouring of the objective function over the residual function. Lastly, the impact of $\breve{\beta}$ is in the form of higher bias in penalizing any iterate with residual value less than $|\mathcal{F}(z) - \Omega|/3$. The bias degree increases with the higher number of generations. This can be seen in the frontal triangular shape of the right-hand side of Figure 3.3(b) by stronger bias at the hundredth

generation. While the bias was less noticeable looking into the upper right frontal triangular shape of Figure 3.3(a) where the generation number was still at 1.

As discussed earlier in this section, the OPM is a universal constraint handling technique that is built on one user-defined parameter (i.e., Ω). This dictates that in most cases, the guessed oracle is at best close to the feasible objective function value or slightly higher. Nevertheless, it is primitive to envisage that a poorly guessed oracle would negatively impact the performance of a robust method such as the OPM. Therefore, a self-tuning technique had been developed to constantly improve on the guessed oracle based on the obtained feasible or infeasible objective function value. The oracle update role was developed after several numerical tests for over- and under-estimated oracles [115], [116]. At first, the oracle should be selected at a sufficiently low value (e.g., -10^{12}) to enable the dynamic penalty approach by OPM. If the very first run was successful in attaining a feasible solution, then the new oracle value will be changed to this feasible solution and so on, where only feasible solutions will be used to update future values of Ω. However, if the first run returned infeasible solution, then Ω is set at a sufficiently high value (e.g., 10^{12}) and that will push the penalty function to the upper left-hand side oblique plane for the 3-D shapes of Figure 3.3. Subsequently, the method will concentrate on finding any feasible solution initially and conclude by a death penalty approach as soon the feasible $\mathcal{F}(z)$ is attained (i.e., moving on the front orthogonal triangular plane on the left-hand side of the 3-D shapes of Figure 3.3).

3.5 The Hybrid Strategy in Mixed-Integer Ant Colony Optimization

So far, the general framework for expanding the ACO into mixed-integer domains as well as the important aspects of the robust penalty method used, i.e., OPM, were given. Subsequently, more detailed description about the implementation and structure of ACOmi as used within the MIDACO algorithm is presented here. The ACOmi metaheuristic presented in this work consists of four novel heuristic stages, viz., dynamic population heuristic (DPH), single dimension tuning (SDT) heuristic, weighted average best ant (WABA) heuristic, and final stage heuristic (FSH) [129].

The execution of ACOmi involves incorporating a deterministic local solver called the mixed-integer sequential quadratic programming (MISQP) within the extended ACO metaheuristic routine as proposed by [130]. This combination of stochastic and deterministic solvers is believed to improve the overall performance of the ACOmi [115]. Moreover, within the framework of ACOmi, the fitness of an ant is based on its designated objective function result or that of its penalty function value in case of a constrained MINLP. A detailed explanation of the four heuristic stages is given as follows:

3.5.1 Dynamic Population Heuristic

The dynamic nature here implies that the population size in ACOmi is not constant, instead it changes value according to a heuristic. Three main parameters are used in DPH to dynamically obtain the actual population size (N_{pop}). These include the minimum ants population allowed per generation (N_{ants}), the maximum dynamic ants population allowed (DP_{max}), and the iteration where the maximum dynamic ants population is reached (DP_{mean}) [129]. Furthermore, ensuring a minimum number of ants in each generation corresponds to having a population size that is always in the range $N_{pop} > N_{ants}$. Likewise, by avoiding a constant population size, more efficient distribution of ants is obtained in every generation, where the growth and decay in ants population occurs in a linear fashion [129].

The DPH has two different stages, before and after reaching the maximum population value of DP_{max}, and this is marked by an iteration number equals to DP_{mean}. The stage before DP_{max} is reached is quite critical where more ants are required in every generation, this shall provide important searching capability by the algorithm [129]. Once that threshold has been reached (i.e., $N_{pop} = DP_{max}$), then population of ants is instantly dropped down by 50%. From there onward, the dynamic population of ants continues to decrease in a linear fashion until it reaches the minimum population allowed N_{ants}. The graphical representation of the dynamic population size N_{pop} in ACOmi over a total number of iterations (i.e., $\#iteration$) equals to 150 is shown in Figure 3.4 [129].

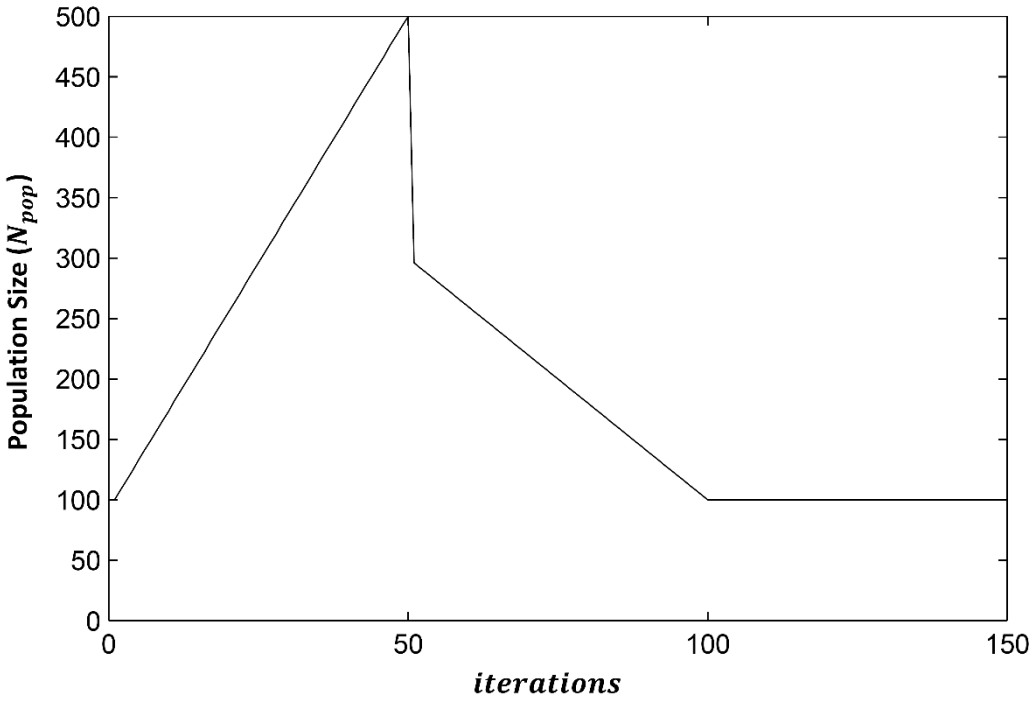

Figure 3.4: Dynamic population size during 150 iterations using the parameters as follow: $N_{ants} = 100$, $DP_{max} = 500$, $DP_{mean} = 50$ [129]

From Figure 3.4, one can see the gradual decline in population size after reaching the maximum number of ants. Noteworthy here is that the sudden drop in dynamic population to 50% after completing the critical stage will significantly reduce the calculation time as less function evaluations are required. This is attributed to the low significance given to search stages after the critical search phase has been reached at the DP_{mean} iteration. Accordingly, a pseudo-code for dynamic population heuristic is given in Algorithm 2 [129].

Algorithm 2. DPH Heuristic

Initialize DPH parameters
if $\#iteration \leq DP_{mean}$ **then**
  $N_{pop} = \left(N_{ants} + (DP_{max} - N_{ants}) \cdot \frac{\#iteration - 1}{DP_{mean} - 1}\right)$
else
  if $\#iteration > DP_{mean}$ **and** $\#iteration \leq 2 \cdot DP_{mean}$
    $N_{pop} = \left(DP_{max} + (N_{ants} - DP_{max}) \cdot \frac{\#iteration}{2 \cdot DP_{mean}}\right)$
  else
    $N_{pop} = N_{ants}$
  end if
end if

This simplified algorithm for DPH, i.e., Algorithm 2, shall enable the implementation of the dynamic population heuristic and getting the desired N_{pop} within the ACOmi framework.

3.5.2 Single Dimension Tuning Heuristic

The tuning action in this stage evolves around improving the current best solution of the highest rank in the SA, i.e., $\mathcal{S}_1^i$. This is obtained by sampling randomly around the current best component of $\mathcal{S}_1^i$ out of its d-dimensional components using an appropriate deviation approach. This heuristic aims to slightly improve the current best solution for problems with high number of dimensions d [129]. Furthermore, in MINLPs, the SDT heuristic shall offer better treatment of variables that belong to the integer domain [129]. For continuous variables domain, i.e., $i \leq n_{con}$, the SDT starts by creating an ant a_{sdt}^i as given by the following equation:

$$a_{sdt}^i = \mathcal{S}_1^i + \frac{\left(a_u^i - a_l^i\right) \cdot a_{rnd}^i}{\#iteration} \tag{3.21}$$

where a_u^i and a_l^i are, respectively, the upper and lower limits of the interval for the created ant a_{sdt}^i. Such limits, along with $\#iteration$, shall create the appropriate deviation required around the best current component $\mathcal{S}_1^i$. a_{rnd}^i is a d-dimensional vector ant with a uniformly distributed random number covering the range $[0,1]$. As for integer variables domain

on the other hand, i.e., $n_{con} + 1 \leq i \leq n_{int}$, a random unity adjustment is applied to the current best component by comparing an additional uniform random number distribution within the interval $[0,1]$ to the value 0.5 as follows [129]:

$$a_{sdt}^{i} = \mathcal{S}_{1}^{i} + \begin{cases} 1, & \text{if } a_{rnd}^{i} \geq 0.5 \\ -1, & \text{if } a_{rnd}^{i} < 0.5 \end{cases} \tag{3.22}$$

The SDT heuristic stage amounts to substantial and additional function evaluation burden on the ACOmi algorithm, where d function evaluations are required per iteration. This is attributed by the need to tune every single dimension i of the current best solution for every iteration to achieve the desired improvement in $\mathcal{S}_{1}^{i}$. It is to be pointed out that when $\mathcal{S}_{1}^{i}$ has reached its boundaries, further created a_{sdt}^{i} will lead to undesired violations in $\mathcal{S}_{1}^{i}$. In this case, the SDT heuristic is abandoned for the saturated current best solution.

3.5.3 Weighted Average Best Ant Heuristic

Contrary to SDT heuristic, the WABA heuristic target is to create a better solution by taking all ranked solutions in the SA. What is more, the WABA is computationally cheap compared to SDT as no uniform random number sampling is required at all. This is due to the need to perform one additional function evaluation per iteration contrary to the d function evaluations per iteration required by SDT. The WABA heuristic works by creating a weighted average ant considering all archive's k_r solutions (i.e., $\mathcal{S}_{\ell}^{i}$) as follows [129]:

$$a_{waba}^{i} = \sum_{\ell=1}^{k_r} \mathcal{W}_{\ell}^{i} \cdot \mathcal{S}_{\ell}^{i} \tag{3.23}$$

where $a_{waba}^{i}$is the weighted average created ant for every dimension i considering the weight $\mathcal{W}_{\ell}^{i}$ as linearly calculated in the previous sub-section. However, if the solution dimension belonging to $n_{con} + 1 \leq i \leq n_{int}$, then $a_{waba}^{i}$is corrected to the next available integer [129].

3.5.4 Final Stage Heuristic

This heuristic stage is where ACOmi will perform its final routine by executing a local search procedure around the current best solution saved in the SA, that is, $\mathcal{S}_{1}^{i}$. The FSH is initiated once a certain degree of deterioration in the fitness of generated ants is detected. The degree of deterioration is determined at every iteration of the algorithm based on certain criteria to judge non-improvement in the objective function (or penalty function value in constrained problems). In other words, considering every two successive iterations, the

difference in fitness between the current and the previous best ants is calculated. That is, the difference in maximum (da_{max}) and average (da_{ave}) fitness between consecutive best ants is attained. The values of da_{max} and da_{ave} provide the threshold for the final stage heuristic, where a Boolean constant is assigned to an FSH flag called $stage_{final}$ such that [129]:

$$stage_{final} = \begin{cases} 1, & \text{if } da_{ave} < {da_{max}}/{W_{final}}, \left(W_{final} \in \mathbb{N}^{+}\right) \\ 0, & \text{otherwise} \end{cases} \tag{3.24}$$

where a true value to $stage_{final}$ flag will indicate initiation of the FSH. W_{final} is weight constant that relates da_{ave} with da_{max}. A reasonable value for the weight constant W_{final} should be set to 100 [129]. Similarly, when $stage_{final}$ is active this will imply that no further global search is considered by the algorithm. Once FSH is activated, the hybrid algorithm of ACOmi will call the deterministic local solver, i.e., MISQP [130], to perform local search using the current best solution $\mathcal{S}_1$. The aim of this local search is to reach a value equal or lower than a user desired but feasible value for the objective function referred to here as $\mathcal{F}_{ex}$. Nonetheless, the MISQP might fail to find $\mathcal{F}_{ex}$, hence a restart in the ACOmi algorithm with a concentrated population around $\mathcal{S}_1$ is excuted after clearing the SA directory. This way the triplets ($\mathcal{W}_\ell^i$, μ_ℓ^i, σ_ℓ^i) will be initialized with means identical to those from $\mathcal{S}_1^i$ with very slight deviation around them to avoid retuning again to the solution $\mathcal{S}_1$ [129].

Meanwhile, with multiple restarts of the algorithm around the current best solution $\mathcal{S}_1$, the MISQP solver might be called multiple times as well. The frequency of the deterministic local solver calls per iteration is observed by a variable called $freq_{call}$. Furthermore, as ACOmi is a hybrid algorithm, calling the local solver for further exploitation of the local search space is optional. Meaning that the algorithm can operate with or without the MISQP solver based on the user's choice. This can be determined by having two choices for running the local solver, either frequently at every generation using best solution $\mathcal{S}_1$ (i.e., option 1: heavy local solver use) or at least once at the very last generation using $\mathcal{S}_1$ as the starting point (i.e., option 2: light local solver use).

3.6 Implementation of Mixed-Integer Ant Colony Optimization

There are two major phases in the application of ACOmi to solve MINLP, those are ACO_{main} and ACO_{final}. In the beginning, a random initialization of the pheromones, i.e., the triplets ($\mathcal{W}_\ell^i$, μ_ℓ^i, σ_ℓ^i) as described in section 3.3, is performed. By utilizing the DPH, a dynamic population of ants (N_{pop}) is established throughout the ACOmi search process as explained in sub-section 3.5.1. Subsequently, within ACO_{main} phase, the best current solution $\mathcal{S}_1^i$ and the

averaged best solution out of all solutions $\mathcal{S}_\ell^i$ in SA are improved in every generation of ants according to SDT and WABA heuristics, respectively. Once a true condition of $stage_{final}$ flag is determined using equation (3.24), the ACO_{final} phase commence by performing local search around the current best solution obtained so far. This can be achieved by either calling the local solver MISQP or initiating a restart by the ACOmi using means identical to those of $\mathcal{S}_1^i$ as demonstrated in FSH. The complete ACOmi pseudo-code as presented in this thesis is given in Algorithm 3 [115], [129].

Algorithm 3. ACOmi

Initialize termination criteria: Set ($\mathcal{F}_{eval}$, $\mathcal{F}_{time}$, $\mathcal{F}_{ex}$)
Initialize dynamic population N_{pop} parameters: Set (N_{ants} , DP_{max} , DP_{mean})
Initialize kernel size and oracle: Set (k_r, Ω)
Initialize $option\#1$ (MISQP heavy runs around $\mathcal{S}_1$ initial point): Set ($option\#1$ flag: On/Off)
Initialize $option\#2$ (MISQP light runs around $\mathcal{S}_1$ initial point): Set ($option\#2$ flag: On/Off)
Initialize empty SA with size k_r
Random pheromone ($\mathcal{W}_\ell^i$, μ_ℓ^i, σ_ℓ^i) initialization
while termination criteria not met **do**
  if $stage_{final} = 0$ **then**
    for i $= [1, N_{pop}]$
      Construct ant a_i
      Evaluate fitness of ant a_i against constraints
      Update SA with ant a_i
      Improve best ant a_{sdt}^i using SDT heuristic
      Improve SA by ant a_{waba}^i using WABA heuristic
    end for
    Update pheromone by SA information
    if $ACO_{final} = 0$ **then**
      Evaluate $stage_{final}$ flag
      if $stage_{final} = 1$ **then**
        Set $ACO_{final} = 1$
      end if
    else
      Run MISQP as $option\#1$
    end if
  else
    Run MISQP as $option\#2$
    Set $stage_{final} = 0$
    if terminate criteria not met **then**
      Chose pheromone according to $\mathcal{S}_1$
      Clear SA
    end if
  end if
end while

The ACOmi in Algorithm 3 above is terminated when a specific criterion, which is checked at every iteration of the algorithm, is reached. The termination criteria are dependent on three factors, viz., maximal function evaluations ($\mathcal{F}_{eval}$), maximal computation time ($\mathcal{F}_{time}$), or the feasible objective function value ($\mathcal{F}_{ex}$). The latter is referred to as an algorithmic stopping

condition which depends on a value that is equal or below a user defined value. Based on multiple runs of ACOmi on several benchmark optimization problems, the developers have made some recommendation on how to setup the algorithm for best results [115], [129]. Those include, but not limited to, setting the kernel number to a suitable integer value such that $k_r \in [5-50]$; the minimum number of ants per generation should be an integer multiple of k_r such that $N_{ants} \in [10-500]$; the maximal number of ants per generation should be an integer multiple of N_{ants} such that $DP_{max} \in [20-2000]$; the iteration at which the maximum number of ants is achieved should be half to four times k_r such that $DP_{mean} \in [2-200]$.

3.7 Multi-Objective Optimization

Multi-objective optimization belongs to a class of complex optimization problems that considers more than one objective simultaneously. That is, there exist no one global solution for all considered objectives concurrently. Contrary to single objective problems, where a single solution may exist as the global optimal for a given problem, multi-objective problems will offer a set of equally traded non-dominated (Pareto optimal) solutions where no one solution dominates (better than) the other. The set that keeps all non-dominated solutions is referred to as the Pareto front. Moreover, when more than three objectives are considered these optimization problems are often referred to as many-objective optimization which are far more complex to solve efficiently [117], [126]. Likewise, the handling of many-objective optimisation in MIDACO involves a decomposition technique to fragment the original many-objective problem into a group of several single-objective sub-problems. These decomposed problems are then evaluated in a massive parallelization strategy as implemented by reverse communication technique [117], [126], [131]. The utopia-nadir balance concept was introduced in MIDACO to enable many-objective optimization using the above-mentioned decomposition approach. Furthermore, the advantage of utopia-nadir balance against traditional muti-objective techniques such as non-dominated sorting is concentrating the algorithm search effort on a user defined area of interest. This shall enhance the algorithm exploration ability by focusing on a particular area of the Pareto front, unlike non-dominating sorting technique which gives equal significance to all Pareto front solutions [126]. In that regard, a utopia (U_i) of an individual objective function $\mathcal{F}_i(x)$ is defined as an indicator of the best global minima among all $\mathcal{F}_i(x)$ values such that [118]:

$$U_i = min\{\mathcal{F}_i(x) \; \forall \; x \in \mathbb{F}\} \tag{3.25}$$

where $\mathbb{F}$ is the set of all feasible solutions x for a constrained optimization problem. Conversely, the nadir (N_i) of an objective $\mathcal{F}_i(x)$ corresponds to the worst value with every x solution associated with a utopia U_k of an objective function $\mathcal{F}_k(x)$. The nadir is given by [118]:

$$N_i = max\{\mathcal{F}_i(x)\ \forall\ x : \exists\ k\ \neq i : \mathcal{F}_k(x) = U_k\} \tag{3.26}$$

Given an $\mathcal{O}$ multi-objective problem having an $\hat{S}$ decomposed single-objective sub-problems, by denoting j for a decomposed sub-problem and using the utopia-nadir information, then we can define for an x optimal solution in each individual objective function, respectively, the weighted distance $d_i^j(x)$ and the average distance $D_j(x)$ as follows [118]:

$$d_j^i(x) = \ w_i^{\ j} \cdot \left(\frac{\mathcal{F}_i(x)-U_i}{N_i-U_i}\right) \tag{3.27}$$

$$D_j(x) = \ \frac{\sum_{i=1}^{\mathcal{O}} d_i^j(x)}{\mathcal{O}} \tag{3.28}$$

where $w_i^{\ j}$ is an $\mathcal{O} \times \hat{S}$ sized matrix of weights with values between $[0,1]$. Based on the average and weighted distances as well as the utopia-nadir information, a scalar function denoted as the balance function $B_j(x)$ is introduced. Subsequently, the average distance for each solution x is known with respect to the utopia and nadir values of each $\mathcal{F}_i(x)$ [118], [126].

$$B_j(x) = \ \sum_{i=1}^{\mathcal{O}} \left| d_i^j(x) - D_j(x) \right| \tag{3.29}$$

Figure 3.5 illustrates the utopia-nadir-balance concept for two objectives with equal weights [118].

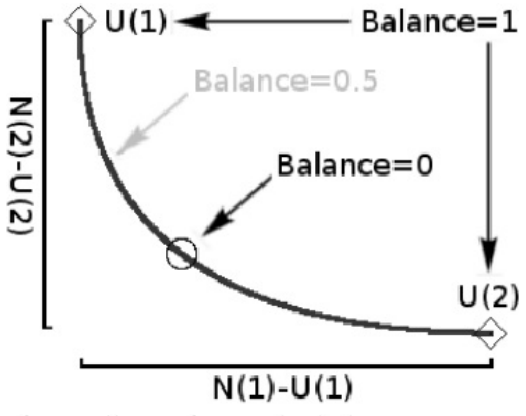

Figure 3.5: Utopia-Nadir-Balance concept [118]

From Figure 3.5 we note that $B_j(x)$ can have any value between 0 and 1, with the former being the default (central) value. Based on the average distance $d_i^j(x)$ and balance function $B_j(x)$, a target function $T_j(x)$ for each j sub-problem is created and solved as a single objective by a separate ACOmi instance [118]:

$$T_j(x) = \sum_{i=1}^{\mathcal{O}} d_i^j(x) + B_j(x) \quad (3.30)$$

Considering the number of decomposed sub-problems, a total of $\hat{S}$ target functions will be created $T_j \in \{T_1, T_2, \cdots, T_{\hat{S}}\}$, where each is evaluated in parallel with an independent ACOmi instance. The number of parallel ACOmi instances in each thread is equal to the number of decomposed sub-problem [117]. However, for every given interval, all independent ACOmi instances would share the utopia-nadir and best solution information in between them. Eventually, a master framework will aggregate all non-dominated solutions found by all ACOmi slave instances to form an approximate set of the final non-dominated solution for the original multi-objective problem [117]. As for the very first sub-problems evaluation by the individual ACOmi instances, no utopia and nadir information are available. Hence, a heuristic solution is proposed to create the first target functions based on weights assigned to the single objective problems as follows [118]:

$$\hat{T}_j(x) = \sum_{i=1}^{\mathcal{O}} w_i^j \cdot \mathcal{F}_i(x) \quad (3.31)$$

Noting that the algorithmic performance of MIDACO is highly dependent on the initial target function $\hat{T}_j(x)$ and the subsequent one of $T_j(x)$ [117], [132].

3.8 MIDACO Solver Features and Parameters

MIDACO software is a general-purpose global optimization solver that offer black-box programming capabilities. This implies that MIDACO does not require knowledge of the theory or implementation of the objectives and constrains, thus giving a complete freedom to the user. Besides, there are no specific conditions for the objective functions or constraints in MIDACO. This means, an objective function or constraint can be highly non-convex, nonlinear, non-differentiable, non-smooth, discontinuous, or even stochastic noise. MIDACO is a hybrid optimization solver that offers back-tracking local search to enhance exploitation capability. Moreover, for CPU expensive optimization problems where each function evaluation consumes around a second or more, MIDACO offers a very efficient parallelization strategy to significantly expedite the running time. MIDACO can handle hundreds of objectives with thousands of constraints and 100,000 decision variables. However, the free version of MIDACO is limited to four decision variables.

One of the best features of MIDACO is the fast convergence ability for many benchmark problems, that means MIDACO can perform thousands of functions evaluations in a reasonable amount of time. Two main stopping criteria exists in MIDACO, viz., hard and algorithmic. As for hard criteria, the maximum number of function evaluations (MAXEVAL) or

the maximum elapsed time allowed (MAXTIME) would determine the termination of MIDACO. Conversely, algorithmic stopping is determined by the achievement of a specific objective function value or non-improvement in the objective function value for some consecutive iterations number. Another distinctive feature of MIDACO is the default parameter choice, where automatic parameter selection is very helpful in many optimization problems. There are 14 parameters that directly influence the solution provided by MIDACO, the exploration and exploitation of the algorithm, and the overall calculation time. The default value for all parameters is zero which corresponds to a specific value of that parameter in the internal algorithm implementation. Below is brief description of these parameters as follows [126]:

- ACCURACY: This parameter is responsible for the tolerance degree in constraint handling. Hence, higher value of ACCURACY like 0.1 or 0.01 will lead to a small degree of constraint violation. Conversely, a very small ACCURACY value like 0.00001 or less will apply strict constraint violation penalties.
- SEED: This parameter is one of the most influential in stochastic optimization techniques as it controls the seed for the internal random number generator. A fixed integer value of SEED will normally reproduce the results by MIDACO for the same machine, while a repeated run with multiple integer SEEDs will result in different solutions by MIDACO. Subsequently, having multiple SEED runs will increase the probability of achieving the global optimum solution. Thus, transforming the optimization technique from a stochastic choice into a deterministic approach with higher degree of certainty about the global optimal solution.
- FSTOP: This parameter is responsible for implementing the algorithmic stopping criterion based on an objective function value. The user can set FSTOP to a value close or equal to the desired objective function value. Subsequently, the algorithm will halt as soon as FSTOP value is obtained or anything below it.
- ALGSTOP: This parameter has a similar class as FSTOP, since it handles an algorithmic stopping criterion as well. However, ALGSTOP works by specifying the number of internal ACOmi restarts before any improvement in the objective function value. By setting ALGSTOP to a positive integer like 12, MIDACO will wait for twelve consecutive internal restarts of ACOmi before it terminates in case of non-improving objective function value. This parameter is known to enhance the algorithm speed, albeit no guarantee in the improvement of the objective function value.
- EVALSTOP: This is the third parameter that handles an algorithmic stopping criterion. Unlike ALGSTOP, EVALSTOP is concerned with the number of function evaluations executed before any noticeable improvement in the objective function, otherwise the algorithm will terminate. Furthermore, EVALSTOP is less computationally expensive than

ALGSTOP parameter. Another parameter imbedded within EVALSTOP is the precision. This gives the criteria of how to judge improvement in the objective function or not in the form of a percentage. For example, to make MIDACO stop after 500 function evaluations without improvements in the objective value within a percentage of 0.15%, then EVALSTOP should be set to 500.0015.

- ANTS: The ANTS parameter is used to fix the number of ants or iterates (a major iteration in ACOmi) within one generation. This parameter must be used in conjunction with KERNEL, which might be promising for some problems and could expedite convergence. However, using a default value for this parameter will allow MIDACO to dynamically change the number of populations per generation.
- KERNEL: Inversely, KERNEL is responsible for fixing the number of kernels in the multi-kernel Gaussian PDF. The kernel number is equal to the number of solutions stored in the SA. Similarly, KERNEL must be used alongside the ANTS parameter. A lower value of KERNEL such as 2 will increase the convergence speed, albeit increasing the probability of local optimal solutions. Conversely, a higher number of KERNEL like 50 will slow the solution convergence, but it will increase the globality chances of the optimal solution.
- ORACLE: For constrained problems, ORACLE is the reasonable value given by the user to Ω within the OPM implementation in MIDACO. If the ORACLE value was set to zero, then MIDACO will use the default value of 10^9 for Ω (i.e., ORACLE).
- FOCUS: This is one of the most advanced parameters of MIDACO, which dictates how much exploitation is done locally by the algorithm around the current best solution. By tuning FOCUS to an integer value, the algorithm will perform local search and become greedier. Hence, expediting the convergence speed in many problems. Furthermore, FOCUS is very helpful in refinement runs, where the user is having high confidence of the solution in a particular area. The influence of this parameter is seen as implicitly dictating the call frequency of MIDACO's pseudo-gradient backtracking line-search local solver.
- BALANCE: This is another highly influential parameter by MIDACO, where the advantage of certain objective over the others can be determined. If BALANCE was set to zero, then MIDACO will focus its multi-objective optimization search at the centre of the Pareto front. However, if an integer value equal to the index number of a given objective was given to BALANCE, then MIDACO will give the highest weight for that objective. If BALANCE was set as a decimal number, then MIDACO will distribute the balance of weights (importance) for each objective based on its index and the decimal value given for that index. The balance of weights from lower to higher for a decimal number corresponds to a scale from 1 to 9, respectively. For a two objectives problem, setting BALANCE as 0.28 will give importance to the second objective four times as much the importance of the first.

- EPSILON: Another multi-objective problem parameter is the EPSILON parameter which dictates the precision for Pareto points filtration by MIDACO. By default, the value for EPSILON is 0.001 for two-objective problems and 0.01 for three or more objective problems. Having a very low value of EPSILON like 0.00001 will result in many Pareto points collection with very small difference between them. However, such high number of points will slow down the speed of MIDACO calculation. Inversely, high value of EPSILON like 0.1 will result in lower number of Pareto points but with much more information. This lower number of Pareto points collected shall increase the speed of MIDACO algorithm.
- PARETOMAX: This parameter is given to limit the number of Pareto points collected by MIDACO with a default value of 1000. Subsequently, higher values of PARETOMAX will result in slower calculation times with more memory required. Conversely, a much lower value such as 50 will result in faster calculation times with less memory required.
- CHARACTER: Using this parameter will activate a pre-defined internal character setting in MIDACO. Three values for CHARACTER are used, viz., 1, 2, and 3. Using 1 will produce more fine-grained search process for continuous variables, while 2 will result in coarse-grained search for integer variables. Lastly, using the setting 3 will result in having solutions generated to satisfy a special constraint within MIDACO called all-different. However, leaving CHARACTER as zero will automatically enable MIDACO to decide the problem type and the search character it needs.
- PARALLEL: Using this parameter will activate parallelization option in MIDACO. If a single function evaluation is CPU-time expensive, then an integer value of 2 or above is given to PARALLEL. This value will determine the parallelization factor of MIDACO. Assigning a value larger than the available cores/threads in the machine will enable overclocking parallelization. This is beneficial when average single evaluation time significantly varies.

3.9 Summary

In this chapter, the proposed metaheuristic optimization technique, MIDACO, is presented in detail. General framework for discrete optimization method ACO is presented, followed by the extension of ACO to continuous and mixed-integer domains. Moreover, a robust and universal penalty method is highlighted as OPM which depends only on one parameter, the oracle. Further emphases were given to the extended ACO implementation and its hybridization strategy in four heuristic stages: dynamic population, single dimension tuning, weighted average best ant, and final stage. Moreover, the multi-objective optimization by the decomposition approach of MIDACO as well as the utopia-nadir-balance concept were explained in detail. Lastly, a brief description of MIDACO's parameters and their common usage were also provided.

4 Chapter Four: Load Flow Analysis in Islanded Microgrids

4.1 Introduction

In this chapter, the three load flow methods for IMG that were developed in this thesis are presented. As mentioned previously in Chapter 2, Jacobian based LF methods are not suitable for distribution systems with high R/X ratio. Furthermore, most IMGs are ill-conditioned networks with radial or weakly meshed topologies, and that makes derivative free LF methods more popular. This new class of load flow methods are known as BFS [90]. Furthermore, different variations were proposed to BFS which can be broadly classified into basic and quadratic BFS methods [105]. However, the three proposed LF methods in this thesis to solve the IMG power flow problem are based on the basic and robust BFS given in [106]. Conversely, load flow analysis in IMG belongs to a completely different class of power flow analysis studies. In one hand, IMG does not have a slack bus like grid-connected LF, where an infinite bus with fixed voltage is responsible for balancing any power mismatch.

On the other hand, IMG system frequency is not fixed due to the absence of a strong grid to withstand any load variation. Additionally, in an IMG, generation units are setup to operate in V-f control, thus sharing the load proportionally. Unlike the grid-connected MG wherein DGs are restricted to PQ control regardless of load change [69]. As mentioned previously, three load flow methods for IMG are developed, viz., SBFS, SBFS-II, and GBFS. The first two methods are based on a global voltage at a reference bus distributed among all DGs, whereas SBFS-II has faster convergence and fewer number of loops than SBFS. Contrariwise, GBFS offers more general approach to solve IMG power flow by considering local voltage measurement at each generating bus. The three methods were applied to the IEEE 33-, 69-, and 118-bus systems with promising convergence reported in all investigated cases. Likewise, the proposed LF methods were compared with other published BFS-based load flow methods such as DBFS [107], MBFS [108], and NBFS [109] and a real time simulator such as PSCAD/EMTDC. Moreover, to validate the efficacy of GBFS, an additional six bus IMG was used to demonstrate the significance of the stochastic dynamic damping factors proposed in GBFS.

4.2 Load Flow Analysis in Droop Controlled Islanded Microgrids (DCIMG)

In this section, the developed load flow analysis is described in more detail, including the basic BFS method for grid-connected microgrid.

4.2.1 Load Flow Analysis for Grid-Connected Microgrid

The basic unit for LF analysis in this thesis is derived from the conventional BFS technique for grid-connected radial and weakly meshed distribution networks [106]. This BFS method is very efficient, robust, and offer better solution to distribution systems with high R/X ratio if compared against Jacobian based methods [90], [104], [106]. The main three elements of BFS are, namely, equivalent current injects, branch-inject branch-current matrix (BIBC), and branch-current bus-voltage matrix (BCBV). For a distribution network, the injected apparent power (S_i) at the bus i in the c-th iteration is given by:

$$S_i^c = P_i^c + jQ_i^c \tag{4.1}$$

where P_i and Q_i are bus i's injects for active and reactive powers, respectively. There are two notions for generated power at any given bus, either positive or negative. That is, if generated power were negative, then consumed power is deemed positive. It might seem trivial for the first instance, but this notation has a significant influence on the LF solution and must be defined properly for any LF analysis. Since improper use of signs with generated and consumed power will eventually lead to divergence in the LF solution. Similarly, an injected current I_i^c at the bus i in the c-th iteration is given by:

$$I_i^c = \left(\frac{P_i^c + jQ_i^c}{V_i^c}\right)^* \tag{4.2}$$

where V_i^c is the bus i's voltage at the c-th iteration. The advantage of radial and weakly meshed topologies of distribution networks makes it possible to apply Kirchhoff's current law (KCL). This is to express all branch currents $[\boldsymbol{B_i^c}]$ in the network at the c-th iteration as a function of system current injects $[\boldsymbol{I_i^c}]$. This relationship is expanded into a systems with large number of buses using the BIBC mapping as follows [106]:

$$[\boldsymbol{B_i^c}] = [\boldsymbol{BIBC}][\boldsymbol{I_i^c}] \tag{4.3}$$

For a system with n buses and m branches, $[\boldsymbol{BIBC}]$ is an m by $n-1$ constant upper triangular matrix with $zeros$ and $ones$ as obtained using the following procedure [106]:

- Initialize m by $n-1$ matrix filled with $zeros$.
- For a branch B_b, defined as the b-th branch located between bus i and bus ii, replace the i-th column with the ii-th column and replace 0 with 1 in the cell at the b-th row and the ii-th column (b^{branch}, ii^{bus}).
- Apply the previous procedure to the 1st branch until the m-th branch.

Similarly, bus voltages $[\boldsymbol{V_i^c}]$ at the c-th iteration are defined mathematically as a function of line impedance, branch currents $[\boldsymbol{B_i^c}]$, and the slack bus voltage $[\boldsymbol{V^s}]$ as follows:

$$[\boldsymbol{V^{\Delta}}] = [\boldsymbol{V^s}] - [\boldsymbol{V_i^c}] = [\boldsymbol{BCBV}][\boldsymbol{B_i^c}] \quad (4.4)$$

where $[\boldsymbol{V^{\Delta}}]$ is the bus voltage mismatch vector. $[\boldsymbol{BCBV}]$ is an $n-1$ by m matrix that can be obtained as follows [106]:

- Initialize $n-1$ by m matrix filled with $zeros$.
- For the branch B_b, replace the ii-th row with the i-th row and replace 0 with Z_b in the cell at the i-th row and b-th column (i^{bus}, b^{branch}). Accordingly, Z_b is defined as the line impedance of the branch B_b.
- Apply the previous procedure to the 1st branch until the m-th branch.

Different termination criteria are used in BFS, most commonly, is the error in voltage vector $[\boldsymbol{V^{\Delta}}]$ [106]. Lastly, the notable calculation speed advantage of BFS against N-R and G-S based methods is a well-documented subject in literature which can be found in studies [106], [108], [109]. This is mainly attributed to the derivative free nature of BFS-based load flow calculation and the elimination of the computationally expensive matrices.

4.2.2 Islanded Microgrid System Models

Adequate modelling of the system components is vital for accurate LF analysis. In an IMG, two main models are often considered, namely, load and DG models.

4.2.2.1 Load Model

The load model chosen to represent the loads in the IMG in this thesis follows the static exponential load model. The use of static load model is a sufficient approximation to account for static and dynamic load components [133], [134]. The instantaneous load behaviour as a function of V-f is given mathematically as [134]:

$$P_{Li} = P_{Li0}\left(\frac{|V_i|}{|V_0|}\right)^{nP}\left(1 + (f - f_0)\,.F_p\right) \quad (4.5)$$

$$Q_{Li} = Q_{Li0}\left(\frac{|V_i|}{|V_0|}\right)^{nQ}\left(1 + (f - f_0)\,.F_q\right) \quad (4.6)$$

where P_{Li} and Q_{Li} are the consumed active and reactive power by the load at bus i, respectively. P_{Li0} and Q_{Li0} are the active and reactive power for the load at bus i considering nominal voltage, respectively. nP and nQ are, respectively, the load's active and reactive

power dependence on voltage. F_p and F_q are, respectively, the load's frequency dependence coefficients. f and f_0 are the operational and nominal frequency at bus i, respectively. V_i and V_0 are the operational and nominal voltage at bus i, respectively. A list of settings for static load model with brief description of load type are given in Table 4.1 [96], [108].

Table 4.1: Static load model voltage and frequency coefficients

Static Load Type	Setting	nP	nQ	F_p	F_q
Constant Power Load	Set 1	0	0	0	0
Voltage Dependent load	Set 2	1	1	0	0
Frequency Dependent Load	Set 3	0	0	1	1
Constant Current Load	Set 4	1	1	1	1
Constant Impedance Load	Set 5	2	2	1	1

Furthermore, by the proper selection of the load coefficients nP, nQ, F_p, and F_q, as given in Table 4.1, different load behaviours can be achieved to represent constant power, current, and impedance models.

4.2.2.2 Distributed Generation Model

Mainly, DG units within an IMG are operated as voltage source converters (VSC). This shall enable bidirectional power flow, where power electronics facilitates autonomous power sharing capability by droop control [9]–[11]. To that end, P-f and Q-V droop relations are embedded within the inverter control system of DGs to facilitate active and reactive power sharing in the IMG, respectively. A common model selected to represent dispatchable DGs in IMG studies follows the VSC model. In case non-dispatchable DGs were considered by the load flow solution, it will follow the behaviour of PQ unit with maximum power point tracking (MPPT). Droop relations that enable VSC load following within an IMG according to IEEE std.1547.7 are given by [108], [69]:

$$f - f_0 = m_{pi}\,(P_{Gi} - P_{Gi0}) \tag{4.7}$$

$$|V_i| - |V_0| = n_{qi}\,(Q_{Gi} - Q_{Gi0}) \tag{4.8}$$

where P_{Gi} and P_{Gi0} are the generated and nominal active power at bus i, respectively. Q_{Gi} and Q_{Gi0} are, respectively, the generated and nominal reactive power at bus i. m_{pi} and n_{qi} are respectively, the coefficients for the active and reactive droops. The above equations for droop control is based on the assumption that, typically, DG output impedance is highly inductive according to IEEE std.1547.7 [69]. However, the active and reactive power output of

VSC might not be completely decoupled. This would lead to a concurrent relationship between V-f and output power in a DG. Therefore, the previous droop equations can be adjusted into P-V-f and Q-V-f forms to account for complex output impedance in VCS (or inverter-based DG (IBDG) when the DG is injecting real power) as follows [103]:

$$f - f_0 = m_{pi}\,(P_{Gi} - Q_{Gi}) \tag{4.9}$$

$$|V_i| - |V_0| = n_{qi}\,(P_{Gi} + Q_{Gi}) \tag{4.10}$$

Unless stated otherwise, the standard droop equations that corresponds to inductive response of IBDG were considered as bases for most of simulations conducted in this thesis. Conversely, m_{pi} and n_{qi} are defined as the slopes of the linear droop curves that dictates power sharing among DGs. Moreover, the active and reactive power updates of the DGs are inversely proportional to the frequency and voltage change, respectively. This is illustrated in the steps of Figure 4.1.

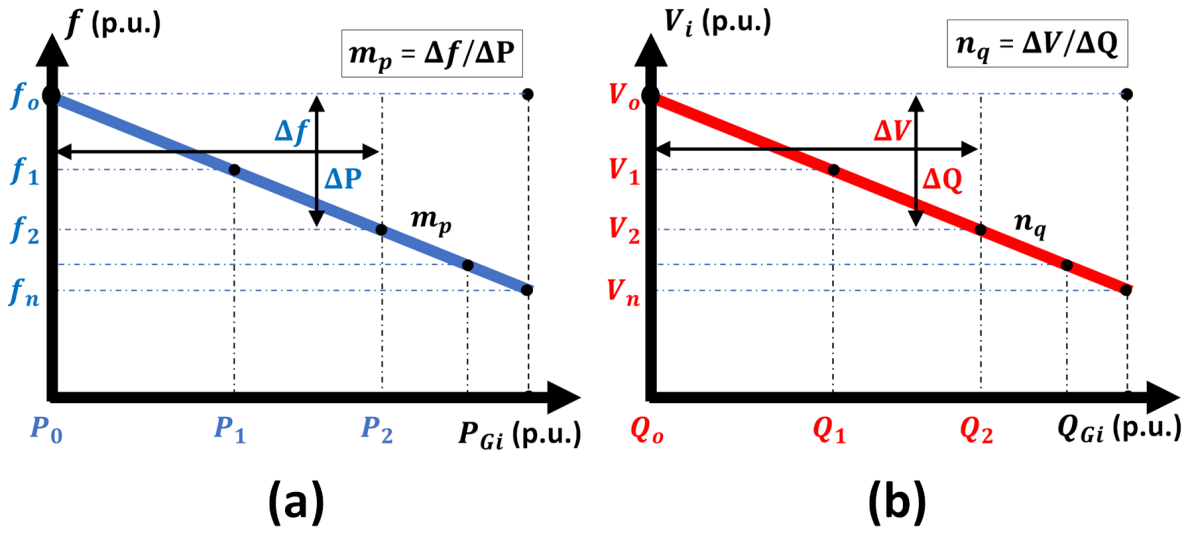

Figure 4.1: Droop control curves and steps relation: (a) P-f (b) Q-V

Similarly, the steps of Figure 4.1 indicate the amount of change in output power in response to load variations. Thus, steps are defined in case of active power and frequency relationship as step 1 from (f_0,P_0) to (f_1,P_1) then step 2 from (f_1,P_1) to (f_2,P_2), and so on. The same applies when considering reactive power and terminal voltage, i.e., step 1 from (V_0,Q_0) to (V_1,Q_1) then step 2 from (V_1,Q_1) to (V_2,Q_2), and so on. It is to be noted though that the first steps in P-f and Q-V curves above tend to be quite significant compared to the steps thereafter. Thus, it has the largest influence of the final values of IBDG output powers as well as bus voltage and system frequency.

4.2.3 Proposed Special Backward\Forward Sweep (SBFS)

As mentioned earlier, to enable conventional LF techniques to account for variable frequency and slack bus absence, some fundamental changes are required to the original BFS. Furthermore, the way DGs share the load within an IMG plays a significant role in representing generating buses. There are three known buses in any grid-connected LF method, viz., slack bus, generator bus, and load bus. Similarly, these buses are also defined in terms of electrical quantities, such as voltage and complex power, into reference, PV, and PQ buses. On the other hand, in an IMG there is no slack bus but rather a VB is defined to act as an exchange to a pseudo grid. Apart from its constant voltage angle acting as a reference for the power system, a VB voltage is not constant and will change based on the reactive power imbalance in the system. Likewise, a VB acts as a buffer between the IMG and the pseudo grid which mimics the behaviour of a slack bus in traditional LF sense, but not exactly the same. Given that a VB voltage is changing in every iteration, whereas for slack bus the voltage remains constant regardless of power mismatch across the system.

Additionally, frequency of an IMG will change based on active power imbalance in the system. The implementation of SBFS is based on the decentralized control strategy found in most IMG (i.e., droop control). Thus, in addition to VB, another type of LF bus is defined here as either droop bus (DRB) or non-droop bus (NDB). Let $\mathcal{N}$ be a set of all n buses in an IMG, then a subset containing all generating buses operating with droop control, i.e., DRB, is defined as $\mathcal{GK}: \mathcal{GK} \subseteq \mathcal{N}$. Based on that definition, we can define any system bus using the bus subscript i as follows (Noting that, for the sake of simplicity, bus_1 was selected to act as the VB for all tests considered in this thesis):

$$bus_i \asymp \begin{cases} \text{VB}, & \forall\, i \in \mathcal{GK}: i = 1 \\ \text{DRB}, & \forall\, i \in \mathcal{GK}: i \neq 1 \\ \text{NDB}, & \forall\, i \notin \mathcal{GK}: i \neq 1 \end{cases} \tag{4.11}$$

As mentioned previously in chapter 2, LF methods such as DBFS [107] and MBFS [108] suffer from convergence issues for ill-conditioned problems. Therefore, the proposed LF method here, SBFS, acts as a robust LF analysis for the IMG with a high convergence rate. The fundamental difference between previous methods and SBFS is epitomized as follows:

- Adopting one external loop to update V-f with higher convergence tolerance threshold, whereas in DBFS two external loops were required to update V-f.
- The DG power update in MBFS is conducted twice before and after converged internal BFS loop, while in SBFS the DG power update is restricted only in one stage which is at the external loop.

- In DBFS and MBFS, two matrix subroutines were required for BIBC and BCBV matrices, whereas in SBFS only one subroutine is required for BIBC wherein BCBV is obtained in one operation.

The SBFS method has four stages in total, viz., initialization stage, backward and forward sweep stages, and the update stage. These are explained in more details as follows:

4.2.3.1 Stage 1 (Initializations)

An initialisation process starts by setting all bus voltages, V_i, including VB voltage (V_1) to $1\angle 0^{\circ}$ p.u.; initialize the frequency deviation (Δf), VB voltage deviation (ΔV_1), and system buses voltage deviations ΔV_i to a user-defined value; reset iteration counters c_1 and c_2 to zero; determine the voltage tolerance threshold ε_{Th} (unless stated otherwise $\varepsilon_{Th} = 10^{-8}$); initialize DG units and loads coefficients. Based on that, the initial active and reactive powers for all DG buses are obtained using (4.12) and (4.14), respectively, which are equal initially to the pre-islanding DG power output. This situation is identical to the grid-connected DG operation with PQ control where V-f are regulated by utility grid.

$$P_{Gi} = \Delta P_{Gi} + P_{Gi0}\ ;\ \forall\, i \in \mathcal{GK};\ \mathcal{GK} \subseteq \mathcal{N} \tag{4.12}$$

$$\Delta f = \Delta P_{Gi} \cdot m_{pi}\ ;\ \forall\, i \in \mathcal{GK} \tag{4.13}$$

$$Q_{Gi} = \Delta Q_{Gi} + Q_{Gi0}\ ;\ \forall\, i \in \mathcal{GK} \tag{4.14}$$

$$\Delta V_i = \Delta Q_{Gi} \cdot n_{qi}\ ;\ \forall\, i \in \mathcal{GK} \tag{4.15}$$

4.2.3.2 Stage 2 (Backward Sweep)

During the backward sweep, the pre-islanding apparent power injects and bus voltages are known at each bus. Thus, at each bus, the apparent power followed by current injects are calculated using (4.16) and (4.17), respectively, sweeping backward towards the VB. Noting that in SBFS implementation the values of generated and consumed powers at bus i are all substituted as positive values in (4.16).

$$S_i = (P_{Li} - P_{Gi}) + j(Q_{Li} - Q_{Gi}) \tag{4.16}$$

$$I_i = \left({}^{S_i}/_{V_i}\right)^{*} \tag{4.17}$$

To attain branch currents in each system line, the equation (4.18) is used, albeit the $BIBC$ matrix should be generated first as explained in sub-section 4.2.1.

$$[\boldsymbol{B_i}] = [\boldsymbol{BIBC}][\boldsymbol{I_i}] \tag{4.18}$$

where $[\boldsymbol{I_i}]$ and $[\boldsymbol{B_i}]$ are, respectively, an inject and branch currents single column matrices of size an $n-1$ by 1. Likewise, for a tie-line free system of radial nature with n buses, the $[\boldsymbol{BIBC}]$ is an $n-1$ by $n-1$ matrix containing $ones$ and $zeros$ [106].

4.2.3.3 Stage 3 (Forward Sweep)

The forward stage refers to voltage calculations moving froward away from the VB. Subsequently, new voltage values at each system bus, except the VB, are obtained using combination of line parameters, branch currents, and the VB voltage. This is achieved in one-step matrix computation for enhanced efficiency.

$$[\boldsymbol{V_{in}}] = [\boldsymbol{V_1}] - [\boldsymbol{BCBV}][\boldsymbol{B_i}] \tag{4.19}$$

$$[\boldsymbol{BCBV}] = [\boldsymbol{BIBC}]^T \odot \left[[\mathbf{1}][\boldsymbol{Z_i}]\right] \tag{4.20}$$

For a pure radial distribution system with n buses, $[\boldsymbol{V_{in}}]$ and $[\boldsymbol{V_1}]$ are column vectors of size $n-1$ by 1 for system buses' new voltages and the VB voltage, respectively. $[\boldsymbol{BCBV}]$ is $n-1$ by $n-1$ matrix for branch current-branch voltage that will expedite the forward sweep efficiently in the matrix form. That is, by aligning the corresponding line impedances and currents seen in the path between the VB voltage and the voltage at bus i. Contrariwise with the additional matrix sub-routine required for $[\boldsymbol{BCBV}]$ in BFS, MBFS, DBFS, and NBFS methods, in SBFS this is not required as a simple matrix manipulation is used instead as given in equation (4.20). $\odot$ and T are, respectively, matrix operators for Hadamard product and transpose. Likewise, $[\mathbf{1}]$ is a $ones$ column vector of size $n-1$ by 1, while $[\boldsymbol{Z_i}]$ is a row vector of size 1 by $n-1$ for the impedance Z_i as seen by branch current B_i. The 2nd and 3rd stages of SBFS are often referred to as the internal BFS loop. This internal loop is required to minimize the deviation in the voltage error $|\Delta V_{in}|$ across the system. Hence, a voltage error tolerance value (E) is defined to ensure convergence of the internal loop as follows:

$$|\Delta V_{in}| = |V_{in} - V_i| \tag{4.21}$$

$$\mathrm{E} = max\{|\Delta V_{in}|\} \tag{4.22}$$

4.2.3.4 Stage 4 (the Update Stage)

This stage is activated when the condition $\mathrm{E} < \varepsilon_{Th}$ is satisfied. During the update stage V-f at VB are adjusted to reach a state of equilibrium in the IMG. This is necessary to replicate the behaviour of a power system where the slack bus voltage and the grid frequency are also variables. Moreover, the frequency and VB voltage updates act as a buffer between the IMG and the pseudo grid, where net power imbalance is calculated and compared to zero. Hence, any deviations in V-f will be reflected upon the values of reactive and active power by all DG units in the IMG, respectively. Subsequently, the V-f of the system are updated according to (4.24) and (4.23), respectively:

$$\Delta f = -m_{pT} \cdot (P_1 - \Re\{V_1 \cdot B_1^*\}) \tag{4.23}$$

$$\Delta V_1 = -n_{qT} \cdot (Q_1 - \Im\{V_1 \cdot B_1^*\}) \tag{4.24}$$

where m_{pT} and n_{qT} are the frequency and voltage equivalent droop coefficients of the system, respectively. P_1 and Q_1 are the active and reactive power exchange at the VB, respectively. B_1 is the sum of all currents leaving or terminating at the VB and is equal to the algebraic sum of all IMG current injects. To provide the best initial value for Δf and ΔV_1, the equivalent droops are used in equations (4.25) and (4.26) rather than using the individual droops m_{p1} and n_{q1} at the VB. The equivalent active (m_{pT}) and reactive (n_{qT}) droops represent the stiffness of the MG assuming a lossless system where the aggregated effect of all DG units is transferred into the VB as if they were working in parallel, as follows:

$$m_{pT} = \left(\sum_{i \in \mathcal{GK}}^{gk} m_{pi}^{-1}\right)^{-1} \tag{4.25}$$

$$n_{qT} = \left(\sum_{i \in \mathcal{GK}}^{gk} n_{qi}^{-1}\right)^{-1} \tag{4.26}$$

$$P_1 = P_{Gb} + P_{ex} \tag{4.27}$$

$$Q_1 = Q_{Gb} + Q_{ex} \tag{4.28}$$

where P_{Gb} and Q_{Gb} are the DG's generated active and reactive power at the VB. P_{ex} and Q_{ex} are, respectively, the exchanged active and reactive power with the pseudo grid. If no DG is present at the VB, then P_{Gb} and Q_{Gb} are set to zero. Similarly, to achieve converged LF solution and ensure autonomous operation of the IMG, P_{ex} and Q_{ex} must equal zero upon

convergence of the load flow solution. Hence, P_{ex} and Q_{ex} are set to zeros at the initialization stage to implement an initial state of equilibrium. Furthermore, P_{ex} and Q_{ex} might also be set to a different value other than zero to imitate any rate of exchange with adjacent MG or the main gird. Nonetheless, the operation of adjacent and clustered IMG is out of the scope for this thesis and shall be the focus of future work. Subsequently, the new frequency and voltage values at the VB become:

$$f_{c_2+1} = f_{c_2} + \Delta f \tag{4.29}$$

$$V_{1_{c_2+1}} = V_{1_{c_2}} + \Delta V_1 \tag{4.30}$$

where f_{c_2+1} and f_{c_2} are the system frequency at $c_2 + 1$ and c_2 iterations, respectively. Noting that SBFS has two loops, viz., internal BFS loop with counter c_1 and external V-f loop with counter c_2. $V_{1_{c_2+1}}$ and $V_{1_{c_2}}$ are the VB voltage at $c_2 + 1$ and c_2 iterations, respectively. After V-f update, the line reactance X_i is updated as in (4.31), while the total system's active (P_{loss}) and reactive (Q_{loss}) power losses are obtained as in (4.32) and (4.33), respectively.

$$Z_i = R_i + \mathrm{j}\, X_i \left({f_{c_2+1}}/{f_{c_2}} \right) \tag{4.31}$$

$$P_{loss} = \sum_{i=1}^{n-1} \Re\{Z_i\} \cdot |B_i|^2 \tag{4.32}$$

$$Q_{loss} = \sum_{i=1}^{n-1} \Im\{Z_i\} \cdot |B_i|^2 \tag{4.33}$$

where Z_i and R_i are the line impedance and resistance as seen by the branch current B_i, respectively. Load active and reactive power is updated using the static exponential model given in equations (4.5) and (4.6), while the DG active and reactive power are updated according to equations (4.34) and (4.35).

$$P_{Gi} = \Delta f / m_{pi} + P_{Gi0}\ ;\ \forall\, i \in \mathcal{GK};\ \mathcal{GK} \subseteq \mathcal{N} \tag{4.34}$$

$$Q_{Gi} = \Delta V_1 / n_{qi} + Q_{Gi0}\ ;\ \forall\, i \in \mathcal{GK} \tag{4.35}$$

Lastly, SBFS terminates when the condition for convergence is satisfied at the virtual bus. This is achieved when the error in virtual bus voltage decays and approaches zero (i.e., $|\Delta V_1| < \varepsilon_{Th}$). Moreover, convergence of SBFS indicates a new state of equilibrium in the power system following islanding. This means that all power mismatches across the system including

that of the virtual bus are eliminated. A flow chart of the proposed special backward forward sweep load flow method is given in Figure 4.2.

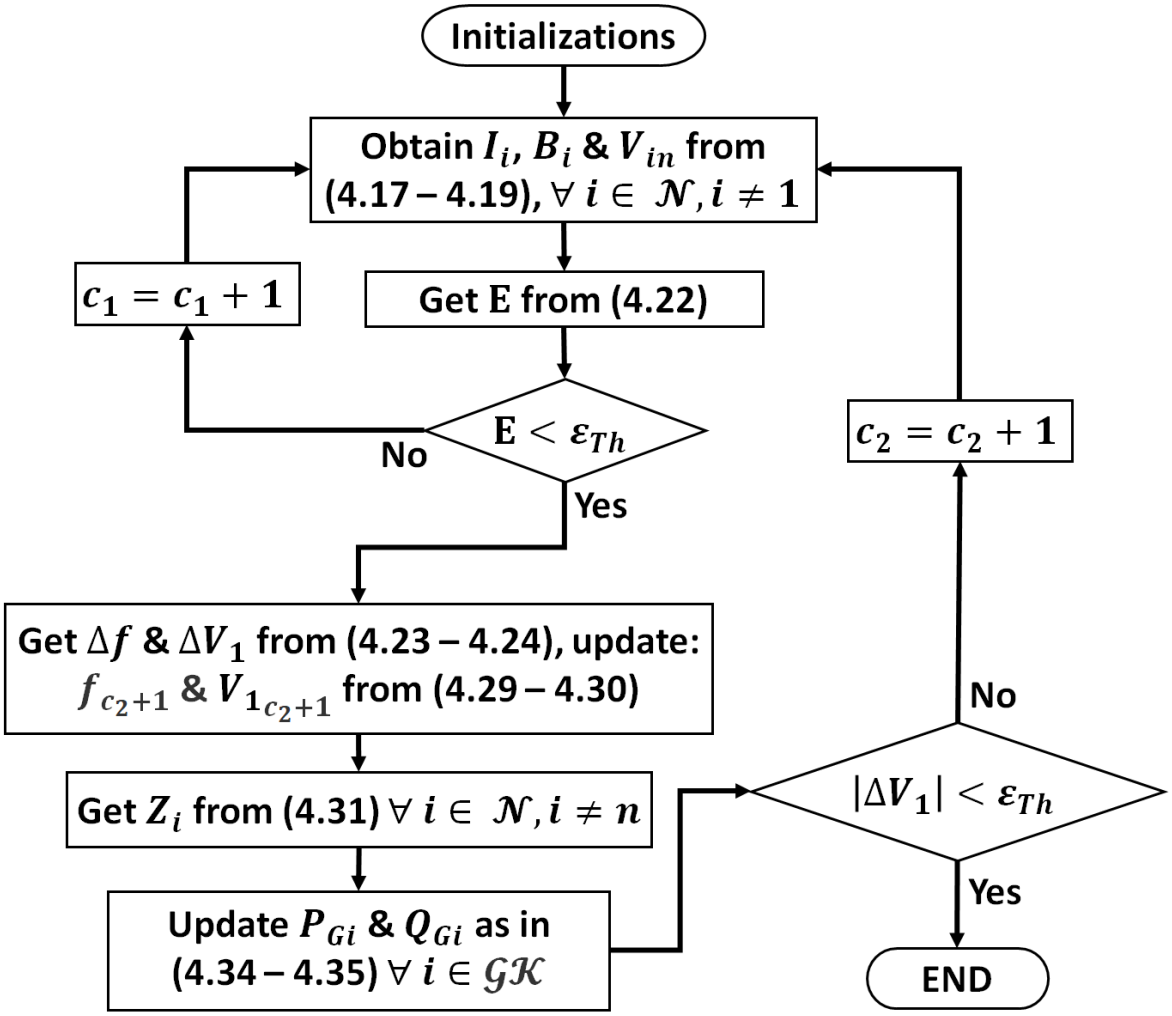

Figure 4.2: SBFS method flow chart

From Figure 4.2, two loops can be observed. That is, an internal BFS loop to attain branch currents and bus voltages, while the external loop of SBFS is required to update VB voltage, system frequency, and DG output powers.

4.2.4 Proposed Improved Special Backward\Forward Sweep (SBFS-II)

In this sub-section, the novel extension to the original SBFS [48], named here as SBFS-II, is presented. One major issue of DBFS, which depend on global voltage update, is having three main nested loops for voltage, frequency, and BFS updates. This usually causes divergence problems in ill-conditioned problems such as the DL allocation problem addressed in this thesis. The convergence problem has been mitigated in SBFS by adopting one update loop for VB voltage and one internal loop for BFS with higher tolerance threshold (i.e., $\varepsilon_{Th} =$

10^{-8}). The proposed improvement to SBFS in this sub-section is based on the voltage update equation (4.19) and the tolerance equation (4.22). Furthermore, only one loop is required in SBFS-II to update all system variables. Power flow of IMG is a challenging problem, hence higher number of iterations is required to see off the oscillations in the system's voltage error ($|\Delta V_{in}|$). However, this is not required in SBFS-II, as the reason for $|\Delta V_{in}|$ oscillations is eliminated by the removal of the BFS loop. This can be understood by examining the advantage of having a global voltage variable (V_1) dictating the rate of reactive power updates based on static droop coefficients at each DRB. Thus, the need for voltage deviation vector across the system at this stage becomes redundant.

Therefore, removing equation (4.22) by presuming the impact of $|\Delta V_{in}|$ as zero, will have a huge impact on the speed and convergence of the LF. In other words, recalculating the voltages across the system before updating the VB voltage and then doing it again after VB update will have a negative impact on convergence and will result in more iterations required. Hence, taking the second or third guess of the vector $[\boldsymbol{V_{in}}]$ and simultaneously calculating VB voltage will expedite the convergence as, eventually, the required state of equilibrium in BFS stage is for the VB and not for the other DRBs. Therefore, the voltage across the system is extended following another forward sweep to be $[\boldsymbol{V'_{in}}]$ which can be obtained simply as follows:

$$I'_i = \left({}^{S_i}/_{V_{in}}\right)^* \tag{4.36}$$

$$[\boldsymbol{B'_i}] = [\boldsymbol{BIBC}][\boldsymbol{I'_i}] \tag{4.37}$$

$$[\boldsymbol{V'_{in}}] = [\boldsymbol{V_1}] - [\boldsymbol{BCBV}][\boldsymbol{B'_i}] \tag{4.38}$$

where $[\boldsymbol{I'_i}]$ and $[\boldsymbol{B'_i}]$ are column vectors of size $n-1$ by 1 which represent, respectively, the inject and branch currents following another backward sweep. Bearing in mind that VB voltage and complex power injects are still constant at this stage. This is surly advantageous, as the whole focus of the LF method is in reducing the VB voltage error. By removing the internal BFS loop in the islanded mode, we implicitly neglect the unnecessary tolerance check for grid-connected mode by the original BFS [106]. This way SBFS-II continues to update V-f at the VB using the obtained voltages in $[\boldsymbol{V'_{in}}]$, while reflecting the change of each DRB generation by using the obtained global variables ΔV_1 and Δf. Thus, equations (4.29) and (4.30) were edited to include the only remaining iteration counter (c) of SBFS-II:

$$f_{c+1} = f_c + \Delta f \tag{4.39}$$

$$V_{1_{c+1}} = V_{1_c} + \Delta V_1 \tag{4.40}$$

Due to the foregoing, a convergence criterion in SBFS-II must be more rigorous to ensure zero power exchange at the VB and avoid any conflicting results. Ultimately, both SBFS and SBFS-II shall give the exact same results for voltages and current injects at each bus of the system. A flow chart of the proposed SBFS-II is depicted in Figure 4.3.

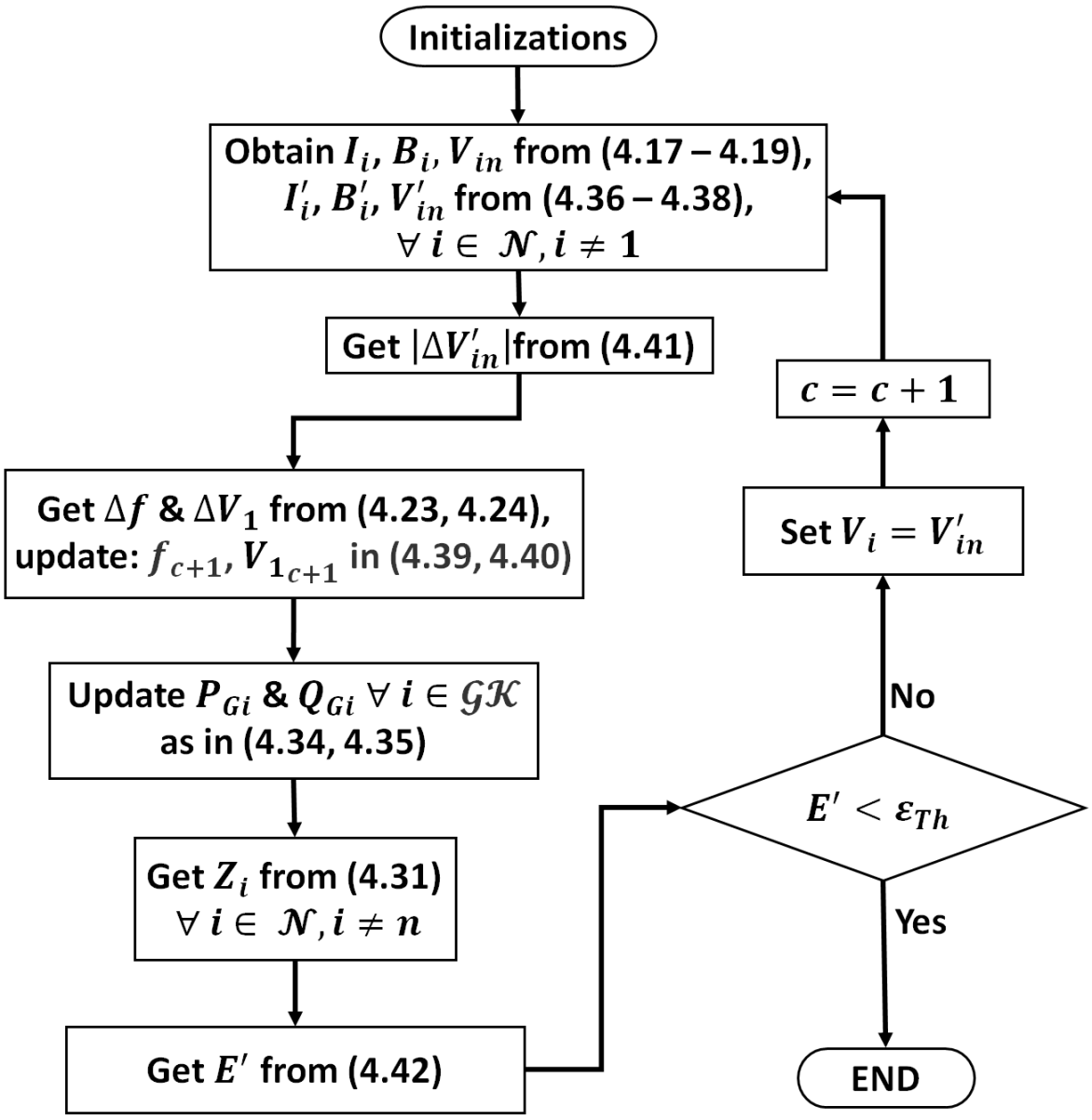

Figure 4.3: SBFS-II method flow chart

From Figure 4.3, the main difference between SBFS-II and SBFS is illustrated by having one loop to update all system variables, while having a tougher convergence criterion. Therefore, SBFS-II terminates when the updated condition for convergence is satisfied across

system buses including the VB. This will signal that all generation mismatches across the system are satisfied accordingly.

$$|\Delta V'_{in}| = |V'_{in} - V_{in}| \tag{4.41}$$

$$\mathrm{E}' = |\Delta V_1| + max\{|\Delta V'_{in}|\} \tag{4.42}$$

where E' is the new voltage error tolerance across the system.

4.2.5 Proposed General Backward\Forward Sweep (GBFS)

The reactive power update in the global voltage-based LF methods such as the method proposed by Diaz et al. [107], SBFS, and SBFS-II are based on the global voltage variable ΔV_1 and the respective droop setting of each DG unit. This reactive power update procedure relies on distributing the value of ΔV_1 to all DGs using an existing communication protocol between DG units and the point of common coupling (PCC). However, communication in many IMGs may be limited or prone to delays, hence the need for an LF solution that accounts for the local voltage measurement of individual DGs along with their respective droop gains. On this point, a similar pattern is followed to the methods proposed in [108], [109], i.e., by adopting local voltage measurements to update reactive power. However, the novel extension by the proposed GBFS herein, is the use of dynamic damping factors and reactive power correction to enhance convergence. Furthermore, similarly with SBFS-II, the proposed GBFS uses only one loop to update $\Delta V'_{in}$, Δf, ΔV_1, and DG power. This was in contrast with MBFS [108] and NBFS [109] as they require three loops for BFS, V-f update, and DG reactive power update. In that regard, the proposed third LF method continues by updating equation (4.35) of SBFS to reflect the nominal voltage ($|V_0|$) recovery by individual DG's reactive droop response.

$$Q_{Gi} = (|V_i| - |V_0|)/n_{qi} + Q_{Gi0}\ ;\ \forall\ i \in \mathcal{GK} \tag{4.43}$$

Additionally, as another novel extension of BFS-based IMG methods, the introduction of P-V-f and Q-V-f droop equations to account for the complex impedance found at the IBDG output in highly resistive distribution lines where active and reactive powers of the DG are not completely decoupled. Therefore, more general approach is adopted by having the choice of considering either inductive or complex output impedance of the IBDG. The choice, however, is left to the user knowledge about the requirement of the optimization study or the LF analysis targets. Based on that, the coupled active and reactive DG output powers are given by:

$$P_{Gi} = \frac{1}{2}\left((|V_{in}| - |V_0|)/n_{qi} + \Delta f/m_{pi}\right);\ \forall\ i \in \mathcal{GK} \tag{4.44}$$

$$Q_{Gi} = \frac{1}{2}\left((|V_{in}| - |V_0|)/n_{qi} - \Delta f/m_{pi}\right);\ \forall\ i \in \mathcal{GK} \tag{4.45}$$

However, upon changing the reactive power update equations, significant convergence and stability issues were observed. This was true with smaller values for reactive droop coefficient, higher line impedance, and the initial guess for reactive power Q_{Gi0} (i.e., DG reactive power reference points). The issue of small droop values is of particular importance in many DCIMG optimization problems that may require smaller values of reactive droop coefficients to achieve the best possible technical and economic objectives [5], [65]. To overcome convergence issues and thus minimize voltage deviations caused by lower droop values and inaccurate reactive power sharing, a dynamic damping factor denoted as ζ_1 is used. The role of ζ_1 is to eliminate oscillations in $|\Delta V_{in}|$, that is, by editing the voltage update equation (4.19). The new magnitude of the voltage error vector across the system becomes as $|\Delta V'_{in}|$ such that:

$$V'_{in} = V_{in} - \zeta_1.(V_{in} - V_i) \tag{4.46}$$

where V'_{in} is the voltage across all system buses as obtained with the help of ζ_1 following another forward sweep for V_i. Static damping factors application in iterative methods is a common practice in literature [109], [135]. Furthermore, it is very difficult to analytically calculate the exact value of such damping factors, whereas it is often time consuming and involve trial and error to obtain a value suitable for the current system state variables. However, in many IMG power flow problems, the system state variables are not constant and hence a fixed value of damping for one problem might cause divergence in the other. Conversely, it is not possible to have analytical calculation of the exact value of ζ_1 that will simultaneously minimize voltage error across the VB and the rest of system buses wherein a better LF convergence is achieved [110], [136].

Similarly, in many IMG optimization problems, LF convergence is fundamental in every function evaluation. Therefore, determining the damping factor by trial-and-error techniques become inefficient and sometimes not possible. Furthermore, since most LF problems in IMG will have some degree of non-convexity and nonlinearity, metaheuristic techniques have become a sought choice to approximate solutions by stochastic optimization [5], [110]. Hence, for adequate damping of $\Delta V'_{in}$, the value of ζ_1 is dynamically selected using a suitable metaheuristic technique such that the VB voltage error (ΔV_1) and $\Delta V'_{in}$ are minimized below a desired tolerance threshold such as ε_{Th}. Various stochastic optimization techniques are available in literature which offer different accuracy, speed, programming difficulty, and calculation burdens [45]. Nonetheless, the decision on which one is more suited than the other

to a specific optimization problem is open for debate. Considering all forgoing factors in the choice to elect a suitable metaheuristic, speed and accuracy were the main criteria for choosing the technique adopted in GBFS. Moreover, MIDACO's high-speed advantage makes it a good choice based on speed and accuracy. On average, MIDACO algorithm is faster by a factor of 1500 compared to other established evolutionary and swarm algorithms that employ a massive parallelization strategy such as GA [131]. Therefore, MIDACO was used to select and dynamically adjust the value of the damping factor with each iteration of the LF evaluation.

To enhance GBFS convergence and ensure adequate damping for voltage error across the system due to inaccurate reactive power sharing, an additional dynamic damping factor was used and denoted as ζ_2. The difference between factors ζ_2 and ζ_1 is that the former was applied to expedite the decay in ΔV_1, while the latter was used to suppress the error in $\Delta V_{in}'$. Contrary to the static deceleration factors used in [109], the nature of ζ_1 and ζ_2 is different as they can have any value within a specified range and therefore not constant. The advantage of having dynamic damping, is that they are applicable to a wide range of LF problems with different state variables as opposed to static damping which are problem specific. Therefore, by using ζ_2, a new VB voltage is obtained as:

$$V_{1_{c+1}} = V_{1_c} + \zeta_2 \cdot \Delta V_1 \tag{4.47}$$

Similarly, to ensure sufficient minimization in both ΔV_1 and $\Delta V_{in}'$, i.e., to reach convergence criterion, the value of ζ_2 must be dynamically changed as it was the case for ζ_1. Therefore, ζ_2 is also obtained by means of stochastic optimization. For best convergence response, a wide range of positive values is considered for ζ_1 and ζ_2 which is also used as bases for the lower and upper bounds of the decision variables that minimize the objective function in GBFS. Nevertheless, with smaller droop values as well as higher line impedance, achieving accurate reactive power sharing without adequate communication between DGs is unlikely. Furthermore, reactive power correction studies [5], [137], [138] based on virtual impedance compensation or reference points setting aimed to equate reactive power updates among DGs. Thus, eliminating reactive power error at the very last LF iteration such that:

$$|\Delta Q_{G1}| + \gamma_1 = |\Delta Q_{G2}| + \gamma_2 = \cdots = |\Delta Q_{Gi}| + \gamma_i \tag{4.48}$$

where ΔQ_{Gi} is the reactive power error vector at a generating bus i. γ_i is the reactive power correction vector needed when the updated reactive power value exceeds the limits of the DG. Likewise, when the selected reactive droops by the MG central controller (MGCC) are below a critical range, γ_i application becomes important. This critical reactive droop range is defined as the range wherein reactive power ceases to exhibit normal linear droop

relationship. This means that DG units start to either limit power output to a min-max value or change to constant power control. Contrariwise, in other circumstances, DG output power may exceed its ratings leading eventually to sequential failure in the IMG. Since, typically, all DGs in DCIMG are often of equal rating and no single DG can support all MG demand. Therefore, the introduction of γ_i to mimic the corrective control action by limiting the reactive power updates of the DG between the minimum and the maximum power ratings [137]–[139]:

$$\gamma_i = \left(\frac{Q_c}{\sum_{i\in\mathcal{GK}}|\Delta Q_{Gi}|} - 1\right) \cdot \{|\Delta Q_{Gi}|\} \cdot \beta \tag{4.49}$$

where Q_c is the average reactive power correction factor that is determined by MGCC and sent to DGs with dedicated low bandwidth communication channels. This is equal to the residual reactive power at VB or difference in system's generated\consumed reactive power:

$$Q_c = -(Q_1 - \Im\{V_1 \cdot B_1^*\}) \tag{4.50}$$

Moreover, the effect of γ_i correction is similar to distributing the reactive power sharing burden evenly on all DGs in the IMG taking into account their local voltage measurement, individual reactive droop, and the residual reactive power in the system. This can be achieved by adjusting the reactive power set-point at each DG unit (i.e., reference power Q_{Gi0}) to an appropriate value based on Q_c as determined by the MGCC [137]–[139]. Accordingly, the corrected reference reactive power (Q'_{Gi0}) for each DG becomes:

$$Q'_{Gi0} = Q_{Gi0} + \gamma_i \; ; \; \forall \, i \in \mathcal{GK} \tag{4.51}$$

Subsequently, the desired reactive power generation at each DRB is obtained as:

$$Q'_{Gi} = |\Delta Q_{Gi}| + Q'_{Gi0} \; ; \; \forall \, i \in \mathcal{GK} \tag{4.52}$$

Depending on reactive power keeping requirements in the MG, a binary constant (β) was introduced to (4.49) which enables or disables the correction procedure by γ_i such that:

$$\beta = \begin{cases} 0, & \forall \, Q_{min} < Q_{Gi} < Q_{max} \\ 1, & \forall \, Q_{Gi} \leq Q_{min}, Q_{Gi} \geq Q_{max} \end{cases} \tag{4.53}$$

where Q_{min} and Q_{max} are, respectively, the minimum and maximum reactive power output by any DG. If $\beta = 0$, then the reactive power will not change, i.e., $Q'_{Gi} = Q_{Gi}$. Lastly, GBFS terminates when convergence criterion is satisfied across the system. This indicates that GBFS objective function (i.e., $min\{|\Delta V'_{in}|, |\Delta V_1|\}$) is minimized below ε_{Th} as will be shown in next sub-section. A flow chart of the proposed GBFS is illustrated in Figure 4.4.

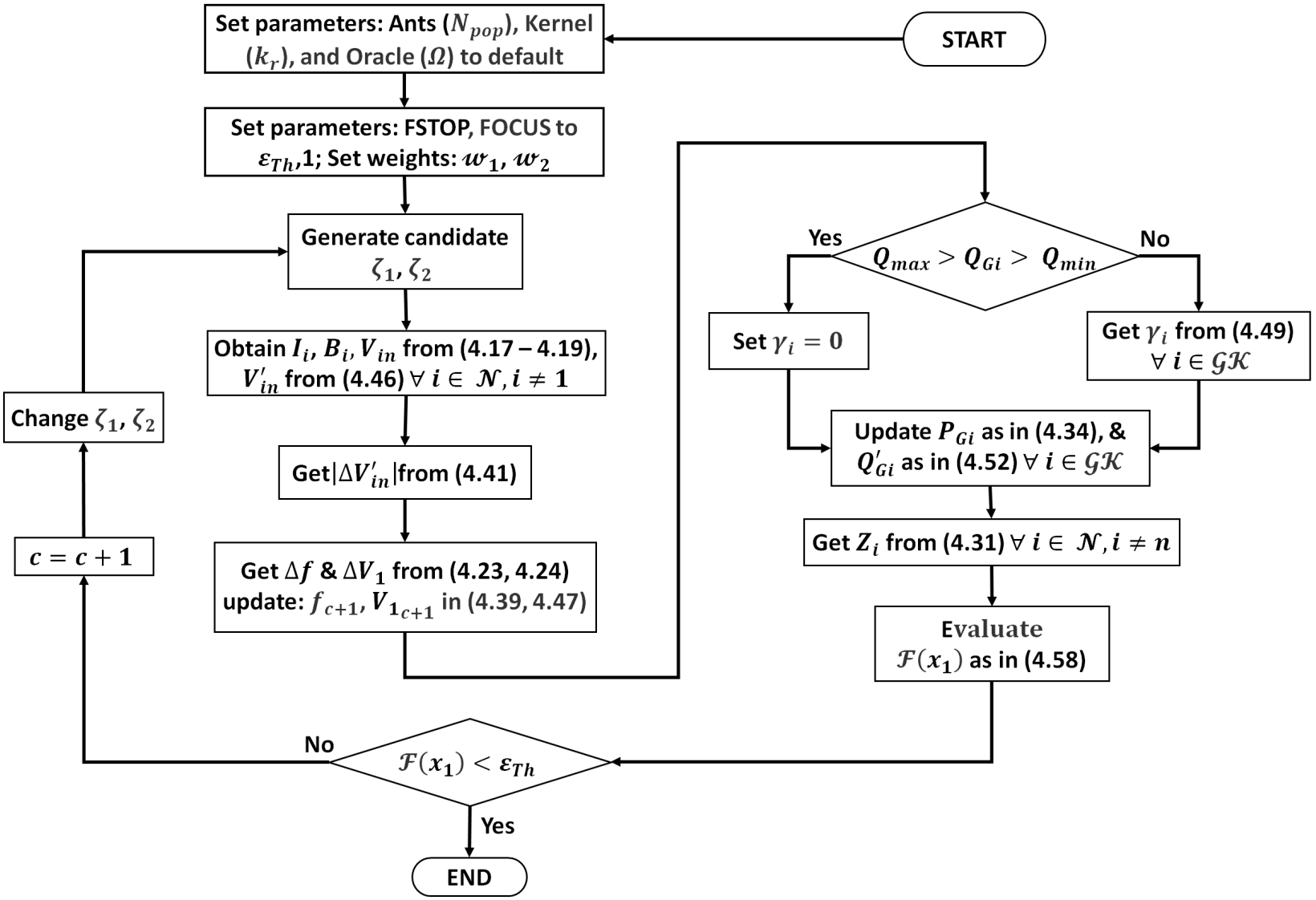

Figure 4.4: GBFS method flow chart

From Figure 4.4, GBFS general nature is demonstrated by taking DGs' local voltage measurements as well as their respective droop gains to calculate reactive power update without any form of communication. Concomitantly, ensuring that min-max reactive power limits are adhered for each DG by using the vector γ_i in collaboration with any IMG available communication infrastructure. Therefore, GBFS was the name given to the third proposed LF method since it exhibits general characteristics of a robust and efficient LF method for a DCIMG with embedded corrective control action and communication infrastructure.

4.2.5.1 General Backward\Forward Sweep Optimization Problem Formulation

In this sub-section, further details are given on the optimization problem presented in GBFS. A general form for any MINLP optimization problem is represented mathematically as:

Minimize: $\{\mathcal{F}_i(x)\}\,,\ i = \{1,2,\dots,\mathcal{O}\}$ (4.54)

Subject to: $\{\mathcal{g}_i(x)\} = 0,\ i = \{1,2,\dots,\mathcal{C}_e\}$ (4.55)

$$\{\mathcal{g}_i(x)\} \geq 0,\ i = \{\mathcal{C}_e + 1,\dots,\mathcal{C}\} \quad (4.56)$$

$$x_{min} \leq x \leq x_{max} \quad (4.57)$$

where $\mathcal{F}_i(x)$ is the objective function(s) of the optimization problem corresponding to a mixed-integer decision variable vector x. x_{min} and x_{max} are the lower and upper bounds of the decision variable x, respectively. $\mathcal{O}$ is the total number of i objective functions considered for minimization simultaneously. $\mathcal{g}_i(x)$ is the constraint handling function(s) for the MINLP problem. $\mathcal{C}$ and $\mathcal{C}_e$ are the total number of constraints and equality constraints, respectively.

Before we proceed further in this thesis, an important definition must be cleared first. There are two optimization problems considered herein based on non-decision variables state, viz., deterministic MINLP problems and stochastic MINLP problems.

As for the former, they belong to an MINLP class of problems where the variables defining the problem, which are not considered by the optimization metaheuristic as decision variables, are deterministic in nature and have a fixed value.

As for the latter problem, it refers to a class of stochastic MINLP problems where both decision and non-decision variables are random variables in nature and defined by their PDFs. As a result, the objective function is defined as $\mathcal{F}_i(x)$ for deterministic optimization problems, and as $\check{\mathcal{F}}_i(x)$ for stochastic optimization problems.

4.2.5.1.1 Objective Function

The aim of GBFS optimization problem is to obtain a concurrent minimization for the two major voltage error vectors $|\Delta V_1|$ and $|\Delta V_{in}'|$. This can be achieved by dynamically selecting and changing the damping factors ζ_1 and ζ_2. To alleviate the burden in function evaluation time, the desired objective functions were considered using average weighted sum approach. The use of average weighted sum to convert certain class of multi-objective problems into single objective, is useful to simplify the optimization problem complexity and enhances calculation speed. This approach is justified as pre-knowledge of the maximum threshold for a desired objective function value, i.e., in GBFS case it equals to ε_{Th}, makes the search for optimal value below that target a relatively simple task. In contrast with the standard approach by many metaheuristics in the exploration and exploitation of the solution search space to figure out what the global optima looks like, the objective function in GBFS is simplified with the pre-knowledge of the desired value. This criterion implementation, i.e., to locate a specific and known objective value, is straightforward in MIDACO. Wherein the simple tuning of the parameters FOCUS and FSTOP will expedite the convergence of the optimization technique. In one hand, FOCUS influences the solution search space by steering the search efforts towards a local region where the desired objective threshold value lies, while FSTOP on the other hand, stops the algorithm as soon as the value of the objective function falls below the specified threshold [126]. Moreover, in spite of MIDACO's multi-objective abilities, the use of weighted sum approach against Pareto front technique is well known to massively expedite the speed of individual function evaluation if speed was desired over accuracy [5], [45]. Based on that, the objective function adopted by GBFS is given as follows:

$$\mathcal{F}(x_1) = \varpi_1 \cdot max\{\,|\Delta V_{in}'|\} + \varpi_2 \cdot |\Delta V_1| \tag{4.58}$$

$$x_1 = \{\zeta_1, \zeta_2\} \tag{4.59}$$

$$0 < \zeta_1 \leq 10 \tag{4.60}$$

$$0 < \zeta_2 \leq 10 \tag{4.61}$$

where ϖ_1 and ϖ_2 are weights for $|\Delta V_{in}'|$ and $|\Delta V_1|$, respectively, such that $\varpi_1, \varpi_2 \in [0,1]$. $\mathcal{F}(x_1)$ is the GBFS objective function corresponding to a decision variable x_1. In some cases of computationally expensive optimization problems that rely on heavy LF calculations, each function evaluation is expected to exceed the 0.001 second mark. Therefore, the speed of GBFS can be enhanced further by reducing the number of decision variables in the

optimization problem. However, it is recommended to adopt both damping factors in the optimization problem first, to determine how fixing the value of ζ_1 will influence the load flow convergence. If after multiple short runs of the algorithm, the influence of fixing ζ_1 on convergence was not significant. Then, the speed of the optimization problem can be enhanced further by setting the values w_1 and w_2 to 0 and 1, respectively, while setting ζ_1 to a low value below 0.0001. Likewise, the advantage of FOCUS can be utilized further by selecting different values for FOCUS between the range $[1,100]$. Noting that, a default value for FOCUS in GBFS implementation is 1, while values exceeding 100 are not known to enhance GBFS speed over a variety of problems. Moreover, depending on the MINLP's flexibility, reducing x_1 search space will result in an expedited convergence process of GBFS.

4.2.5.1.2 Constraints

Constraints handling in GBFS optimisation problem is not required since the goal here is to minimize the objective function $\mathcal{F}(x_1)$ below ε_{Th} regardless of other system variables. This provides complete freedom in the selection process of ζ_1 and ζ_2, so long they do not exceed the upper and lower bounds of the decision variable x_1. Moreover, bus voltage, frequency, and branch thermal limits are often associated with the main allocation or dispatch optimization study. Thus, not interfering with GBFS purpose of providing a converged LF solution regardless of operational system limits. As a result, to further enhance the speed of GBFS, the constraint handling function, $g(x_1)$, was disabled by setting $\mathcal{C}$ to zero in MIDACO.

4.3 Results And Discussion

In this section, an analysis of the numerical results obtained by the proposed three LF methods on the IEEE 33-bus system is given. Additionally, a comparison with other published LF methods' results as well as the real-time simulation results of PSCAD/EMTDC is provided. Moreover, further attention was given to GBFS to highlight the significance of the two dynamic damping factors ζ_1 and ζ_2 on various test systems such as IEEE 33-, 69-, and 118-bus systems. Lastly, the robustness of GBFS was tested using two droop response for inductive and complex output impedances models. Noting that further analysis of SBFS, SBFS-II, and GBFS will be given in chapter 5 considering DL allocation. All simulations were conducted using the MATLAB® environment while adopting system specifications: Intel core i7 9th Generation, 2.60 GHz, and 8 GB RAM.

4.3.1 Islanded Microgrid Test Systems

Multiple benchmark test systems were considered as bases for many case studies considered throughout this thesis. Unless stated otherwise, all considered test systems were

adopted from established published work in distribution systems analysis and design. Likewise, unless stated otherwise, all obtained numerical results in this chapter were obtained using the per-unit system while considering the constant power load model (i.e., setting all load coefficients to zero).

4.3.1.1 6-Bus System

This small-scale radial distribution test system was adopted form a realistic distribution network with 11 kV nominal voltage as depicted in Figure 4.5 [140].

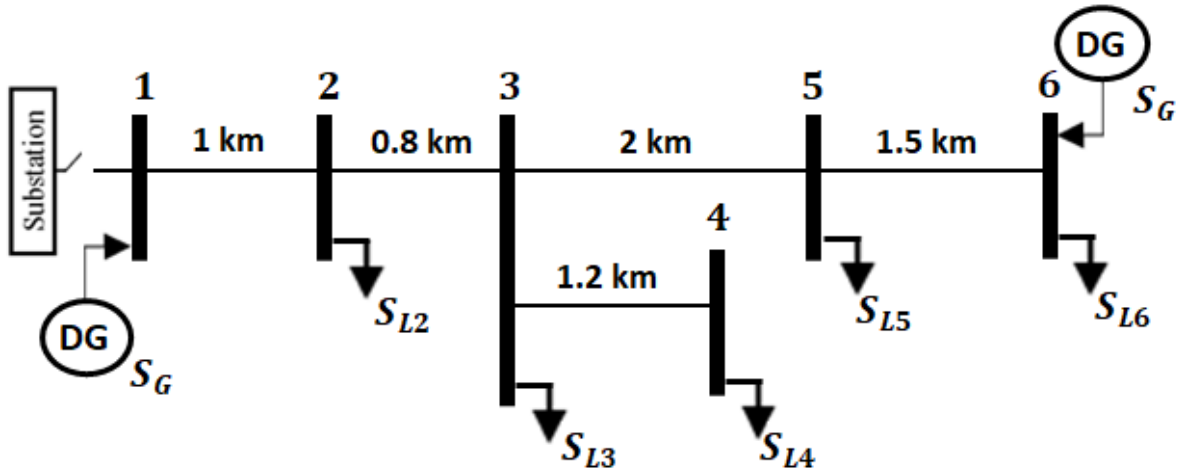

Figure 4.5: Six bus test system

Moreover, the system of Figure 4.5 has a total of 6 buses with 5 identical cross sectional areas for distribution lines with variations in lengths [140]. Furthermore, the six-bus system has a peak system load of 1.56 MW and 0.78 MVAR. Similarly, load power distribution across the system buses were [0.3, 0.05, 0.2, 1, 0.01] MW and [0.15, 0.025, 0.1, 0.5, 0.005] MVAR for buses [2, 3, 4, 5, 6], respectively [140]. As per literature standards for islanded systems testing [43], [110], the system was modified to enable autonomous operation with two identical distributed generation units installed at buses 1 and 6 as depicted by Figure 4.5.

Conversely, to facilitate load flow validation and convergence tests, the system was considered with variations in line impedance per unit length [141], [142]. This has been reported previously in literature which is known to enable variation of R/X ratio or loads' distribution in islanded microgrid systems [43], [48], [110], [143].

4.3.1.2 IEEE 33-Bus System

The IEEE 33-bus system is a well-known hypothetical distribution system of radial topology that is used extensively in microgrids, distribution networks' modelling, and load flow studies [41], [101], [108], [144].

The IEEE 33-bus system can be customized with different tie and sectionalizing switches for weakly meshed topology and problem specific modelling. Nonetheless and for brevity reasons, none of the tie and sectionalizing switches were used during the simulations of this study. Moreover, load flow calculations for islanded systems with meshed topologies requires an independent study, which is beyond the scope of this thesis and will be the subject of future work.

The test system consists of 33 buses with 32 main lines and 5 additional tie lines. The system nominal voltage is 12.66 kV, with peak load size of 3.715 MW and 2.3 MVAR [145]. The IEEE-33 bus system is depicted in Figure 4.6.

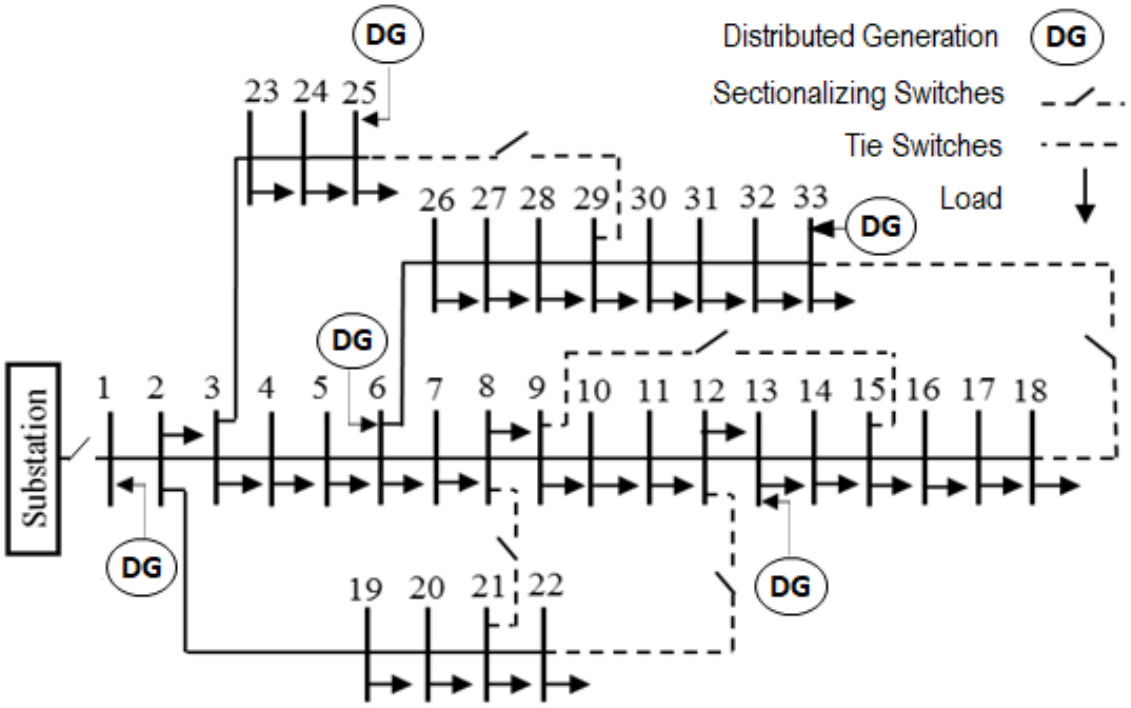

Figure 4.6: IEEE 33-bus test system

The line and load data for the test system of Figure 4.6 were adopted from [145]. Furthermore, to enable autonomous operation, the system had five DG units installed at the locations illustrated by Figure 4.6 [108].

4.3.1.3 IEEE 69-Bus System

The IEEE 69-bus system is a well-known realistic test system derived from a portion of PG&E distribution network. Moreover, the IEEE 69-bus system has been adopted in many microgrids and distribution network optimization and planning studies [48], [101], [108], [109], [144].

On the other hand, the test system has a total of 69 buses with 68 standard distribution lines and an additional 4 tie-lines. Similarly with the IEEE 33-bus system, the 69-bus system can be reconfigured and remodelled to enable different radial and weakly meshed topologies. Nonetheless, the simulations carried out in this thesis were based at the benchmark configuration of the IEEE-69 bus systems as depicted by Figure 4.7.

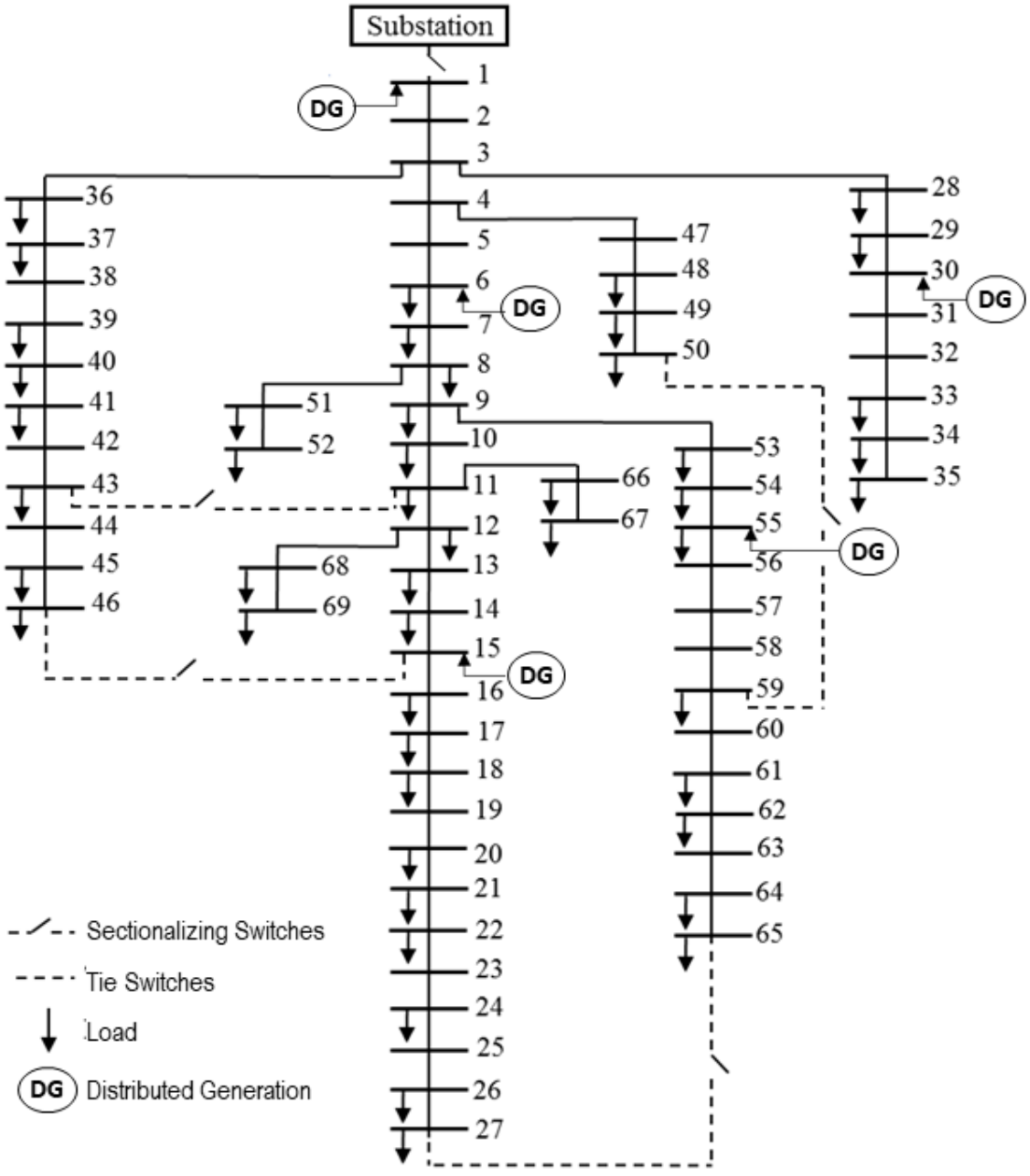

Figure 4.7: IEEE 69-bus test system

Moreover, as illustrated in Figure 4.7, the system was prepared for autonomous operation by installing five DG units at bus locations 1, 6, 15, 30, and 55 as per [43]. Conversely, the IEEE 69-bus system has a total peak load of 3.80 MW and 2.695 MVAR with nominal voltage of 12.66 kV [146]. All system line and load data were adopted from [146].

4.3.1.4 IEEE 118-Bus System

The IEEE 118-bus system is a large-scale radial distribution network with 118 buses and 117 dedicated distribution lines with additional 15 tie-lines as given in [147], [148]. Likewise, the IEEE 118-bus system has been adopted in many large scale microgrids planning and optimization studies [48], [147]–[150]. An illustration of the large test system is depicted in Figure 4.8.

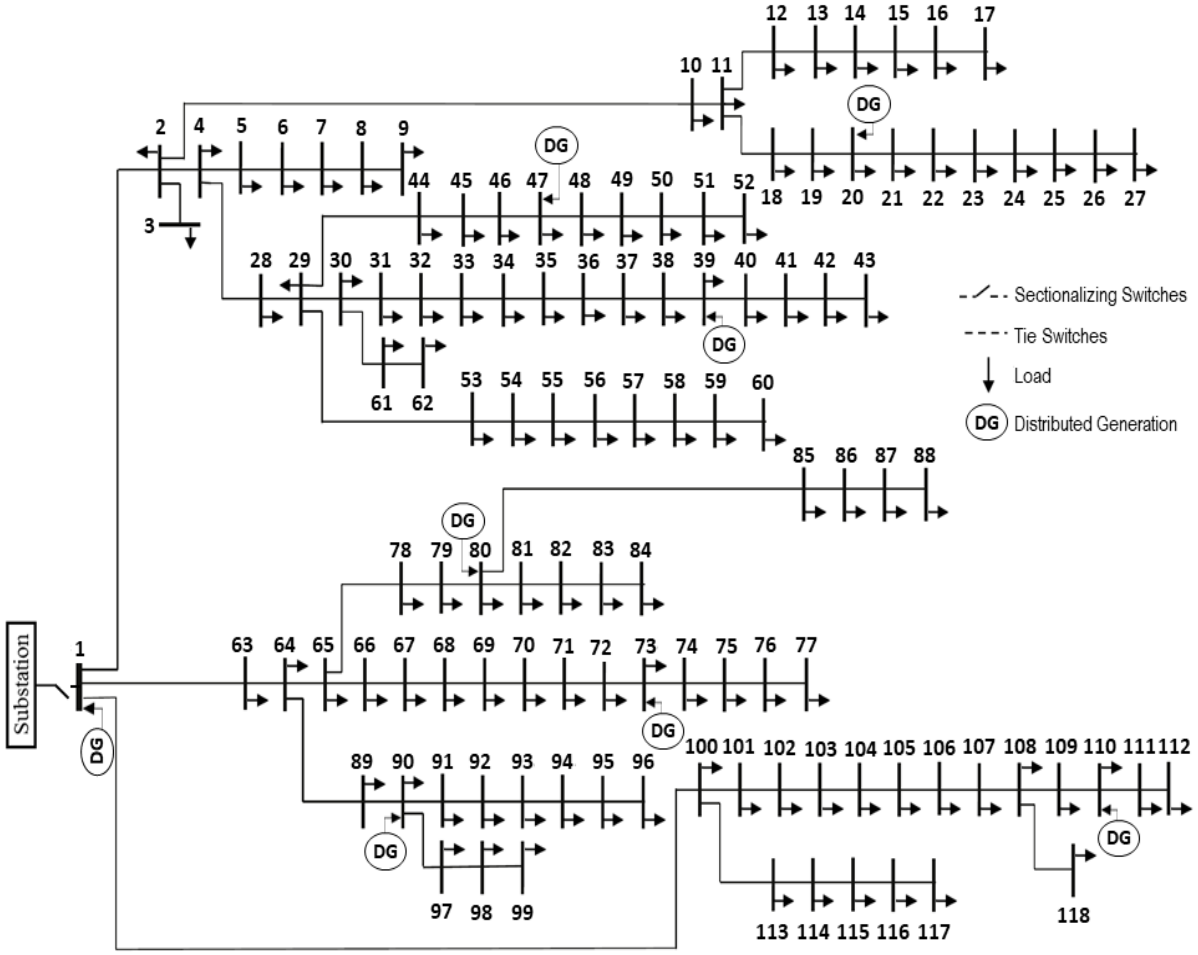

Figure 4.8: IEEE 118-bus test system

Furthermore, the system of Figure 4.8 has an 11 kV nominal voltage with 22.71 MW and 17.04 MVAR peak system demand. All system line and load data were adopted from [147]–[149]. Similarly with previous systems, the IEEE 118-bus system was prepared for autonomous operation by installing DGs at buses with the locations depicted by Figure 4.8 [150]. Moreover, each generating bus has two identical DGs of the same rating connected to it, raising the total number of installed units in the IEEE 118-bus system to 16 DG units. Noteworthy is that the DG locations in all test systems were optimally selected to minimize losses across the system during grid-connected mode [150].

4.3.2 Numerical Results of Load Flow Analysis

In this sub-section, a comparison is presented for LF solution obtained by the proposed three methods against different LF methods for IMG such as DBFS [107], MBFS [108], and NBFS [109]. Moreover, for sake of brevity and real-time simulation suitability, the LF analysis is conducted for the IEEE-33 bus system which was also modelled on PSCAD/EMTDC for accurate validation of the LF results [109]. For a fair comparison the case presented in [108] was adopted as basis for the simulations. All DG units were identical with pre-islanding generation for each DG as $S_{DG} = 0.9 + j0.9$ p.u. at system base of 12.66 kV and 500 kVA. Moreover, the system was assumed to operate at peak load, while the DG's droop coefficients used for the 33-bus numerical LF test are given in Table 4.2 [108].

Table 4.2: DG units droop gains for load flow analysis, 33-bus system

DG Unit	DG_1	DG_2	DG_3	DG_4	DG_5
Bus No.	1	6	13	25	33
$\boldsymbol{m_{pi}}$	-0.05	-1	-0.1	-1	-0.2
$\boldsymbol{n_{qi}}$	-0.05	-1	-0.1	-1	-0.2

As can be seen from the load flow solutions to the IEEE 33-bus systems as given in Table 4.3, all LF methods had very close voltage results taking PSCAD solution as reference. Likewise, the calculated frequency was almost identical in all reported solutions except for DBFS. Nonetheless, the LF methods that rely on global voltage variable such as DBFS, SBFS, and SBFS-II did have slight voltage error of 0.001. On the other hand, the results obtained by GBFS was identical to that of PSCAD, but with significant reduction in computation time if compared to MBFS and NBFS. Moreover, the obtained active and reactive power for DGs by GBFS was almost identical to that obtained by the real-time simulator PSCAD. This can be attributed to the influence of local voltage measurement at each droop bus, which is similar to the embedded control strategy for generating units in PSCAD solution. Conversely, SBFS and SBFS-II adoption of the global voltage update did significantly expedite the calculation time, with only 0.0042 and 0.0069 seconds for SBFS-II and SBFS, respectively. Noteworthy is that in an IMG, the LF solution greatly depends on the method used to update the active and reactive powers of DGs which is derived from droop equations. This was more evident considering the error in DG output power for global voltage LF methods against local voltage LF methods and PSCAD. However, if the control strategy of generating units were to change in PSCAD to implement global voltage distributed among all units, then the LF analysis results would be more aligned with that of SBFS and SBFS-II. The latter methods are classified as global voltage-based methods, while GBFS is a local voltage-based LF method. This was reflected in the difference in the LF results as given by Table 4.3.

Table 4.3: Load flow analysis results for 33-bus system

Bus No.	Bus Voltage (p.u.)							Bus No.	Bus Voltage (p.u.)						
	DBFS	SBFS	SBFS-II	MBFS	NBFS	GBFS	PSCAD		DBFS	SBFS	SBFS-II	MBFS	NBFS	GBFS	PSCAD
1	0.996	0.997	0.997	0.997	0.997	0.997	0.997	18	0.994	0.994	0.994	0.994	0.994	0.994	0.994
2	0.996	0.996	0.996	0.996	0.996	0.996	0.996	19	0.995	0.995	0.995	0.995	0.995	0.995	0.995
3	0.993	0.993	0.993	0.993	0.993	0.993	0.993	20	0.992	0.992	0.992	0.992	0.992	0.992	0.992
4	0.992	0.992	0.992	0.992	0.992	0.992	0.992	21	0.991	0.991	0.991	0.991	0.991	0.991	0.991
5	0.991	0.992	0.992	0.992	0.992	0.992	0.992	22	0.990	0.990	0.990	0.991	0.990	0.990	0.990
6	0.991	0.991	0.991	0.991	0.991	0.991	0.991	23	0.992	0.992	0.992	0.992	0.992	0.992	0.992
7	0.990	0.990	0.990	0.990	0.990	0.990	0.990	24	0.990	0.990	0.990	0.990	0.990	0.990	0.990
8	0.990	0.990	0.990	0.990	0.990	0.990	0.990	25	0.991	0.991	0.991	0.991	0.991	0.991	0.991
9	0.992	0.992	0.992	0.992	0.992	0.992	0.992	26	0.990	0.990	0.990	0.990	0.990	0.990	0.990
10	0.994	0.994	0.994	0.994	0.994	0.994	0.994	27	0.989	0.989	0.989	0.990	0.989	0.989	0.989
11	0.995	0.995	0.995	0.995	0.995	0.995	0.995	28	0.985	0.986	0.986	0.986	0.986	0.986	0.986
12	0.996	0.996	0.996	0.995	0.995	0.995	0.995	29	0.983	0.984	0.984	0.984	0.984	0.984	0.984
13	1.001	1.001	1.001	1.001	1.001	1.001	1.001	30	0.983	0.983	0.983	0.984	0.983	0.983	0.983
14	0.999	0.999	0.999	0.999	0.999	0.999	0.999	31	0.985	0.986	0.986	0.986	0.986	0.986	0.986
15	0.998	0.998	0.998	0.997	0.997	0.997	0.997	32	0.987	0.987	0.987	0.988	0.988	0.988	0.988
16	0.997	0.997	0.997	0.996	0.996	0.996	0.996	33	0.990	0.990	0.990	0.990	0.990	0.990	0.990
17	0.995	0.995	0.995	0.994	0.994	0.994	0.994	error[a]	0.001	0.001	0.001	0.001	0.000	0.000	-
Bus No.	**Active Power (p.u.)**							**Bus No.**	**Reactive Power (p.u.)**						
1	2.494	2.503	2.503	2.502	2.502	2.502	2.502	1	0.978	0.968	0.968	0.967	0.967	0.967	0.967
6	0.981	0.980	0.980	0.980	0.980	0.980	0.980	6	0.904	0.903	0.903	0.909	0.909	0.909	0.909
13	1.707	1.701	1.701	1.701	1.701	1.701	1.701	13	0.931	0.934	0.934	0.893	0.893	0.893	0.893
25	0.981	0.980	0.980	0.980	0.980	0.980	0.980	25	0.904	0.903	0.903	0.909	0.909	0.909	0.909
33	1.304	1.301	1.301	1.301	1.301	1.301	1.301	33	0.916	0.917	0.917	0.948	0.948	0.948	0.948
error[a]	0.008	0.001	0.001	0.000	0.000	0.000	-	error[a]	0.038	0.041	0.041	0.000	0.000	0.000	-
	Active Power Losses (p.u.)								**Reactive Power Losses (p.u.)**						
value	0.037	0.035	0.035	0.034	0.035	0.035	0.035	value	0.033	0.026	0.026	0.026	0.026	0.026	0.027
	Frequency (p.u.)								**Calculation Time (s)**						
value	0.919	0.920	0.920	0.920	0.920	0.920	0.920	value	0.521	0.0069	0.0042	0.165	0.018	0.0095	462.14

[a] refers to maximum absolute error.

Similarly, as given in Table 4.3, the obtained active and reactive power losses using GBFS's solution were very close to the other local voltage based LF methods such as MBFS and NBFS. Additionally, the reported losses by SBFS and SBFS-II did not deviate from those obtained by PSCAD.

4.3.3 Significance of the Damping Factors ζ_1 and ζ_2 in GBFS

To better understand the significance of GBFS's proposed two dynamic damping factors (ζ_1, ζ_2) and their influence on LF convergence in an IMG, the 6-bus test system of Figure 4.5 was used as a case study. Likewise, the 6-bus system has a load distribution across all buses except the VB. Load data of the 6-bus system are based on [140]. Two identical DGs were installed at buses 1 and 6 with pre-islanding generation $S_G = 2 + j1$ p.u. (by considering 11 kV and 500 kVA as system base). Additionally, three variations for system line impedance and reactive droop were considered to imitate the ill-conditioning expected in an IMG with radial topology. Line data are based on [141], [142], while droop sets are adopted in accordance with common literature practice [99], [101]–[103], [108], [109]. This should further increase the complexity of finding a converged LF solution by the three LF methods, viz., MBFS, NBFS, and GBFS. Based on that, the 6-bus system was put through five convergence tests (1A - 5A) using combinations of line impedances and droop sets as given in Table 4.4.

Table 4.4: Line impedance and droop sets for 6-bus system

Convergence Test	1A	2A	3A	4A	5A
$\boldsymbol{R_o}$ **(Ω/km)**	0.187	1.097	1.463	0.187	0.187
$\boldsymbol{X_o}$ **(Ω/km)**	0.619	1.074	1.432	0.619	0.619
$\boldsymbol{m_{po}}$ **(p.u.)**	9.51e-3	9.51e-3	9.51e-3	4.52e-3	3.53e-3
$\boldsymbol{n_{qo}}$ **(p.u.)**	2.23e-2	2.23e-2	2.23e-2	9.63e-3	7.51e-3

R_o and X_o are the resistance and reactance of branch in the 6-bus system; m_{po} and n_{qo} are active and reactive droops for DGs in the 6-bus system.

Considering the values from Table 4.4, the superior convergence performance of GBFS over MBFS and NBFS methods is given in Table 4.5.

Table 4.5: Load flow iteration number for convergence, 6-bus system

Convergence Test	**Load Flow Method**				
	MBFS	NBFS	GBFS		
	Iterations			ζ_1	ζ_2
1A	837	307	7	1.7556	0.7610
2A	NC	NC	15	2.4475	1.2928
3A	NC	NC	26	1.1218	1.5277
4A	NC	NC	22	1.2303	1.4782
5A	NC	NC	66	0.2626	1.8314

NC: Not Converged.

As can be deduced from Table 4.5, when using lower reactive droop values, the reactive power update in MBFS and NBFS suffered significantly making the LF convergence not possible. Contrariwise, GBFS has managed to provide a converged load flow solution within a reasonable number of iterations throughout all considered droop sets. Moreover, altering the line impedance values, i.e., changing the R/X ratio, convergence issues were also observed with MBFS and NBFS as they have failed to converge for both tests 2A and 3A.

To further demonstrate the importance and susceptivity of ζ_1 and ζ_2, a sensitivity analysis for load flow convergence was considered by changing the optimal value of damping to observe the impact on load flow solution convergence as given in Table 4.6.

Table 4.6: Sensitivity of load flow solution to ζ_1 and ζ_2 for the 6-bus system

Test 1A	ζ_1	1.76e-3	1.76e-1	1.7556*	4.7556	8.7556	15.755
	Iterations	7	7	7	11	14	21
	ζ_2	1.60e-3	0.0610	0.7610*	1.2610	1.7610	2.2610
	Iterations	NC	253	7	26	103	NC
Test 3A	ζ_1	0.1218	0.6218	1.1218*	1.6218	2.1218	3.1218
	Iterations	31	30	26	50	90	NC
	ζ_2	1.0277	1.2277	1.5277*	1.8277	2.0277	2.2277
	Iterations	NC	NC	26	86	NC	NC
Test 5A	ζ_1	2.63e-4	2.63e-2	0.2626*	1.2626	2.2626	3.2626
	Iterations	90	77	66	85	153	NC
	ζ_2	1.6314	1.7314	1.8314*	1.9314	2.0314	2.1314
	Iterations	NC	NC	66	165	NC	NC

NC: Not Converged, * indicates an optimal value for the damping factor.

From the results in Table 4.6, convergence tolerance to the value of ζ_2 is much lower than it is for ζ_1. This was evident upon the divergence caused in GBFS due to a very slight change in optimal ζ_2 value. Conversely, a relative larger deviation in ζ_1 did not significantly impact the convergence of GBFS for cases with higher reactive droop or lower R/X ratios.

4.3.4 Convergence of GBFS Against Other Load Flow Methods

In this sub-section, the robustness of GBFS against MBFS and NBFS, which are local voltage-based IMG load flow methods, is further validated on the IEEE 33-, 69-, and 118-bus systems. Four additional convergence tests were considered using the two models for inductive and complex droop equations. Wherein inductive and complex IBDG's output impedance models were considered for tests (1B - 4B) and (1C - 4C), respectively. Moreover, tests were performed using peak system demand with the constant power load model. Considering 500 kVA as system base for all systems, every DG of both 33- and 69-bus systems were assumed to have the pre-islanding powers as $S_{DG} = 0.9 + j0.9$ p.u., while the pre-islanding output power of each single DG unit in the 118-bus system was assumed as

$S_{DG} = 1.52 + j1.52$ p.u.. Noting that at each DRB of the 118-bus system the total generated apparent power was $S_{DG} = 3.04 + j3.04$ p.u. for the two identical units located at a single DRB.

Moreover, the variation in droop gains considered to define convergence tests 1B to 4C are given in Table 4.7 for the IEEE 33-, 69-, and 118-bus systems. The selection of different and realistic droop sets for validation and convergence test purposes is a common practice in literature and have been reported previously in studies [99], [101]–[103], [108], [109].

Table 4.7: DG unit droop coefficients for load flow test at peak system demand, all bus systems

Test System	DG Unit	Bus No.	Convergence Test (1B,1C)		Convergence Test (2B,2C)		Convergence Test (3B,3C)		Convergence Test (4B,4C)	
			m_{pi}	n_{qi}	m_{pi}	n_{qi}	m_{pi}	n_{qi}	m_{pi}	n_{qi}
33	DG_1	1	-0.05	-0.05	-0.016	-0.016	-0.002	-0.009	-0.001	-0.004
	DG_2	6	-1	-1	-0.016	-0.016	-0.003	-0.03	-0.0014	-0.014
	DG_3	13	-0.1	-0.1	-0.016	-0.016	-0.003	-0.015	-0.0014	-0.014
	DG_4	25	-1	-1	-0.016	-0.016	-0.004	-0.03	-0.0014	-0.014
	DG_5	33	-0.2	-0.2	-0.016	-0.016	-0.008	-0.015	-0.0014	-0.014
69	DG_1	1	-0.05	-0.05	-8.5e-3	-8.5e-3	-1.0e-3	-9.0e-3	-9.0e-4	-5.0e-3
	DG_2	6	-1	-1	-8.5e-3	-8.5e-3	-4.0e-3	-7.7e-3	-1.0e-4	-6.9e-3
	DG_3	15	-0.1	-0.1	-8.5e-3	-8.5e-3	-4.0e-3	-8.0e-3	-1.0e-4	-7.1e-3
	DG_4	30	-1	-1	-8.5e-3	-8.5e-3	-4.0e-3	-7.5e-3	-1.0e-4	-6.8e-3
	DG_5	55	-0.2	-0.2	-8.5e-3	-8.5e-3	-1.5e-3	-8.0e-3	-1.0e-4	-7.1e-3
118	DG_1	1	-0.001	-0.005	-9.7e-4	-9.9e-3	-9.0e-4	-9.2e-3	-8.8e-4	-8.8e-3
	DG_2	20	-0.001	-0.05	-9.7e-4	-0.015	-9.2e-4	-0.01	-8.8e-4	-8.8e-3
	DG_3	39	-0.001	-0.05	-9.7e-4	-9.9e-3	-9.1e-4	-9.5e-3	-8.8e-4	-8.8e-3
	DG_4	47	-0.001	-0.05	-9.7e-4	-0.015	-9.2e-4	-0.01	-8.8e-4	-8.8e-3
	DG_5	73	-0.001	-0.05	-9.7e-4	-9.9e-3	-9.1e-4	-9.5e-3	-8.8e-4	-8.8e-3
	DG_6	80	-0.001	-0.05	-9.7e-4	-0.01	-9.2e-4	-9.5e-3	-8.8e-4	-8.8e-3
	DG_7	90	-1.5e-3	-0.015	-9.7e-4	-0.01	-9.0e-4	-9.7e-3	-8.8e-4	-8.8e-3
	DG_8	110	-0.001	-0.05	-9.7e-4	-0.01	-9.1e-4	-9.8e-3	-8.8e-4	-8.8e-3

The given droop sets in Table 4.7 are based on a realistic droop coefficients range to imitate different cases of ill-conditioning expected in islanded systems. The values were derived in accordance with previous literature practice while considering units' ratings and relaxed system voltage and frequency limits [48], [102], [151]. Conversely, the number of iterations required to obtain a converged load flow solution by MBFS, NBFS, and GBFS considering inductive and complex droop responses are given in Table 4.8 for the IEEE 33-, 69-, and 118-bus systems.

Table 4.8: Load flow iterations for convergence using inductive and complex droop responses, all bus systems

Test System	Droop Response	Convergence Test	Load Flow Method				
			MBFS	NBFS	GBFS		
			Iterations			ζ_1	ζ_2
33	Inductive	1B	62	29	5	0.6299	0.8667
		2B	NC	NC	86	2.6396	1.9720
		3B	NC	NC	60	0.4552	1.9958
		4B	NC	NC	66	2.8848	2.0929
	Complex	1C	468	279	45	0.1036	2.5128
		2C	NC	NC	42	9.9158	3.1934
		3C	NC	NC	64	9.8912	4.2152
		4C	NC	NC	34	3.2531	4.1295
69	Inductive	1B	82	52	14	0.2730	0.4314
		2B	NC	NC	23	0.0013	0.9918
		3B	NC	NC	10	9.23e-5	1.0373
		4B	NC	NC	20	3.5572	0.7339
	Complex	1C	NC	NC	46	1.9062	2.8755
		2C	NC	NC	53	0.0103	0.8921
		3C	NC	NC	54	5.22e-6	0.8602
		4C	NC	NC	46	0.0833	0.2519
118	Inductive	1B	312	159	18	0.0417	0.6938
		2B	NC	NC	53	0.0111	1.3346
		3B	NC	NC	58	0.0174	1.3511
		4B	NC	NC	155	2.46e-6	1.6468
	Complex	1C	868	517	39	0.0815	2.5079
		2C	NC	NC	40	9.33e-6	0.6337
		3C	NC	NC	35	5.12e-6	0.3119
		4C	NC	NC	51	0.0176	0.7756

NC: Not Converged.

As can be seen from the results in Table 4.8, both MBFS and NBFS have failed to converge with lower droop selection for tests 2B-4B and 2C-4C for every bus system investigated. Conversely, GBFS had lower number of iterations if compared to MBFS and NBFS for both tests 1B and 1C for the 33- and 118-bus systems. Nevertheless, both MBFS and NBFS have failed to converge using the complex droop response for every considered convergence test using the 69-bus system.

4.4 Summary

In this chapter, three load flow methods based on BFS for DCIMG were presented as SBFS, SBFS-II, and GBFS. The former two load flow methods rely on global voltage variable distributed among all DGs within an IMG, while the later has more general approach by

adopting local voltage measurement for each DG along with two dynamic damping factors and one reactive power correction vector. Accuracy of the proposed load flow methods was validated via numerical results and real-time simulation of the IEEE 33-bus system. The significance of the two dynamic damping factors used in GBFS was demonstrated on a 6-bus system. Lastly, multiple convergence tests were considered to demonstrate GBFS method's efficacy in finding a converged load flow using variations of IBDG droop response for IEEE 33-, 69-, and 118-bus systems. Results were compared against other local voltage based-LF methods such as MBFS and NBFS methods.

5 Chapter Five: Dump Load Allocation in Islanded Microgrid Considering Deterministic Mismatch Scenarios

5.1 Introduction

In this chapter, the methodology developed for DL allocation in DCIMG using MIDACO is presented. In highly penetrated MGs, the problem of significant over-generation mismatch during islanding operation is very much critical at off-peak hours. Moreover, V-f deviations caused by such mismatch must be kept within acceptable limits as per islanding standards such as IEEE std. 1547.4 [4]. Hence, a DL could help with V-f control by absorbing excess generation at off-peak hours. Nonetheless, the work presented in this chapter provides an insight to the significance of DL allocation to assist the EMS of isolated microgrids considering highly probable mismatch scenarios. To that end, the DL allocation problem was investigated considering single and two objectives for V-f deviations, while a four objectives problem was formulated for V-f deviations, active, and reactive power losses. Additionally, four power mismatch scenarios were considered for the many-objective problem, while the effect of different load models were observed to highlight DL allocation advantage. Moreover, the proposed optimization technique of chapter 3 (i.e., MIDACO) was teamed up with the three LF methods of chapter 4 (i.e., SBFS, SBFS-II, and GBFS). This was done to compare the sensitivity of DL allocation problem to the load flow method used, while MIDACO's parameters influence on the solution was also investigated. The DL allocation was validated on three benchmark test systems, viz., IEEE 33-, 69-, and 118-bus systems with plenty of convergence tests. Lastly, the performance of the proposed optimization method was compared with other competitive swarm and evolutionary algorithms.

5.2 Background to Dump Load Allocation Problem in DCIMG

Different EMSs are used to handle power variations in IMGs, those include BESSs, EVs smart charging, and DR programs. However, different economic and environmental challenges impact the expansion of BESSs to handle large power mismatch in DCIMG [21]. Likewise, DR and EV smart charging are not suitable for excessive over-generation control due to coordination and behavioural obstacles [75]. Conversely, ELC controllers were utilized as DLs to handle excess power generation in hydro and wind power generation in MGs [25], [76]–[78]. Moreover, the control of existing power to attain the V-f regulation by means of heating and pumping application via DL was seen as a promising power management solution

in MGs [79], [80]. Nevertheless, DL application was restricted to generating buses, while thermal limits and power losses were considered as major barriers to the expansion of DL allocation into IMGs [25], [43].

Conversely, the IEEE std. 1547.4 necessitates the existence of adequate V-f control strategy to facilitate safe islanding operation. Due to the absence of utility main grid in most IMGs, load following must be executed by all available dispatchable DGs. This can be achieved by the centralized droop control strategy at the primary level. As mentioned previously in chapter 2, a complete IMG control strategy is implemented in three main levels. These are, droop control (primary level), nominal V-f recovery (secondary level), and observation and optimization of the IMG by an MGCC (tertiary control). The latter level is of particular importance as the proposed optimization strategy can be implemented within 15 mins of an optimization cycle. First, a planning (off-line) study is conducted to allocate DLs in the IMG, then an online optimization is carried out by the MGCC based on different microgrid parameters to distribute the size and droop setting for DL and DG, respectively. As discussed previously in chapter 4, the P-f and Q-V droop equations given in (4.7) and (4.8), respectively, are fundamental to enable the droop control strategy for IBDG units as stated by the IEEE std.1547.7 [108], [69]. Moreover, the DG model used for the optimization problem in this chapter is identical to an IBDG unit with highly inductive output impedance. This is attributed to the common practice in literature to assume the existence of a coupling inductor at the output of an IBDG [69], [103]

The contribution of an individual IBDG to load variation is characterized by the inverse relation of the droop coefficient, wherein an IBDG with lower droop will contribute higher to load change. For the sake of facilitating DL allocation herein, we define the base case as the case without any DL allocation (i.e., No DL case) nor any droop setting adjustments. Furthermore, the pre-defined droop gains used for the No DL base case for all test systems are given in Table 5.1 as obtained from [43], [107], [108].

Table 5.1: Base case DGs arrangement for deterministic dump load allocation MINLP, all bus systems

DG Unit		DG_1	DG_2	DG_3	DG_4	DG_5	DG_6	DG_7	DG_8
m_{pi}		-0.05	-1	-0.1	-1	-0.2	-1	-0.1	-1
n_{qi}		-0.05	-1	-0.1	-1	-0.2	-1	-0.1	-1
Bus No.	**33-bus**	1	6	13	25	-	-	-	-
	69-bus	1	6	15	30	55	-	-	-
	118-bus	1	20	39	47	73	80	90	110

Noting that DG locations in Table 5.1 will not change throughout all case studies implementation herein, but rather the droop setting for DL allocation. The update procedure

for DG output power based on over-generation situation is of particular importance to define the influence of DL allocation. That is by minimizing the steps required to reach the state of equilibrium in an IMG. As depicted in Figure 4.1 (see sub-section 4.2.2.2 for further information), a steps or iterative process dictates the updates between V-f and DG reactive and active power, respectively. This implies, in either over- or under-generation situations, the P-f and Q-V curves will facilitate a rate of change in the IBDG output power manifested by droop steps change in the load flow solution. Bearing in mind that the first step in both P-f and Q-V relationships are the most significant in size, while the remaining steps are very small and insignificant. Hence, in the DL allocation problem all V-f minimization objectives were aimed at minimizing the first step only. By doing so, the remaining droop steps will become very small and eventually approach zero. In other words, the bus voltage and system frequency rely heavily on the first step size, thus minimizing it will implicitly minimize V-f deviations.

Static load models are sufficient to express the dependency of load power on V-f of the MG [134]. Moreover, loads are based on static and dynamic components that reflects the type of load as residential, commercial, or industrial. Similarly, load model coefficients dictate the type of load as constant power, constant impedance, or constant current load as given in Table 4.1 [108]. Therefore, the previously discussed static exponential load model as given in equations (4.5) and (4.6) (see chapter 4 sub-section 4.2.2) are also used to model the loads in the DL allocation problem herein. Likewise, DL static and dynamic components are based on the exponential load model given in equations (4.5) and (4.6) as well. More technical details regarding ELC operation and design as used in DL applications in MGs are found in [25], [76]–[80]. Most previous DL utilization attempts were located near the main generating bus. Nonetheless, in this thesis's problem formulation, the DL location is random satisfying certain constraints. Hence, it might be allocated far from generator buses. Accordingly, the equilibrium in (5.1) and (5.2) must hold upon the installation of the DL into the IMG [48]:

$$\sum_{i=1}^{gk} P_{Gi} = \sum_{i=1}^{lk} P_{Li} + P_{DL} + P_{loss} \tag{5.1}$$

$$\sum_{i=1}^{gk} Q_{Gi} = \sum_{i=1}^{lk} Q_{Li} + Q_{DL} + Q_{loss} \tag{5.2}$$

where lk and gk are, respectively, the total number loads and DGs in the IMG. P_{DL} and Q_{DL} are, respectively, the active and reactive powers consumed by the DL.

5.3 Mathematical Validation

The motivation for DL allocation to minimize V-f deviations could be explained mathematically using a pseudo-radial IMG as depicted in Figure 5.1.

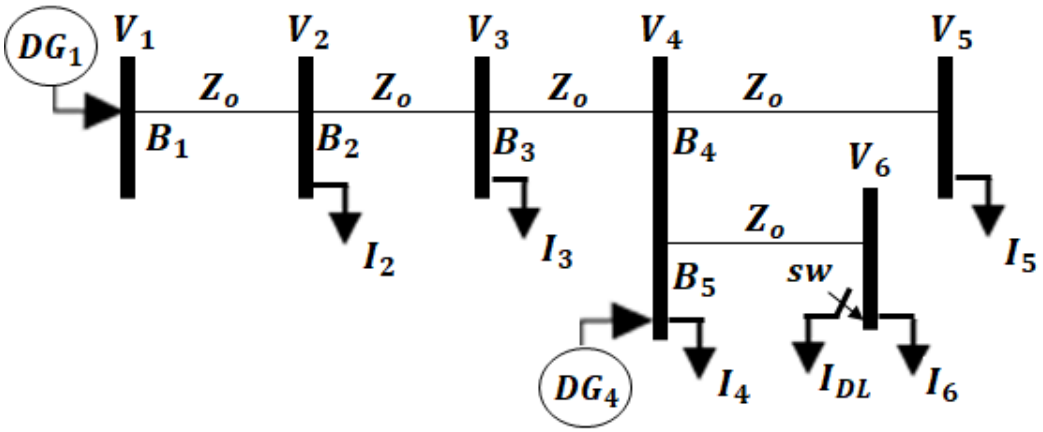

Figure 5.1: Pseudo islanded microgrid [48]

The pseudo-IMG of Figure 5.1 consists of six buses with bus 1 selected as the VB, while V_1 and f are updated based on n_{q1} and m_{p1} droop gains, respectively. Contrariwise, the DG unit connected to bus 4 is assumed at constant PQ control with significant over-generation situation. Therefore, the total generated power by DG_1 and DG_4 are given as $S_{G1} = P_{G1} + jQ_{G1}$ and $S_{G4} = P_{G4} + jQ_{G4}$, respectively, noting that $S_{G4} > S_{G1}$. It is further assumed that the system has a balanced load distribution except at the VB with five identical load's complex power such that $S_L = P_L + jQ_L$ [43], [48]. To simplify, we can assume a lossless system (i.e., $Z_o \approx 0$) with a converged load flow solution after one iteration [43], [48], while the switch (sw) is left open initially. Moreover, we denote negative for generated power and positive for consumed power. By using Kirchhoff's current law to obtain the VB branch current in a backward sweep, we have:

$$B_1 = I_2 + I_3 + I_4 + I_5 + I_6 \tag{5.3}$$

By substituting (4.17) in equation (5.3) we rewrite VB branch current as:

$$B_1 = \sum_{i=2}^{6} (S_i/V_i)^* \tag{5.4}$$

Under the assumption that the system is lossless with a flat start, then the voltage becomes a global variable as is the frequency (i.e., $|V_1| = |V_i| = 1$). By considering bus 4 in high over-generation situation, we have $S_{G4} \gg S_{L4}$. Hence, B_1 equation is updated as follows:

$$B_1 = 4(S_L)^* - (S_{G4})^* \tag{5.5}$$

Now, sweeping forward for the pseudo-IMG of Figure 5.1 from bus 1, then Δf and ΔV_1 are obtained by substituting (5.4) in equations (4.23) and (4.24), respectively:

$$\Delta f = -m_{p1} \cdot (P_{G1} + P_{G4} - 4P_L) \tag{5.6}$$

$$\Delta V_1 = -n_{q1} \cdot (Q_{G1} + Q_{G4} - 4Q_L) \quad (5.7)$$

If sw is now closed, then a DL is included into the system at bus 6 and B_1 is changed to B_1' as follows:

$$B_1' = I_2 + I_3 + I_4 + I_5 + I_6 + I_{DL} \quad (5.8)$$

In practical DL application into MGs, such DL size is typically large enough to absorb the surplus generation. By substituting (4.17) in (5.8) and using the same $|V_i|$ substitution used in (5.5), then B_1' becomes as:

$$B_1' = 4(S_L)^* - (S_{G4})^* + (S_{DL})^* \quad (5.9)$$

From (5.5) and (5.9) we note that $B_1' > B_1$. Moreover, the addition of DL into the system will be reflected upon f and V_1 as new updates in frequency and voltage deviations at the VB.

$$\Delta f' = -m_{p1} \cdot (P_{G1} + P_{G4} - 4P_L) + m_{p1} \cdot (P_{DL}) \quad (5.10)$$

$$\Delta V_1' = -n_{q1} \cdot (Q_{G1} + Q_{G4} - 4Q_L) + n_{q1} \cdot (Q_{DL}) \quad (5.11)$$

Based on that we can rewrite (5.10) and (5.11) as functions of Δf and ΔV_1 as follows:

$$\Delta f' = \Delta f + m_{p1} \cdot (P_{DL}) \quad (5.12)$$

$$\Delta V_1' = \Delta V_1 + n_{q1} \cdot (Q_{DL}) \quad (5.13)$$

Because m_{p1} and n_{q1} are negative values while P_{DL} and Q_{DL} are positive values, then the terms $m_{p1} \cdot (P_{DL})$ and $n_{q1} \cdot (Q_{DL})$ are also negative quantities. Therefore, by looking at (5.6) – (5.7) and (5.12) – (5.13), we can certainly deduce that $|\Delta f'| < |\Delta f|$ and $|\Delta V_1'| < |\Delta V_1|$. This surely satisfies the assumption that DL application into highly penetrated IMG will lead to V-f deviation minimization.

5.4 Deterministic Dump Load Optimization Formulation

As described in sub-section 4.2.6, a general MINLP optimization problem takes the mathematical form given in equations (4.54) – (4.57). Whereas the multi-objective DL optimization problem presented herein is an NP-hard and non-convex MINLP. This is true for the many-objective problem as will be detailed in the following sub-sections.

5.4.1 Objective Functions

In this sub-section, the four objective functions for deterministic DL allocation problem are presented as follows:

$$\mathcal{F}_i(x_2) = \begin{cases} \mathcal{F}_1(x_2) = |\Delta V_1| \\ \mathcal{F}_2(x_2) = |\Delta f| \\ \mathcal{F}_3(x_2) = P_{loss} \\ \mathcal{F}_4(x_2) = Q_{loss} \end{cases}, x_2 = \{P_{DL}, Q_{DL}, mn_{DL}, N_{DL}\} \quad (5.14)$$

where $\mathcal{F}_i(x_2)$ is the objective function for DL allocation considering a small set of highly probable mismatch scenarios during off-peak hours. x_2 is the mixed-integer decision variable vector corresponding to DL allocation. Nevertheless, the DL allocation problem was fragmented into three independent problems to shed more light on DL application impact on DCIMG stability and performance considering different objectives.

1) First problem: Two individual single-objective problems to minimize V-f deviations separately by optimizing DL size and location during off-peak hours. Hence, for the first problem, the objective function denoted as $\mathcal{F}_s(x_2)$ is having one value at a time as follows:

$$\mathcal{F}_s(x_2) \in \{\mathcal{F}_1(x_2), \mathcal{F}_2(x_2)\}, \; x_2 = \{P_{DL}, Q_{DL}, N_{DL}\} \quad (5.15)$$

2) Second problem: In the second problem implementation, both V-f deviations are minimized simultaneously as a multi-objective problem to optimize DL size and location during off-peak hours:

$$\mathcal{F}_i(x_2) = \{\mathcal{F}_1(x_2), \mathcal{F}_2(x_2)\}, \; x_2 = \{P_{DL}, Q_{DL}, N_{DL}\} \quad (5.16)$$

3) Third problem: Lastly, to account for power losses caused by the DL, a many-objective problem was formulated to minimize V-f deviations and network active and reactive power losses concurrently. Noting that the decision variable x_2 has been extended to include the optimal droop setting for dispatchable DGs which work best with the DL application into the IMG:

$$\mathcal{F}_i(x_2) = \{\mathcal{F}_1(x_2), \mathcal{F}_2(x_2), \mathcal{F}_3(x_2), \mathcal{F}_4(x_2)\}, x_2 = \{P_{DL}, Q_{DL}, mn_{DL}, N_{DL}\} \quad (5.17)$$

where N_{DL} is the DL bus location. mn_{DL} is the optimal droop setting for DL allocation in DCIMG. Accordingly, m_{pi} and n_{qi} were substituted with mn_{DL} for the purpose of DL allocation in this chapter such that:

$$mn_{DL} = m_{pi} = n_{qi}, \; \forall \, i \in \mathcal{GK} \quad (5.18)$$

5.4.2 Constraints

As per IEEE std 1547.7 for the connection of DGs [69] and IEEE std 1547.4 for systems with islanding operation [4], certain technical constraints must be satisfied to ensure safe and reliable autonomous MG operation. Therefore, a pre-defined set of constraints for voltage and line thermal limits were considered and applied to the first two problems in compliance with the forgoing standards. Unless stated otherwise, all numerical values in this chapter were given using the per-unit system considering base power as 500 kVA for all test systems. Whereas a system base voltage of 12.66 kV, 12.66 kV, and 11 kV was assumed for the 33-, 69-, and 118-bus systems, respectively. Moreover, a system base frequency is assumed at $f_o = 50$ Hz. For the first two problems' implementations, the following constraint handling functions ($g_i(x_2)$) were considered [48]:

- Bus i's voltage magnitude limits:

$$0.95 \leq |V_i| \leq 1.05 \tag{5.19}$$

- Thermal limits considering B_i magnitude [142], [152]:

$$|B_i| \leq \left|B_{i\_max}\right| \tag{5.20}$$

- Size limits for the dump load as given in [43]:

$$0.002 \leq P_{DL} \leq 1 \tag{5.21}$$

$$0.002 \leq Q_{DL} \leq 1 \tag{5.22}$$

Accordingly, while incorporating all foregoing constraints for the third problem, the droop gains has been restricted to a min-max limit. Furthermore, a DG output power limit has been imposed to ensure that all dispatchable units are within their min-max ratings while guaranteeing autonomous MG operation. This minimum-maximum limit for DGs is vital to keep units in a lagging power factor (PF) operation within the range (0.8 – 1). Additionally, as per IEEE std.1547.4, an operational frequency tolerance was considered to guarantee the quality of supply [48].

$$0 \leq P_{DG} \leq 2 \tag{5.23}$$

$$0 \leq Q_{DG} \leq 2 \tag{5.24}$$

$$0.996 \leq f \leq 1.004 \tag{5.25}$$

Likewise, considering the third problem's case, a DL allocation problem specific droop sets were assumed as mn_{DL} with the defined range given below; since values exceeding that range would be unsuitable for dispatchable units and sound unrealistic for an IMG [48], [151].

$$10^{-4} \leq mn_{DL} \leq 1 \tag{5.26}$$

5.5 Results And Discussion

The test MGs under consideration herein are the IEEE 33-, 69-, and 118-test systems which were adjusted by installing distributed generation units at the locations specified by Table. 5.1, that is, to ensure autonomous operation with minimal pre-islanding losses.

Noteworthy for the IEEE 33-bus case study, is that the number of DGs was reduced to four units according to the original test case presented in [43]. The IEEE 33-, 69-, and 118-test systems line and load data were taken from [145], [146], and [149], respectively, while the DG ratings and locations for IEEE 33- and 69-bus systems were obtained from [43].

Conversely, the DG locations for the IEEE 118-bus system were taken from [150]. Moreover, the locations of distributed generation units in the microgrid were adopted based on optimal DG allocation studies that aimed to minimize power losses across the network for grid-connected mode [150].

Additionally, all IMGs generation/loading mismatch states considered for the deterministic DL allocation MINLP are based on typical load pattern during early morning summer days as presented by studies on addressing DCIMG power management [43], [48].

Without loss of generality, any considered scenario in this chapter exhibits a mismatch event for generation and demand states with high probability in a massively penetrated MG. Nonetheless, for an adequate multi-scenario model that accounts for every possible diurnal and seasonal generation/demand state, this needs a stochastic scenario-based modelling of uncertainty which would be the topic of the next chapter.

However, to provide a preliminary investigation for DL impact on IMG stability, four scenarios in total were adopted in this chapter. Wherein, scenario 1 was adopted from [43], [107], [108], whereas scenarios 2 – 4 were acquired from [153].

Subsequently, the considered islanded microgrid's generation/loading power mismatch states/scenarios for the deterministic DL allocation MINLP are given in Table 5.2 for the IEEE 33-, 69-, 118-bus systems [43], [48].

Additionally, a weak correlation was assumed between the events for generation and load diurnal states which would not impact the outcome, and therefore was not considered within the chosen scenarios [48], [153].

Table 5.2: Test system generation to loading mismatch states, all bus systems

Scenario		-			1			2			3			4	
Test system	33	69	118	33	69	118	33	69	118	33	69	118	33	69	118
Load (%)		100			50			40.6			51.0			58.5	
$\sum P_{Li}$ (p.u.)	7.43	7.60	45.42	3.72	3.80	22.71	3.02	3.09	18.44	3.79	3.88	23.16	4.35	4.45	26.57
$\sum Q_{Li}$ (p.u.)	4.60	5.39	34.08	2.30	2.69	17.04	1.87	2.19	13.84	2.35	2.75	17.38	2.69	3.15	19.94
Generation (%)		100			63.63			84.99			84.99			84.99	
$\sum P_{Gi}$ (p.u.)	7.47	8.0	43.24	4.20	4.5	24.32	6.35	6.8	36.75	6.35	6.8	36.75	6.35	6.8	36.75
$\sum Q_{Gi}$ (p.u.)	5.60	6.0	32.43	4.20	4.5	24.32	4.76	5.1	27.56	4.76	5.1	27.56	4.76	5.1	27.56
Mismatch (%)	+6.84	+7.29	-4.82	+35.81	+36.56	+21.14	+160.64	+124.62	+99.24	+107.61	+78.82	+58.64	+81.00	+55.89	+38.28

The selected load percentages indicate a scenario of typical residential load profile during summer days considering off-peak hours (i.e., between 4:00 and 6:00 am) [43], [48]

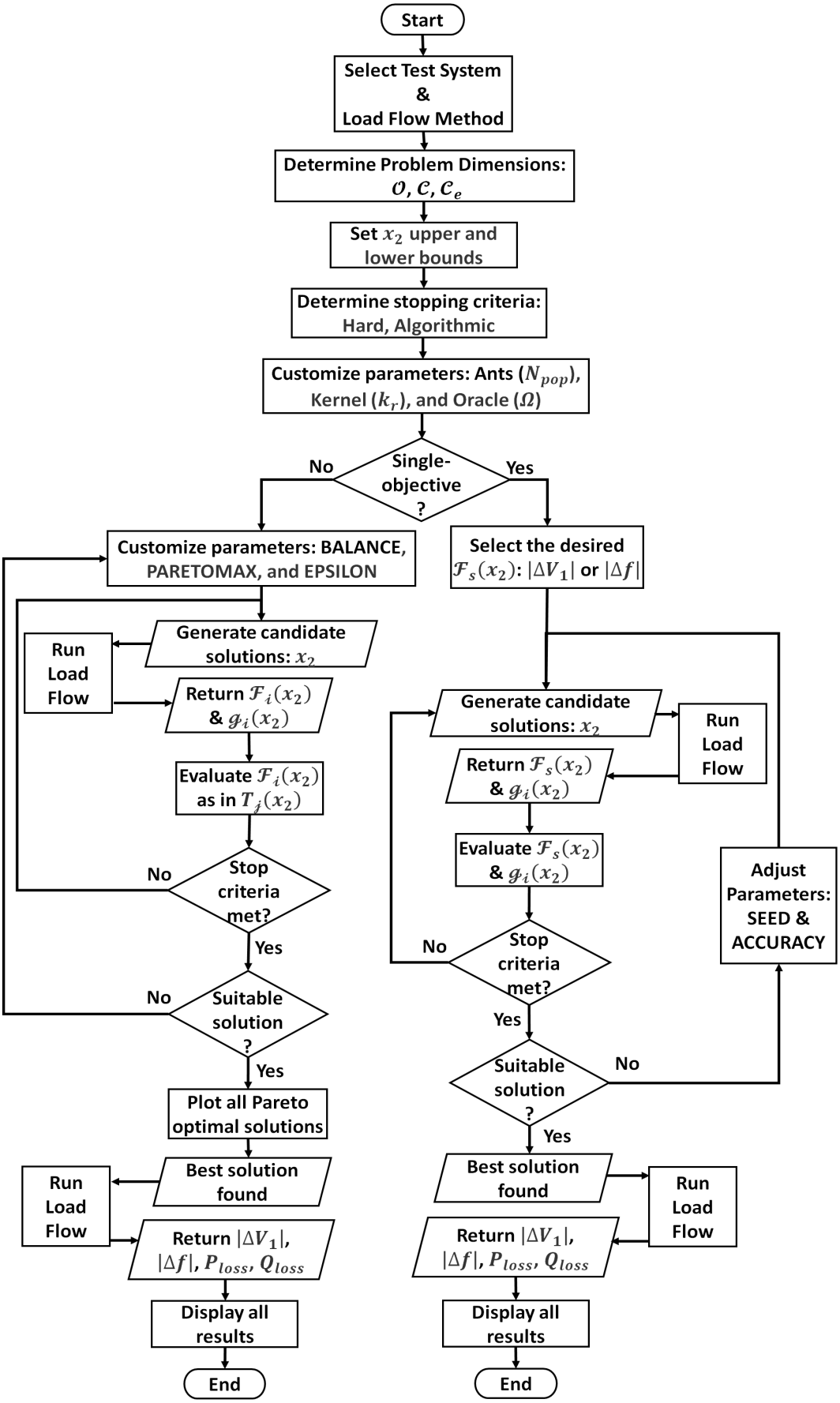

Figure 5.2: Flow chart of the proposed method for deterministic DL optimization problem

The flow chart of the optimization algorithm implementation for the deterministic dump load allocation problem as presented in this chapter is depicted in Figure 5.2. Moreover, the flow chart of Figure 5.2 illustrates the influence of SEED parameter on refining and improving the single and multi-objective problems by altering the seed for the random generated solutions.

On the other hand, the simulation conditions were identical to those of chapter 4. Accordingly, to simulate each of the three problems given in the previous section (5.4.1), MIDACO algorithm must be initialized first.

The parameters N_{pop}, k_r, and Ω were selected as zero (the default value) to enable dynamic population construction according to the problem convexity. Therefore and to handle the feasible and unfeasible solution regions, MIDACO will change N_{pop} in a dynamic manner within k_r default kernels assuming the oracle (i.e., Ω) with a value of 10^9 [48], [126].

Furthermore, for the sake of brevity, the first and second problems implementation were only based on generation\loading scenario 1 for the 33-, 69-, and 118-bus systems.

5.5.1 Single Objective Optimization Using Special Backward\Forward Sweep

The single objective problem to minimize voltage and frequency deviations, individually, was attained by concurrently minimizing the droop steps of Figure 4.1. This was done using the proposed special backward\forward sweep load flow method with the proposed optimization technique, MIDACO, to minimize $|\Delta V_1|$ and $|\Delta f|$ as single objectives.

However, as per the assumed notion of this study, in a significant over-generation situation and during low demand hours, the first step of Figure 4.1 tends to have the biggest impact on the solution. This is attributed to the fact that droop control relations are executed in step-by-step bases within the proposed load flow method.

On the other hand, by having uneven distribution for the droop control, the weight of the remaining steps as compared to the first step will become negligible. Therefore, voltage and frequency deviation results considering all investigated cases and all simulated test systems were represented by the first step size only.

Furthermore, due to fact that the final settlement values for $|\Delta V_1|$ and $|\Delta f|$ upon convergence of the load flow solution were approaching zero approximately, thus their influence was redundant and had been omitted from the results.

Subsequently, the single objective voltage and frequency deviation results for the dump load allocation problem number one (that is, by considering the first problem as defined in section 5.4.1) for the three test systems (i.e., IEEE 33-, 69-, 118-bus systems) is given in Table 5.3.

Table 5.3: Single- and two-objectives results for mismatch scenario 1, all bus systems

Optimization Problem	No DL			Min ($\|\Delta V_1\|$)			Min ($\|\Delta f\|$)			Min ($\|\Delta V_1\|$&$\|\Delta f\|$)		
Test System	33	69	118	33	69	118	33	69	118	33	69	118
N_{DL}	-	-	-	33	64	60	16	7	60	33	27	68
P_{DL} **(p.u.)**	-	-	-	0.5663	0.8172	0.9999	0.4506	0.6259	0.9999	0.4641	0.6294	0.9999
Q_{DL} **(p.u.)**	-	-	-	0.9999	0.9999	0.9999	0.9952	0.9993	0.9999	0.9999	0.9999	0.9999
$\|\Delta V_1\|$ **(p.u.)**	0.0586	0.0480	0.1454	0.0260	0.0197	0.1243	0.0274	0.0210	0.1243	0.0261	0.0208	0.1253
$\|\Delta f\|$ **(p.u.)**	0.0141	0.0170	0.0281	0.0052	0.0082	0.0066	0	0	0.0066	0.0019	0.0005	0.0081
P_{loss} **(p.u.)**	0.0195	0.0578	0.1335	0.0787	0.1766	0.1895	0.0374	0.0674	0.1895	0.0742	0.0880	0.1373
Q_{loss} **(p.u.)**	0.0153	0.0251	0.0908	0.0621	0.0710	0.1238	0.0308	0.0287	0.1238	0.0587	0.0358	0.0888
MVE **(p.u.)**	0.0642	0.0500	0.1636	0.0317	0.0366	0.1452	0.0319	0.0249	0.1452	0.0317	0.0228	0.1390
f_{ss} **(p.u.)**	1.0145	1.0173	1.0301	0.9950	0.9920	1.0086	0.9999	1.0001	1.0086	0.9983	0.9995	1.0097
Time[a] (s)	-	-	-	32	35	51	32	35	51	38	40	56

First step size only for $|\Delta V_1|$ and $|\Delta f|$, [a]algorithm computation time.

According to the $|\Delta f|$ case given in Table 5.3, the frequency at steady state (f_{ss}) due to the single objective minimization of $|\Delta f|$ were slightly off the nominal value of 1.00 p.u. This is true for all test systems studies, as f_{ss} before and after DL allocation has dropped from 1.0145 p.u., 1.0173 p.u., and 1.0301 p.u. to 0.999 p.u. 1.0001 p.u., and 1.0086 p.u. for the 33-, 69-, and 118-bus systems, respectively.

Therefore, the frequency regulation has improved considerably assuming the pre-islanding mismatch for the active power as (4.2/3.7) p.u., (4.5/3.8) p.u., and (24.3/22.7) p.u. for the 33-, 69-, and 118-bus systems, respectively.

Contrariwise, by examining the results of $|\Delta V_1|$ case as given in Table 5.3, we can deduce that the MVE (i.e., the voltage maximum deviation for all system buses against their nominal values given in absolute term [48]) did rise above the MVE reported for $|\Delta f|$ case considering generation\loading scenario 1 for the three test systems. This can be explained by the notion that typically at downstream nodes higher voltage drop is expected.

Similarly, the attained voltage profile for the three test systems considering $|\Delta V_1|$ and $|\Delta f|$ as the first ($\mathcal{F}_1$) and second ($\mathcal{F}_2$) objectives, respectively, is depicted in Figure 5.3. Noteworthy is that the single objective solution for the 118-bus system was different form the 33- and 69-bus systems. This is attributed to the larger mismatch in active and reactive power between 118-bus and the other two test systems. Moreover, the solution search space for the 118-bus was outside the boundaries for the allocated limits for the DL. Thus, the need to include additional factors to influence the solution search space such as droop settings or change in the DL size limits are warranted.

Considering the power losses across the network, the DL allocation as a single objective problem did in fact increase the incurred power losses. This was based on the assumed power mismatch scenarios as +35.81%, +36.56%, and +21.14% over-generation for the 33-, 69-, and 118-bus systems, respectively.

The power loss is attributed to the DL behaviour in prevailing inductive current network where it acts as a lagging current addition (i.e., inductive compensation in highly inductive network). Consequently, the total generated apparent power ($\sum S_{Gi}$) for the $|\Delta V_1|$ case was (5.51∠37.64° p.u.), (6.10∠38.14° p.u.), and (30.02∠37.24° p.u.) for the 33-, 69-, and 118-bus systems, respectively. This was an increase from the No DL case which was at (4.39∠31.80° p.u.), (4.72∠35.16° p.u.), and (28.55∠36.87° p.u.) for the 33-, 69-, and 118-bus systems, respectively.

Whereas, on the other hand, the attained $\sum S_{Gi}$ for the $|\Delta f|$ case has been as (5.35∠38.36° p.u.), (5.84∠39.62° p.u.), and (30.02∠37.24° p.u.) for the 33-, 69-, and 118-bus systems, respectively. The network power losses profile for the first problem implementation is depicted in Figure 5.4.

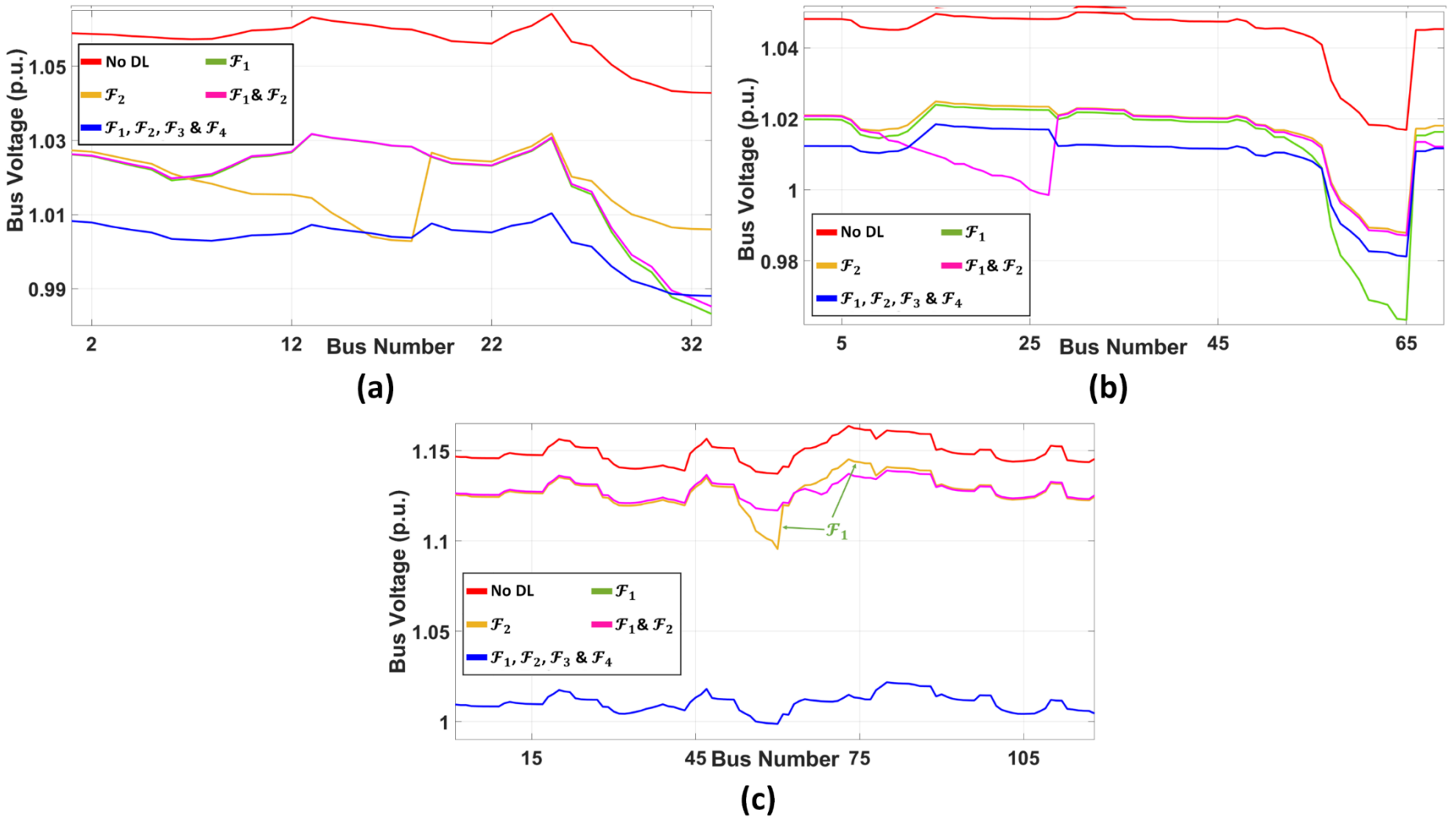

Figure 5.3: Dump load allocation impact on voltage profile considering scenario 1 for: (a) 33-bus (b) 69-bus (c) 118-bus

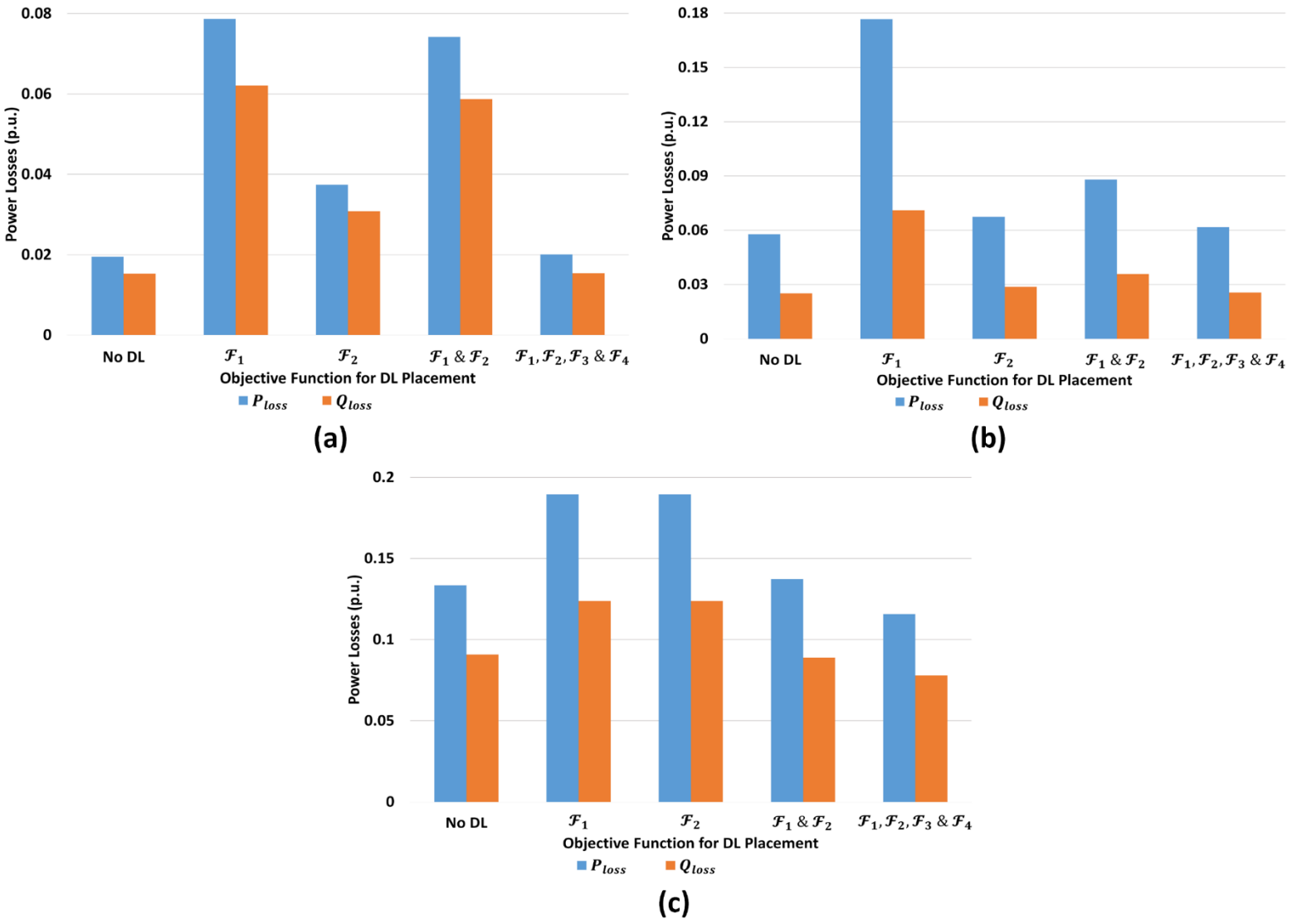

Figure 5.4: Dump load allocation impact on losses profile considering scenario 1 for: (a) 33-bus (b) 69-bus (c) 118-bus

Figure 5.4 shows a detailed comparison for network active and reactive power losses considering the base case (i.e., without DL) and the first problem implementation (i.e., single objective minimization of $|\Delta V_1|$ or $|\Delta f|$) without changing the droop setting of the dispatchable DG units. Conversely, better voltage profiles are noted in Figure 5.3 for the singular objectives against the No DL case. Consequently, the DL role in voltage regulation for IMGs is significant.

5.5.2 Multi-Objective Optimization Using Special Backward\Forward Sweep

As for the multi-objective formulation, two implementations were investigated, viz., two-objectives (second problem) and four-objectives (third problem). The two-objectives were studied using only scenario 1 for the 33-, 69-, and 118-bus systems. Whereas the four-objectives problem was studied using scenarios 1 – 4 as given in Table 5.2 to exemplify the power mismatches for the three test systems. To simulate the multi-objective problem in MIDACO, the parameters PARETOMAX, BALANCE, and EPSILON were set as 1000, 0, and 0, respectively, for all investigated multi-criteria cases.

5.5.2.1 Two-Objectives Optimization

By expanding the dimension of the DL allocation problem into two-objectives, better and stable results were achieved but with slightly higher calculation times as given in Table 5.3. The non-dominated solution was obtained by the proposed optimization technique via choosing from a Pareto front using the utopia-nadir-balance technique. Moreover, the balance concept is reflected in the results by the slightly flatter voltage profile with lower MVE against the cases for individual $|\Delta V_1|$ and $|\Delta f|$ objectives and the No DL case. Numerically, the MVEs for the two-objectives problem were, respectively, 0.0317 p.u., 0.0228 p.u., 0.1390 p.u. for the 33-, 69-, and 118-bus systems compared to the No DL case's MVEs of 0.0642 p.u., 0.0500 p.u., and 0.1636 p.u. for the 33-, 69-, and 118-bus systems, respectively. The two-objectives' voltage profile for all test systems is depicted in Figure 5.3.

Noteworthy, that the obtained maximum voltage error for the 118-bus system was still outside the desired safe operating region for an islanded system according to IEEE std 1547.4. This is attributed to the significant pre-islanding reactive power mismatch of (24.3/17.0) p.u. that could not be handled only with DL inclusion. However, as will be shown in the next section, by optimally selecting the DG droop settings an improved voltage profile can be achieved for the 118-bus system. Accordingly, to enable better understanding of the influence of the BALANCE parameter on the solution, the non-dominated solution using the utopia-nadir-balance approach by the proposed algorithm is depicted in Figure 5.5 for the IEEE 33-, 69-, and 118-bus systems.

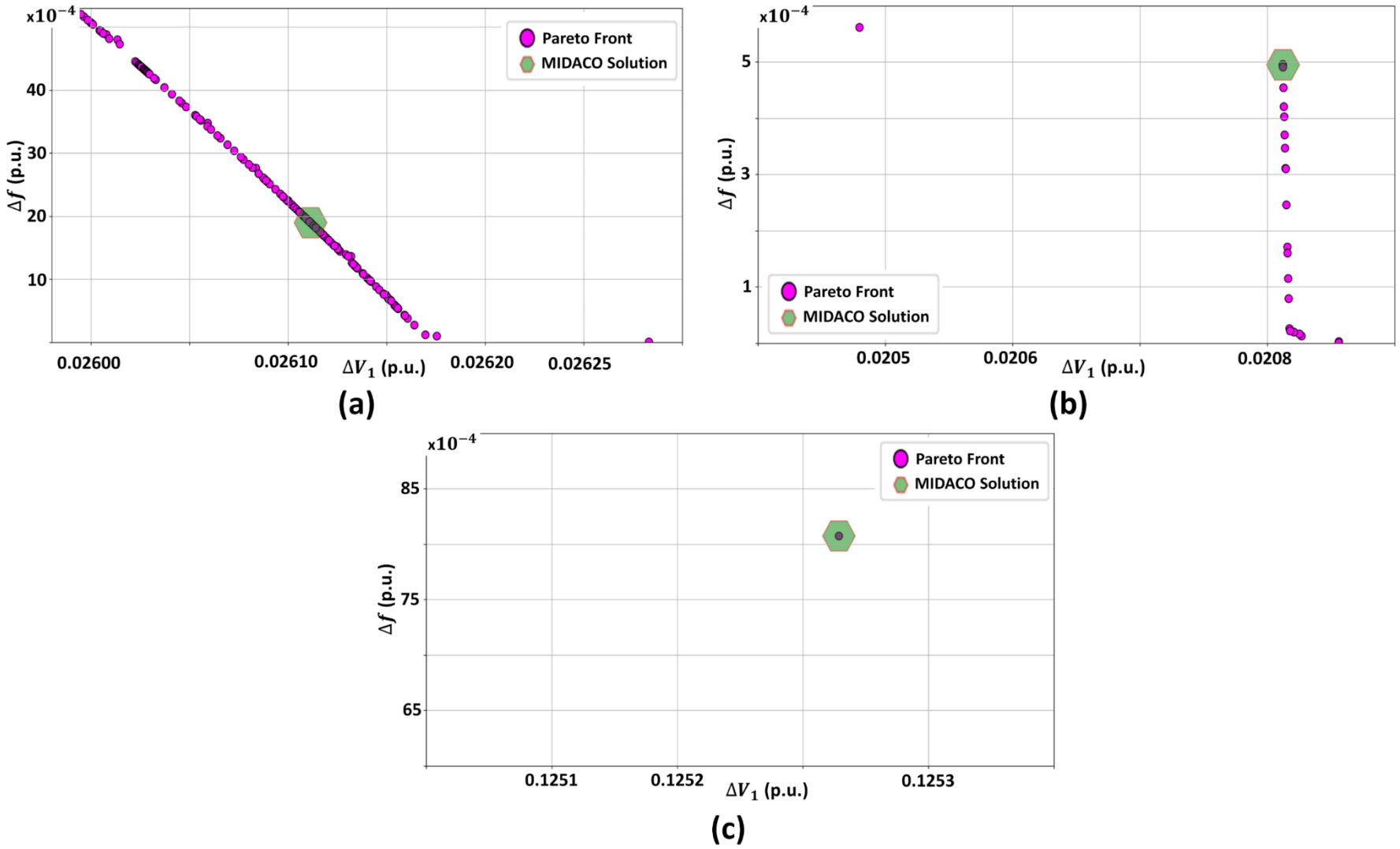

Figure 5.5: Multi-objective Pareto front considering deterministic mismatch scenario 1, the proposed method solution is highlighted in the hexagon green shape for: (a) 33-bus (b) 69-bus (c) 118-bus

Despite the utopia-nadir balance approach as illustrated by Figure 5.5 to solve the multi-objective problem, the obtained $\sum S_{Gi}$ by the solution were, respectively, (5.42∠38.30° p.u.), (5.86∠39.53° p.u.), and (29.96∠37.24° p.u.) for the 33-, 69-, and 118-bus systems. As a result, power losses did not improve further if compared with the individual $|\Delta f|$ objective (with the exception for the 118-bus two-objectives case where losses were improved against the individual $|\Delta f|$ case).

The rise in power demand compared to the $|\Delta f|$ case is explained by the rise in the DL size as given in Table 5.3. Nonetheless, the benefit of multi-objective DL allocation in radial IMG with large power mismatch was apparent by the improvements in MVE and steady state frequency (f_{ss}) if compared with the individual objectives. Moreover, the attained bus locations for DL as given in Table 5.3 concur with the assumption of allocating the DL randomly distant from a generator bus to assist in the high over-generation situation by providing V-f regulation. Similarly, DL allocation in radial distribution systems has improved the voltage profile of the network and enhanced f_{ss} where the active power generation/load ratio is high.

However, system losses were degraded after the inclusion of DL for the single- and two-objectives optimization as seen in Figure 5.4 for all three bus systems. Lastly, by having the BALANCE parameter at a default value, the algorithm managed to find the best equally traded non-dominated solution as depicted in Figure 5.5 for all three test systems. Noting that the solution for the 118-bus system case did have very little number of Pareto points. Since, as mentioned earlier, the significant over-generation mismatch has pushed the solution search space beyond the boundaries of the assumed DL problem dimensions (Figure 5.5(c)). Nonetheless, the advantage of multi-objective optimization against single objective is manifested in the 118-bus system critical case. This is explained by finding a better DL location at bus 68 using multi-objective optimization. Accordingly, better overall system losses for the same sized DL were attained as compared to the single objective solution of 118-bus system.

5.5.2.2 Four-Objectives Optimization

5.5.2.2.1 33-Bus System

The problem was formulated as a four-objectives optimization problem to find the optimal size and location of dump load and the optimum droop settings. That is, to minimize voltage and frequency deviations as well as active and reactive system power losses.

This was done for all generation/loading power mismatch scenarios as given in Table 5.2. Similarly, the four-objectives problem managed to find a better equally traded no-dominated solution to satisfy all problem dimensions. That is, by minimizing deviations in voltage and frequency during off-peak hours while keeping the impact of DL on system losses to minimum. Subsequently, the non-dominated solution for the IEEE 33-bus system via

utilizing the proposed optimization method, MIDACO, and the proposed load flow technique, SBFS, is given in Table 5.4

Table 5.4: Many-objective results at different mismatch scenarios, 33-bus system

Scenario	1		2		3		4	
Case	No DL	w/DL	No DL	w/DL	No DL	w/DL	No DL	w/DL
N_{DL}	-	13	-	13	-	13	-	13
P_{DL} **(p.u.)**	-	0.2319	-	0.1745	-	0.2176	-	0.2555
Q_{DL} **(p.u.)**	-	0.1594	-	0.1389	-	0.1737	-	0.1962
mn_{DL} **(p.u.)**	-	0.0191	-	0.0038	-	0.0052	-	0.0070
$\|\Delta V_1\|$ **(p.u.)**	0.0586	0.0082	0.0886	0.0026	0.0740	0.0029	0.0633	0.0032
$\|\Delta f\|$ **(p.u.)**	0.0141	0.0011	0.1015	0.0029	0.0779	0.0030	0.0607	0.0030
P_{loss} **(p.u.)**	0.0195	0.0201	0.0199	0.0134	0.0228	0.0212	0.0271	0.0280
Q_{loss} **(p.u.)**	0.0153	0.0154	0.0167	0.0103	0.0192	0.0163	0.0224	0.0215
MVE **(p.u.)**	0.0642	0.0119	0.1022	0.0138	0.0853	0.0178	0.0730	0.0206
f_{ss} **(p.u.)**	1.0145	1.0011	1.1034	1.0030	1.0792	1.0030	1.0617	1.0030

First step size only for $|\Delta V_1|$ and $|\Delta f|$

As given in Table 5.4, the four-objectives dump load allocation results for the IEEE 33-bus system, i.e., P_{DL}, Q_{DL}, and N_{DL}, were (0.2319 p.u., 0.1594 p.u., 13), respectively. Inversely, the optimum droop setting (mn_{DL}) for the IEEE 33-bus system was obtained as 0.0191. In addition, the f_{ss} frequency was obtained as 1.0011 p.u. which is inside the acceptable range for steady state frequency in IMGs to comply with IEEE std.1547.4. Furthermore, the MVE was further improved for the 33-bus system if compared to the No DL case and the other individual cases (i.e., considering $|\Delta V_1|$ and $|\Delta f|$ as single and two-objectives).

Likewise, the MVE of the 33-bus system had significantly improved by (-0.0198) if compared with the two-objectives case for the same test system. This was reflected upon the progress of the optimal solution by a better overall voltage profile according to Figure 5.3(a).

On the other hand, changing the generation/loading scenarios did not negatively impact the performance of DL allocation method. This was more evident with more balanced voltage profiles for all investigated scenarios for the 33-bus system as illustrated in Figure 5.6(a). Subsequently, the results obtained considering each highly probable mismatch scenario are given in Table 5.4.

Meanwhile, upon tackling the optimization problem taking into consideration system power losses as objectives, the resultant power loss values were satisfactory for the four-objectives if compared to the No DL case (see Figure 5.4(a)). Similarly, the impact of DL allocation on losses was further reduced considering different loading and generation scenarios as depicted in Figure 5.7(a), while the best non-dominated solution's location on the Pareto front is illustrated in Figure 5.8(a).

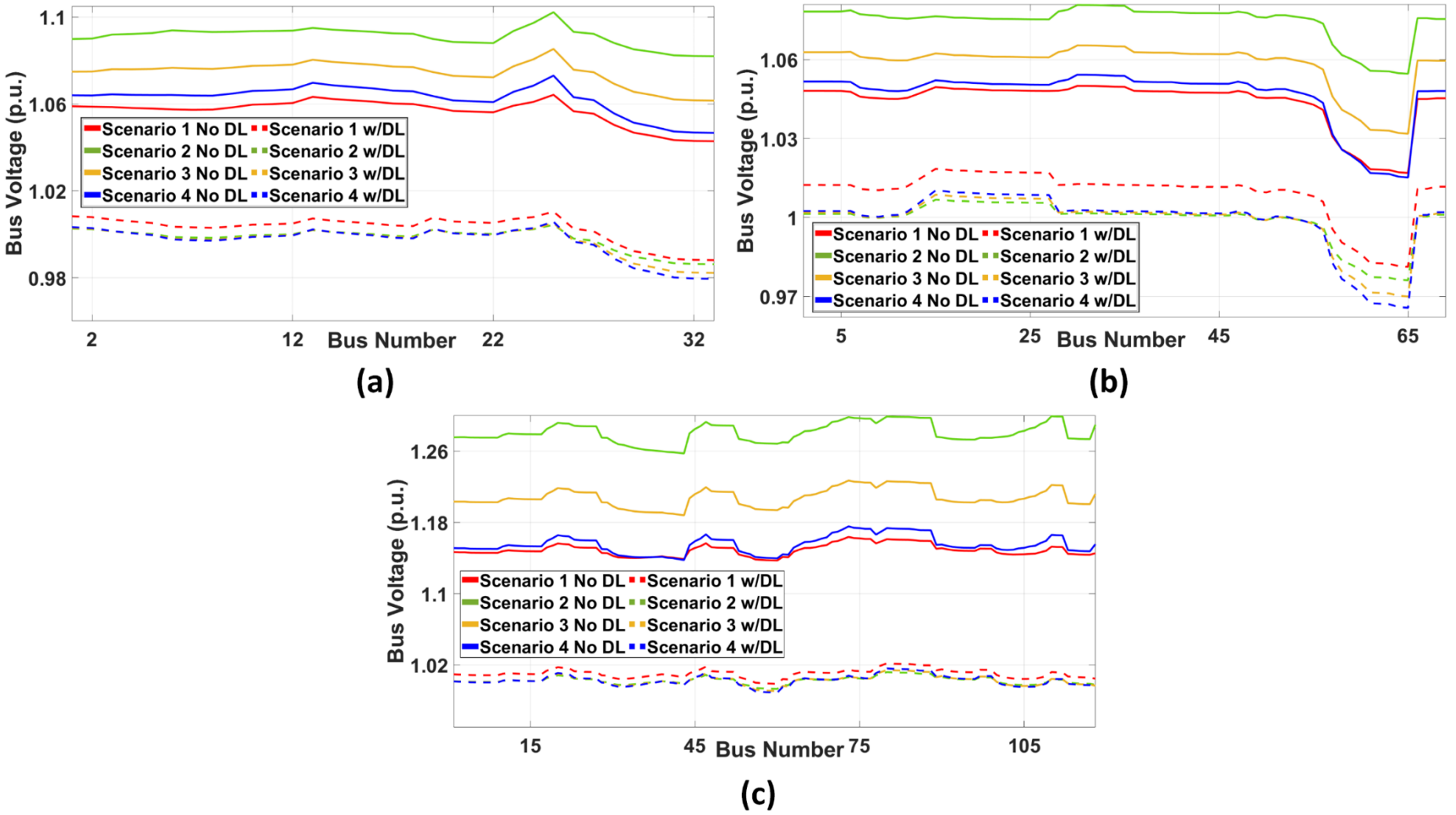

Figure 5.6: Dump load impact on voltage profile considering all scenarios for: (a) 33-bus (b) 69-bus (c) 118-bus

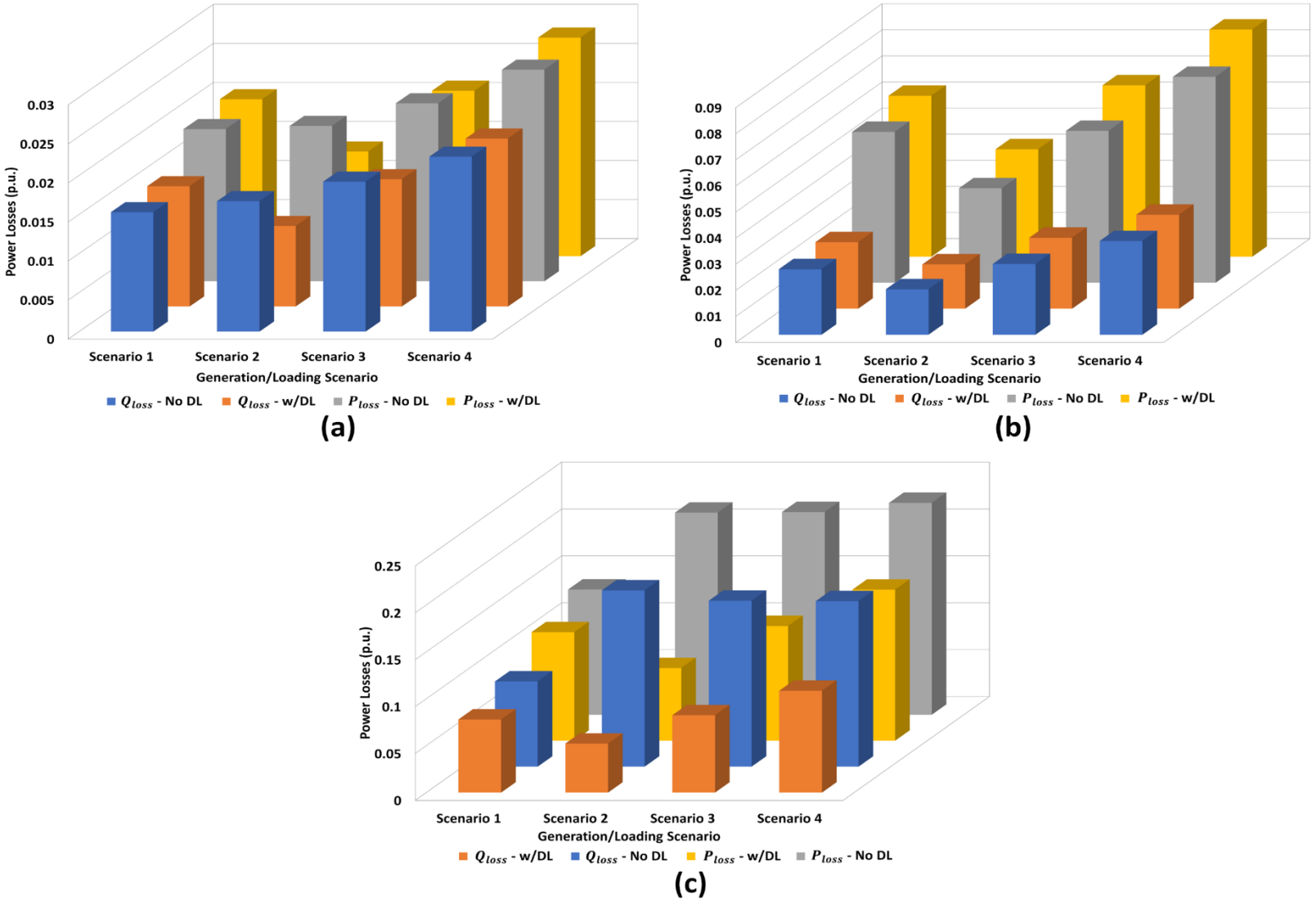

Figure 5.7: Dump load impact on losses profile considering all scenarios for: (a) 33-bus (b) 69-bus (c) 118-bus

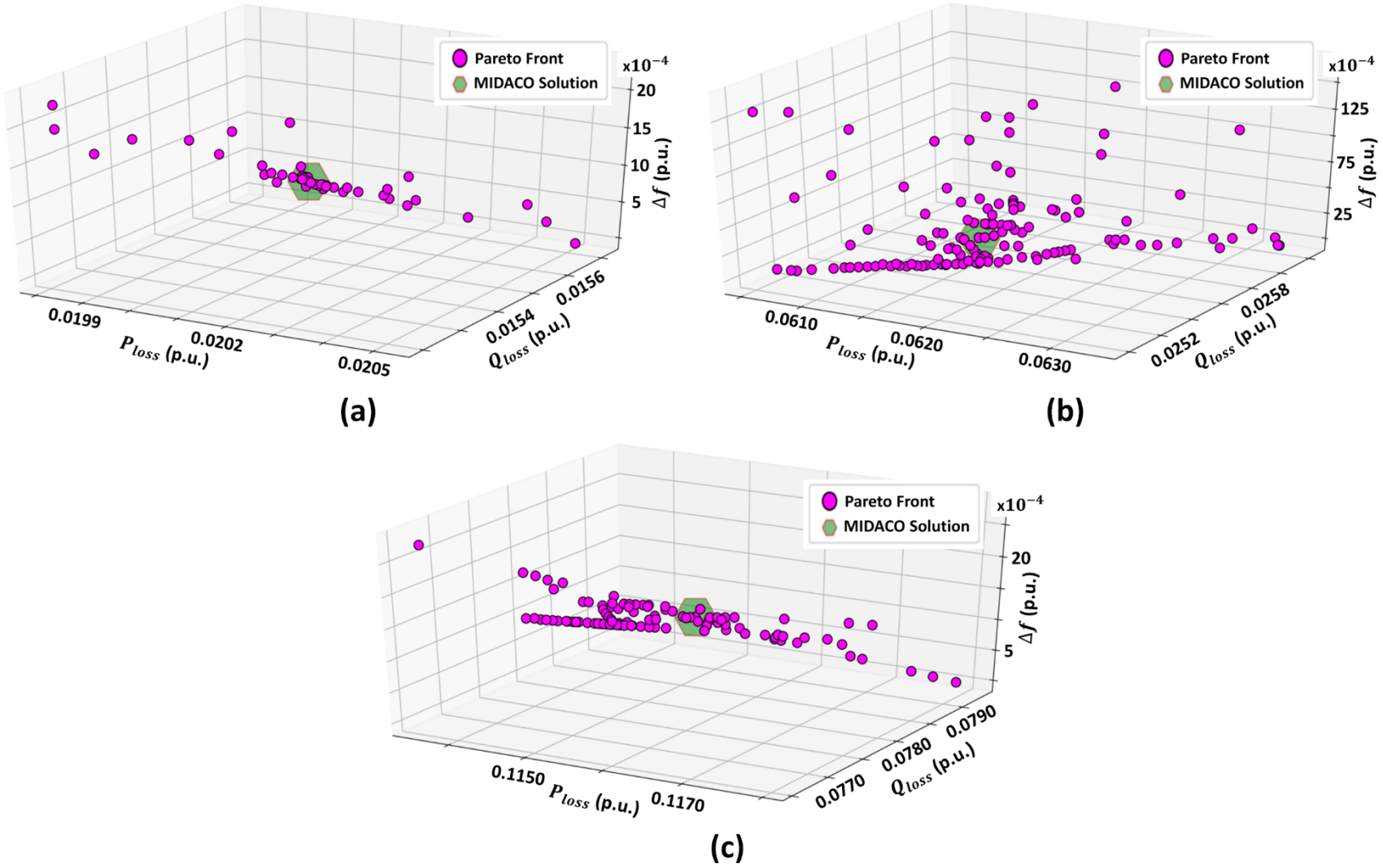

Figure 5.8: Many-objective Pareto front considering deterministic mismatch scenario 1, the proposed method solution is highlighted in the hexagon green shape for: (a) 33-bus (b) 69-bus (c) 118-bus

Noteworthy here according to Figure 5.8, is the number of collected non-dominated Pareto points which is not identical for the IEEE 33-, 69- and 118-bus cases. This was despite the fact that all simulated cases had the same value for BALANCE, EPSILON, and PARETOMAX parameters. Nonetheless, the influence on the number and shape of Pareto front after fixing the latter parameters becomes dictated by the solution search space which is problem specific.

5.5.2.2.2 69-Bus System

The 69-bus many-objective's results considering scenario 1 are given in Table 5.5. Accordingly, the effect of DL inclusion into the IMG on power losses was enhanced further by tackling all four objectives. Considering scenario 1, the attained $\sum S_{Gi}$ was equal to (5.56∠35.57° p.u.) which were lower in comparison with the individual $|\Delta V_1|$ and $|\Delta f|$ objectives considering scenario 1.

Table 5.5: Many-objective results at different mismatch scenarios, 69-bus system

Scenario	1		2		3		4	
Case	No DL	w/DL	No DL	w/DL	No DL	w/DL	No DL	w/DL
$\boldsymbol{N_{DL}}$	-	30	-	30	-	30	-	30
$\boldsymbol{P_{DL}}$ **(p.u.)**	-	0.6580	-	0.6253	-	0.7781	-	0.9332
$\boldsymbol{Q_{DL}}$ **(p.u.)**	-	0.5135	-	0.4065	-	0.4928	-	0.5274
$\boldsymbol{mn_{DL}}$ **(p.u.)**	-	0.0487	-	0.0027	-	0.0052	-	0.0088
$\boldsymbol{\|\Delta V_1\|}$ **(p.u.)**	0.0480	0.0123	0.0779	0.0014	0.0626	0.0019	0.0515	0.0024
$\boldsymbol{\|\Delta f\|}$ **(p.u.)**	0.0170	0.0003	0.0985	0.0016	0.0767	0.0021	0.0609	0.0023
$\boldsymbol{P_{loss}}$ **(p.u.)**	0.0578	0.0617	0.0362	0.0412	0.0582	0.0657	0.0789	0.0871
$\boldsymbol{Q_{loss}}$ **(p.u.)**	0.0251	0.0255	0.0174	0.0170	0.0271	0.0272	0.0359	0.0360
$\boldsymbol{MVE}$ **(p.u.)**	0.0500	0.0188	0.0807	0.0239	0.0654	0.0301	0.0542	0.0344
$\boldsymbol{f_{ss}}$ **(p.u.)**	1.0173	0.9998	1.0994	1.0017	1.0774	1.0022	1.0614	1.0023

First step size only for $|\Delta V_1|$ and $|\Delta f|$

This reduction in losses as given by Table 5.5, is due to the advantage of considering DG droop as a decision variable of the problem. A comparison bar graph between all optimization cases investigated against the base case (i.e., No DL) for power losses considering scenario 1 is depicted in Figure 5.4(b). Moreover, as given in Table 5.5, an enhancement of -0.004 was observed on the 69-system's MVE in comparison with the two objectives problem. This was also reflected on the voltage profile as illustrated in Figure 5.3(b). Noteworthy is that the correction of voltage as achieved by the many-objective problem is the maximum attainable considering the assumed range for the DL values under the assumed mismatch scenario 1.

Conversely, the optimal solution located at the centre of the Pareto front with the default balance value is depicted in Figure 5.8(b). To further strengthen the proposed method's

efficacy for DL allocation in a DCIMG with high penetration, different generation/loading scenarios were utilized, while results are given in Table 5.5. According to the results, significant stability enhancements were observed by absorbing the excess power with minimal additional losses to the IMG. This advancement against the No DL case considering all four scenarios is manifested by the enhanced profiles for voltage considering every scenario in the DL allocation as depicted in Figure 5.6(b). Similarly, the frequency f_{ss} considering all four scenarios did not exceed the allowable range for frequency (i.e., 0.996 – 1.004 p.u.) for the IMG to conform with the international standards such as IEEE std.1547.

5.5.2.2.3 118-Bus System

By using the 118-bus system which has a larger capacity and demand compared to the 33- and 69-bus systems, the DL allocation problem complexity was expanded. However, the results based on this expansion had conformed with the desired outcome to maintain V-f deviations within acceptable limits without degrading system losses. Better voltage profile is observed for the 118-bus system if compared with the No DL case and that of the individual single objective cases considering $|\Delta V_1|$ and $|\Delta f|$ as depicted in Figure 5.3(c). Moreover, the Pareto optimal front considering scenario 1 for the 118-bus system is illustrated in Figure 5.8(c). As given in Table 5.6, the obtained DL bus locations were similar for all four scenarios at bus 73 for the 118-bus system.

Table 5.6: Many-objective results at different mismatch scenarios, 118-bus system

Scenario	1		2		3		4	
Case	No DL	w/DL	No DL	w/DL	No DL	w/DL	No DL	w/DL
$\boldsymbol{N_{DL}}$	-	73	-	73	-	73	-	73
$\boldsymbol{P_{DL}}$ **(p.u.)**	-	0.4771	-	0.3820	-	0.4896	-	0.5613
$\boldsymbol{Q_{DL}}$ **(p.u.)**	-	0.7289	-	0.5860	-	0.7293	-	0.8467
$\boldsymbol{mn_{DL}}$ **(p.u.)**	-	0.0117	-	0.0011	-	0.0015	-	0.0019
$\boldsymbol{\lvert\Delta V_1\rvert}$ **(p.u.)**	0.1454	0.0094	0.2694	0.0018	0.1994	0.0017	0.1486	0.0016
$\boldsymbol{\lvert\Delta f\rvert}$ **(p.u.)**	0.0281	0.0014	0.3587	0.0025	0.2655	0.0024	0.1978	0.0022
$\boldsymbol{P_{loss}}$ **(p.u.)**	0.1335	0.1157	0.2155	0.0774	0.2161	0.1223	0.2258	0.1610
$\boldsymbol{Q_{loss}}$ **(p.u.)**	0.0908	0.0779	0.1879	0.0522	0.1769	0.0824	0.1764	0.1085
$\boldsymbol{MVE}$ **(p.u.)**	0.1636	0.0218	0.2991	0.0120	0.2269	0.0145	0.1755	0.0161
$\boldsymbol{f_{ss}}$ **(p.u.)**	1.0301	1.0015	1.3687	1.0026	1.2722	1.0025	1.2025	1.0023

First step size only for $|\Delta V_1|$ and $|\Delta f|$

By considering the DL locations given in Table 5.6, a dump load allocation can be valued as a cost-effective and efficient technique to manage power deviations at the planning stage. Similarly, the obtained bus locations considering all four scenarios were at buses 13 and 30 for the 33- and 69-bus systems, respectively. Furthermore, as depicted in Figure 5.6(c),

the theme for the obtained voltage profiles considering all four mismatch scenarios for the 118-bus system did not deviate from those reported by the 33- and 69-bus systems. However, in comparison with the 33- and 69-bus systems, much higher MVE was observed for the 118-bus system considering scenario 1 as given in Table 5.6. This is attributed to the high mismatch in reactive power (24.32/17.04 over-generation) in the 118-bus pre-islanding situation. Nonetheless, the foregoing reactive power mismatch condition has created a system with leading branch currents. Hence, the reduction of losses after DL inclusion is attributed as an inductive correction in predominantly capacitive network (i.e., the system during the No DL case). The losses profile for 118-bus system considering each generation/loading scenario is depicted in Figure 5.7(c). It can be deduced that network losses were further reduced below the No DL case threshold as the generation and demand mismatch increased (i.e., varying the mismatch scenarios). This was true for both 33- and 118-bus systems case studies. However, the losses profile of the 69-bus system did not further improve with different generation/loading scenarios after DL inclusion. This is true if compared with the No DL case for the same test system as seen in Figure 5.7(b). The increased losses situation is explained by having a higher value for the DL's active and reactive powers in the 69-bus system case if compared with the other two test systems (i.e., 33- and 118-bus systems).

5.5.3 Impact of Varying MIDACO Parameters Using Special Backward\Forward Sweep

By considering SBFS as the LF tool within MIDACO algorithm, the DL allocation problem was studied considering the proposed method's most influential parameters and their variations. This was done only for the many-objective problem in each test system. The parameters' variation tests were applied to the optimization problem's non-dominated solution considering test systems, viz., IEEE 33-, 69-, and 118-bus systems. Furthermore, every parameter variation test was conducted using the power mismatch scenario 1 of Table 5.2 (see page 103). Moreover, the load model set 1 from Table 4.1 (see page 66) was selected to act as the constant power load model. Accordingly, the effect of the parameter BALANCE on the non-dominated solution for the IEEE 33-, 69-, and 118-bus systems is given in Table 5.7. The results show the importance of this parameter with different obtained results as the value of BALANCE changed from the default value of zero to a selected integer and non-integer values. The use of integer values for BALANCE parameter will alter the search effort towards a particular objective. That is, for example, selecting value of 2 will force MIDACO to search for solutions where the second objective is more dominant than the others. This is due to influence of BALANCE on the algorithm search efforts and concentration at the Pareto front. To visualise the impact of BALANCE parameter on the solution for the IEEE 33-, 69-, and 118-bus systems, the Pareto front for different BALANCE values is depicted in Figure 5.9.

Table 5.7: Impact of BALANCE parameter on the solution for mismatch scenario 1, all bus systems

BALANCE	Test System	Pareto Points	N_{DL}	P_{DL} (p.u.)	Q_{DL} (p.u.)	mn_{DL} (p.u.)	$\lvert\Delta V_1\rvert$ (p.u.)	$\lvert\Delta f\rvert$ (p.u.)	P_{loss} (p.u.)	Q_{loss} (p.u.)
0	33	45	13	0.2319	0.1594	0.0191	0.0082	0.0011	0.0201	0.0154
	69	131	30	0.658	0.5135	0.0487	0.0123	0.0003	0.0617	0.0255
	118	99	73	0.4771	0.7289	0.0117	0.0094	0.0014	0.1157	0.0779
1	33	7	33	0.9999	0.9999	0.0001	2.0×10^{-5}	1.6×10^{-5}	0.1083	0.0863
	69	11	61	0.6579	0.9999	0.0001	1.5×10^{-5}	2.6×10^{-6}	0.1631	0.0654
	118	10	60	0.9999	0.9999	0.0001	7.6×10^{-5}	0.4×10^{-5}	0.2008	0.1307
2	33	43	13	0.4611	0.9754	0.0001	2.3×10^{-5}	0	0.0280	0.0215
	69	27	25	0.6261	0.2758	0.0001	3.0×10^{-5}	0	0.0717	0.0302
	118	8	60	0.9999	0.9999	0.0001	7.6×10^{-5}	0.4×10^{-5}	0.2008	0.1307
3	33	179	13	0.2144	0.1771	0.0468	0.0199	0.0028	0.0197	0.0151
	69	145	30	0.6672	0.5171	0.0831	0.0210	0.0006	0.0606	0.025
	118	135	73	0.4759	0.6806	0.0245	0.0198	0.0029	0.1133	0.0765
4	33	186	13	0.1904	0.1504	0.0461	0.0199	0.0031	0.0197	0.0151
	69	220	30	0.9319	0.5425	0.0848	0.021	0.0051	0.0607	0.0249
	118	164	73	0.4947	0.7279	0.0247	0.0198	0.0028	0.1134	0.0764
0.8411	33	142	1	0.3585	0.9185	0.0001	2.4×10^{-5}	0.2×10^{-5}	0.0250	0.0189
	69	124	30	0.7592	0.5785	0.0085	0.002	0.0002	0.0631	0.0260
	118	62	73	0.4951	0.7633	0.0015	0.0012	0.0002	0.1177	0.0791
0.2681	33	235	13	0.3437	0.1588	0.0456	0.0196	0.0013	0.0199	0.0153
	69	161	30	0.6341	0.455	0.0699	0.0185	4.0×10^{-5}	0.0609	0.0252
	118	106	80	0.9999	0.8542	0.018	0.0142	0.0009	0.1151	0.0782
0.6119	33	196	13	0.1867	0.1647	0.0073	0.0031	0.0005	0.0204	0.0156
	69	222	30	0.9886	0.5795	0.0652	0.0156	0.0047	0.0615	0.0252
	118	140	73	0.4982	0.7227	0.0193	0.0155	0.0022	0.1143	0.0771

First step size only for $\lvert\Delta V_1\rvert$ and $\lvert\Delta f\rvert$

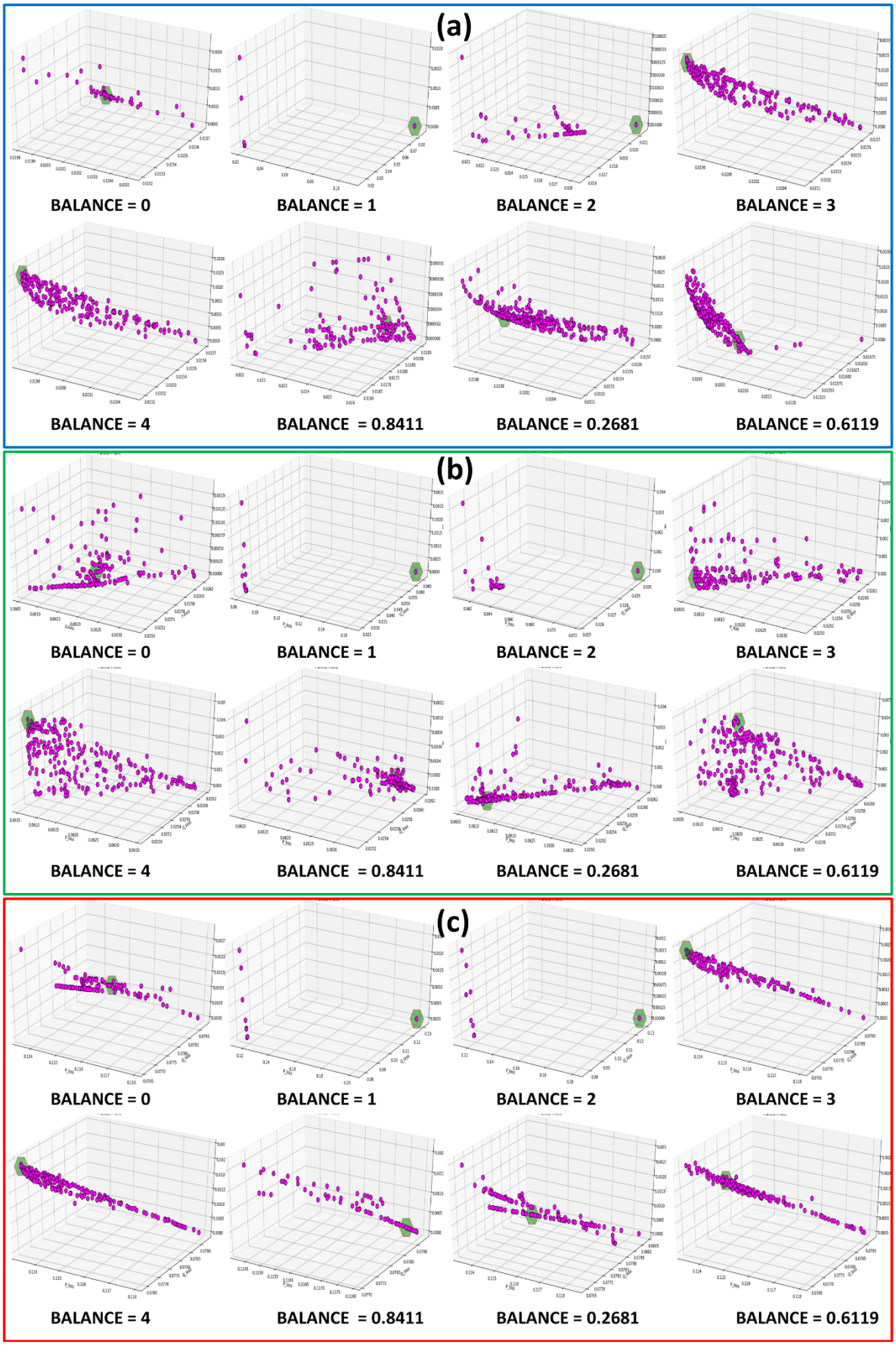

Figure 5.9: The impact of BALANCE on Pareto front for: (a) 33-bus (b) 69-bus (c) 118-bus

From Figure 5.9 and Table 5.7, the advantage of BALANCE parameter can be realized by the number of Pareto points collected for each test system at different BALANCE values. In addition, BALANCE impact is felt by the overall shape of the Pareto curve as well as the location of the chosen optimal solution.

In one hand, by having the BALANCE value at zero, the produced Pareto front curve will tend to have equal distribution across the solution search space. Thus, the optimal solution chosen by MIDACO is located at the centre of the Pareto front.

On the other hand, having a different value for BALANCE will result in movement of the selected optimal solution away from the centre. This movement is attributed to the change in the balance of weights between the objectives. Therefore, an integer value for BALANCE will result in steeply movement for the optimal solution toward one of the corners defining the optimal solution's search space. Conversely, by choosing a floating BALANCE value, the movement of the green hexagon shaped marker will tend to slightly abandon the centre of the Pareto front.

It is nevertheless noteworthy that the number of generated Pareto points has significantly dropped when considering a BALANCE value of 1 or 2. This implies a biased shift towards either the first or the second objective functions, that is, $|\Delta V_1|$ or $|\Delta f|$ for BALANCE values of 1 or 2, respectively.

This kind of behaviour is attributed to the influence of either objectives for voltage or frequency deviations on the resultant DL value. In one hand, by considering the minimization of $|\Delta V_1|$ or $|\Delta f|$ as the main pilot for the multi-objective problem, a higher value for the active and reactive DL power is indeed expected. On the other hand, in a significant over-generation situation, while considering the single objective problem of section 5.5.1, the value of the first droop step tends to be large. This would require a high dumping of power in the system to achieve the maximum voltage and frequency regulation objectives. As a result, all DL values for the single objective problem were high as given in Table 5.3 in page 106.

Contrariwise, using lower values for ANTS and KERNEL, very important parameters, has worsened the many-objective solution. However, the solution improved when the value of KERNEL parameter has increased as given in Table 5.8 for all three test systems.

Noting that the value of ANTS must be set equal or above the value of KERNEL, more information is given in section 3.6. The explanation for this improvement is down to the impact of higher values for K_r and how it reduces the possibility of getting stuck at a local minima during the exploration stage of the algorithm.

Furthermore, the impact of ORACLE parameter is given in Table 5.9 for all three test systems. In one hand, lower guessed oracles influence the constrained problem's solution sensitivity. Whereas, on the other hand, a reasonable solution was attained considering an adequately high value for the oracle (i.e., when ORACLE was set to 10^9).

Table 5.8: Impact of ANTS/KERNEL parameters on the solution for mismatch scenario 1, all bus systems

N_{pop}	0			2			30			500			100		
K_r	0			2			5			10			50		
Test System	33	69	118	33	69	118	33	69	118	33	69	118	33	69	118
$\|\Delta V_1\|$ **(p.u.)**	0.0082	0.0123	0.0094	4.3 x 10^{-5}	0.0136	0.0104	0.0099	0.0127	0.0098	0.01	0.0128	0.0102	0.0095	0.0109	0.0083
$\|\Delta f\|$ **(p.u.)**	0.0011	0.0003	0.0014	0.7 x 10^{-5}	2.0 x 10^{-5}	0.0008	0.0015	0.0009	0.0013	0.0014	0.0008	0.0009	0.0014	0.0011	0.0011
P_{loss} **(p.u.)**	0.0201	0.0617	0.1157	0.0205	0.0615	0.1159	0.0201	0.0617	0.1158	0.0201	0.0616	0.1159	0.0201	0.0619	0.116
Q_{loss} **(p.u.)**	0.0154	0.0255	0.0779	0.0157	0.0255	0.0787	0.0154	0.0254	0.0779	0.0154	0.0254	0.0787	0.0154	0.0255	0.0781

First step size only for $|\Delta V_1|$ and $|\Delta f|$

Table 5.9: Impact of ORACLE parameter on the solution for mismatch scenario 1, all bus systems

Ω	10^{-3}			10^{3}			10^{6}			10^{9}		
Test System	33	69	118	33	69	118	33	69	118	33	69	118
$\|\Delta V_1\|$ **(p.u.)**	0.023	0.0250	0.0152	0.0146	0.0217	0.0163	0.0134	0.0170	0.0167	0.0082	0.0123	0.0094
$\|\Delta f\|$ **(p.u.)**	0.0013	0.0007	0.0017	0.0018	0.0007	0.0012	0.0016	0.0005	0.0014	0.0011	0.0003	0.0014
P_{loss} **(p.u.)**	0.0198	0.0601	0.1150	0.0199	0.0605	0.1146	0.0199	0.0611	0.1145	0.0201	0.0617	0.1157
Q_{loss} **(p.u.)**	0.0152	0.0248	0.0774	0.0153	0.0250	0.0778	0.0153	0.0252	0.0777	0.0154	0.0255	0.0779

First step size only for $|\Delta V_1|$ and $|\Delta f|$

Table 5.10: Impact of MAXEVAL parameter on the solution for mismatch scenario 1, all bus systems

MAXEVAL	500			1000			5000			10000			20000		
Test System	33	69	118	33	69	118	33	69	118	33	69	118	33	69	118
$\|\Delta V_1\|$ **(p.u.)**	0.0012	0.0095	8.2 x 10^{-5}	0.0083	0.0129	0.0035	0.0082	0.0113	0.0094	0.0082	0.0123	0.0094	0.0095	0.0123	0.0099
$\|\Delta f\|$ **(p.u.)**	0.0003	0.0006	1.1 x 10^{-5}	0.0011	0.0003	0.0005	0.0011	0.0004	0.0014	0.0011	0.0003	0.0014	0.0014	0.0003	0.0014
P_{loss} **(p.u.)**	0.0212	0.0633	0.1212	0.0201	0.0618	0.1204	0.0201	0.0618	0.1157	0.0201	0.0617	0.1157	0.0201	0.0617	0.1156
Q_{loss} **(p.u.)**	0.0161	0.0266	0.0826	0.0154	0.0256	0.0821	0.0154	0.0255	0.0779	0.0154	0.0255	0.0779	0.0154	0.0255	0.0779
Time[a] (s)	2	3	3	4	5	6	21	21	31	41	43	62	91	94	123

First step size only for $|\Delta V_1|$ and $|\Delta f|$, [a]algorithm computation time.

Table 5.11: Impact of EPSILON parameter on the solution for mismatch scenario 1, all bus systems

EPSILON	0.01			0.001			0.0001			0.00001		
Test System	33	69	118	33	69	118	33	69	118	33	69	118
Pareto Points	45	131	99	409	708	433	917	1000	493	128	1000	764
$\|\Delta V_1\|$ **(p.u.)**	0.0082	0.0123	0.0094	0.0074	0.0124	0.0072	0.0083	0.0101	0.0086	0.0012	0.0108	0.0093
$\|\Delta f\|$ **(p.u.)**	0.0011	0.0003	0.0014	0.0011	0.0007	0.0010	0.0012	0.0007	0.0012	0.0003	0.0010	0.0012
P_{loss} **(p.u.)**	0.0201	0.0617	0.1157	0.0202	0.0617	0.1163	0.0201	0.0620	0.1159	0.0204	0.0619	0.1158
Q_{loss} **(p.u.)**	0.0154	0.0255	0.0779	0.0155	0.0254	0.0783	0.0154	0.0256	0.0780	0.0156	0.0255	0.0780
Time[a] (s)	41	43	62	48	51	66	56	63	68	43	56	75

First step size only for $|\Delta V_1|$ and $|\Delta f|$, [a]algorithm computation time.

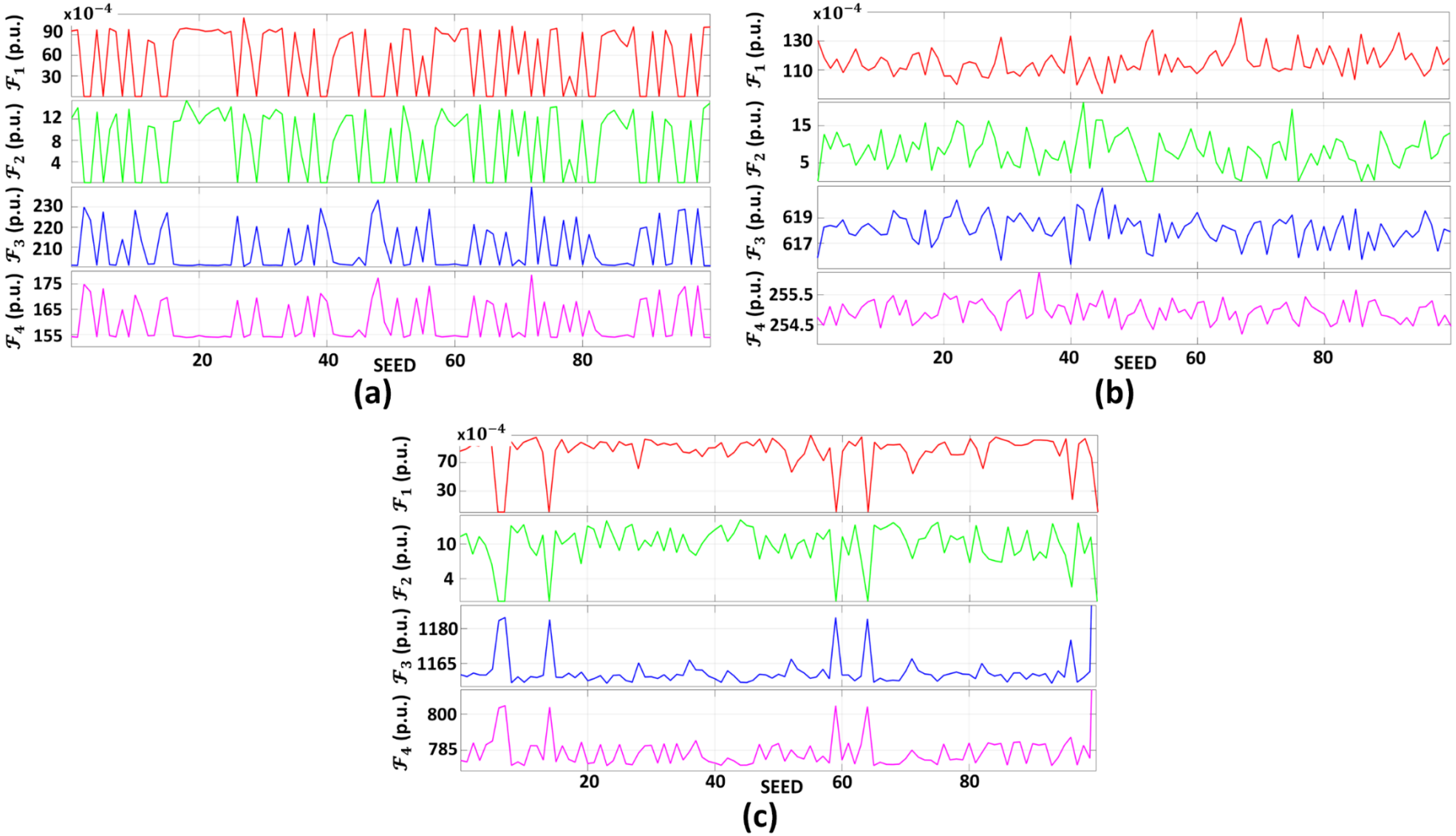

Figure 5.10: The impact of SEED on the optimal solution of the four objectives problem for: (a) 33-bus (b) 69-bus (c) 118-bus

The influence of MAXEVAL parameter on the solution fitness is given in Table 5.10 for all three test systems. The impact of MAXEVAL is manifested by dictating the maximum number of function evaluations, that is, with higher values for MAXEVAL the probability for reaching a global optima increases. Nonetheless, values beyond 10000 for MAXEVAL did not further improve the non-dominated solution offered by MIDACO.

Conversely, EPSILON parameter effect on the solution is given in Table 5.11 for all three test systems. The chances of introducing a new solution into the Pareto front increase when the value given to EPSILON decreases. However, selecting smaller values for EPSILON will result in an increased calculation time for MIDACO and higher memory usage.

Finally, to understand the impact of the parameter SEED on the optimal solution of the problem, one can examine Figure 5.10. The impact of varying SEED has influenced the optimization problem's intricacy by having subtle differences in the generated optimal solutions using different seeds.

Hence, any inconsistencies in the results have been significantly reduced, leading to a higher degree of certainty that the generated solution is as close as possible to the global optimal solution. In other words, SEED impacts the optimization process of the problem by changing it from a random stochastic search into a global optimization technique via deterministic search. Through influencing the probability for global optimality, the chances that the obtained solution is in fact the global optima become very high.

5.5.4 Impact of Different Load Models Using Special Backward\Forward Sweep

To further validate the feasibility of the proposed method's solution using SBFS load flow, results were tested considering different load models. Simulation results of the IEEE 33-, 69-, and 118-bus systems are given in Table 5.12. Noteworthy about Table 5.12 is that the selected load model variations were according to Table 4.1 sets, while adopting the mismatch scenario1 from Table 5.2 for all three test systems. Results have shown the effectiveness of the proposed method in mitigating the impact of load dependency on V-f deviations.

The solution has minimized the effect of different load models on LF convergence by reducing the number of iterations required as shown in Table 5.12. Moreover, the resultant differences between f_{ss} and MVE values for different load models were negligible if compared with the No DL case for all three test systems. The optimal allocation of DL into the MG returned more consistent voltage profiles if compared with the No DL case. As shown in Figure 5.11, by varying the load model settings under the same generation/loading scenario 1, the distortion in voltage profiles for the No DL case was notably reduced by the inclusion of the DL. This can be explained by the influence of higher V-f deviations on load values if compared with the load values after the DL allocation with minimal V-f deviations.

Table 5.12: Load model impact on four objectives problem's solution for scenario 1, all bus systems

Test System	**33-bus system**									
Case	No DL[a]					w/ DL[a] (Proposed Method)				
Load Model	Set 1	Set 2	Set 3	Set 4	Set 5	Set 1	Set 2	Set 3	Set 4	Set 5
$\sum P_{Gi}$	3.7345	3.9307	3.7833	3.9583	4.1178	3.9670	3.9768	3.9711	3.9807	3.9908
$\sum Q_{Gi}$	2.3153	2.4308	2.3455	2.4478	2.5395	2.4749	2.4748	2.4774	2.4772	2.4774
$\sum P_{Li} + P_{DL}$	3.7150	3.9097	3.7634	3.9369	4.0951	3.9469	3.9570	3.9509	3.9609	3.9713
$\sum Q_{Li} + Q_{DL}$	2.3000	2.4144	2.3299	2.4312	2.5220	2.4594	2.4596	2.4619	2.4620	2.4624
MVE	0.0642	0.0600	0.0631	0.0594	0.0564	0.0119	0.0117	0.0120	0.0117	0.0115
f_{ss}	1.0145	1.0084	1.0130	1.0076	1.0026	1.0011	1.0011	1.0011	1.0010	1.0010
Iterations	16	33	25	40	58	15	27	15	27	34
Test System	**69-bus system**									
Case	No DL[a]					w/ DL[a] (Proposed Method)				
Load Model	Set 1	Set 2	Set 3	Set 4	Set 5	Set 1	Set 2	Set 3	Set 4	Set 5
$\sum P_{Gi}$	3.8600	3.9823	3.8616	4.0296	4.1264	4.5218	4.5173	4.5210	4.5167	4.5149
$\sum Q_{Gi}$	2.7197	2.8054	2.7367	2.8385	2.9064	3.2336	3.2308	3.2331	3.2303	3.2294
$\sum P_{Li} + P_{DL}$	3.0822	3.9222	3.9215	3.9679	4.0633	4.4602	4.4577	4.4594	4.4571	4.4572
$\sum Q_{Li} + Q_{DL}$	2.6946	2.7793	2.7627	2.8117	2.8790	3.2081	3.2060	3.2076	3.2056	3.2053
MVE	0.0500	0.0477	0.0489	0.0468	0.0450	0.0188	0.0184	0.0188	0.0184	0.0183
f_{ss}	1.0173	1.0140	1.0156	1.0127	1.0101	0.9998	0.9998	0.9998	0.9998	0.9999
Iterations	16	30	26	39	53	16	20	19	24	21
Test System	**118-bus system**									
Case	No DL[a]					w/ DL[a] (Proposed Method)				
Load Model	Set 1	Set 2	Set 3	Set 4	Set 5	Set 1	Set 2	Set 3	Set 4	Set 5
$\sum P_{Gi}$	22.8433	25.3568	23.313	25.069	NC	23.3026	23.5264	23.3357	23.5520	23.7608
$\sum Q_{Gi}$	17.132	19.0038	17.483	18.789	NC	17.8479	18.0110	17.8728	18.0301	18.1821
$\sum P_{Li} + P_{DL}$	22.843	25.2107	23.177	24.925	NC	23.1868	23.4095	23.2196	23.4347	23.6426
$\sum Q_{Li} + Q_{DL}$	17.132	18.9087	17.392	18.694	NC	17.7700	17.9324	17.7946	17.9513	18.1027
MVE	0.1636	0.1252	0.1565	0.1296	NC	0.0218	0.0216	0.0218	0.0215	0.0213
f_{ss}	1.0301	0.9788	1.0206	0.9847	NC	1.0015	1.0012	1.0014	1.0011	1.0008
Iterations	18	66	62	438	NC	16	30	18	31	40

[a]All values in per unit system except for iterations (i.e., integers).

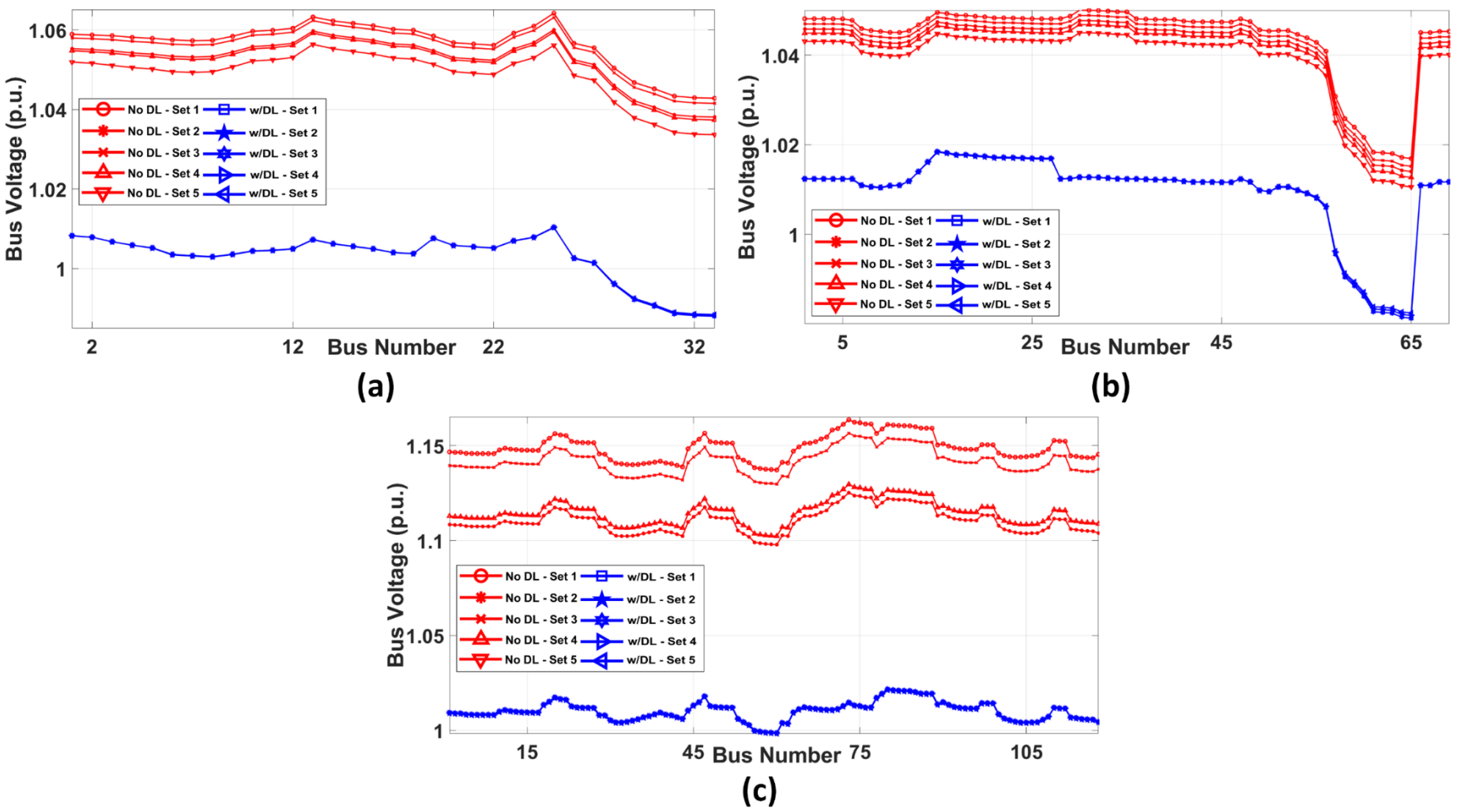

Figure 5.11: Load model impact on voltage profile considering DL allocation scenario 1 for: (a) 33-bus (b) 69-bus (c) 118-bus

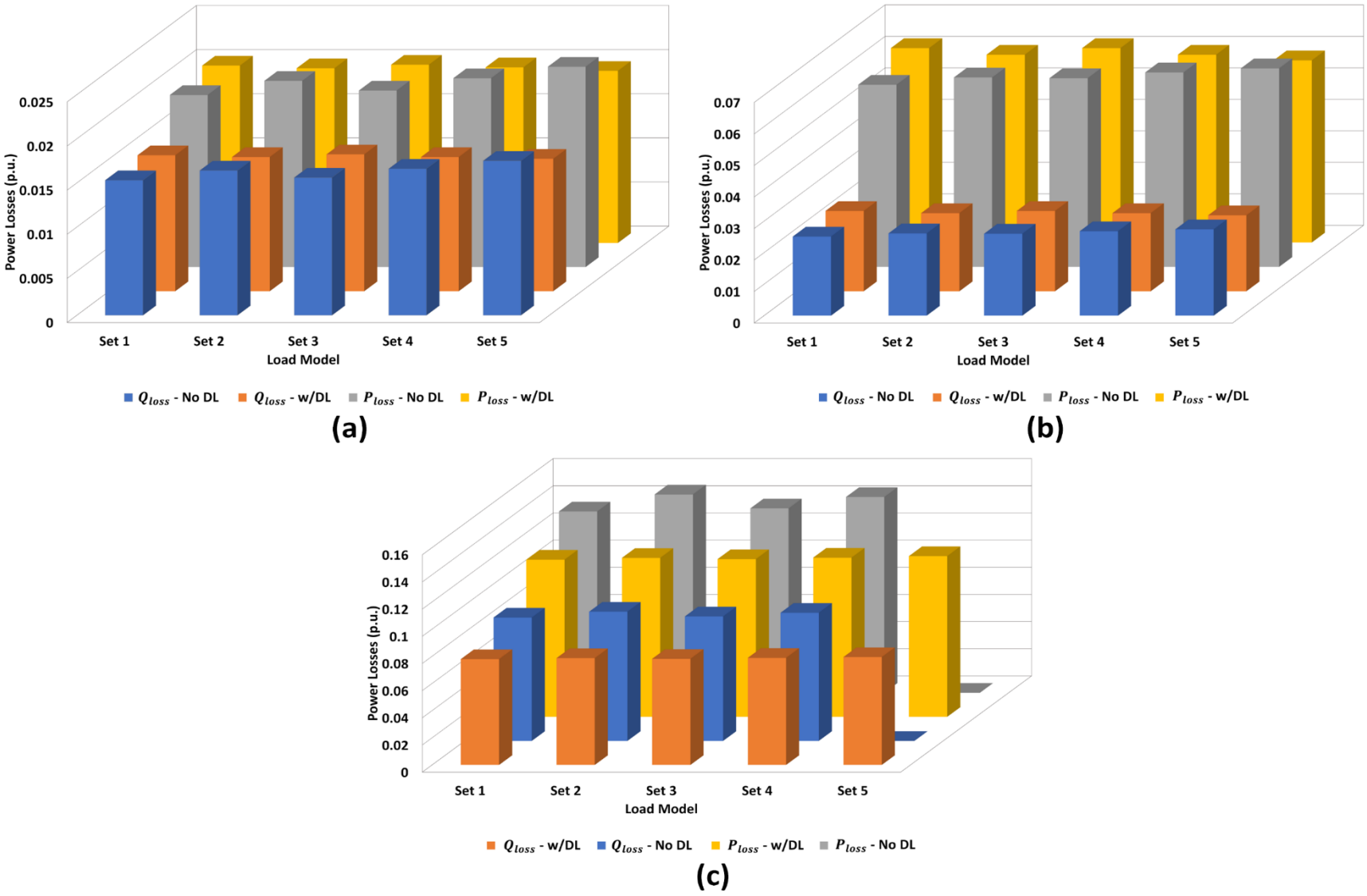

Figure 5.12: Load model impact on losses profile considering DL allocation scenario 1 for: (a) 33-bus (b) 69-bus (c) 118-bus

Moreover, the losses profiles for the three test networks considering different load models are depicted in Figure 5.12. It is observed that losses of the network were further reduced below the No DL case threshold considering the different load models. This was true for all test systems investigated, bearing in mind that the No DL case in the 118-bus system did not converge to a solution using load set 5 as shown in Figure 5.12(c).

5.5.5 Dump Load Allocation with Different Load Flow Methods

In this sub-section, the optimal DL allocation considering scenario 1 from Table 5.2 for all three bus systems had been simulated with different LF methods. This would shed more light at the influence of LF technique on MIDACO performance and the solution accuracy. To simulate the many-objective problem, parameters BALANCE, PARETOMAX, and EPSILON were initialized as 0,1000, and 0.01, respectively. Whereas parameters ANTS, KERNEL, and ORACLE were set to zero (the default value). This will ensure dynamic population in each generation with sufficiently high oracle in MIDACO. Given in Table 5.13 are the 33-bus system's obtained results using different LF methods, viz., SBFS, SBFS-II, and GBFS.

Table 5.13: Many-objective results with different load flow methods, 33-bus system

Load Flow Method	SBFS		SBFS-II		GBFS	
Case	No DL	w/DL	No DL	w/DL	No DL	w/DL
N_{DL}	-	13	-	13	-	13
P_{DL} **(p.u.)**	-	0.2319	-	0.2377	-	0.3399
Q_{DL} **(p.u.)**	-	0.1594	-	0.1752	-	0.7282
mn_{DL}	-	0.0191	-	0.0188	-	0.0053
$\lvert\Delta V_1\rvert$ **(p.u.)**	0.0586	0.0082	0.0586	0.0080	0.0586	0.0015
$\lvert\Delta f\rvert$ **(p.u.)**	0.0141	0.0011	0.0141	0.0011	0.0141	0.0002
P_{loss} **(p.u.)**	0.0195	0.0201	0.0195	0.0202	0.0194	0.0197
Q_{loss} **(p.u.)**	0.0153	0.0154	0.0153	0.0154	0.0152	0.0151
MVE **(p.u.)**	0.0642	0.0119	0.0642	0.0121	0.0628	0.0189
f_{ss} **(p.u.)**	1.0145	1.0011	1.0145	1.0012	1.0146	1.0002
Time[a] (s)	-	41	-	35	-	84

First step size only for $\lvert\Delta V_1\rvert$ and $\lvert\Delta f\rvert$, [a]algorithm computation time.

According to the results in Table 5.13, the benefit of DL allocation was evident upon combining the different LF methods with MIDACO. Thereby, significant improvement in the V-f regulation for the 33-bus system by minimizing deviations in compliance with IEEE std.1547.4 [4]. Taking the 33-bus system's base case (i.e., No DL using droop set from Table 5.1), the proposed SBFS-II method was able to obtain the exact same LF solution as that of the SBFS base case. However, the LF solution obtained by GBFS for the No DL case was not

identical to SBFS for the same No DL case. This is due to the core difference between the two methods of adopting local and global voltage approaches for GBFS and SBFS, respectively.

Moreover, lower losses were incurred by the DL allocation using GBFS/MIDACO combination despite having a large size for the DL. Similarly, in some cases the DL application has matched or reduced losses below the case when there was no DL in the system. Additionally, in comparison with SBFS/MIDACO run time and that of SBFS-II/MIDACO, the calculation time has improved by 6 seconds via adopting SBFS-II as the LF method within MIDACO. Nevertheless, almost identical objective function values for both SBFS and SBFS-II approaches were obtained. This highlighted accuracy of the optimization method using SBFS-II instead of SBFS is necessary to warrant the decrease in calculation speed. Contrariwise, the accuracy of DL allocation using MIDACO with GBFS has significantly improved on the expense of increased calculation time.

According to Table 5.13, the optimized objectives for V-f deviations, active, and reactive losses were smaller if compared with SBFS- and SBFS-II-based solutions. Moreover, despite the increased DL size by GBFS/MIDACO solution, the obtained losses were slightly lower than those of the other LF methods (SBFS and SBFS-II). This improvement is explained by the advantage of LF methods based on local voltage measurement, such as GBFS, against global voltage distribution based LF methods, such as SBFS and SBFS-II. The reason behind this lies in the unnecessary increase in generated power by all DGs to match a remote bus voltage (i.e., the VB herein). Furthermore, in comparison with the No DL case, the reduced reactive power losses obtained by GBFS/MIDACO combination indicates having a situation of inductive reactive compensation in a highly capacitive network. This was caused by the large over-generation reactive power mismatch which has occurred pre-islanding.

On the other hand, the variation in LF methods' combination with MIDACO for the 69- and 118-bus systems are given in Table 5.14 and Table 5.15, respectively. Similarly with 33-bus system, the achieved No DL case LF solutions for the 69- and 118-bus systems were identical using either SBFS or SBFS-II. Moreover, the obtained DL allocation results for the objective functions using SBFS-II/MIDACO for 69- and 118-bus systems were very similar to those previously obtained by SBFS/MIDACO in [48] (see Tables 5.14 and 5.15). However, the slight error in the obtained DL size between SBFS and SBFS-II solutions did not have any effect on the accuracy of the obtained four objective values for the 69- and 118-bus systems. Conversely, further improvements in calculation times were achieved by using SBFS-II/MIDACO combinations. According to the results, the calculation times for the 69- and 118-bus systems were improved by 5 and 8 seconds, respectively. The advancement in calculation times by SBFS-II/MIDACO is explained by the faster function evaluation instance in MIDACO caused by removing the internal BFS loop in SBFS. Therefore, adopting SBFS-II/MIDACO combination has notably improved the calculation time without impacting the accuracy of the

original implementation using SBFS/MIDACO. This was true for small, medium, and large sized test systems such as the IEEE 33-, 69-, and 118-bus systems, respectively.

Table 5.14: Many-objective results with different load flow methods, 69-bus system

Load Flow Method	SBFS		SBFS-II		GBFS	
Case	No DL	w/DL	No DL	w/DL	No DL	w/DL
N_{DL}	-	30	-	30	-	30
P_{DL} **(p.u.)**	-	0.6580	-	0.6551	-	0.6282
Q_{DL} **(p.u.)**	-	0.5135	-	0.5246	-	0.8000
mn_{DL}	-	0.0487	-	0.0489	-	0.0102
$\lvert\Delta V_1\rvert$ **(p.u.)**	0.0480	0.0123	0.0480	0.0123	0.0480	0.0020
$\lvert\Delta f\rvert$ **(p.u.)**	0.0170	0.0003	0.0170	0.0002	0.0171	0.0000
P_{loss} **(p.u.)**	0.0578	0.0617	0.0578	0.0617	0.0577	0.0606
Q_{loss} **(p.u.)**	0.0251	0.0255	0.0251	0.0255	0.0250	0.0251
MVE **(p.u.)**	0.0500	0.0188	0.0500	0.0188	0.0503	0.0290
f_{ss} **(p.u.)**	1.0173	0.9998	1.0173	0.9998	1.0173	1.0000
Time[a] (s)	-	43	-	38	-	50

First step size only for $|\Delta V_1|$ and $|\Delta f|$, [a]algorithm computation time.

Table 5.15: Many-objective results with different load flow methods, 118-bus system

Load Flow Method	SBFS		SBFS-II		GBFS	
Case	No DL	w/DL	No DL	w/DL	No DL	w/DL
N_{DL}	-	73	-	73	-	80
P_{DL} **(p.u.)**	-	0.4771	-	0.5073	-	0.9996
Q_{DL} **(p.u.)**	-	0.7289	-	0.6658	-	0.8461
mn_{DL}	-	0.0117	-	0.0117	-	0.0083
$\lvert\Delta V_1\rvert$ **(p.u.)**	0.1454	0.0094	0.1454	0.0095	0.1453	0.0066
$\lvert\Delta f\rvert$ **(p.u.)**	0.0281	0.0014	0.0281	0.0013	0.0281	0.0004
P_{loss} **(p.u.)**	0.1335	0.1157	0.1335	0.1157	0.1316	0.1065
Q_{loss} **(p.u.)**	0.0908	0.0779	0.0908	0.0779	0.0893	0.0712
MVE **(p.u.)**	0.1636	0.0218	0.1636	0.0219	0.1607	0.0125
f_{ss} **(p.u.)**	1.0301	1.0015	1.0301	1.0014	1.0302	1.0005
Time[a] (s)	-	62	-	54	-	100

First step size only for $|\Delta V_1|$ and $|\Delta f|$, [a]algorithm computation time.

Contrariwise, all four objectives were further improved using GBFS as the LF method in the optimization technique. According to the 69- and 118-bus system results in Tables 5.14 and 5.15, respectively, the attained first objective ($|\Delta V_1|$) was much lower in comparison with $|\Delta V_1|$ found by SBFS and SBFS-II. Whereas $|\Delta f|$ value was further improved by GBFS against the other two LF methods. This improvement is attributed to the impact of GBFS on MIDACO's best solution by offering accurate reactive power representation based on droop coefficients

and local voltage measurement. On the other hand, SBFS and SBFS-II reactive power update is relying on the global VB voltage, neglecting the impact of line impedance and local DG terminal voltage. Additionally, improvements were observed for P_{loss} and Q_{loss} values obtained by GBFS/MIDACO wherein the advantage of local voltage measurements to update reactive power is manifested. In other words, the difference between total network demand including DL during off-peak hours and the total generated power by each DG before islanding was reduced according to the solution obtained by GBFS/MIDACO for all three test systems. This reduction was achieved even though the new DL value obtained by GBFS was higher than that of SBFS and SBFS-II for the 33-, 69-, and 118-bus systems. However, the resultant branch currents for all three bus systems were significantly reduced by GBFS/MIDACO combination if compared to the other load flow methods solution.

5.5.6 Convergence of SBFS, SBFS-II, and GBFS Considering Dump Load Allocation

To further validate the proposed LF methods' efficacy in solution convergence within finite iterations number, four convergence tests were considered based on DL solution. As given in Table 5.16, those tests were 1D, 2D, 3D, and 4D for No DL, SBFS-II's DL, GBFS's DL, and MIDACO's random DL, respectively. The convergence curves of ΔV_1 considering DL solution over 100 iterations for different LF methods on the 33-, 69- and 118-bus systems are illustrated in Figure 5.13. Noting that all convergence tests in this chapter were subjected to $\varepsilon_{Th} = 10^{-8}$ threshold for all LF methods adopted. From the Figure 5.13, it was observed that SBFS-II method recorded the best convergence response among all investigated convergence tests for all three bus systems. Whereas GBFS has better response compared to its counter parts as local voltage measurement based LF methods (i.e., MBFS and NBFS).

Table 5.16: Load flow convergence tests at different dump load solutions, all bus systems

Convergence Test	1D			2D			3D			4D		
Description	Base case (No DL) [a]			w/DL using SBFS-II solution			w/DL using GBFS solution			w/DL using random initial guess[c]		
Test System	33	69	118	33	69	118	33	69	118	33	69	118
N_{DL}	-	-	-	13	30	73	13	30	80	1	1	1
P_{DL} (p.u.)	-	-	-	0.2377	0.6551	0.5073	0.3399	0.6282	0.9996	0.0046	0.0043	0.0034
Q_{DL} (p.u.)	-	-	-	0.1752	0.5246	0.6658	0.7282	0.8000	0.8461	0.0032	0.0051	0.0075
mn_{DL} (p.u.)	-	-	-	0.0188	0.0489	0.0117	0.0053	0.0102	0.0083	0.0125	0.0075	0.0093
Scenario[b]	1			1			1			1		

[a]Using droop values from Table 5.1, [b]Loading/Generation scenario from Table 5.2, [c]Refers to a random generated solution by MIDACO within the first 10 function evaluations.

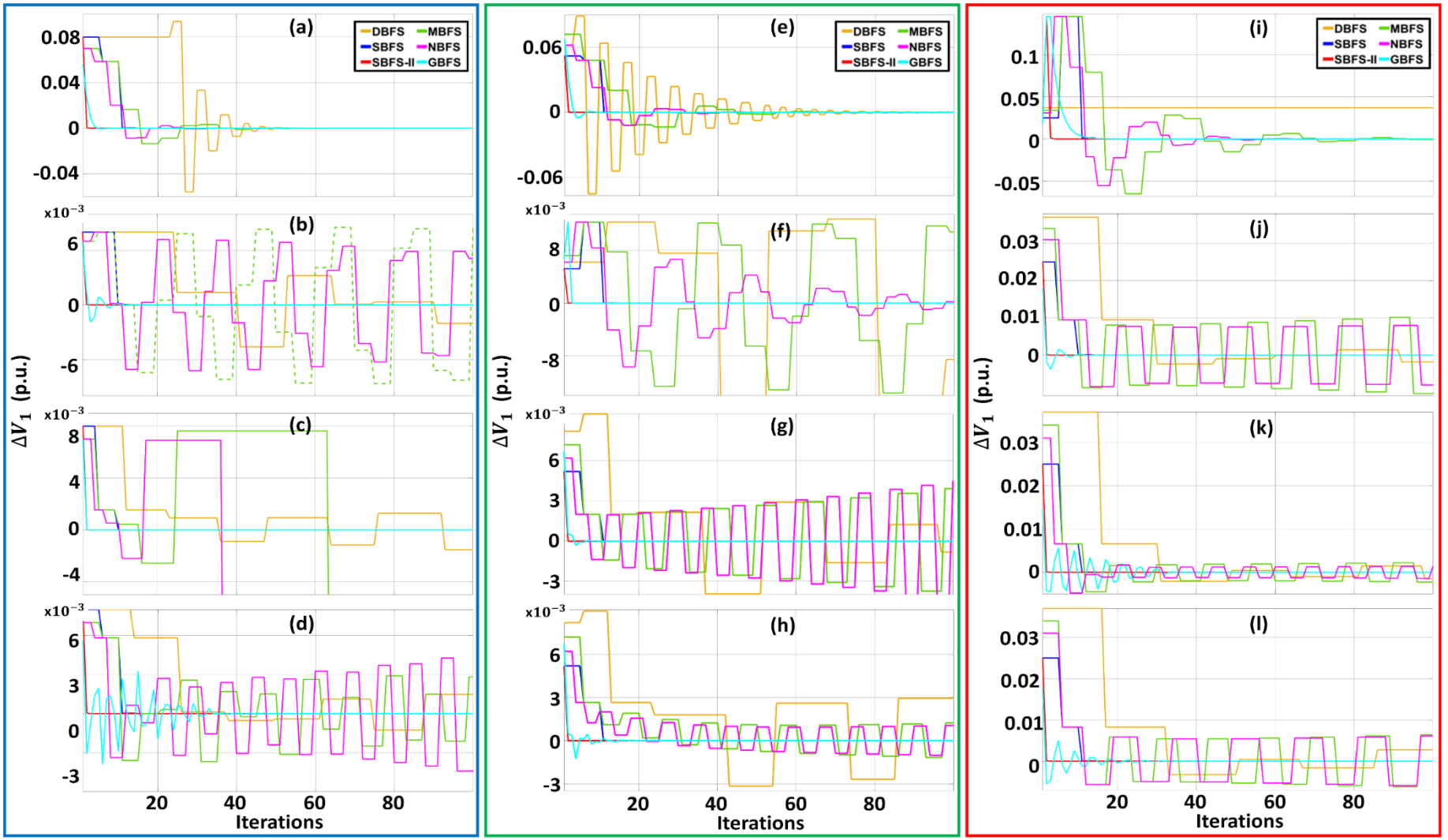

Figure 5.13: Convergence curves of ΔV_1 over 100 iterations considering DL solution with different load flow methods for: (a) 33-bus test 1D (b) 33-bus test 2D (c) 33-bus test 3D (d) 33-bus test 4D (e) 69-bus test 1D (f) 69-bus test 2D (g) 69-bus test 3D (h) 69-bus test 4D (i) 118-bus test 1D (j) 118-bus test 2D (k) 118-bus test 3D (l) 118-bus test 4D

Table 5.17: Different load flow methods calculation times in seconds for all bus systems

Convergence Test		1D			2D			3D			4D		
Test System		33	69	118	33	69	118	33	69	118	33	69	118
Load Flow Method & Calculation Time (s)	DBFS	0.0160	0.0461	NC	NC	NC	NC	NC	NC	NC	NC	NC	NC
	SBFS	0.0063	0.0080	0.0103	0.0054	0.0075	0.0095	0.0059	0.0070	0.0085	0.0061	0.0070	0.0092
	SBFS-II	0.0044	0.0054	0.0070	0.0036	0.0048	0.0063	0.0038	0.0042	0.0055	0.0040	0.0042	0.0058
	MBFS	0.0187	0.0238	0.0421	NC	NC	NC	NC	NC	NC	NC	NC	NC
	NBFS	0.0181	0.0219	0.0400	NC	0.0325	NC	NC	NC	NC	NC	NC	NC
	GBFS	0.0074	0.0085	0.0126	0.0059	0.0092	0.0146	0.0065	0.0096	0.0461	0.0112	0.0096	0.0248

NC: Not Converged.

Inversely, the advancements in calculation times using SBFS, SBFS-II, and GBFS were validated against DBFS, MBFS, and NBFS methods using the same convergence tests of Table 5.16 and the same tolerance threshold for fair comparison. The resultant calculation times are given in Table 5.17 for the three bus systems.

It was deduced that SBFS-II holds the fastest calculation time between all available LF methods, while the calculation times of SBFS and GBFS are second and third best. The speed advantage of SBFS and SBFS-II methods over the rest of local voltage measurement methods such as GBFS, MBFS, and NBFS is attributed to the influence of the global voltage variable. That is, the spread of one voltage among all DGs will expedite the convergence process by dictating the same rate of reactive power update between all DGs.

Furthermore, the superior performance of GBFS over MBFS and NBFS, is attributed to using ζ_1 and ζ_2 for voltage error damping and the correction vector (γ_i) which prevents the divergence of the LF solution in case reactive power is updated at lower droop values. Noting that the latter two LF methods, MBFS and NBFS, have failed to converge on different tests as given in Table 5.17.

5.5.7 Comparison with Other Metaheuristic Optimization Methods

In this sub-section, the efficiency and accuracy of the proposed optimization technique was further validated for effectiveness considering SBFS and GBFS as the LF methods. Therefore, the attained results were evaluated against other competitive metaheuristics such as multi-objective GA (MOGA) [154], multi-objective PSO (MOPSO) [155], [156], and NSGA-II [157], [158].

For a fair comparison, the results of each metaheuristic technique were calculated using the generation/loading scenario 1 and the load model set 1 as given in Tables 5.2 and 4.1, respectively. The four objectives optimization problem was simulated using the parameters for MOGA, NSGA-II, and MOPSO as obtained from [48]. Thus, the selected parameters for MOGA were 100, 0.8, and 0.001 for population size, crossover, and mutation probabilities, respectively.

Furthermore, MOPSO parameters were as follows: repository and population size were both 100, grid per dimension was 7, cognitive and social learning coefficients 0.1 and 0.2, respectively, deletion and leader selection pressures were both 2, mutation and inflation rates were both 0.1, starting and ending inertial weights were 0.5 and 0.001, respectively.

Lastly, NSGA-II had four parameters in total: population size 100, crossover and mutation distribution indexes 100 and 20, respectively, and mutation probability 0.25. The results obtained by all four metaheuristics using SBFS as the LF technique are given in Table 5.18 for all three test systems.

Table 5.18: Deterministic DL problem comparison with other metaheuristics using SBFS, all bus systems

Optimization Method	MOGA			NSGA-II			MOPSO			MIDACO		
Test System	33	69	118	33	69	118	33	69	118	33	69	118
N_{DL}	13	30	80	13	30	80	13	30	80	13	30	73
P_{DL} **(p.u.)**	0.3305	0.7741	0.6505	0.2428	0.7985	0.7219	0.3148	0.9031	0.7183	0.2319	0.6580	0.4771
Q_{DL} **(p.u.)**	0.2076	0.4623	0.7885	0.1874	0.6714	0.8864	0.2256	0.5634	0.6862	0.1594	0.5135	0.7289
mn_{DL} **(p.u.)**	0.0394	0.0747	0.0178	0.0255	0.0613	0.0205	0.0374	0.0519	0.0179	0.0191	0.0487	0.0117
$\lvert\Delta V_1\rvert$ **(p.u.)**	0.0165	0.0149	0.0141	0.0108	0.0136	0.0160	0.0154	0.0126	0.0144	0.0082	0.0123	0.0094
$\lvert\Delta f\rvert$ **(p.u.)**	0.0012	0.0030	0.0017	0.0014	0.0020	0.0018	0.0013	0.0028	0.0015	0.0011	0.0003	0.0014
P_{loss} **(p.u.)**	0.0200	0.0617	0.1152	0.0200	0.0617	0.1146	0.0200	0.0618	0.1152	0.0201	0.0617	0.1157
Q_{loss} **(p.u.)**	0.0154	0.0253	0.0782	0.0154	0.0253	0.0779	0.0154	0.0254	0.0783	0.0154	0.0255	0.0779
MAXEVAL	400	400	400	200	200	200	500	500	500	10000	10000	10000
Time[a] (s)	216	235	397	839	922	1495	583	642	798	41	43	62

First step size only for $|\Delta V_1|$ and $|\Delta f|$, [a]algorithm computation time.

As given by Table 5.18, the $|\Delta V_1|$ results for MIDACO in the IEEE 33-bus system were superior to all other metaheuristics, while the obtained active and reactive power losses were very close by all the optimization techniques applied on the IEEE 33-bus system.

Moreover, by looking into the results of the IEEE 69-bus system, one can deduce that MIDACO's evolutionary algorithm outperforms MOGA, NSGA-II, and MOPSO metaheuristics in the $|\Delta V_1|$ and $|\Delta f|$ objectives.

Similarly with the IEEE 33-bus system case, the active and reactive power loss objectives as given in the 69-bus system results were very close by all four metaheuristics. As for the IEEE 118-bus system results, considering all four metaheuristics for the first objective (i.e., $|\Delta V_1|$), the voltage deviation objective achieved by MIDACO was significantly lower among all methods.

Contrariwise, NSGA-II's attained P_{loss} and Q_{loss} were the best if compared to the other metaheuristics in the IEEE 118-bus system case. However, the obtained voltage and frequency deviations thereof were the worst compared to MIDACO, MOGA, and MOPSO metaheuristics for the 118-bus system.

Similarly, the efficacy of the proposed optimization method, MIDACO, was compared with the foregoing evolutionary and swarm intelligence techniques but while considering the general backward\forward sweep as the load flow method.

The obtained results by each of the four optimization techniques using GBFS as the load flow method are given in Table 5.19 for all three test systems. Simulations were carried out using the same load model set 1, generation/loading scenario 1, and the metaheuristics' parameters identical to those of the SBFS case mentioned previously.

As given in Table 5.19, the obtained power loss objectives (i.e., P_{loss} and Q_{loss}) by MOGA, NSGA-II, MOPSO, and MIDACO were close for the IEEE 33- and 69-bus systems. However, considering the IEEE 118-bus system case, the active power losses obtained by MOGA were the highest overall.

Conversely, $|\Delta V_1|$ and $|\Delta f|$ objectives attained by MIDACO were significantly lower than the rest of the metaheuristics, this was true for both 69- and 118-bus system cases. As for the 33-bus case, the obtained $|\Delta f|$ value by MIDACO was just 0.0001 higher.

Finally, MIDACO's clear speed advantage, as the proposed optimization technique in this thesis, is manifested by accomplishing thousands of function evaluations in significantly lower time if compared with the other metaheuristics.

This was evident for the IEEE 33-, 69-, and 118-bus systems while using either of the two load flow methods (that is, SBFS or GBFS). The calculations times for MIDACO against MOGA, NSGA-II, and MOPSO are given in Table 5.18 and Table 5.19 for the MIDACO/SBFS and MIDACO/GBFS combinations, respectively.

Table 5.19: Deterministic DL problem comparison with other metaheuristics using GBFS, all bus systems

Optimization Method	MOGA			NSGA-II			MOPSO			MIDACO		
Test System	33	69	118	33	69	118	33	69	118	33	69	118
N_{DL}	13	30	80	13	30	80	13	30	80	13	30	80
P_{DL} **(p.u.)**	0.4506	0.8544	0.4203	0.4125	0.6877	0.9720	0.4334	0.7228	0.7096	0.3399	0.6282	0.9996
Q_{DL} **(p.u.)**	0.4574	0.5556	0.9540	0.5021	0.4768	0.9800	0.5406	0.5454	0.5628	0.7282	0.8000	0.8461
mn_{DL} **(p.u.)**	0.0055	0.0543	0.0084	0.0056	0.0511	0.0088	0.0052	0.0488	0.0086	0.0053	0.0102	0.0083
$\lvert\Delta V_1\rvert$ **(p.u.)**	0.0020	0.0133	0.0065	0.0019	0.0133	0.0068	0.0017	0.0120	0.0071	0.0015	0.0020	0.0066
$\lvert\Delta f\rvert$ **(p.u.)**	0.0001	0.0024	0.0010	0.0001	0.0006	0.0005	0.0001	0.0009	0.0007	0.0002	0.0000	0.0004
P_{loss} **(p.u.)**	0.0198	0.0607	0.1077	0.0197	0.0606	0.1065	0.0199	0.0607	0.1066	0.0197	0.0606	0.1065
Q_{loss} **(p.u.)**	0.0153	0.0250	0.0716	0.0152	0.0251	0.0713	0.0153	0.0251	0.0712	0.0151	0.0251	0.0712
MAXEVAL	400	400	400	200	200	200	500	500	500	10000	10000	10000
Time[a] (s)	3941	4564	5223	6468	8479	9811	3245	4587	5870	84	50	100

First step size only for $|\Delta V_1|$ and $|\Delta f|$, [a]algorithm computation time.

According to Table 5.19, the calculation times for MOGA, NSGA-II, MOPSO relying on GBFS as the load flow method were very slow if compared to the calculation times recorded by MIDACO. Speed and accuracy come hand in hand when considering real-time applications. This significant time and accuracy advantage of the proposed optimization method shall enable real-time application for optimization cycles with the shortest times possible.

5.6 Summary

In this chapter, the deterministic MINLP problem of DL allocation in highly penetrated DCIMG during off-peak hours with four highly probable mismatch scenarios was investigated. The methodology for DL allocation has been developed as a novel application of MIDACO algorithm in microgrids combined with three newly developed load flow methods, viz., SBFS, SBFS-II, and GBFS. The methodology was validated on the IEEE 33-, 69-, and 118-bus systems using three problem formulations. These were, namely, first problem as a single objective minimization of V-f deviations, second problem as a two objectives problem to minimize V-f deviations simultaneously, and third problem as a four objectives problem to minimize V-f deviations, active, and reactive power losses. Moreover, different load models were considered to highlight the significance of DL allocation in DCIMG, while the impact of using different load flow techniques had also been investigated. Various convergence tests were considered to demonstrate the robustness of the proposed methodology, while the impact of MIDACO's parameters on the non-dominated solution was also highlighted. Likewise, the efficacy of the used metaheuristic technique, MIDACO, was compared with other evolutionary and swarm intelligence techniques. Results have shown the significance and importance of DL allocation to provide adequate voltage and frequency regulation as a promising power management solution. Moreover, the superior speed and accuracy advantage of the proposed optimization technique shall facilitate further real-time optimization cycles. This will entail the shortest optimization time possible while having a significant number of forecasted generating and loading data.

6 Chapter Six: Dump Load Allocation in Islanded Microgrid Considering Stochastic Mismatch Scenarios

6.1 Introduction

In this chapter, the proposed EMS strategy for DL planning and real-time operation during off-peak hours is presented. Existing EMS strategies such as storage facilities and demand programs can only handle small power mismatch during peak hours. However, due to the uncertainties associated with renewable generation and demand forecast, higher mismatch is expected during off-peak hours. In the previous chapter, the allocation of DL in highly penetrated IMG was investigated considering fixed number of highly probable generation/demand mismatch scenarios. However, in this chapter, further distinction was given to the generation and demand mismatch by tackling the optimization problem within scenario based stochastic uncertainty framework. Initially, roulette wheel mechanism (RWM) was utilized to generate a very high number of mismatch scenarios, while scenario elimination technique was considered to reduce the number of scenarios. Subsequently, a methodology for the optimal DL allocation in DCIMG considering uncertainties in wind generation and load percentage error was developed. This was done to minimize the expected total microgrid cost (TMC), the expected maximum voltage error (MVE), the expected frequency deviation $|\Delta f|$, and the expected total energy loss (TEL). Furthermore, the methodology was implemented using the fine-grained parallelization strategy within MIDACO solver combined with GBFS as the load flow technique. The stochastic optimization problem was applied to the IEEE 33-, 69-, and 118-bus systems to vary the scalability of the stochastic DL allocation problem. Moreover, different evolutionary and swarm intelligence techniques were selected to compare the accuracy and speed of the proposed optimization technique. Lastly, a cost benefit analysis study was considered to highlight the significance and cost-effectiveness of DL-based EMS against BESS-based EMS to handle large power mismatch during low demand hours.

6.2 Dump Load Based Energy Management System

As discussed previously, there are various technical, economic, and environmental factors that affect the optimal operation of IMGs. The implication of uncertainty in demand forecast and renewable power generation will significantly interfere with the optimal operation of IMGs. Therefore, a comprehensive EMS is necessary to ensure adequate IMG operation and supply quality.

According to the international standard IEC 61970 [61], an EMS is defined as a software solution that drives a computerized environment responsible for the basic services and applications of a system. This is necessary for adequate management of power generation and transmission platforms in a cost-effective and reliable power system operation.

A successful EMS often involves communication with different elements of the microgrid, such as DG, ESS, and smart loads. The computerized environment in an EMS often involves supervisory control and data acquisition (SCADA) systems as well as human machine interfaces (HMIs) that facilitates the efficient interaction between all elements of a microgrid [61]. Furthermore, two distinct types of supervisory control for an EMS are identified as centralized and decentralized [61], [159].

In the centralized EMS approach, a main MG central controller (MGCC) is utilized to gather and analyse all forecasted data of demand and generation. This is followed by optimization cycles that distribute the optimal set-points to all participating elements of an MG. Contrariwise, a decentralized EMS compromises of multiple smaller local controllers with certain degree of intelligence. Such smart elements would constantly interact with each other and the main MGCC to achieve the optimal and cost-effective operation of an IMG [159].

The proposed EMS herein is based on utilizing DL as a viable solution to the power management problem in highly penetrated DCIMG. Moreover, the proposed DL-based EMS in this study follows a hybrid of the foregoing EMS strategies. That is, by having a dedicated MGCC responsible for analysing load and wind power forecast, collecting data from DG units, and producing optimization cycles for the MG in real-time.

Moreover, each dispatchable unit are equipped with their local droop controller to ensure effective load sharing in the primary level control. As per the assumed notion of this study, BESSs and DR programs are not suitable to handle large power mismatches, especially at the low load hours.

Therefore, a planning stage is first done by allocating an optimal DL at an optimum location in the network. Subsequently, real-time control ensures that optimal DL size as well as optimal droop gains of DGs are optimized and transmitted by the MGCC during off-peak hours to absorb excess generation.

By utilizing DL, the excess power is put to do useful work as heating and pumping applications via electric boilers and water circulation systems. The participation of BESS in this scenario, or any other suitable DR program, would be merely to balance any slight power deviations during peak load hours. The proposed dump load-based energy management system of this study is depicted in Figure 6.1.

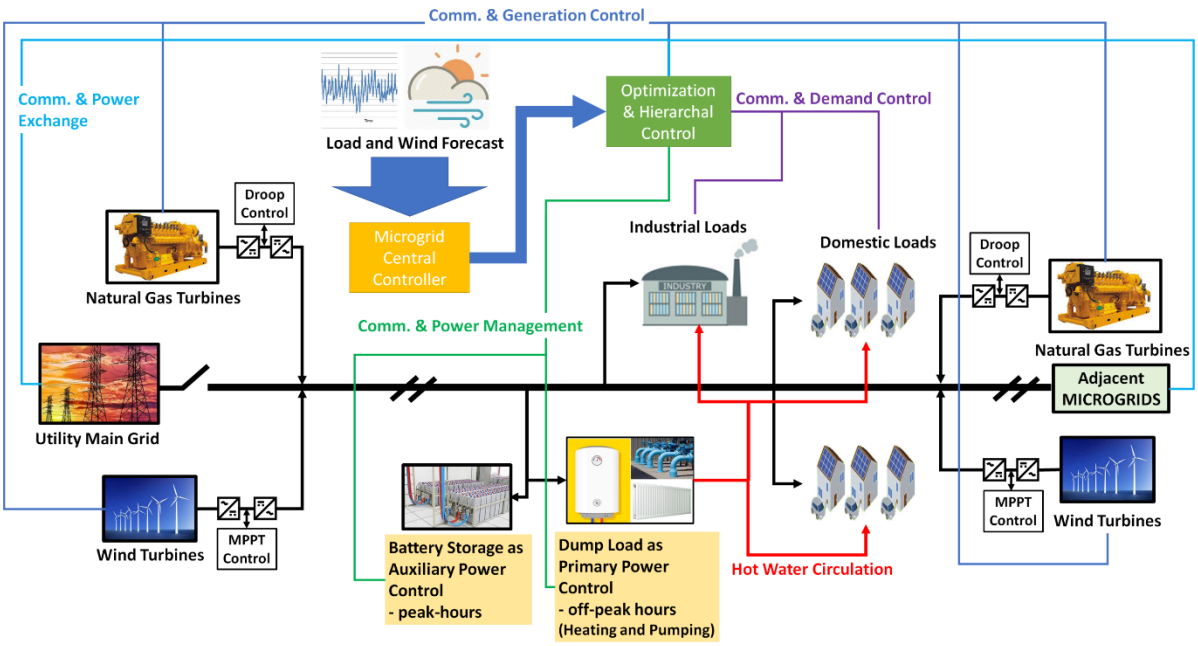

Figure 6.1: Proposed dump load-based real-time energy management system

According to Figure 6.1, the utilization of DL via heating and pumping applications as a real-time solution to the excess power imbalance problem during off-peak hours is still in the elementary stage. Thus, it requires further research and independent thermal study which is beyond the scope of this research work. Hence, more future research is needed to investigate and accommodate efficient ways to dump excess power to do useful work during off-peak hours in the IMGs. Nonetheless, the proposed work in this chapter herein, is an early attempt to highlight the significance of DL as a real-time power management solution considering uncertainties in wind power and demand variations.

6.3 Scenario Based Stochastic Uncertainty Modelling

There are different factors that might impact the certainty in a variable of interest. Most of these factors are of natural occurrence and relate to errors in future data forecast, historical data collection, and acquisition of data related to that variable [160], [161]. Similarly, uncertainty in MG variables originates from the nature of the used variable itself. For example, volatility in fuel prices, change in demand behaviour due to weather and diurnal states, variation in wind speeds, and solar irradiance contrast. All these variables are random by nature and are all determined by different aspects not seen by the MG operator. Therefore, random variables surrounding an IMG analysis and planning framework dictate the need to change the nature of the optimization problem. That is, form deterministic problem type with fixed variables to become stochastic type of a problem with random variables. To that end, an adequate uncertainty analysis tool must be incorporated within planning problems for IMGs.

Probabilistic modelling is a preferred choice when it comes to stochastic framework, where each uncertain variable is modelled as a PDF. These PDFs are used to give the probability of occurrence to a given random variable, where each PDF is fragmented into several distinct probability levels [160], [161]. The more levels selected, the higher is the accuracy grade for uncertainty modelling. However, computational burden increases by higher number of probability levels [160], [162].

6.3.1 Stochastic Load Modelling

Electricity demand uncertainty is strongly linked with the nature of load (i.e., residential, commercial, or industrial) and its interaction with the different variables such as weather, time, humidity, temperature, and demand programs instigated by governments' green policies [161]. The nature of load error is a combination of forecast, historical, and measured load data. The assumption in this study herein is that historical yearly load data is available, and the system peak load follows the hourly shape of IEEE reliability test system (RTS) load model [163], [164]. Moreover, in line with literature standards of adopting normal distribution in load forecast error, an hour-by-hour prediction scheme is utilized to model load uncertainty as normal distribution PDF [165], [166].

Therefore, to achieve accurate representation of load forecast error, sufficient historical hourly load data are indeed required [165]. For any given hour and considering the load factor from the total system demand, a load is distributed normally around the mean. This mean describes the accumulated percentage of that load from annual system peak load. Moreover, since we are concerned about accurate load uncertainty representation during off-peak hours in this study, a seven-hour period has been considered from 12 am to 7 am to represent off-peak hours scenario. Likewise, to achieve better uncertainty modelling, the normal distribution of each load has been divided into fifteen levels with lengths equal to half of the standard deviation from the mean.

Moreover, the load active and reactive power in any probability level corresponds to the middle point between the minimum and maximum load percentage of that level. The probability of that load's level equals to the PDF integration over the interval of that level. The PDF of any given load with mean μ_{L_i} and standard deviation σ_{L_i} in the IMG, denoted as ϕ_{L_i}, is given by the equation (6.1):

$$\phi_{L_i}(\wp) = \left(1/\sigma_{L_i}\sqrt{2\pi}\right) e^{-0.5\left(\frac{\wp-\mu_{L_i}}{\sigma_{L_i}}\right)^2} \tag{6.1}$$

where $\mathcal{p}$ is the accumulative percentage of load from hourly, daily, and weekly percentages of annual peak system demand, while the discretised PDF of that load is depicted in Figure 6.2.

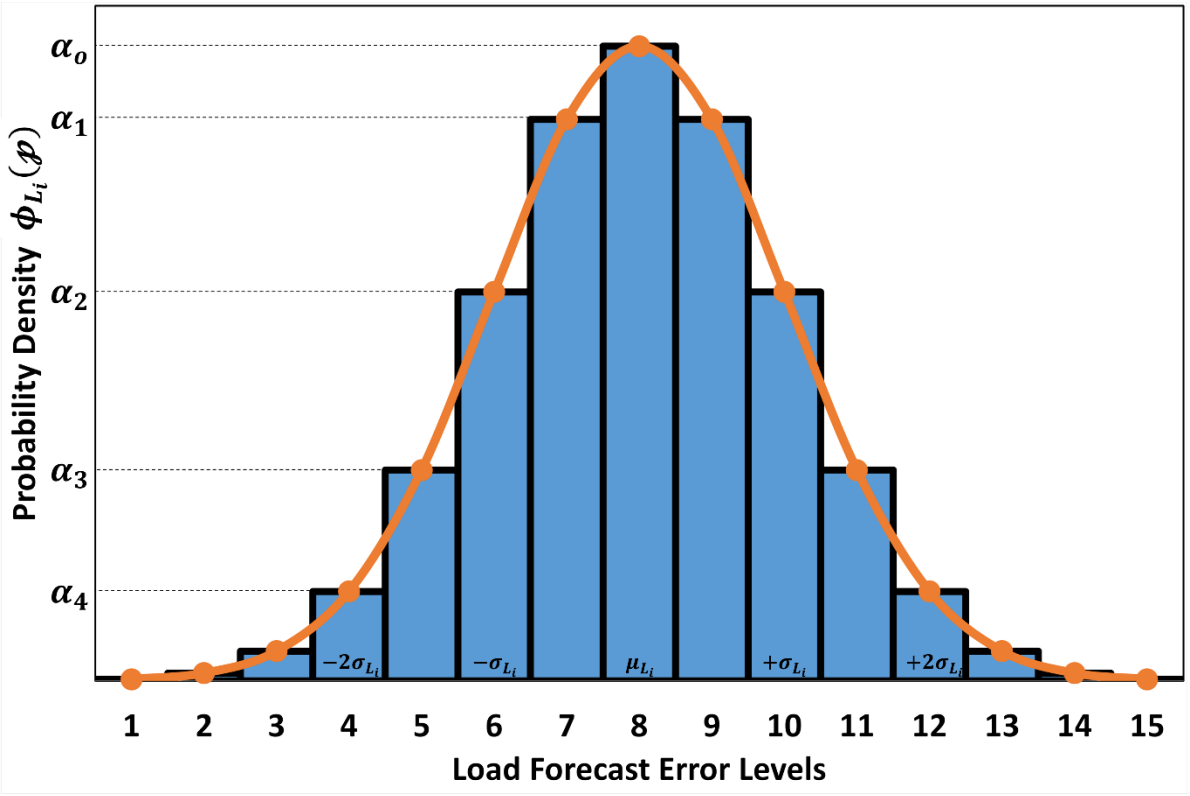

Figure 6.2: Load probability density function with discretized probability levels

Frome Figure 6.2, one can see that the highest load percentage is centred around the PDF's mean, while each level length is defined by multiple quarters of standard deviation either above or below the mean. Similarly, the probability of load percentage power during a specific load level or state L_{st} is given as

$$\Lambda(L_{st}) = \int_{\mathcal{p}_{st}^{l}}^{\mathcal{p}_{st}^{u}} \phi_{L_i}(\mathcal{p})\, d\mathcal{p} \tag{6.2}$$

where $\Lambda(L_{st})$ is the probability of a load state L_{st}. $\mathcal{p}_{st}^{u}$ and $\mathcal{p}_{st}^{l}$ are the upper and lower limits of load's accumulative percentage for that level, which are multiple quarters of the PDF's standard deviation added or subtracted from the mean until the desired number of levels is defined. Subsequently, load active and reactive power during a specific state is given by:

$$P_{L_i}(\mathcal{p}_{st}) = P_{Li0} \cdot \mathcal{p}_{st} \tag{6.3}$$

$$Q_{L_i}(\mathcal{p}_{st}) = Q_{Li0} \cdot \mathcal{p}_{st} \tag{6.4}$$

$$\wp_{st} = \frac{\wp_{st}^{u} + \wp_{st}^{l}}{2} \tag{6.5}$$

where $\wp_{st}$ is the mean load accumulative percentage for the load level L_{st}.

6.3.2 Stochastic Wind Modelling

Wind energy is considered as one of the most important renewable energy sources in the world. According to the IEA projections, wind power will account for at least 18% of the world's generation capacity by 2050 [12]. This is attributed to the advancement in wind turbine (WT) manufacturing and the eco-friendly wind farms. Nevertheless, like many other unreliable RESs, wind power is pretty much dependent on wind speeds and thus inherently intermittent in nature. Therefore, adequate probabilistic uncertainty modelling is fundamental to account for wind speed impact on wind power. Contrariwise to load probabilistic model, wind speed does not fit normal distribution PDF but rather the Weibull distribution PDF [164], [167]. The PDF of wind speed, denoted as ϕ_W, that follows the Weibull distribution with shape factor k_s and scale index c_s is given by [167]:

$$\phi_W(v) = \frac{k_s}{c_s}\left(\frac{v}{c_s}\right)^{k_s-1} e^{-\left(\frac{v}{c_s}\right)^{k_s}} \tag{6.6}$$

where v is the wind speed, e is the natural number. There are several ways to calculate k_s and c_s for a Weibull distribution. However, if the average wind speed μ_W and its standard deviation σ_W of a given site are known, then k_s and c_s can be calculated approximately using the following equations [164], [167], [168]:

$$k_s = \left(\frac{\sigma_W}{\mu_W}\right)^{-1.086} \tag{6.7}$$

$$c_s = \frac{\mu_W}{\Gamma\left(1+{}^{1}/_{k_s}\right)} \tag{6.8}$$

where $\Gamma(\ )$ is the gamma function, more about the derivation of k_s and c_s equations for wind speed PDF can be found in [168], [169]. Another way to model wind speed uncertainty is the Rayleigh distribution PDF which is a special case of Weibull distribution. This case occurs when the shape factor is equal to 2 and the scale index is calculated form average wind speed at a given day or month [153]. However, in this study and according to the assumed scenario, wind data is available in the form of historical yearly data covering a period

of three consecutive years for a typical wind farm [167]. Therefore, the average and standard deviation of wind speed are known.

Furthermore, as per the assumed notion in this study, generation is always available during peak hours. Also, wind speeds on average tend to gradually increase at off-peak hours with higher altitudes [170]. Therefore, the chosen mean and standard deviation of wind speed translate the idea of high wind power generation at low electricity demand during off-peak hours. Like load uncertainty modelling, the wind power PDF is discretized into various levels or states, where each level represents expected wind speed range. The wind speed states are chosen in a way to cover the average wind speed and increase the accuracy of wind power uncertainty modelling. Therefore, a 1 m/s increment was chosen to build 30 wind levels (states) starting with zero wind speed. Thus, the probability of each level is given as (Detailed wind and load power outputs are found in Tables A.1 and A.2, respectively, in Appendix A):

$$\Lambda(W_{st}) = \int_{v_{st}^{l}}^{v_{st}^{u}} \phi_W(v)\, dv \tag{6.9}$$

where $\Lambda(W_{st})$ is the probability of wind state W_{st}. v_{st}^{u} and v_{st}^{l} are the upper and lower limits of wind speed for that state. The relationship between wind state and output power of a typical WT with rated power (P_{Wr}) is given by [164], [167]:

$$P_W(v_{st}) = \begin{cases} 0, & v_{st} < v_{ci} \\ P_{Wr}\left(\frac{v_\mu - v_{ci}}{v_r - v_{ci}}\right), & v_{ci} \le v_{st} < v_r \\ P_{Wr}, & v_r \le v_{st} < v_{co} \\ 0, & v_{st} \ge v_{co} \end{cases} \tag{6.10}$$

$$v_{st} = \frac{v_{st}^{u} + v_{st}^{l}}{2} \tag{6.11}$$

where v_{st} is the mean wind speed for each individual wind state W_{st}. $P_W(v_{st})$ is the WT output power at wind speed v_{st}. v_{ci} and v_{co} are the cut-in and cut-off wind speeds, respectively, with the latter often referred to as the furling wind speed. v_r is the rated wind speed for the WT. v_μ is the average wind speed at the site.

6.3.3 Roulette Wheel Mechanism and Scenario Generation

At this stage, a sufficiently large number of load and wind states is generated as possible scenarios derived from load forecast and wind speed PDFs. In this study, an RWM is considered, where each distinct PDF is associated with different RWM. The RWM is utilized to generate 10000 scenarios, where each s scenario represents a set (Ω_s) of uncertain

variables. The set Ω_s corresponds to the value of each load and wind powers along with their respective probability of occurrence Λ_s^i. For an IMG with n number of buses, the set of uncertain variables Ω_s is given by:

$$\Omega_s = \left\{P_{L1}^s, \dots, P_{Li,lk}^s, Q_{L1}^s, \dots, Q_{Li,lk}^s, P_{W1}^s, \dots, P_{Wi,wk}^s\right\}, \forall\, i \in \mathcal{N} \tag{6.12}$$

$$NV = 2lk + wk \tag{6.13}$$

where P_{Li}^s and Q_{Li}^s are the load active and reactive powers at bus i during scenario s, respectively. P_{Wi}^s is the WT power at bus i during scenario s. lk and wk are the total number of loads and WT in the network, respectively. NV is the number of uncertain variables in scenario s. The RWM is segmented into several slots based on the number of uncertainty levels for their associated PDF. Furthermore, each slot corresponds to one of the normalized probability levels of that uncertain variable. In this study, the RWM has been segmented into 15 and 30 slots corresponding to load forecast error and wind speed levels, respectively. The load's RWM is depicted in Figure 6.3.

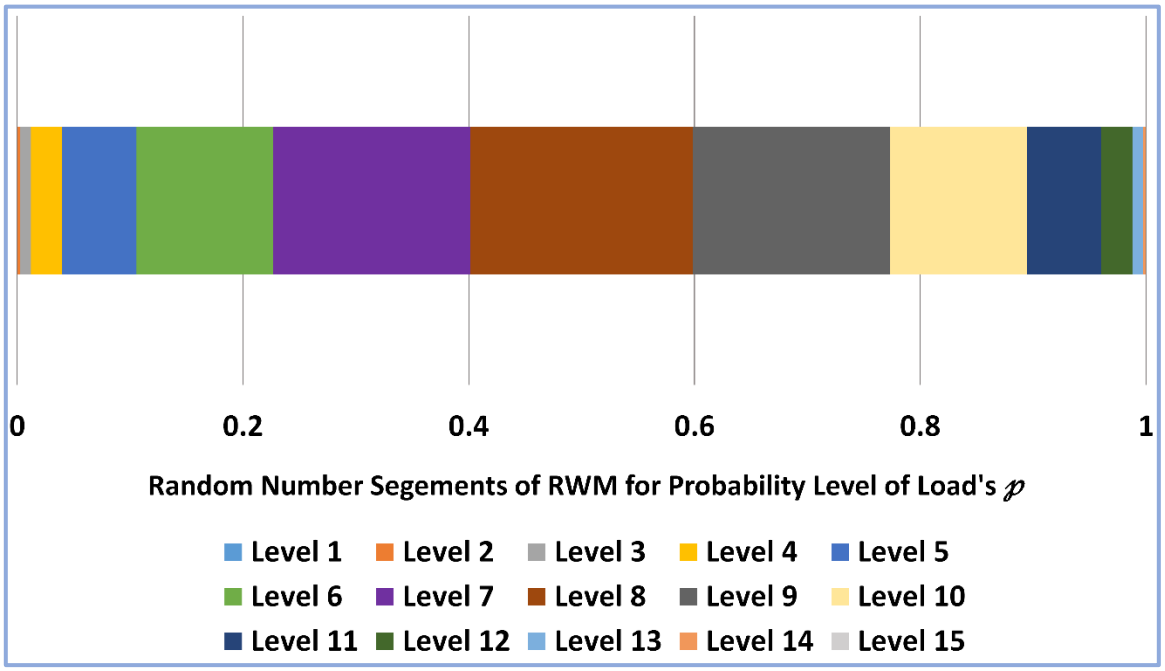

Figure 6.3: Roulette wheel mechanism for load probability level selection

According to the RWM of Figure 6.3, each level is represented by a unique colour code which corresponds to a slot for the normalized probability level and the designated load's accumulative percentage value. Subsequently, the value of each uncertain variable in the RWM is obtained by a random number generated between 0 and 1. Consequently, a slot is chosen based on the location of the generated random number on the RWM, while the value

of the uncertain variable associated with that slot is picked with its respective normalized probability. The process is repeated for each uncertain variable of load forecast and wind speed in each specific scenario s until the desired number of scenarios is generated.

6.3.4 Scenario Reduction and Aggregation

Out of the desired 10000 generated scenarios, some will have low probability and hence not affect the outcome while some might be duplicates which are not desired. Consequently, an elimination method is considered to filter out invaluable and duplicated scenarios by taking reduced number of unsimilar scenarios with the highest probability.

In accordance with current uncertainty modelling practices as reported in literature [41], [160], the reduced number of scenarios (NR) for this work was set to 20. This implies a rate of filtration (or sampling) that is equal to 0.002 is applied. Hence, the highly probable scenario in each group of 500 scenarios is considered.

After obtaining the highly probable desired scenarios NR of the stochastic planning problem, each scenario can be used to build a deterministic optimization problem of its own. Accordingly, each deterministic problem optimal solution will have a probability that is equal to the convolution of all probabilities of all uncertain variables in the scenario s [60].

What's worth mentioning here is that the assumption in this study considers the events associated with load forecast error and wind speed to be uncorrelated. In other words, the occurrence of a specific wind speed state does not impact the occurrence of a particular load state or vice versa. This assumption coincides with the notion of this study that during off-peak hours the demand is almost certain to be lower than generation.

Based on that, the normalized convolved probability Λ_s^N of scenario s would be as follows:

$$\Lambda_s^N = \frac{\prod_{i=1}^{NV} \Lambda_s^i}{\sum_{s=1}^{NR} \prod_{i=1}^{NV} \Lambda_s^i} \tag{6.14}$$

Furthermore, to accumulate the optimal solutions for the deterministic problem of each scenario, an aggregation or weighted average sum method is utilized. This shall account for the contribution of each scenario based on its probability impact. By adopting this approach, we ensure that bigger influence on the overall aggregated solution is given to scenarios with the highest probability.

Subsequently, the expected value for the objective function of the stochastic problem considering all NR scenarios will become [160], [161]:

$$\check{\mathcal{F}}_i(x) = \sum_{s=1}^{NR} \mathcal{F}_i^s(x) \cdot \Lambda_s^N \tag{6.15}$$

6.4 Stochastic Dump Load Optimization Formulation

In this section, the stochastic optimization problem's objective functions and constraints are given. Moreover, the optimal DL allocation along with optimal DG droop setup considering uncertainty in wind and load powers are described in detail.

6.4.1 Objective functions

There are four objective functions considered accounting for all reduced NR scenarios spanning across the selected off-peak hours in this study. These are, namely, the expected total MG cost (TMC) of the IMG, the expected maximum voltage error (MVE) across all system buses, the expected frequency deviation ($|\Delta f|$), and the expected total energy loss (TEL). Hence, the objective function $\breve{\mathcal{F}}_i(x_3)$ corresponding to the decision variable x_3 is given by:

$$\breve{\mathcal{F}}_i(x_3) = \{\text{TMC}, \text{MVE}, |\Delta f|, \text{TEL}\},\ x_3 = \{P_{DL}, Q_{DL}, mn_{DL}, N_{DL}\} \tag{6.16}$$

where P_{DL}, Q_{DL}, and N_{DL} are the DL's active power, reactive power, and bus location, respectively. mn_{DL} is the droop gain for DL allocation, which were reflected upon DG droops as shown below.

$$m_{pi} = mn_{DL} \tag{6.17}$$

$$n_{qi} = 10 \cdot mn_{DL} \tag{6.18}$$

The choice of reactive droop slightly higher than active droop is a common practice in literature [33], [151] and is known to further improve the convergence of LF solution. This was in contrast with the equal active and reactive droop settings as presented by the deterministic DL allocation problem of [48]. Meanwhile, LF convergence and calculation times are expected to be longer in the proposed stochastic optimization problem against the deterministic DL allocation problem herein. Furthermore, each individual stochastic objective function is considered as the aggregated weighted sum of all deterministic objective function values during a scenario s across the off-peak horizon set of hours ($\mathcal{H}$) such that:

$$\breve{\mathcal{F}}_i(x_3) = \begin{cases} \breve{\mathcal{F}}_1(x_3) = \sum_{h=1}^{H} \sum_{s=1}^{NR} \mathcal{F}_1^{h,s}(x_3) \cdot \Lambda_s^N \\ \breve{\mathcal{F}}_2(x_3) = \max\limits_{h \epsilon \mathcal{H}} \left\{ \sum_{s=1}^{NR} \mathcal{F}_2^{h,s}(x_3) \cdot \Lambda_s^N \right\} \\ \breve{\mathcal{F}}_3(x_3) = \max\limits_{h \epsilon \mathcal{H}} \left\{ \sum_{s=1}^{NR} \mathcal{F}_3^{h,s}(x_3) \cdot \Lambda_s^N \right\} \\ \breve{\mathcal{F}}_4(x_3) = \sum_{h=1}^{H} \sum_{s=1}^{NR} \mathcal{F}_4^{h,s}(x_3) \cdot \Lambda_s^N \end{cases} \tag{6.19}$$

where H is the total number of all off-peak hours. The objectives in equation (6.19) are addressed in this study as a multi-objective problem to provide an expected non-dominated solution using Pareto front optimization. By considering each aggregated and expected single objective value as a many-objective problem, the proposed approach herein constitutes a Pareto optimal technique. Thereby, avoiding the conversion of multi-objective problem into a set of single weighted objectives for each scenario [161]. The advantage of Pareto approach is that eventually one optimal non-dominated solution will satisfy all constraints and minimize all objectives considering all scenarios simultaneously. Inversely, weighted average techniques compromise on accuracy by constructing a single objective out of many single objectives for each scenario as presented by [41], [160], [161].

To facilitate many-objective optimization of the aggregated individual single objectives, a solution matrix (SM) of size H x NR is created for each objective function and constraint within a scenario s during the h off-peak hour. Noteworthy is that the SM referred to here should not be confused with the SA used within MIDACO framework. This is due to the fact that an SA is used to retain and rank solution fitness within deterministic problems. Furthermore, to expedite the speed of the stochastic optimization problem, the generated scenarios for each off-peak hour could be retained in a separate memory after each aggregated function evaluation.

Nonetheless, if more accuracy was desired, the generated scenarios after each function evaluation are cleared and then generated again using different seed for the RWM random number generator. However, this approach is known to significantly deteriorate the calculation times of the optimization technique and therefore was abandoned for this work. The individual probabilistic objectives are described in detail as follows:

6.4.1.1 Total Microgrid Cost

The TMC objective presented in this study is composed of four main cost functions, viz., fuel cost (FC), maintenance cost (MC), emissions cost (EC), and technical costs (TC). These objectives are spread across the off-peak horizon for each reduced scenario. The choice of such combination is ideal to account for the standard technical, environmental, and economic objectives for any IMG optimization problem.

The TMC objective herein focuses on MG running and operational costs as per literature standards [41], [171]–[173]. Thus, it neglects capital and standing costs of the MG such as DL and BESS installation costs. This is because, as per the notion of this thesis, DL costs should at least offset BESS costs. The basis of this assumption is elaborated thoroughly in the analysis of sub-section 6.5.3. Moreover, by taking the active power generation for all dispatchable units as a main factor in the TMC objective, we implicitly minimize emissions and

losses. Likewise, since the relationship between emissions and active power is linear, the need for an independent objective tackling the emissions becomes redundant.

However, the same could not be assumed for losses in the network as they have a nonlinear relation between both branch current and apparent power components. Hence, it is necessary to tackle losses as an independent objective to ensure adequate modelling for losses in DCIMG as it was the case in this study. Based on the forgoing, the TMC is given by:

$$\mathcal{F}_1^{h,s}(x_3) = TMC_h^s = FC_h^s + MC_h^s + EC_h^s + TC_h^s \tag{6.20}$$

where TMC_h^s, FC_h^s, MC_h^s, EC_h^s, and TC_h^s are the total MG, fuel, maintenance, emissions, and technical costs at the scenario s during the off-peak hour h, respectively, and are given by:

$$FC_h^s = \left(\psi_{fuel}/\eta_P\right) \cdot \sum_{i \in \mathcal{GK}} P_{Gi}^{h,s} \tag{6.21}$$

$$MC_h^s = \psi_{main} \cdot \sum_{i \in \mathcal{GK}} P_{Gi}^{h,s} \tag{6.22}$$

$$EC_h^s = \Psi_{emis} \cdot \psi_{emis} \cdot \sum_{i \in \mathcal{GK}} P_{Gi}^{h,s} \tag{6.23}$$

$$TC_h^s = RC_h^s + FRC_h^s \tag{6.24}$$

where $P_{Gi}^{h,s}$ is the active generated power by the dispatchable DG at the scenario s during the off-peak hour h. ψ_{fuel}, ψ_{main}, ψ_{emis} are the fuel, maintenance, and emissions cost coefficients, respectively. Ψ_{emis} is the emissions rate by the dispatchable DG. η_P is the fuel consumption efficiency by the dispatchable DG. RC_h^s and FRC_h^s are the reactive and frequency costs at the scenario s during the off-peak hour h, respectively.

Therefore, the TC_h^s function is based on MG stability and continuity aspects such as RC_h^s and FRC_h^s costs. Despite that reactive power does not consume fuel, the RC_h^s costs are derived from reactive power losses and penalties for generating reactive power [172]. Inversely, FRC_h^s costs are associated with exceeding technical limits for frequency deviations. Quite often, technical costs consider V-f deviation costs simultaneously. However, due to the smaller margin allowed for frequency deviations in most IMG, it was chosen over voltage deviations in this study [174]. Subsequently, RC_h^s and FRC_h^s are given by [175]:

$$RC_h^s = \Psi_{var} \cdot (FC_h^s + MC_h^s + EC_h^s) \cdot \frac{\sum_{i \in \mathcal{GK}} Q_{Gi}^{h,s}}{\sum_{i \in \mathcal{GK}} P_{Gi}^{h,s}} \tag{6.25}$$

$$FRC_h^s = \psi_{freq} \cdot \left(f_{ss}^{h,s} - f_0\right) \quad (6.26)$$

where $Q_{Gi}^{h,s}$ is the reactive generated power by the dispatchable DG at the scenario s during the off-peak hour h. $f_{ss}^{h,s}$ is the steady state frequency of the IMG at the scenario s during the off-peak hour h. Ψ_{var} is the reactive power coefficient of the dispatchable DG [175]. ψ_{freq} is the frequency penalty cost coefficient [171], [174].

Moreover, the need for technical penalty costs is necessary to adhere the safe operating constraints for a DCIMG, where adequacy and quality of supply is maintained within a safe margin [171]. On the other hand, a renewable DG unit does not consume fuel, neither it produces emissions. Also, renewable units are tracked locally for their power output. Hence, it is assumed that the WT in this study follows an MPPT algorithm. Whereas each WT is assumed as an induction generator type, and therefore, they are consuming reactive power with 0.9 leading PF [41], [176].

6.4.1.2 Maximum Voltage Error

Strong indices for stability in an IMG are the objectives addressing voltage variations across the system buses. Different voltage objectives were considered previously in DG allocation studies to ensure stability in the MG such as voltage stability index and total voltage variations [177], [178]. Nonetheless, in this study no DG units were allocated, and the focus is on achieving flattened voltage profile across the IMG. This is done while ensuring that bus voltages are as close as possible to nominal value. Hence, maximum voltage error (MVE) was chosen in this study to achieve a minimal voltage error across all system buses, and is given by [161]:

$$\mathcal{F}_2^{h,s}(x_3) = MVE_h^s = \max_{i \epsilon \mathcal{N}} \left\{ \left| \left| \mathrm{V}_{in}^{h,s} \right| - 1 \right| \right\} \quad (6.27)$$

where $\mathrm{V}_{in}^{h,s}$ is the voltage at bus i at the scenario s during the off-peak hour h. The choice of the voltage objective in this chapter differs from the deterministic DL optimization problems suggested by [43], [44], [48], wherein the voltage objective was selected as the minimization of the VB voltage $|\Delta V_1|$. The choice of ΔV_1 by the latter studies [43], [44], [48] was due to the significant influence of ΔV_1 on the voltage profile for global voltage based LF methods. Hence, it had a stronger influence on network voltage profile.

However, in this chapter, the chosen voltage objective was more suited to the used LF method, GBFS, which depends on local voltage measurements. Therefore, minimizing $|\Delta V_1|$ will not result in a better voltage profile, but rather minimizing MVE will ensure a flatter voltage profile by considering all voltages across the system.

6.4.1.3 Frequency Deviation

The third objective is related to the expected frequency deviation in the IMG. This can be obtained by the following equation:

$$\mathcal{F}_3^{h,s}(x_3) = |\Delta f_h^s| = \left| m_{pT} \cdot \left(P_{G1}^{h,s} - \Re\left\{ V_1^{h,s} \cdot B_1^{h,s^*} \right\} \right) \right| \tag{6.28}$$

where $P_{G1}^{h,s}$, $V_1^{h,s}$, $B_1^{h,s}$ are the active power, voltage, and branch current at the VB considering the scenario s during the off-peak hour h, respectively.

6.4.1.4 Total Energy Loss

Lastly, the fourth objective considered, the expected total energy loss, is given by:

$$\mathcal{F}_4^{h,s}(x_3) = P_{loss}^{h,s} \cdot t^s = \sum_{i=1}^{n-1} \Re\{Z_i\} \cdot \left| B_i^{h,s} \right|^2 \cdot t^s \tag{6.29}$$

where $P_{loss}^{h,s}$ is the active power loss at the scenario s during the off-peak hour h. t^s is the time duration which is equal to one hour at each s scenario. $B_i^{h,s}$ is the branch current at the scenario s during the off-peak hour h.

6.4.2 Constraints

To ensure adequate stability during islanding operation, different technical constraints must be adhered [8], [69]. The power balance constraint has already been considered by the optimization problem during each s scenario. Since each converged load flow will implicitly ensure power balance keeping for generation and demand in the IMG. Thus, the equilibrium balance equations considering uncertainty in generation and demand is given for each s scenario during each off-peak hour h as follows:

$$\sum_{i=1}^{gk} P_{Gi}^{h,s} = \sum_{i=1}^{lk} P_{Li}^{h,s} + P_{DL} + P_{loss}^{h,s} \tag{6.30}$$

$$\sum_{i=1}^{gk} Q_{Gi}^{h,s} = \sum_{i=1}^{lk} Q_{Li}^{h,s} + Q_{DL} + Q_{loss}^{h,s} \tag{6.31}$$

where $P_{Li}^{h,s}$ and $Q_{Li}^{h,s}$ is the load's active and reactive powers at the scenario s during the off-peak hour h. $Q_{loss}^{h,s}$ is the reactive power loss at scenario s during the off-peak hour h. gk is the total number of DGs in the network. For each deterministic optimization problem with any given scenario s and off-peak hour h, there are constraint functions ($g_i^{h,s}(x_3)$) for bus

voltage, branch current, frequency, and dispatchable DG power output that must be satisfied simultaneously for each objective function evaluation as follows:

- Bus i's voltage limit constraints:

$$0.95 \leq \left|\mathrm{V}_{in}^{h,s}\right| \leq 1.05 \tag{6.32}$$

- Thermal limit constraints:

$$\left|\mathrm{B}_{i}^{h,s}\right| \leq \left|B_{i\_max}\right| \tag{6.33}$$

- System steady-state frequency limits:

$$0.996 \leq f_{ss}^{h,s} \leq 1.004 \tag{6.34}$$

- Power output limit for dispatchable DG units:

$$0 \leq P_{Gi}^{h,s} \leq 4 \tag{6.35}$$

$$0 \leq Q_{Gi}^{h,s} \leq 2.5 \tag{6.36}$$

Contrariwise, as per the assumed notion, each non-dispatchable renewable DG follows an MPPT algorithm. Hence, it operates in PQ mode that injects real power and consumes reactive power. This notion indicates that at any scenario, the non-dispatchable units will always remain within their power limits and therefore are excluded from DG constraints for power output. On the other hand, there are constraints that are not affected by individual scenario or hour change, those are associated with the decision variables of the problem for the DL size and location as well as DG units' droop sets. Moreover, the generated optimal solution during each objective function evaluation must adhere to the aggregated effect of all NR reduced scenarios across all H off-peak hours. Hence, the decision variable limits must be satisfied once per each function evaluation as follows:

- Dump load size limits for each single DL unit:

$$0.002 \leq P_{DL} \leq 1 \tag{6.37}$$

$$0.002 \leq Q_{DL} \leq 1 \tag{6.38}$$

- Droop coefficient limits:

$$10^{-4} \leq mn_{DL} \leq 0.05 \tag{6.39}$$

A flow chart of the proposed stochastic optimization problem formulation is depicted in Figure 6.4.

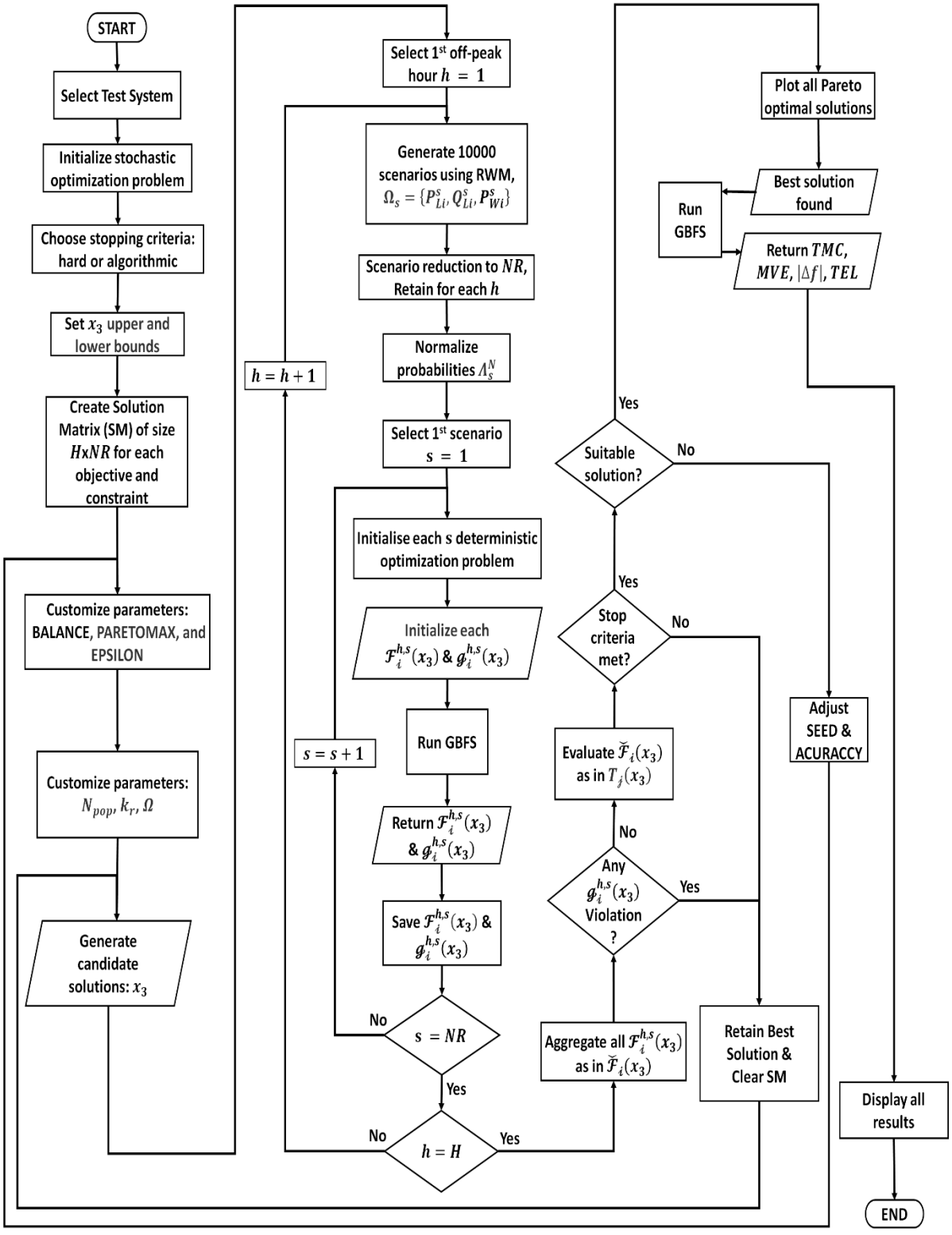

Figure 6.4: Flow chart of the proposed method for stochastic DL optimization problem

From Figure 6.4, the stochastic mixed-integer nonlinear problem can be better understood by having two main loops to account for all reduced scenarios while considering the complete off-peak horizon. Subsequently, the stochastic problem is fragmented into a series of deterministic problems that are evaluated simultaneously to attain the non-dominated solution. Moreover, by utilizing the fine-grained parallelization strategy of the proposed evolutionary metaheuristic technique, MIDACO, the fragmented deterministic optimization problem sets can be co-evaluated for reduced computation overhead. The resultant overall enhanced calculation times would be at least 1000 times faster per function evaluation. In other words, MIDACO's superior parallelization strategy shall facilitate the calculation time reduction for a single function evaluation from a matter of seconds into a matter of milliseconds or less. This would result in an overall reduction in the optimization cycle form hours into a matter of minutes, which is very fundamental for real-time operation with vast chucks of uncertainty data to be analysed, evaluated, and optimized.

It worth noting that all data were given using the per-unit system, with 500 kVA base for the IEEE 33-, 69-, and 118-bus systems. Voltage base of 12.66 kV for the IEEE 33- and 69-bus systems as well as 11 kV for the IEEE 118-bus system. Moreover, it was assumed that the system's nominal frequency is 50 Hz for the IEEE 33-, 69-, and 118-bus systems. For sake of brevity, GBFS was considered as the load flow technique in every simulation in this chapter.

6.5 Results and Discussion

The case studies considered for the IMG in this chapter are the IEEE 33-, 69-, and 118-bus systems, respectively. Noteworthy, is that for the IEEE 33-bus case study, the number of DGs has been reduced to four units as given in the original test case from [43]. The IEEE 33-, 69-, and 118-test systems line and load data were taken from [145], [146], and [149] respectively. Moreover, DG locations for IEEE 33- and 69-bus systems were obtained from [43], while the IEEE 118-bus system's DG locations were taken from [150].

On the other hand, the microgrid technical data and distributed generation ratings are given in Table 6.1 for the dispatchable and non-dispatchable units as obtained from [173] and [41], respectively. Furthermore, all dispatchable DGs were as natural gas turbine (NGT) units, while the non-dispatchable DGs, on the other hand, were as WT units.

Similarly, the DG unit arrangements for the No DL base case are given in Table 6.2. All WT units were set to operate at 0.9 leading PF with 0.5 MW rated capacity, while the assumed pre-islanding generation of all NGT units were $2.545 + j1.909$ p.u. at 0.8 PF. This type of operation ensures that all dispatchable units are loaded at 63.63% of their rated capacity. This is a common and safe operating region for dispatchable units in an IMG during off-peak hours to minimize maintenance costs and prevent equipment failure [43], [48].

Table 6.1: Technical characteristics of DG units and MG under study

NGT Characteristics		**WT Characteristics**		**Other MG & Heating Characteristics**			
Parameter	Value	Parameter	Value	Parameter	Value	Parameter	Value
P_{min} (MW)	0.20	v_r (m/s)	10.5	ψ_{freq} (£/Hz)	77	Ψ_{var}	0.3
P_{Nr} (MW)	2.00	P_{Wr} (MW)	0.5	ψ_{LCOE}^{eleR} (£/MWh)	25.73	η_{hw}^{ele}	0.99
η_P	0.37	v_{ci} (m/s)	4.5	ψ_{LCOE}^{eleN} (£/MWh)	53.95	η_{hw}^{gas}	0.80
Ψ_{emis} (Tonne/MWh)	0.2016	v_{co} (m/s)	22.0	ψ_{LCOE}^{gas} (£/MWh)	43.99	T_{in} (C°)	10
ψ_{emis} (£/Tonne)	31.34	v_{μ} (m/s)	10.5473	ψ_{LCOE}^{Li} (£/MWh)	507.13	T_{st} (C°)	60
ψ_{fuel} (£/MWh)	15.79	v_{σ} (m/s)	3.7282	ψ_{LCOE}^{Ni} (£/MWh)	532.11	C_w (J/Kg. C°)	4200
ψ_{main} (£/MWh)	2.31	-	-	-	-	ρ_w (Kg/m^3)	997

All cost values are given assuming exchange rate: $ = 0.77£ and € = 0.83£

Table 6.2: Base case DGs arrangement for stochastic dump load allocation MINLP, all bus systems

DG Unit Name	**Test System**														
	33-bus system					69-bus system					118-bus system				
	DG Type	No of Units	Bus No.	m_{pi}	n_{qi}	DG Type	No of Units	Bus No.	m_{pi}	n_{qi}	DG Type	No of Units	Bus No.	m_{pi}	n_{qi}
DG_1	NGT	1	1	-0.05	-0.05	NGT	1	1	-0.05	-0.05	NGT	2	1	-0.05	-0.05
DG_2	NGT	1	6	-1	-1	NGT	1	6	-1	-1	NGT	2	20	-1	-1
DG_3	NGT	1	13	-0.1	-0.1	NGT	1	15	-0.1	-0.1	NGT	2	39	-0.1	-0.1
DG_4	WT	1	25	-	-	WT	1	30	-	-	NGT	2	47	-1	-1
DG_5	-	-	-	-	-	WT	1	55	-	-	NGT	2	73	-0.2	-0.2
DG_6	-	-	-	-	-	-	-	-	-	-	WT	2	80	-	-
DG_7	-	-	-	-	-	-	-	-	-	-	WT	2	90	-	-
DG_8	-	-	-	-	-	-	-	-	-	-	WT	2	110	-	-

The technical data as given in Table 6.1 and Table 6.2 will serve as bases for the stochastic optimization problem. Noteworthy, is that all NGT units can withstand the total system demand in case of zero power generation by the WT units. This indicates that the MG is setup for autonomous operation without relying on utility grid or any adjacent MG. Furthermore, two, two, and four identical DLs were considered in the stochastic optimization problem for the 33-, 69-, and 118-bus systems, respectively. These DLs were of equal 500 kVA ratings and allocated concurrently to the same location with the same exact power size.

The problem was modelled and simulated in MATLAB with machine ratings: Intel core i7 Gen.9, 2.60 GHz, and 8 GB RAM. To initialize the stochastic optimization problem, each deterministic problem was simulated with 0, 0, and 10^9 values for N_{pop}, k_r and Ω, respectively. While PARETOMAX, EPSILON, and BALANCE were set to 1000, 0.01, and 0, respectively. To enable the fine-grained parallelization strategy within MIDACO, the parallelization factor was initialized with multiples of 12. This shall distribute the computationally expensive stochastic function evaluation time, evenly, to six cores each with two threads. Lastly, GBFS optimization parameters were set to 10^{-8} and 100 for FSTOP and FOCUS, respectively.

6.5.1 Multi-Objective Optimization Considering Uncertainty

As mentioned in the previous section, a many-objective problem was formulated to obtain an expected minimization of TMC, MVE, $|\Delta f|$, and TEL considering all scenarios simultaneously. The distribution of DGs across all test systems were done in such way that all loads in the network are met by generation satisfactorily during peak demand operation to minimize losses across the distribution feeders [43], [150]. The expected results considering uncertainty in wind generation and demand forecast is given in Table 6.3.

Table 6.3: Expected many-objective results considering uncertainty in wind power and electricity demand, all bus systems

Test System	33-bus system		69-bus system		118-bus system	
Case	No DL	w/DL	No DL	w/DL	No DL	w/DL
$\boldsymbol{N_{DL}}$	-	19	-	30	-	73
$\boldsymbol{P_{DL}}$ **(p.u.)**	-	0.6437	-	1.2831	-	1.7670
$\boldsymbol{Q_{DL}}$ **(p.u.)**	-	1.0009	-	0.4004	-	0.2389
$\boldsymbol{mn_{DL}}$ **(p.u.)**	-	0.0003	-	0.0014	-	0.0003
Expected TMC (£)	4780.78	630.57	5383.61	640.10	5879.41	725.04
Expected MVE (p.u.)	0.1277	0.0137	0.0937	0.0245	0.1024	0.0324
Expected $|\Delta \boldsymbol{f}|$ **(p.u.)**	0.1597	0.0004	0.1901	0.0022	0.2405	0.0005
Expected TEL (kWh)	95.7	89.4	200	228.9	1472.8	1270.25
Time[a] (s)	-	607	-	638	-	872

First step size only for $|\Delta f|$, [a]algorithm computation time.

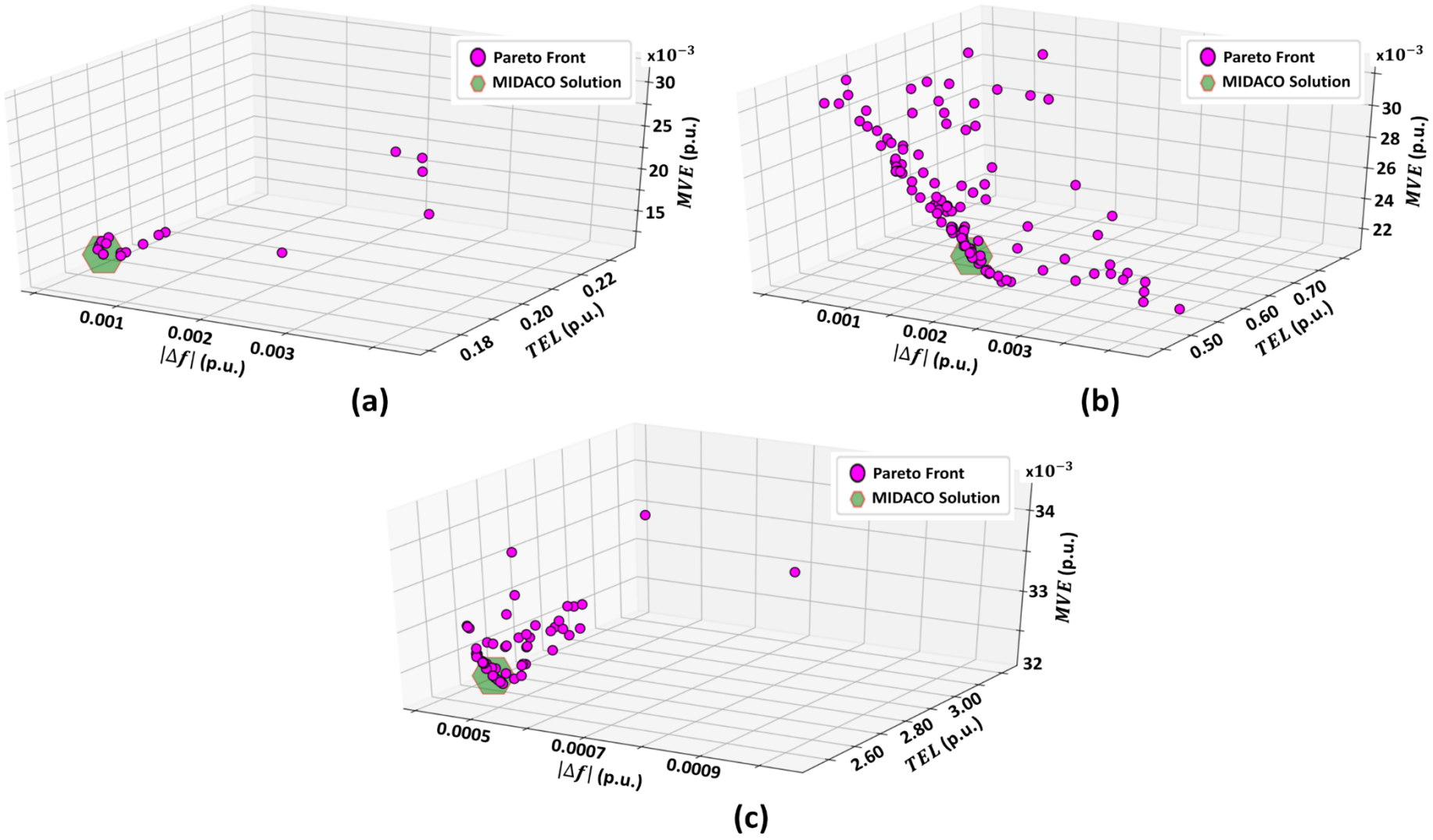

Figure 6.5: Many-objective Pareto front considering uncertainty in wind power and electricity demand, the proposed method solution is highlighted in the hexagon green shape for: (a) 33-bus (b) 69-bus (c) 118-bus

Similarly, the Pareto front for the expected objective function value is depicted in Figure 6.5 for the IEEE 33-, 69-, and 118-bus systems. The non-dominated solution as selected by the utopia-nadir-balance approach of the proposed optimization technique is highlighted in the green shape at the centre of the Pareto front curve.

According to Figure 6.5(a), smaller spread for the Pareto points of IEEE 33-bus is observed if compared with the cases for the IEEE 69- and 118-bus system as illustrated in Figure 6.5(b) and Figure 6.5(c), respectively. Nonetheless, as illustrated by Figure 6.5(b), the spread of Pareto points for the IEEE 69-bus case is most significant compared to IEEE 33- and 118-bus systems. This is attributed to the relatively smaller optimal solution search space for the IEEE 33 and 118-bus system which is affected by various factors. Such factors include: the generation/demand mismatch ratio; number of system buses and lines; number of WT's and loads; size of generated power and consumed demand; the amount of variations in the reduced scenarios. Accordingly, the number of non-dominated Pareto points collected at the default PARETOMAX and EPSILON parameters were 17, 119, and 54 for the IEEE 33-, 69-, and 118-bus systems, respectively.

Moreover, as per the desired accuracy rate, 0.002 sampling rate, 20 reduced scenarios were considered out of 10000 generated ones by the stochastic optimization problem. This has accounted for 20 deterministic optimization problems, each having its fixed load power at each bus as well as it's constant wind power generation. Based on that, the expected non-dominated solution for the stochastic DL allocation problem is given in Table 6.3 for the IEEE 33-, 69-, and 118-bus systems. This was obtained by the proposed stochastic optimization flow chart of Figure 6.4. The resultant aggregated solution was obtained such that all off-peak hours were covered satisfactorily.

On the other hand, according to the results given in Table 6.3, DL significance during off-peak hours considering uncertainty in demand forecast and renewable generation was evident. This was true for the first three allocation objectives if compared with the base case (i.e., the No DL case while using droop sets from Table 6.2 for each bus system).

The expected high TMC for the base case of the IEEE 33-, 69-, and 118-bus systems is attributed to the increased fuel and emissions costs, but more importantly, the technical costs required to ensure adequate supply quality for the microgrid. That is, if the IMG were operated without the optimal dump load allocation and minimal V-f deviations.

Likewise, a breakdown of the expected values for all objectives considering all reduced scenarios on an hour-by-hour basis is illustrated in Figure 6.6, Figure 6.7, and Figure 6.8 for the IEEE 33-, 69-, and 118-bus systems, respectively.

The breakdown of results demonstrated the importance of considering all off-peak hours' horizon in the DL objective function formulation. This has ensured that all hourly values for MVE and $|\Delta f|$ were below the expected individual objective value.

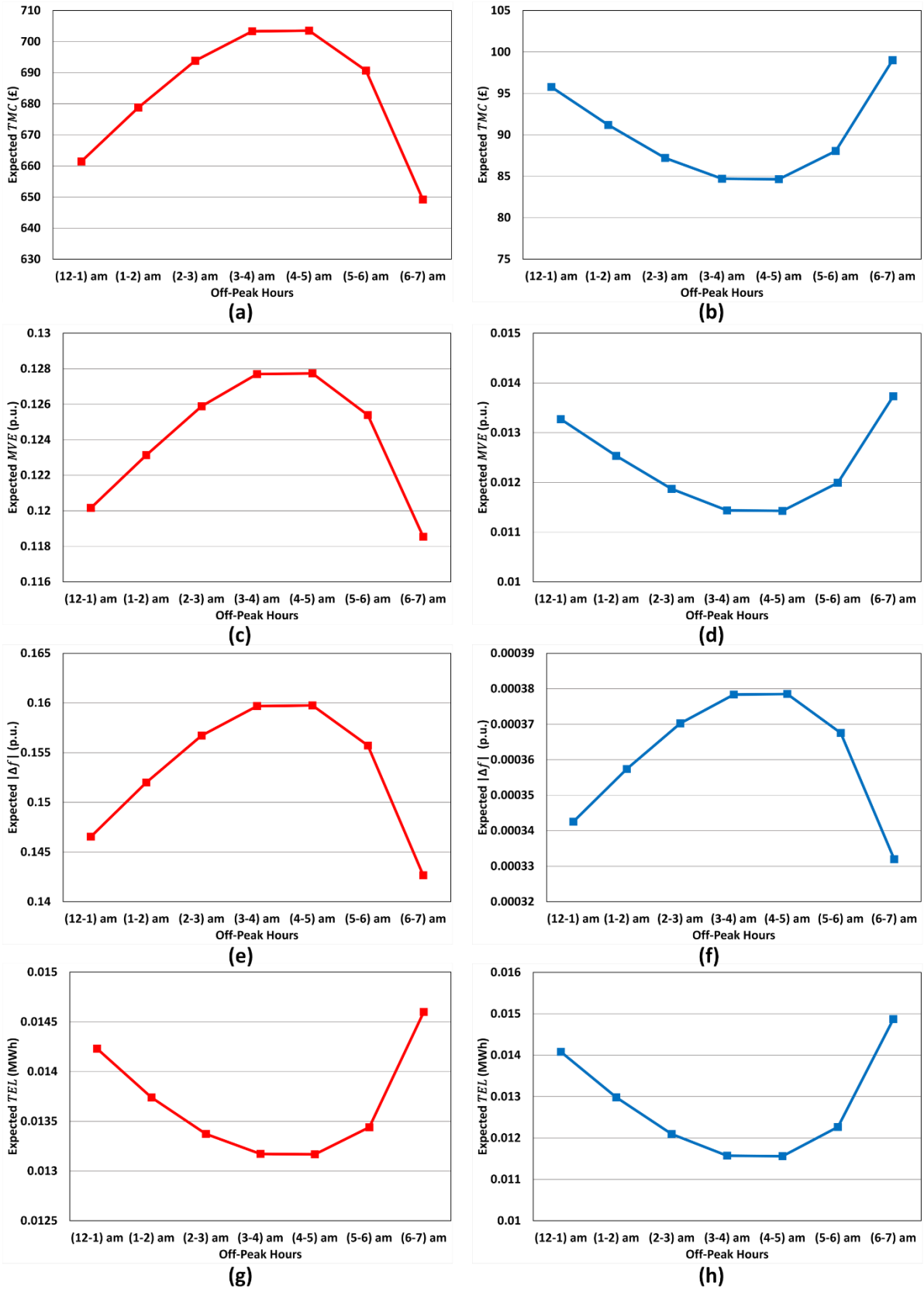

Figure 6.6: Expected 33-bus system hour-by-hour value of the objective function for: (a) TMC No DL (b) TMC w/DL (c) MVE No DL (d) MVE w/DL (e) $|\Delta f|$ No DL (f) $|\Delta f|$ w/DL (g) TEL No DL (h) TEL w/DL

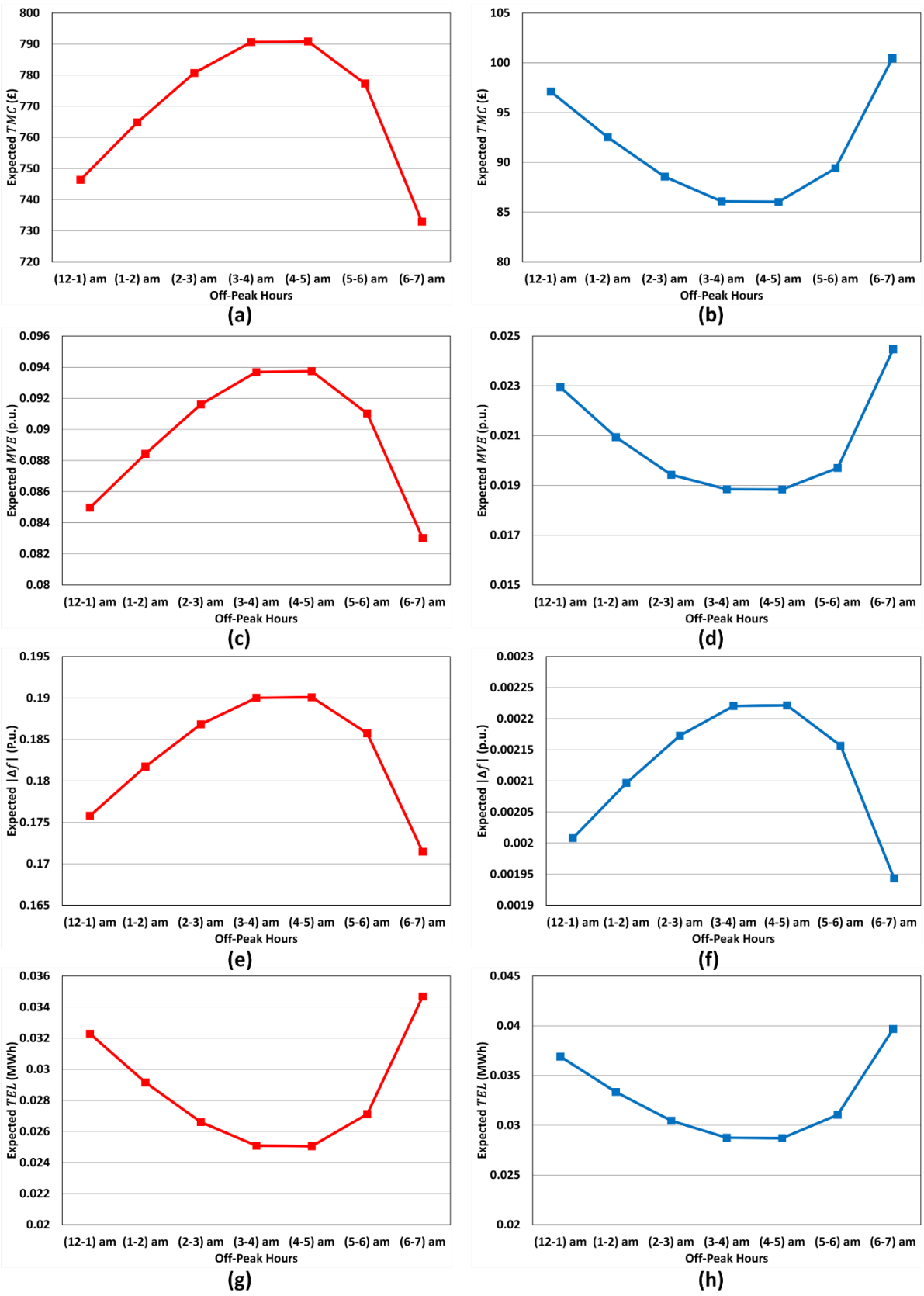

Figure 6.7: Expected 69-bus system hour-by-hour value of the objective function for: (a) TMC No DL (b) TMC w/DL (c) MVE No DL (d) MVE w/DL (e) $|\Delta f|$ No DL (f) $|\Delta f|$ w/DL (g) TEL No DL (h) TEL w/DL

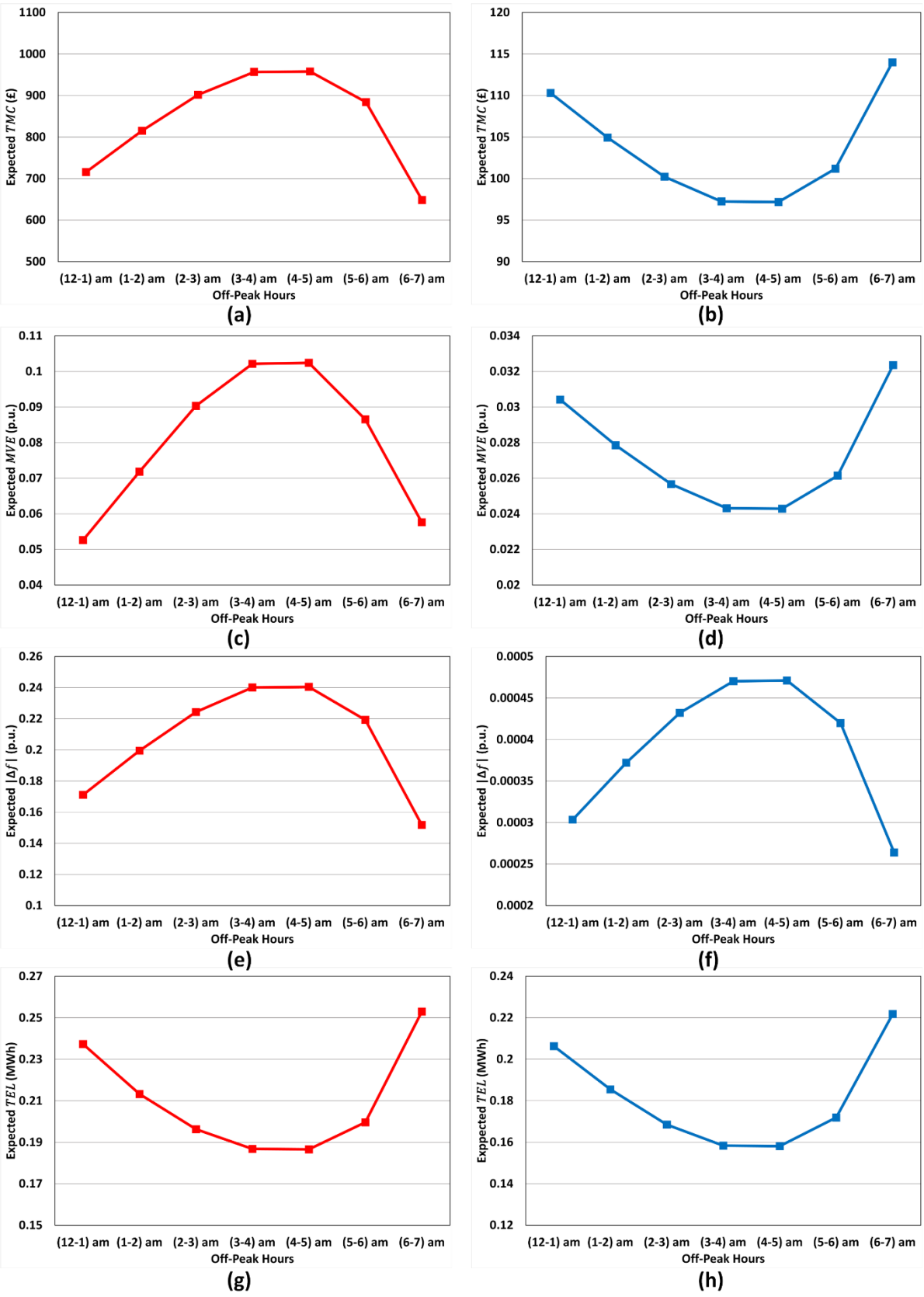

Figure 6.8: Expected 118-bus system hour-by-hour value of the objective function for: (a) TMC No DL (b) TMC w/DL (c) MVE No DL (d) MVE w/DL (e) $|\Delta f|$ No DL (f) $|\Delta f|$ w/DL (g) TEL No DL (h) TEL w/DL

According to Figures 6.6, 6.7, and 6.8, the expected improvement on an hour-by-hour bases from the No DL case to the DL allocation case is better illustrated by the noticeable reduction in voltage and frequency errors. Contrariwise, the breakdown of results for TMC and TEL has confirmed the importance of considering uncertainty in load and wind powers during the off-peak horizon. This implies that the expected costs and losses associated with the IMG are the accumulative sum of all expected costs and losses for each off-peak hour. The voltage profiles during each off-peak hour are illustrated in Figure 6.9 for all three bus systems.

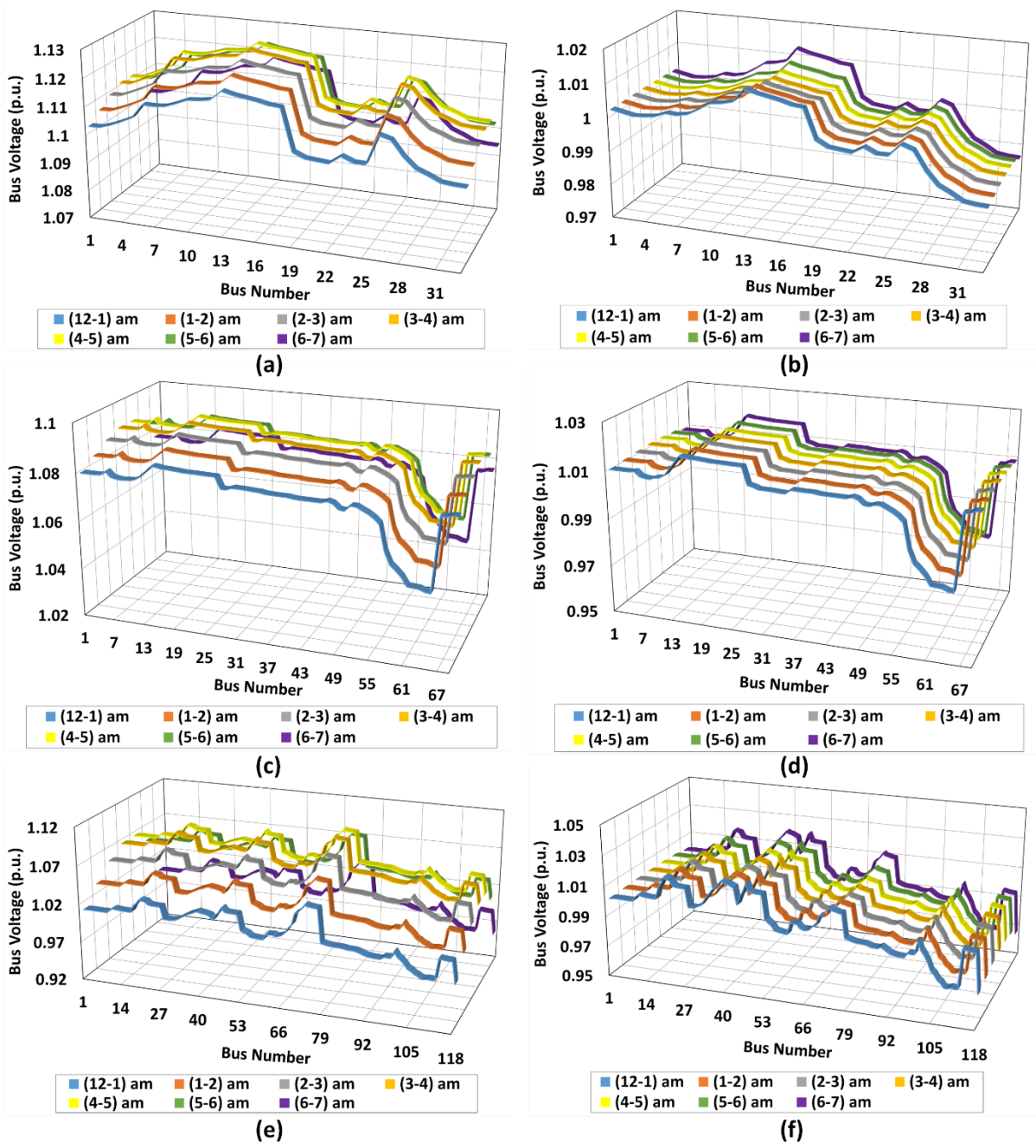

Figure 6.9: Expected voltage profiles during off-peak hours considering DL allocation with uncertainty for: (a) 33-bus No DL (b) 33-bus w/DL (c) 69-bus No DL (d) 69-bus w/DL (e) 118-bus No DL (f) 118-bus w/DL

As can be deduced from Figure 6.9, using an optimally sized DL with optimal droop sets has significantly improved the stability and supply quality of the IMG by having a flatter voltage profile compared to the No DL case. Moreover, a smoother steady state frequency profile is attained due to minimal $|\Delta f|$ after DL allocation if compared against the base case. The expected frequency profile considering uncertainty is depicted in Figure 6.10.

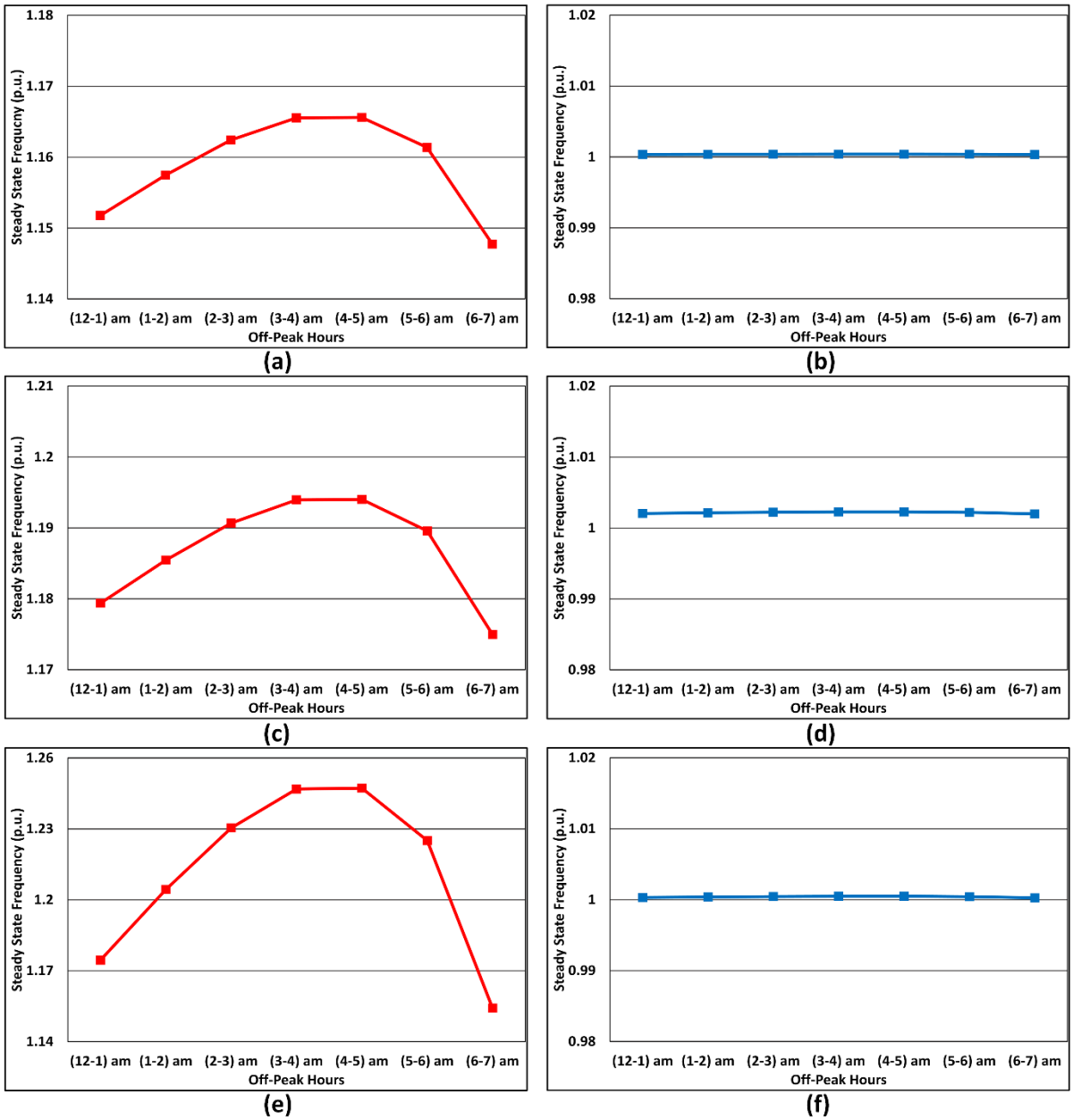

Figure 6.10: Expected steady state frequency profile during off-peak hours considering DL allocation with uncertainty for: (a) 33-bus No DL (b) 33-bus w/DL (c) 69-bus No DL (d) 69-bus w/DL (e) 118-bus No DL (f) 118-bus w/DL

According to Figure 6.10, a negligible frequency difference is observed for all cases after DL inclusion into the system. Conversely, the significant irregularity in voltage profiles for the base case is attributed to the absence of DL to absorb the excessive expected reactive

power mismatch during off-peak hours. Likewise, the large frequency deviation from nominal values during every off-peak hour was due to the expected substantial active power mismatch. Moreover, the resultant hour-by-hour frequency profile is interpreted with average steady state frequency of 1.1588 p.u., 1.1869 p.u., and 1.2118 p.u. for the 33-, 69-, and 118-bus systems, respectively, in the case without DL. This is compared to 1.0004 p.u., 1.0022 p.u., and 1.0004 p.u. for the 33-, 69-, and 118-bus systems, respectively, in the case with DL allocation.

On the other hand, the fourth objective, TEL, depends greatly on the existing reactive power mismatch in the network. In other words, having a relatively lower excess reactive power mismatch in the IMG will lead to higher losses after the inclusion of DL. Contrariwise, having a relatively higher reactive power mismatch will lead to further reduction in losses after the inclusion of DL. This can be understood by visualizing the role of DL allocation and the reactive compensation in predominantly capacitive networks. This was evident for the cases of 33- and 118-bus systems where energy losses were much less after the DL allocation. However, more energy losses were observed for the 69-bus case after DL inclusion.

Nonetheless, regardless of the amount of reactive power mismatch in the network, the optimal DL allocation considering TEL as an objective has considerably reduced losses which otherwise would have been incurred by the general DL utilization in distribution networks. This was true for additional losses incurred as seen from the single- and two-objectives point of view for the DL allocation as presented in sub-section 5.5.1.

6.5.2 Comparison with Other Metaheuristic Optimization Methods

In this section, the advantage of the proposed optimization technique is demonstrated against other established evolutionary and swarm intelligence techniques, viz., MOPSO [155], [156], MOGA [154], and NSGA-II [157], [158]. The parameters for MOPSO, MOGA, and NSGA-II were adopted from [48] and identical to those presented in chapter 5 (section 5.5.7) herein. Given in Table 6.4, the non-dominated expected optimal solution as obtained by MOGA, NSGA-II, MOPSO, and MIDACO for the stochastic DL allocation problem considering GBFS as the load flow method within the optimization technique.

According to results in Table 6.4, the obtained TMC and TEL by MIDACO was better overall for the 33- and 69-bus systems. Similarly, the TEL obtained by the MIDACO was significantly lower if compared to other methods for the 118-bus system. The achieved $|\Delta f|$ by the proposed method was very close to all other methods for all three test systems. Nonetheless, the obtained other objectives by the other methods did not rise to the quality of the non-dominated solution obtained by the proposed method. The reported TMC by MIDACO and NSGA-II were close for all three test systems. However, the obtained MVE and TEL were worst by NSGA-II if compared to MIDACO.

Table 6.4: Stochastic DL problem comparison with other metaheuristics using GBFS, all bus systems

Optimization Method	MOGA			NSGA-II			MOPSO			MIDACO		
Test System	33	69	118	33	69	118	33	69	118	33	69	118
N_{DL}	13	30	79	4	28	62	7	49	69	19	30	73
P_{DL} **(p.u.)**	0.6801	1.5624	2.0357	0.6826	1.2834	1.7750	0.6593	1.6615	2.3868	0.6437	1.2831	1.7670
Q_{DL} **(p.u.)**	0.4777	0.9545	0.4547	0.8779	0.6879	0.4463	1.4145	0.6033	1.1205	1.0090	0.4004	0.2389
mn_{DL} **(p.u.)**	0.0010	0.0014	0.0003	0.0007	0.0015	0.0003	0.0003	0.0014	0.0003	0.0003	0.0014	0.0003
Expected TMC (£)	663.83	690.20	737.44	654.18	642.18	727.40	637.72	705.85	748.88	630.57	640.10	725.04
Expected MVE (p.u.)	0.0132	0.0262	0.0387	0.0138	0.0254	0.0419	0.0218	0.0250	0.0330	0.0137	0.0245	0.0324
Expected $\lvert\Delta f\rvert$ **(p.u.)**	0.0015	0.0021	0.0005	0.0010	0.0022	0.0005	0.0004	0.0020	0.0004	0.0004	0.0022	0.0005
Expected TEL (kWh)	104	247.55	1565.1	102.9	230.8	1479.1	124.15	264.8	1502.95	89.4	228.9	1270.25
MAXEVAL	400	400	400	200	200	200	400	400	400	10000	10000	10000
Time[a] (s)	8526	9763	12061	10661	12203	12843	7331	7617	9214	607	638	872

First step size only for $\lvert\Delta f\rvert$, [a]algorithm computation time.

According to Table 6.4 and despite utilizing a parallelization strategy by MOPSO, MOGA, and NSGA-II for a relatively smaller number of function evaluations, their calculation times were quite high and not practical. On the other hand, the recorded calculation times by MIDACO's fine-grained parallelization provided a competitive solution with decent and practical speed even though MIDACO had 10000 function evaluations. The reason behind this is attributed to the core difference between MIDACO's parallelization strategy [117], [126], [131] and that of the other evolutionary techniques presented herein, which follows the strategy presented by [179]. In one hand, the parallelization strategy implemented by the acclaimed evolutionary techniques herein, i.e., MOGA, NSGA-II, and MOPSO, is a strategy that aims to reduce the algorithmic overhead of the evolutionary metaheuristic. That is, by allowing the parallel computation of one or more specific internal operators of the algorithm. On the other hand, MIDACO's strategy aims to parallelize the execution of individual function evaluation instances for objective and constraint functions. This is executed without performing any parallelization of the internal algorithmic parts of ACOmi. As a result, the fine-grained parallelization strategy implemented by MIDACO aims to reduce the overall calculation times for real-life MINLPs [131].

6.5.3 Cost Benefit Analysis of Different Energy Management Systems

To comprehend the cost effectiveness of DL allocation in a DCIMG during off-peak hours considering uncertainty in demand forecast and renewable generation, a cost benefit analysis (CBA) was considered. The achieved results of the CBA will further showcase the advantage of primary DL-based EMS (DLEMS) for power regulation against primary battery-based EMS (BEMS) for the same purpose. The CBA is done for two distinctive EMS strategies, viz., BEMS and DLEMS. In the first EMS strategy, i.e., BEMS, the overgeneration mismatch in the network is absorbed by BESS, while conventional natural gas boilers are utilized to supply the hot water demand of the system. As for the second EMS strategy (i.e., DLEMS), which is the proposed EMS in this study, the excess generation is absorbed using a DL, while employing the dumped power to supply portion of the hot water heating and pumping demands [44]. This is achieved by employing active and reactive DL power as electric boilers and pumps, respectively, while seeking electricity from non-renewable energy sources to cover the remaining hot water demand.

The aim of the CBA approach presented in this study, is to give a comprehensive economic analysis as a reflection of solving the V-f regulation problem in highly penetrated DCIMG. Furthermore, putting that excess power driving the V-f regulation issues into useful work without compromising on the reliability of the proposed EMS. Contrary to the CBA presented in [44], the CBA of this study is more realistic as it considers all capital, running,

fuel, and maintenance costs. Such costs are associated with installing and maintaining heating systems in an IMG while accounting for uncertainties in demand forecast and wind generation. This was done by considering the levelized cost of energy (LCOE) for electric and gas boilers as well as the LCOE for storage installation and replacement. Furthermore, the amount of dumped power in the IMG was determined based on the stochastic scenario modelling for uncertainty. To have a sufficient investment analysis, the LCOE method is widely used in academia and the industry. This is required to determine the investment return of different energy technologies by assessing the costs of producing energy by such systems [180]. On average, gas boilers are three times more expensive to install and maintain than electric boilers. However, the cost of energy to produce heat via electric boilers is around four times that much for gas boilers. Nonetheless, as per the assumed notion of this study, the power source driving the electric boilers is coming from pure green and renewable source (wind for this study). Hence, the unit price for electricity consumed by electric boilers using P_{DL} is zero.

The CBA conducted to analyse the cost-effectiveness of running two different EMS strategies. This is based on the high probability of excess power congestion that must be dumped at off-peak hours to maintain V-f stability. Thereby, the excess power is either stored or used efficiently in heating purposes. Likewise, to give a realistic point of view, the CBA was conducted without neglecting the costs required to cover the remainder of daily system's hot water demand. This was done by considering two LCOE for electric boilers, one from renewable and another from non-renewable sources. Moreover, acquisition of the system total hot water demand is scheduled during the off-peak hours period to relief network congestion during peak hours. Thus, the hot water is stored in dedicated large hot water cylinders which can be supplied to end users via on-demand water circulation systems [44], [181]. It is further assumed that on average, considering the whole year, the total daily demand for hot water volume (V_{hw}^{tot}) is 680.88 m^3, 817.06 m^3, and 1293.67 m^3 for the IEEE 33-, 69-, and 118-test systems, respectively [41]. A general equation for hot water volume (V_{hw}) as a function of available energy to produce heat is given as follows [181]:

$$\mathrm{V}_{hw} = \frac{P_{hw} \cdot \eta_{hw} \cdot h}{C_w \cdot \rho_w \cdot \Delta \mathrm{T}} \tag{6.40}$$

where P_{hw} is the consumed power for a water heating boiler as utilized to produce hot water. η_{hw} is the efficiency of the water boiler which was assumed as 0.80 and 0.99 for gas (η_{hw}^{gas}) and electric (η_{hw}^{ele}) boilers, respectively [44]. C_w is the specific heat of water, while ρ_w is the water density. $\Delta \mathrm{T}$ is the centigrade difference in desired hot water temperature and the water temperature as it enters the boiler and is given by [44], [181]:

$$\Delta \mathrm{T} = \mathrm{T}_{st} - \mathrm{T}_{in} \tag{6.41}$$

where T_{st} is the set-point temperature which was set to 60 Cº. T_{in} is the inlet temperature and assumed at 10 Cº [181]. Based on that, the costs associated with heating water using electric or gas boilers are as follows:

$$HC_{hw}^{e} = \psi_{LCOE}^{eleR} \cdot P_{DL} \cdot h + \psi_{LCOE}^{eleN} \cdot P_{hw}^{ele} \cdot h \quad (6.42)$$

$$HC_{hw}^{g} = \psi_{LCOE}^{gas} \cdot P_{hw}^{gas} \cdot h + SC_{BESS} \quad (6.43)$$

$$SC_{BESS} = \psi_{LCOE}^{BESS} \cdot P_{DL} \cdot h \quad (6.44)$$

where HC_{hw}^{e} and HC_{hw}^{g} are the water heating costs for DLEMS and BEMS implementations, respectively. P_{hw}^{ele} and P_{hw}^{gas} are the required power to meet total system hot water demand from electric and gas boilers, respectively, subtracting P_{DL} from electric boiler power P_{hw}^{ele}. ψ_{LCOE}^{eleR} and ψ_{LCOE}^{eleN} are the LCOE coefficients for renewable and non-renewable sourced electric boilers, respectively, with their assumed values at 25.73 £/MWh (31 €/MWh) for ψ_{LCOE}^{eleR} and 53.95 £/MWh (65 €/MWh) for ψ_{LCOE}^{eleN} [180]. ψ_{LCOE}^{gas} is the LCOE coefficients for gas boilers, with an assumed value at 43.99 £/MWh (53 €/MWh) [180].

According to the BEMS implementation, the excess power (i.e., P_{DL}) will be stored in BESS which will result in additional costs known as storage costs (SC_{BESS}). The evaluation of SC_{BESS} is based on the amount of power stored in the battery and the associated LCOE for that particular storage technology [6]. Hence, a cost coefficient for storage LCOE is used here and denoted as ψ_{LCOE}^{BESS}. Also, for sufficient comparison, two types of BESS were considered in the CBA of this study, namely, Lithium-ion (Li-ion) and Nickel-Cadmium (Ni-Cd) [44]. Moreover, the assumed ψ_{LCOE}^{BESS} were 507.13 £/MWh (611 €/MWh) and 532.11 £/MWh (641.1 €/MWh) for Li-ion (ψ_{LCOE}^{Li}) and Ni-Cd (ψ_{LCOE}^{Ni}) storage solutions, respectively [6]. Therefore, the total costs for running water heating system per calendar year (HC_{hw}^{tot}) considering the daily hot water demand V_{hw}^{tot} for both EMS implementations is given in the equation below. Noting that SC_{BESS} is zero for the DLEMS implementation, that is, by using DL as the primary power management solution.

$$HC_{hw}^{tot} = \begin{cases} HC_{hw}^{e} \cdot 365.25 \\ HC_{hw}^{g} \cdot 365.25 \end{cases} \quad (6.45)$$

Upon examining the cost benefit analysis results given in Table 6.5, one can deduce that the cost of using BEMS to cover the total hot water demand per calendar year is much higher than the cost of using DLEMS for the same purpose.

Table 6.5: Cost benefit analysis for yearly total hot water demand for all bus systems

Case	Using DL			Using Li-ion			Using Ni-Cd		
Test System	33	69	118	33	69	118	33	69	118
P_{DL} **(MW)**	0.3219	0.6416	0.8835	0.3219	0.6416	0.8835	0.3219	0.6416	0.8835
P_{hw}^{ele} **(MW)**	4.6784	5.3584	8.6165	-	-	-	-	-	-
HC_{hw}^{e} **(£/day)**	2085.33	2444.75	3900.74	-	-	-	-	-	-
P_{hw}^{gas} **(MW)**	-	-	-	6.1875	7.4251	11.7563	7.4251	7.4251	11.7563
HC_{hw}^{g} **(£/day)**	-	-	-	3483.47	5216.04	7721.66	3547.8	5344.27	7898.23
SC_{BESS} **(£/day)**	-	-	-	1305.96	2603	3584.4	1370.3	2731.23	3760.97
V_{hw}^{tot} **(m³/day)**	680.88	817.06	1293.67	680.88	817.06	1293.67	680.88	817.06	1293.67
HC_{hw}^{tot} **(£/year)**	761,665.03	892,944.35	1,424,746.27	1,272,336.87	1,905,156.93	2,820,334.25	1,295,834.61	1,951,994.76	2,884,830.04
Saving Method	-			Using DL instead of Li-ion			Using DL instead of Ni-Cd		
Net Savings (£/year)	-			510,671.84	1,012,212.58	1,395,588.04	534,169.58	1,059,050.41	1,460,083.77

All cost values are given assuming exchange rate: $ = 0.77£ and € = 0.83£.

According to Table 6.5, by using the Li-ion based BEMS, an estimated yearly cost of hot water demand was at £1,272,336.87, £1,905,156.93, and £2,820,334.25 for the IEEE 33-, 69-, and 118-bus systems, respectively. Similarly, using the Ni-Cd based BEMS, the total cost for covering the system demand of hot water was £1,295,834.61, £1,951,994.76, and £2,884,830.04 for the IEEE 33-, 69-, and 118-bus systems, respectively. Contrariwise, the total costs associated with DLEMS for heating the yearly hot water demand was estimated at £761,665.03, £892,944.35, and £1,424,746.27 for the IEEE 33-, 69-, and 118-bus systems, respectively. This significant difference in total costs of the two EMS, can be attributed to two main reasons: storage costs and gas boiler costs. This was evident form the amount of power required by gas boilers to heat the same amount of water produced by the more efficient electric boilers, regardless of the source of electricity. As it was, for gas boilers, 6.1875 MW, 7.4251 MW, and 11.7563 MW for the IEEE 33-, 69-, and 118-bus systems, respectively. This is compared to just 5 MW, 6 MW, and 9.5 MW by relying on electric boilers for the IEEE 33-, 69-, and 118-bus systems, respectively.

Moreover, the current LCOE for BESS is still significant, as it accounts for many cost factors involving the installation, end-of-life, and replacement of batteries [6]. Lastly, it is true that BESS costs are dropping down, but there are still many factors that are not yet evaluated to estimate the true costs for medium- and long-term storage [6]. Furthermore, the assumption here follows the current trend where renewable penetration rates are growing for DCIMG, and that shall lead to significant amounts of excess power that BESS are not cost-effective to handle. Moreover, relaying on such implementation as the main EMS will lead to more investment losses as shown by this CBA. On the other hand, adopting DLEMS in the realistic 69-bus system, as an example, will account to an estimated enormous savings of £1,012,212.58 and £1,059,050.41 for not using the Li-ion and Ni-Cd systems, respectively. Similarly, having the DLEMS utilized for the 118-bus system, a larger sized and practical system, will account to staggering savings of £1,395,588.04 and £1,460,083.77 for not using the Li-ion and Ni-Cd systems, respectively. Moreover, with more renewable energy production on the rise, the cost for running electric boilers is expected to drop drastically. This will make the investment into such venture a more viable and cost-effective solution.

6.6 Summary

In this chapter, the stochastic MINLP for DL allocation considering uncertainty in wind power and load forecast during off-peak hours is presented as DLEMS. A novel methodology was developed using the fine-grained parallelization strategy in MIDACO algorithm combined with GBFS as a robust and efficient load flow method. The methodology was applied to three benchmark testbeds, viz., the IEEE 33-, 69-, and 118-bus systems as a many-objective

problem. This was done to find the expected TMC, MVE, $|\Delta f|$, and TEL considering uncertainty in generation and demand within scenario-based stochastic framework. Further distinction was given to dispatchable and non-dispatchable DGs within the islanded microgrid as V-f and PQ controlled units, respectively. An RWM was utilized to generate 10000 generation/demand mismatch scenarios. Inversely, an elimination criterion based on higher probabilities was used for scenario reduction and aggregation into 20 scenarios. Each of the reduced scenarios was tackled as a deterministic optimization problem. The speed and accuracy advantage of the proposed optimization technique was validated against competitive metaheuristics. Moreover, a detailed cost benefit analysis was provided to highlight the significance and cost-effectiveness of DLEMS against two BEMS relying on Li-ion and Ni-Ca batteries. The results of the cost benefit analysis have demonstrated the advantage of DL as a heating and pumping solution during off-peak hours where the renewable generation is expected to create significant power mismatch. Lastly, the superior performance of MIDACO shall facilitate the real-time implementation of the DLEMS considering uncertainties in DCIMG operation and faster optimization cycles of less than 15 mins.

7 Chapter Seven: Conclusions and Future Work

7.1 Conclusions

In this thesis, a power management solution to the expected large power mismatch problem during off-peak hours of operation in highly penetrated DCIMG was presented as a DL allocation problem.

The motivation and background to the research work undertaken are provided in **chapter 1**. The problem of large power mismatch is expected to intensify with higher share of renewable generation as well as errors in the forecasted demand data.

To that end, a thorough and comprehensive literature survey of the most significant aspects that surround the optimal allocation and operation of DCIMG was briefly presented in **chapter 2**. The main highlights of this chapter were as follows:

- The aforementioned literature survey is published and available in the open literature as in [5].
- The three main identified lacunas were as dump load allocation in DCIMG; load flow analysis in DCIMG; wind power and demand uncertainty in DCIMG.
- The benefits of research in such lacunas are the larger scale expansion of DCIMG, maximized renewable energy potential, rural electrification projects of isolated communities, and reduced electricity carbon footprint.

In **chapter 3**, an elucidation and mathematical background for the proposed optimization method, MIDACO, was given in an immaculate form. The main highlights of this chapter are as follows:

- MIDACO is internally hybridized with a pseudo-gradient backtracking line-search technology for very fast local convergence.
- The multi-criteria decision approach within MIDACO, the utopia-nadir-balance technique, expedites the multi-objective convergence.
- The advanced fine-grained parallelization strategy offered by MIDACO, makes it one of the fastest and most competitive state-of-the-art solvers for many-objective MINLPs.

As for **chapter 4**, the problem of load flow analysis in IMGs had been carefully analysed and addressed. The main highlights of this chapter are given below:

- The first proposed LF method, SBFS, is based on global voltage variable distributed among all DGs with two loops for convergence, namely, BFS internal loop and external V-f update loop.
- The second proposed LF method, SBFS-II, was developed as the improved SBFS by eliminating the internal BFS loop of SBFS while adopting a stricter tolerance criterion for convergence. The proposed SBFS-II method offers better and faster convergence response than SBFS.
- The third proposed LF method, GBFS, is based on local voltage measurement at each generating bus with two additional dynamic damping factors, ζ_1 and ζ_2. Moreover, the introduction of the reactive power correction vector (γ_i) by GBFS to limit the reactive power update by DGs within their min-max limits. Two droop control responses of DGs were implemented in GBFS, inductive and complex.
- The robustness of the three LF methods were validated on the IEEE 33-, 69- and 118-bus systems. Results have shown faster calculation times and better convergence response for SBFS-II over SBFS. Inversely, GBFS has demonstrated higher accuracy over SBFS and SBFS-II with an acceptable convergence and calculation speed.
- The significance of ζ_1 and ζ_2 to enhance load flow convergence was demonstrated on a realistic 6-bus system. This was done via convergence tests by the variations of line impedance and reactive droops to raise the challenge for load flow solution.

In **chapter 5**, the deterministic problem of DL allocation in highly penetrated DCIMG during off-peak hours was addressed. The main highlights of this chapter are as follows:

- A novel methodology using MIDACO as a first-time application in MGs combined with three newly developed load flow methods.
- The DL allocation was investigated on the IEEE 33-, 69-, and 118-bus systems considering four highly probable and deterministic generation/loading scenarios.
- The deterministic DL allocation problem was formulated to minimise V-f, active and reactive power losses. This was done to find the optimal size and location of the DL as well as the optimal droop sets for the optimal DG dispatch.
- The influence of MIDACO's different parameters on the exploration and exploitation capabilities of the algorithm had been carefully analysed.
- Adopting different load models demonstrated the advantage of DL allocation against the base case (i.e., no DL allocation). This has resulted in eliminating the effect of V-f deviations on load behaviour which led to better voltage profile and steady state frequency for all three test systems.
- Changing the load flow method within MIDACO from SBFS to either SBFS-II or GBFS has brought faster and more accurate results, respectively. The advancements of

using the different load flow methods with MIDACO are given in Figure 7.1 and Figure 7.2 for objective function value and calculation times, respectively.

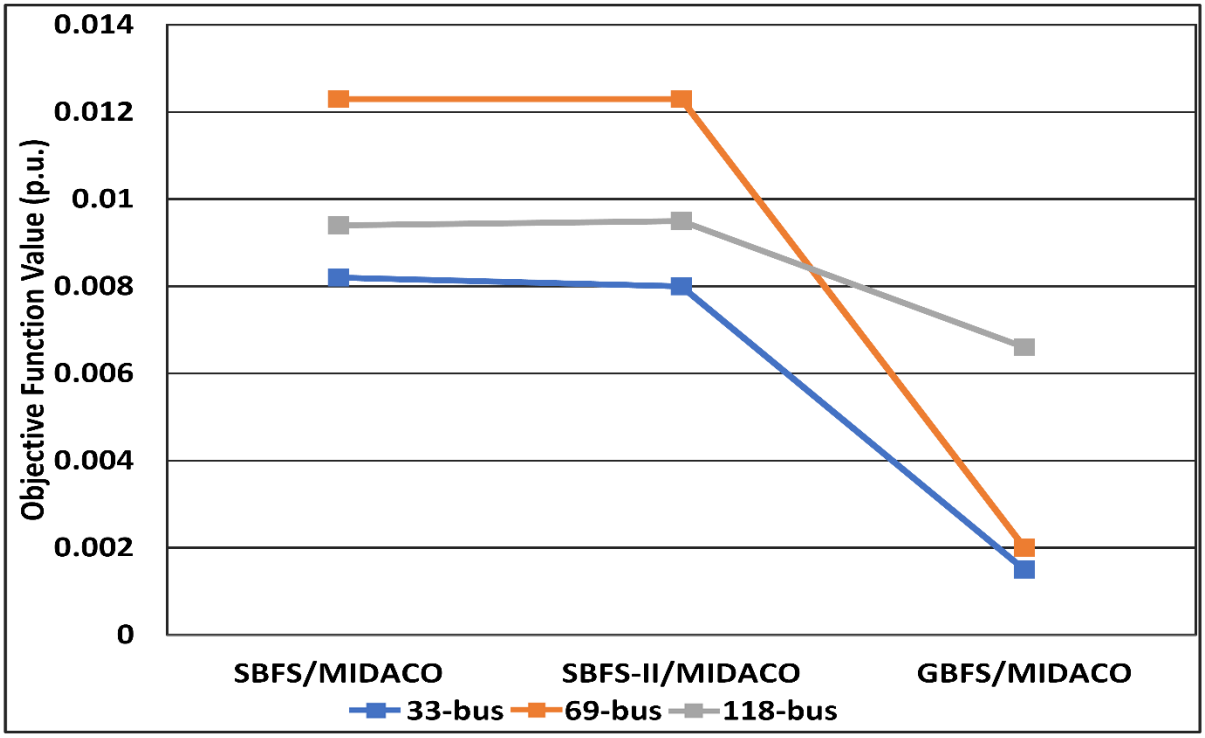

Figure 7.1: Advancement in $|\Delta V_1|$ objective function value by using GBFS with MIDACO for the 33-, 69-, and 118-bus systems.

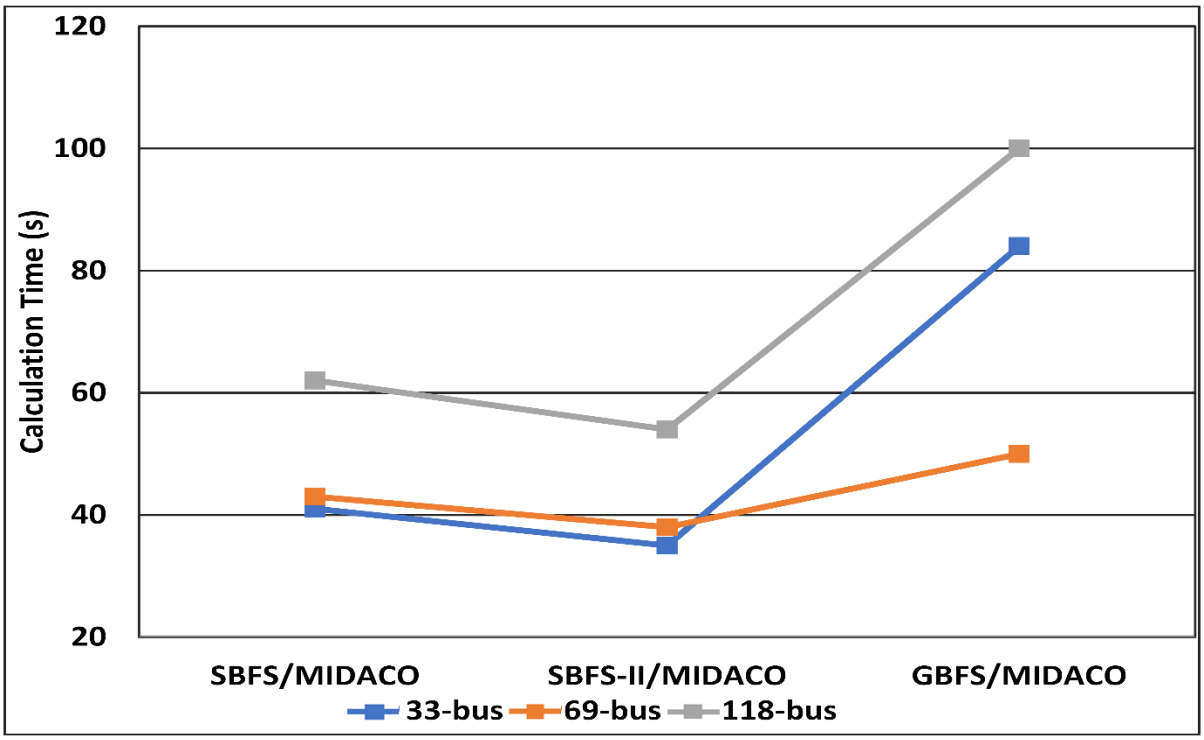

Figure 7.2: Advancements in calculation times by using SBFS-II with MIDACO for the 33-, 69-, 118-bus systems.

- The superior speed and accuracy advantage of the proposed optimization method, MIDACO, was compared and validated against other competitive metaheuristic algorithms, viz., MOGA, NSGA-II, and MOPSO.

The uncertainty surrounding demand and generation for the DL allocation problem to regulate V-f regulation in highly penetrated DCIMG was investigated in **chapter 6** as a stochastic optimization problem. The main highlights were as follows:

- A scenario-based stochastic modelling of uncertainty was used to model load forecast errors and wind generation as random variables. A roulette wheel mechanism was utilized to generate 10000 scenarios of generation/demand variations.
- The stochastic DL allocation problem was formulated as a many-objective problem to account for TMC, MVE, $|\Delta f|$, and TEL. This was achieved by using the state-of-the-art metaheuristic technique, MIDACO, combined with the robust and efficient load flow method GBFS.
- The efficacy of the proposed method was compared with different evolutionary and swarm intelligence techniques, viz., MOGA, NSGA-II, and MOPSO. Accordingly, the obtained results by the proposed method showed better accuracy and significant speed in the calculation times.
- The advantage of the fine-grained parallelization strategy offered by MIDACO was utilized for first time in microgrids. This has resulted in reducing the calculation times for the stochastic MINLP from several hours to a matter of few minutes. This shall enable real-time application for optimization cycles with less than 15 minutes.
- A detailed CBA was given to compare the advantage of covering the hot water demand of a typical MG using DLEMS against using BEMS. Results have shown promising savings via adopting the proposed method, i.e., DLEMS, as a viable EMS.

In the end, with higher demand for renewable energy integration and autonomous MG operation, it is expected that energy management challenge in current and future IMGs persist and prove difficult. Nonetheless, the methodology of optimal DL allocation in DCIMG, as presented herein, offers a legitimate cost-effective and efficient solution to the expected power management problem during off-peak hours in highly penetrated and isolated MGs.

7.2 Future Work

In consonance with the results and discussions reported by this thesis as well as the different research topics covered by the many articles surveyed; it is therefore concluded that the direction of future research should pursue and uncover the identified lacunas in this thesis. Furthermore, if DCIMG studies were to incorporate the identified gaps in this chapter, more

practical and larger scale future DCIMGs would be possible. These future recommendations include but not limited to:

1. Coordination issues in DR programs and EV charging: To drive down fossil fuel emissions and reduce generation costs, smart charging of EVs and friendly DR programs are seen as a viable solution. Nonetheless, many EV and DR studies have often neglected the coordination issues and behavioural challenges associated with these programs as power management solutions. Therefore, any future IMG optimization study must incorporate the uncertainty in DR and EV programs as control variables. This will ensure adequate integration of DR and EV programs as peak hours' power management solution.
2. Uncertainty modelling in IMGs: Most of the uncertainties within DCIMG planning framework are based on historical recorded and pattern observational data for common random variables in demand and generation aspects. This was the case for uncertainty modelling in this thesis. Nevertheless, there are other uncertain factors that interfere with dispatch operations during load cycles that might not be seen by the MGCC. Those unaccounted-for uncertainties may include power transfer capability, loss of generation units, failure in converter systems, loss of cooling equipment, significant load shedding, etc. Such events could lead to the collapse of MGs, increased reliance on fossil fuel generation, and higher costs. Therefore, future DCIMG studies must make use of new uncertainty modelling techniques and allow for a safety margin in the EMS scheduling to mitigate the adverse impact of unaccounted-for uncertainties.
3. Fuel Mix and Generation Allocation: Balancing the generation portfolio in DCIMGs is very important to maximize competitiveness of IMGs with greener and sustainable operation. As a result, future IMG research must consider the different technical, environmental, and economic objectives needed for autonomous operation. Simultaneously, weighing these objectives in selecting the optimal fuel mix, renewable technology, and DG type in any allocation study. Thereby, the presented optimization problem herein, could be expanded by considering different types of DG units aside from NGT and WT.
4. Control and Protection of IMGs: Most of the reported EMS and control strategies in [5] did lack the cost factor for all the extra equipment and communication infrastructure needed to fulfil those strategies. Moreover, many of those control schemes were only applicable to small scale MGs of few nodes making them unpractical. On the other hand, the protection aspect of DCIMGs was seldomly mentioned in the investigated studies. Therefore, future DCIMG optimization studies must consider different protection factors such as X/R ratio impact, fault levels, and short circuit calculations. This is of particular importance to future ESS and DG allocation studies. Moreover, to incorporate the complete costs for control systems particularly those for isolated and remote MGs.

5. Efficiency of BESS and the environmental aspect: Most IMG studies fail to account for environmental degradation and efficiency issues of BESSs operation and allocation. Thus, a thorough analysis for BESSs decommissioning costs and environmental degradation is necessary to analyse the associated costs with ESSs decommissioning. This is of great importance to drive down BESS costs in remote and isolated DCIMG. Similarly, to promote for BESSs role as an auxiliary power management solution. Thus, incorporating BESS as an auxiliary power management solution is an interesting direction for future research.
6. Comprehensive load flow analysis in IMGs: The proposed load flow methods herein are very efficient and robust to handle various loading and droop setting for IMGs. Nonetheless, their application is limited to pure radial distribution networks and systems with balanced loads. Therefore, future IMG load flow analysis methods must incorporate meshed network topologies as well as the transformation for unbalanced distribution systems. Additionally, a future load flow technique for IMGs must incorporate and maintain power exchange operation between adjacent and clustered IMGs.
7. Application of DL during low demand hours: The work presented in this thesis aimed at highlighting the benefit of DL utilization in DCIMG as a primary power management solution. Hence, the focus of future DL studies should be on heating and pumping applications to absorb surplus generation with bigger emphasis on costs, DL design, and uncertainty in demand and renewable generation. Moreover, a comprehensive and real-time EMS implementation is much more needed to manage power mismatch during peak and off-peak hours concurrently. Thus, accommodating different renewable energy options such as solar, wind, and hydro technologies as well as different storage facilities. To expand the coverage of the DL allocation problem presented herein, multiple DLs could be considered at different locations in future studies. This is recommended to enhance the regulation and feasibility aspects for the DL application in future DCIMGs.
8. Practical optimization problem formulation: Many acclaimed metaheuristics often suffer from slow convergence time making them less reliable for practical and real-time implementation of stochastic optimization problems with high uncertainty. Moreover, having state-of-the-art decision-making criteria and efficient parallelization strategy embedded within future optimization techniques is very important for the non-dominated solution accuracy and speed, respectively. Therefore, future optimization studies should expand the application of the proposed metaheuristic technique herein to account for other aspects and issues in DCIMG operation and allocation.

Reference List

[1] H. Fontenot and B. Dong, “Modeling and control of building-integrated microgrids for optimal energy management – A review,” *Applied Energy*, vol. 254, p. 113689, Nov. 2019, doi: 10.1016/j.apenergy.2019.113689.

[2] K. P. Kumar and B. Saravanan, “Recent techniques to model uncertainties in power generation from renewable energy sources and loads in microgrids – A review,” *Renewable and Sustainable Energy Reviews*, vol. 71, pp. 348–358, May 2017, doi: 10.1016/j.rser.2016.12.063.

[3] M. A. Hannan, S. Y. Tan, A. Q. Al-Shetwi, K. P. Jern, and R. A. Begum, “Optimized controller for renewable energy sources integration into microgrid: Functions, constraints and suggestions,” *Journal of Cleaner Production*, vol. 256, p. 120419, May 2020, doi: 10.1016/j.jclepro.2020.120419.

[4] “IEEE Guide for Design, Operation, and Integration of Distributed Resource Island Systems with Electric Power Systems,” *IEEE Std 1547.4-2011*, pp. 1–54, Jul. 2011, doi: 10.1109/IEEESTD.2011.5960751.

[5] M. Z. Kreishan and A. F. Zobaa, “Optimal Allocation and Operation of Droop-Controlled Islanded Microgrids: A Review,” *Energies*, vol. 14, no. 15, Art. no. 15, Jan. 2021, doi: 10.3390/en14154653.

[6] M. H. Mostafa, S. H. E. Abdel Aleem, S. G. Ali, Z. M. Ali, and A. Y. Abdelaziz, “Techno-economic assessment of energy storage systems using annualized life cycle cost of storage (LCCOS) and levelized cost of energy (LCOE) metrics,” *Journal of Energy Storage*, vol. 29, p. 101345, Jun. 2020, doi: 10.1016/j.est.2020.101345.

[7] V. S. Tabar and V. Abbasi, “Energy management in microgrid with considering high penetration of renewable resources and surplus power generation problem,” *Energy*, vol. 189, p. 116264, Dec. 2019, doi: 10.1016/j.energy.2019.116264.

[8] “IEEE Standard for Interconnection and Interoperability of Distributed Energy Resources with Associated Electric Power Systems Interfaces,” *IEEE Std 1547-2018 (Revision of IEEE Std 1547-2003)*, pp. 1–138, Apr. 2018, doi: 10.1109/IEEESTD.2018.8332112.

[9] J. M. Guerrero, J. C. Vasquez, J. Matas, L. G. de Vicuna, and M. Castilla, “Hierarchical Control of Droop-Controlled AC and DC Microgrids—A General Approach Toward Standardization,” *IEEE Transactions on Industrial Electronics*, vol. 58, no. 1, pp. 158–172, Jan. 2011, doi: 10.1109/TIE.2010.2066534.

[10] N. Pogaku, M. Prodanovic, and T. C. Green, “Modeling, Analysis and Testing of Autonomous Operation of an Inverter-Based Microgrid,” *IEEE Transactions on Power Electronics*, vol. 22, no. 2, pp. 613–625, Mar. 2007, doi: 10.1109/TPEL.2006.890003.

[11] A. Engler and N. Soultanis, “Droop control in LV-grids,” in *Proc. ICFPS*, Amsterdam, Netherlands, 2005, p. 6 pp. – 6. doi: 10.1109/FPS.2005.204224.

[12] E. B. Ssekulima, M. B. Anwar, A. A. Hinai, and M. S. E. Moursi, “Wind speed and solar irradiance forecasting techniques for enhanced renewable energy integration with the grid: a review,” *IET Renewable Power Generation*, vol. 10, no. 7, pp. 885–989, 2016, doi: 10.1049/iet-rpg.2015.0477.

[13] S. Chen, T. Zhang, H. B. Gooi, R. D. Masiello, and W. Katzenstein, “Penetration Rate and Effectiveness Studies of Aggregated BESS for Frequency Regulation,” *IEEE Transactions on Smart Grid*, vol. 7, no. 1, pp. 167–177, Jan. 2016, doi: 10.1109/TSG.2015.2426017.

[14] Y.-J. Kim, G. Del-Rosario-Calaf, and L. K. Norford, “Analysis and Experimental Implementation of Grid Frequency Regulation Using Behind-the-Meter Batteries Compensating for Fast Load Demand Variations,” *IEEE Transactions on Power Systems*, vol. 32, no. 1, pp. 484–498, Jan. 2017, doi: 10.1109/TPWRS.2016.2561258.

[15] K. S. El-Bidairi, H. D. Nguyen, T. S. Mahmoud, S. D. G. Jayasinghe, and J. M. Guerrero, “Optimal sizing of Battery Energy Storage Systems for dynamic frequency control in an islanded microgrid: A case study of Flinders Island, Australia,” *Energy*, vol. 195, p. 117059, Mar. 2020, doi: 10.1016/j.energy.2020.117059.

[16] M. Elsisi, M. Soliman, M. A. S. Aboelela, and W. Mansour, “Model predictive control of plug-in hybrid electric vehicles for frequency regulation in a smart grid,” *IET Generation, Transmission & Distribution*, vol. 11, no. 16, pp. 3974–3983, Oct. 2017, doi: 10.1049/iet-gtd.2016.2120.

[17] H. Liu, Y. Yang, J. Qi, J. Li, H. Wei, and P. Li, “Frequency droop control with scheduled charging of electric vehicles,” *IET Generation, Transmission & Distribution*, vol. 11, no. 3, pp. 649–656, Feb. 2017, doi: 10.1049/iet-gtd.2016.0554.

[18] S. Singh, S. Jagota, and M. Singh, “Energy management and voltage stabilization in an islanded microgrid through an electric vehicle charging station,” *Sustainable Cities and Society*, vol. 41, pp. 679–694, Aug. 2018, doi: 10.1016/j.scs.2018.05.055.

[19] A. Elrayyah, F. Cingoz, and Y. Sozer, “Smart Loads Management Using Droop-Based Control in Integrated Microgrid Systems,” *IEEE Journal of Emerging and Selected Topics in Power Electronics*, vol. 5, no. 3, pp. 1142–1153, Sep. 2017, doi: 10.1109/JESTPE.2017.2666786.

[20] A. Nisar and M. S. Thomas, “Comprehensive Control for Microgrid Autonomous Operation With Demand Response,” *IEEE Transactions on Smart Grid*, vol. 8, no. 5, pp. 2081–2089, Sep. 2017, doi: 10.1109/TSG.2016.2514483.

[21] M. Faisal, M. A. Hannan, P. J. Ker, A. Hussain, M. B. Mansor, and F. Blaabjerg, “Review of Energy Storage System Technologies in Microgrid Applications: Issues and Challenges,” *IEEE Access*, vol. 6, pp. 35143–35164, May 2018, doi: 10.1109/ACCESS.2018.2841407.

[22] A. M. A. Haidar, K. M. Muttaqi, and D. Sutanto, “Technical challenges for electric power industries due to grid-integrated electric vehicles in low voltage distributions: A review,” *Energy Conversion and Management*, vol. 86, pp. 689–700, Oct. 2014, doi: 10.1016/j.enconman.2014.06.025.

[23] J. A. Laghari, H. Mokhlis, A. H. A. Bakar, and H. Mohammad, “A comprehensive overview of new designs in the hydraulic, electrical equipments and controllers of mini hydro power plants making it cost effective technology,” *Renewable and Sustainable Energy Reviews*, vol. 20, pp. 279–293, Apr. 2013, doi: 10.1016/j.rser.2012.12.002.

[24] B. N. Roodsari, E. P. Nowicki, and P. Freere, “A New Electronic Load Controller for the Self-excited Induction Generator to Decrease Stator Winding Stress,” *Energy Procedia*, vol. 57, pp. 1455–1464, Jan. 2014, doi: 10.1016/j.egypro.2014.10.137.

[25] R. R. Singh, B. A. Kumar, D. Shruthi, R. Panda, and C. T. Raj, “Review and experimental illustrations of electronic load controller used in standalone Micro-Hydro generating plants,” *Engineering Science and Technology, an International Journal*, vol. 21, no. 5, pp. 886–900, Oct. 2018, doi: 10.1016/j.jestch.2018.07.006.

[26] N. Gyawali, B. Paudel, and B. Subedi, “Improved active power sharing strategy for ELC Controlled Synchronous Generators Based Islanded Micro Grid application,” in *Proc. 9th Inter. Conf. on SKIMA*, Kathmandu, Nepal, 2015, pp. 1–5. doi: 10.1109/SKIMA.2015.7400038.

[27] P. Freere, “Electronic load/excitation controller for a self-excited squirrel cage generator micro-hydro scheme,” in *Proc. 5th ICEMD Publ. No. 341*, London, UK, 1991, pp. 266–270.

[28] T. S. Bhatti, A. A. F. Al-Ademi, and N. K. Bansal, “Load-frequency control of isolated wind-diesel-microhydro hybrid power systems (WDMHPS),” *Energy*, vol. 22, no. 5, pp. 461–470, May 1997, doi: 10.1016/S0360-5442(96)00148-X.

[29] A. L. M. Mufaris and J. Baba, “Coordinated Consumer Load Control by Use of Heat Pump Water Heaters for Voltage Rise Mitigation in Future Distribution System,” in *Proc. 7th IEEE AGTC*, New Orleans, LA, USA, 2015, pp. 176–182. doi: 10.1109/GREENTECH.2015.14.

[30] M. H. Nehrir, B. J. Lameres, G. Venkataramanan, V. Gerez, and L. A. Alvarado, “An approach to evaluate the general performance of stand-alone wind/photovoltaic generating systems,” *IEEE Transactions on Energy Conversion*, vol. 15, no. 4, pp. 433–439, Dec. 2000, doi: 10.1109/60.900505.

[31] S. Doolla and T. S. Bhatti, “Load Frequency Control of an Isolated Small-Hydro Power Plant With Reduced Dump Load,” *IEEE Transactions on Power Systems*, vol. 21, no. 4, pp. 1912–1919, Nov. 2006, doi: 10.1109/TPWRS.2006.881157.

[32] H. M. Goodarzi and M. H. Kazemi, “An optimal autonomous microgrid cluster based on distributed generation droop parameter optimization and renewable energy sources

using an improved grey wolf optimizer," *Engineering Optimization*, vol. 50, no. 5, pp. 819–839, May 2018, doi: 10.1080/0305215X.2017.1355970.

[33] Y. Gupta, R. Nellikkath, K. Chatterjee, and S. Doolla, "Volt-var Optimization and Reconfiguration: Reducing Power Demand and Losses in a Droop-Based Microgrid," *IEEE Transactions on Industry Applications*, pp. 1–1, 2021, doi: 10.1109/TIA.2021.3057008.

[34] D. K. Dheer, N. Soni, and S. Doolla, "Improvement of small signal stability margin and transient response in inverter-dominated microgrids," *Sustainable Energy, Grids and Networks*, vol. 5, pp. 135–147, Mar. 2016, doi: 10.1016/j.segan.2015.12.005.

[35] M. Džamarija and A. Keane, "Autonomous Curtailment Control in Distributed Generation Planning," *IEEE Transactions on Smart Grid*, vol. 7, no. 3, pp. 1337–1345, May 2016, doi: 10.1109/TSG.2015.2427378.

[36] Q. Sun, B. Huang, D. Li, D. Ma, and Y. Zhang, "Optimal Placement of Energy Storage Devices in Microgrids via Structure Preserving Energy Function," *IEEE Transactions on Industrial Informatics*, vol. 12, no. 3, pp. 1166–1179, Jun. 2016, doi: 10.1109/TII.2016.2557816.

[37] C. Chen, S. Duan, T. Cai, B. Liu, and G. Hu, "Optimal Allocation and Economic Analysis of Energy Storage System in Microgrids," *IEEE Transactions on Power Electronics*, vol. 26, no. 10, pp. 2762–2773, Oct. 2011, doi: 10.1109/TPEL.2011.2116808.

[38] A. S. A. Awad, T. H. M. EL-Fouly, and M. M. A. Salama, "Optimal ESS Allocation and Load Shedding for Improving Distribution System Reliability," *IEEE Transactions on Smart Grid*, vol. 5, no. 5, pp. 2339–2349, Sep. 2014, doi: 10.1109/TSG.2014.2316197.

[39] M. M. A. Abdelaziz, H. E. Farag, and E. F. El-Saadany, "Optimum Reconfiguration of Droop-Controlled Islanded Microgrids," *IEEE Transactions on Power Systems*, vol. 31, no. 3, pp. 2144–2153, May 2016, doi: 10.1109/TPWRS.2015.2456154.

[40] M. Marzband, N. Parhizi, M. Savaghebi, and J. M. Guerrero, "Distributed Smart Decision-Making for a Multimicrogrid System Based on a Hierarchical Interactive Architecture," *IEEE Transactions on Energy Conversion*, vol. 31, no. 2, pp. 637–648, Jun. 2016, doi: 10.1109/TEC.2015.2505358.

[41] A. Maulik and D. Das, "Optimal Operation of Droop-Controlled Islanded Microgrids," *IEEE Transactions on Sustainable Energy*, vol. 9, no. 3, pp. 1337–1348, Jul. 2018, doi: 10.1109/TSTE.2017.2783356.

[42] J. Jithendranath and D. Das, "Scenario-based multi-objective optimisation with loadability in islanded microgrids considering load and renewable generation uncertainties," *IET Renewable Power Generation*, vol. 13, no. 5, pp. 785–800, Feb. 2019, doi: 10.1049/iet-rpg.2018.5795.

[43] A. Uniyal and S. Sarangi, "Optimal allocation of ELC in microgrid using droop controlled load flow," *Transmission Distribution IET Generation*, vol. 13, no. 20, pp. 4566–4578, Oct. 2019, doi: 10.1049/iet-gtd.2018.5174.

[44] A. Uniyal, S. Sarangi, and M. S. Rawat, “Optimal Dump Load Allocations in High RBDG Penetrated Microgrid for Voltage and Frequency Regulation,” *Arab J Sci Eng*, vol. 46, no. 2, pp. 1511–1528, Feb. 2021, doi: 10.1007/s13369-020-05240-9.

[45] M. Pesaran H.A, P. D. Huy, and V. K. Ramachandaramurthy, “A review of the optimal allocation of distributed generation: Objectives, constraints, methods, and algorithms,” *Renewable and Sustainable Energy Reviews*, vol. 75, pp. 293–312, Aug. 2017, doi: 10.1016/j.rser.2016.10.071.

[46] A. Ahmad Khan, M. Naeem, M. Iqbal, S. Qaisar, and A. Anpalagan, “A compendium of optimization objectives, constraints, tools and algorithms for energy management in microgrids,” *Renewable and Sustainable Energy Reviews*, vol. 58, pp. 1664–1683, May 2016, doi: 10.1016/j.rser.2015.12.259.

[47] M. Schlüter, M. Gerdts, and J.-J. Rückmann, “A numerical study of MIDACO on 100 MINLP benchmarks,” *Optimization*, vol. 61, no. 7, pp. 873–900, Jul. 2012, doi: 10.1080/02331934.2012.668545.

[48] M. Z. Kreishan and A. F. Zobaa, “Allocation of Dump Load in Islanded Microgrid Using the Mixed-Integer Distributed Ant Colony Optimization,” *IEEE Systems Journal*, vol. 16, no. 2, pp. 2568–2579, Jun. 2022, doi: 10.1109/JSYST.2021.3100409.

[49] S. D. Pohekar and M. Ramachandran, “Application of multi-criteria decision making to sustainable energy planning—A review,” *Renewable and Sustainable Energy Reviews*, vol. 8, no. 4, pp. 365–381, Aug. 2004, doi: 10.1016/j.rser.2003.12.007.

[50] P. S. Georgilakis and N. D. Hatziargyriou, “Optimal Distributed Generation Placement in Power Distribution Networks: Models, Methods, and Future Research,” *IEEE Transactions on Power Systems*, vol. 28, no. 3, pp. 3420–3428, Aug. 2013, doi: 10.1109/TPWRS.2012.2237043.

[51] S. Parhizi, H. Lotfi, A. Khodaei, and S. Bahramirad, “State of the Art in Research on Microgrids: A Review,” *IEEE Access*, vol. 3, pp. 890–925, Jul. 2015, doi: 10.1109/ACCESS.2015.2443119.

[52] C. Gamarra and J. M. Guerrero, “Computational optimization techniques applied to microgrids planning: A review,” *Renewable and Sustainable Energy Reviews*, vol. 48, pp. 413–424, Aug. 2015, doi: 10.1016/j.rser.2015.04.025.

[53] A. R. Jordehi, “Allocation of distributed generation units in electric power systems: A review,” *Renewable and Sustainable Energy Reviews*, vol. 56, pp. 893–905, Apr. 2016, doi: 10.1016/j.rser.2015.11.086.

[54] V. A. Evangelopoulos, P. S. Georgilakis, and N. D. Hatziargyriou, “Optimal operation of smart distribution networks: A review of models, methods and future research,” *Electric Power Systems Research*, vol. 140, pp. 95–106, Nov. 2016, doi: 10.1016/j.epsr.2016.06.035.

[55] O. Badran, S. Mekhilef, H. Mokhlis, and W. Dahalan, “Optimal reconfiguration of distribution system connected with distributed generations: A review of different

methodologies," *Renewable and Sustainable Energy Reviews*, vol. 73, pp. 854–867, Jun. 2017, doi: 10.1016/j.rser.2017.02.010.

[56] B. Singh and J. Sharma, "A review on distributed generation planning," *Renewable and Sustainable Energy Reviews*, vol. 76, pp. 529–544, Sep. 2017, doi: 10.1016/j.rser.2017.03.034.

[57] M. H. Andishgar, E. Gholipour, and R. Hooshmand, "An overview of control approaches of inverter-based microgrids in islanding mode of operation," *Renewable and Sustainable Energy Reviews*, vol. 80, pp. 1043–1060, Dec. 2017, doi: 10.1016/j.rser.2017.05.267.

[58] S. Kakran and S. Chanana, "Smart operations of smart grids integrated with distributed generation: A review," *Renewable and Sustainable Energy Reviews*, vol. 81, pp. 524–535, Jan. 2018, doi: 10.1016/j.rser.2017.07.045.

[59] S. M. Dawoud, X. Lin, and M. I. Okba, "Hybrid renewable microgrid optimization techniques: A review," *Renewable and Sustainable Energy Reviews*, vol. 82, pp. 2039–2052, Feb. 2018, doi: 10.1016/j.rser.2017.08.007.

[60] Y. Liu, S. Yu, Y. Zhu, D. Wang, and J. Liu, "Modeling, planning, application and management of energy systems for isolated areas: A review," *Renewable and Sustainable Energy Reviews*, vol. 82, pp. 460–470, Feb. 2018, doi: 10.1016/j.rser.2017.09.063.

[61] M. F. Zia, E. Elbouchikhi, and M. Benbouzid, "Microgrids energy management systems: A critical review on methods, solutions, and prospects," *Applied Energy*, vol. 222, pp. 1033–1055, Jul. 2018, doi: 10.1016/j.apenergy.2018.04.103.

[62] L. A. Wong, V. K. Ramachandaramurthy, P. Taylor, J. B. Ekanayake, S. L. Walker, and S. Padmanaban, "Review on the optimal placement, sizing and control of an energy storage system in the distribution network," *Journal of Energy Storage*, vol. 21, pp. 489–504, Feb. 2019, doi: 10.1016/j.est.2018.12.015.

[63] M. Pourbehzadi, T. Niknam, J. Aghaei, G. Mokryani, M. Shafie-khah, and J. P. S. Catalão, "Optimal operation of hybrid AC/DC microgrids under uncertainty of renewable energy resources: A comprehensive review," *International Journal of Electrical Power & Energy Systems*, vol. 109, pp. 139–159, Jul. 2019, doi: 10.1016/j.ijepes.2019.01.025.

[64] A. Cagnano, E. De Tuglie, and P. Mancarella, "Microgrids: Overview and guidelines for practical implementations and operation," *Applied Energy*, vol. 258, p. 114039, Jan. 2020, doi: 10.1016/j.apenergy.2019.114039.

[65] A. A. Anderson and S. Suryanarayanan, "Review of energy management and planning of islanded microgrids," *CSEE Journal of Power and Energy Systems*, vol. 6, no. 2, pp. 329–343, Jun. 2020, doi: 10.17775/CSEEJPES.2019.01080.

[66] O. Saad and C. Abdeljebbar, "Historical Literature Review of Optimal Placement of Electrical Devices in Power Systems: Critical Analysis of Renewable Distributed

Generation Efforts," *IEEE Systems Journal*, pp. 1–12, Sep. 2020, doi: 10.1109/JSYST.2020.3023076.

[67] M. A. Hannan, M. Faisal, P. Jern Ker, R. A. Begum, Z. Y. Dong, and C. Zhang, "Review of optimal methods and algorithms for sizing energy storage systems to achieve decarbonization in microgrid applications," *Renewable and Sustainable Energy Reviews*, vol. 131, p. 110022, Oct. 2020, doi: 10.1016/j.rser.2020.110022.

[68] M. A. Jirdehi, V. S. Tabar, S. Ghassemzadeh, and S. Tohidi, "Different aspects of microgrid management: A comprehensive review," *Journal of Energy Storage*, vol. 30, p. 101457, Aug. 2020, doi: 10.1016/j.est.2020.101457.

[69] "IEEE Guide for Conducting Distribution Impact Studies for Distributed Resource Interconnection," *IEEE Std 1547.7-2013*, pp. 1–137, Feb. 2014, doi: 10.1109/IEEESTD.2014.6748837.

[70] S. R. Sinsel, R. L. Riemke, and V. H. Hoffmann, "Challenges and solution technologies for the integration of variable renewable energy sources—a review," *Renewable Energy*, vol. 145, pp. 2271–2285, Jan. 2020, doi: 10.1016/j.renene.2019.06.147.

[71] K. Tantrapon, P. Jirapong, and P. Thararak, "Optimal Operation of Battery Energy Storage System for Mitigating Voltage Fluctuation in Microgrid Using Cuckoo Search Optimization," in *Proc. 16th ECTI-CON*, Pattaya, Thailand, 2019, pp. 877–880. doi: 10.1109/ECTI-CON47248.2019.8955195.

[72] R. Rana, M. Singh, and S. Mishra, "Design of Modified Droop Controller for Frequency Support in Microgrid Using Fleet of Electric Vehicles," *IEEE Transactions on Power Systems*, vol. 32, no. 5, pp. 3627–3636, Sep. 2017, doi: 10.1109/TPWRS.2017.2651906.

[73] P. Li, W. Hu, X. Xu, Q. Huang, Z. Liu, and Z. Chen, "A frequency control strategy of electric vehicles in microgrid using virtual synchronous generator control," *Energy*, vol. 189, p. 116389, Dec. 2019, doi: 10.1016/j.energy.2019.116389.

[74] X. Zhu, M. Xia, and H.-D. Chiang, "Coordinated sectional droop charging control for EV aggregator enhancing frequency stability of microgrid with high penetration of renewable energy sources," *Applied Energy*, vol. 210, pp. 936–943, Jan. 2018, doi: 10.1016/j.apenergy.2017.07.087.

[75] M. C. Falvo, G. Graditi, and P. Siano, "Electric Vehicles integration in demand response programs," in *Proc. SPEEDAM*, Ischia, Italy, 2014, pp. 548–553. doi: 10.1109/SPEEDAM.2014.6872126.

[76] C. P. Ion and C. Marinescu, "Autonomous micro hydro power plant with induction generator," *Renewable Energy*, vol. 36, no. 8, pp. 2259–2267, Aug. 2011, doi: 10.1016/j.renene.2011.01.028.

[77] I. Şerban and C. Marinescu, "Aggregate load-frequency control of a wind-hydro autonomous microgrid," *Renewable Energy*, vol. 36, no. 12, pp. 3345–3354, Dec. 2011, doi: 10.1016/j.renene.2011.05.012.

[78] V. Rajagopal, B. Singh, and G. K. Kasal, “Electronic load controller with power quality improvement of isolated induction generator for small hydro power generation,” *IET Renewable Power Generation*, vol. 5, no. 2, pp. 202–213, Mar. 2011, doi: 10.1049/iet-rpg.2010.0081.

[79] P. S. Bhakar, G. K. Rao, and S. Sarangi, “A Novel Adaptive Frequency Control Strategy for Micro Grid,” in *Proc. 14th IEEE INDICON*, Roorkee, India, 2017, pp. 1013–1018. doi: 10.1109/INDICON.2017.8487532.

[80] A. Tomar, D. Sharma, and S. Mishra, “An active power management strategy in a microgrid having static and rotating generators considering generation limits using water pumping loads,” in *Proc. ICCCE*, Jaipur, India, 2017, pp. 484–488. doi: 10.1109/COMPTELIX.2017.8004018.

[81] U. K. Kalla, B. Singh, and S. S. Murthy, “Modified electronic load controller for constant frequency operation with voltage regulation of small hydro driven single-phase SEIG,” in *Proc. IEEE IASAM*, Addison, TX, USA, 2015, pp. 1–8. doi: 10.1109/IAS.2015.7356931.

[82] B. N. Roodsari and E. P. Nowicki, “Analysis and Experimental Investigation of the Improved Distributed Electronic Load Controller,” *IEEE Transactions on Energy Conversion*, vol. 33, no. 3, pp. 905–914, Sep. 2018, doi: 10.1109/TEC.2018.2823334.

[83] B. Nia Roodsari, E. P. Nowicki, and P. Freere, “An experimental investigation of the Distributed Electronic Load Controller: A new concept for voltage regulation in microhydro systems with transfer of excess power to household water heaters,” in *Proc. IEEE Canada IHTC*, Montreal, QC, Canada, 2014, pp. 1–4. doi: 10.1109/IHTC.2014.7147548.

[84] N. L. Hinov, R. H. Stanev, and G. I. Vacheva, “A power electronic smart load controller for nanogrids and autonomous power systems,” in *Proc. 25th ISCE (ET)*, Sozopol, Bulgaria, Sep. 2016, pp. 1–4. doi: 10.1109/ET.2016.7753485.

[85] H. Le Nguyen, “Newton-Raphson method in complex form [power system load flow analysis],” *IEEE Transactions on Power Systems*, vol. 12, no. 3, pp. 1355–1359, Aug. 1997, doi: 10.1109/59.630481.

[86] F. Zhang and C. S. Cheng, “A modified Newton method for radial distribution system power flow analysis,” *IEEE Transactions on Power Systems*, vol. 12, no. 1, pp. 389–397, Feb. 1997, doi: 10.1109/59.575728.

[87] K. A. Birt, J. J. Graffy, J. D. McDonald, and A. H. El-Abiad, “Three phase load flow program,” *IEEE Transactions on Power Apparatus and Systems*, vol. 95, no. 1, pp. 59–65, Jan. 1976, doi: 10.1109/T-PAS.1976.32077.

[88] R. Burch, P. Yang, P. Cox, and K. Mayaram, “A new matrix solution technique for general circuit simulation,” *IEEE Transactions on Computer-Aided Design of Integrated Circuits and Systems*, vol. 12, no. 2, pp. 225–241, Feb. 1993, doi: 10.1109/43.205003.

[89] X.-P. Zhang, “Fast three phase load flow methods,” *IEEE Transactions on Power Systems*, vol. 11, no. 3, pp. 1547–1554, Aug. 1996, doi: 10.1109/59.535696.

[90] D. Shirmohammadi, H. W. Hong, A. Semlyen, and G. X. Luo, “A compensation-based power flow method for weakly meshed distribution and transmission networks,” *IEEE Transactions on Power Systems*, vol. 3, no. 2, pp. 753–762, May 1988, doi: 10.1109/59.192932.

[91] G. X. Luo and A. Semlyen, “Efficient load flow for large weakly meshed networks,” *IEEE Transactions on Power Systems*, vol. 5, no. 4, pp. 1309–1316, Nov. 1990, doi: 10.1109/59.99382.

[92] M. Z. Kamh and R. Iravani, “Unbalanced Model and Power-Flow Analysis of Microgrids and Active Distribution Systems,” *IEEE Transactions on Power Delivery*, vol. 25, no. 4, pp. 2851–2858, Oct. 2010, doi: 10.1109/TPWRD.2010.2042825.

[93] A. C. Lisboa, L. S. M. Guedes, D. A. G. Vieira, and R. R. Saldanha, “A fast power flow method for radial networks with linear storage and no matrix inversions,” *International Journal of Electrical Power & Energy Systems*, vol. 63, pp. 901–907, Dec. 2014, doi: 10.1016/j.ijepes.2014.07.002.

[94] C. S. Cheng and D. Shirmohammadi, “A three-phase power flow method for real-time distribution system analysis,” *IEEE Transactions on Power Systems*, vol. 10, no. 2, pp. 671–679, May 1995, doi: 10.1109/59.387902.

[95] M. H. Moradi, V. B. Foroutan, and M. Abedini, “Power flow analysis in islanded Micro-Grids via modeling different operational modes of DGs: A review and a new approach,” *Renewable and Sustainable Energy Reviews*, vol. 69, pp. 248–262, Mar. 2017, doi: 10.1016/j.rser.2016.11.156.

[96] F. Mumtaz, M. H. Syed, M. A. Hosani, and H. H. Zeineldin, “A simple and accurate approach to solve the power flow for balanced islanded microgrids,” in *Proc. IEEE 15th EEEIC*, Rome, Italy, 2015, pp. 1852–1856. doi: 10.1109/EEEIC.2015.7165454.

[97] R. A. Jabr, I. Džafić, and B. C. Pal, “Compensation in Complex Variables for Microgrid Power Flow,” *IEEE Transactions on Power Systems*, vol. 33, no. 3, pp. 3207–3209, May 2018, doi: 10.1109/TPWRS.2018.2816809.

[98] M. E. Nassar and M. M. A. Salama, “A novel branch-based power flow algorithm for islanded AC microgrids,” *Electric Power Systems Research*, vol. 146, pp. 51–62, May 2017, doi: 10.1016/j.epsr.2017.01.019.

[99] Y. Vilaisarn and M. Abdelaziz, “An inversion-free sparse Zbus power flow algorithm for large-scale droop controlled islanded microgrids,” *International Journal of Electrical Power & Energy Systems*, vol. 121, p. 106048, Oct. 2020, doi: 10.1016/j.ijepes.2020.106048.

[100] A. Esmaeli, M. Abedini, and M. H. Moradi, “A novel power flow analysis in an islanded renewable microgrid,” *Renewable Energy*, vol. 96, pp. 914–927, Oct. 2016, doi: 10.1016/j.renene.2016.04.077.

[101] M. Abedini, “A novel algorithm for load flow analysis in island microgrids using an improved evolutionary algorithm,” *International Transactions on Electrical Energy Systems*, vol. 26, no. 12, pp. 2727–2743, 2016, doi: 10.1002/etep.2231.

[102] M. M. A. Abdelaziz, H. E. Farag, E. F. El-Saadany, and Y. A. I. Mohamed, “A Novel and Generalized Three-Phase Power Flow Algorithm for Islanded Microgrids Using a Newton Trust Region Method,” *IEEE Transactions on Power Systems*, vol. 28, no. 1, pp. 190–201, Feb. 2013, doi: 10.1109/TPWRS.2012.2195785.

[103] F. Mumtaz, M. H. Syed, M. A. Hosani, and H. H. Zeineldin, “A Novel Approach to Solve Power Flow for Islanded Microgrids Using Modified Newton Raphson With Droop Control of DG,” *IEEE Transactions on Sustainable Energy*, vol. 7, no. 2, pp. 493–503, Apr. 2016, doi: 10.1109/TSTE.2015.2502482.

[104] A. Dukpa, B. Venkatesh, and M. El-Hawary, “Application of continuation power flow method in radial distribution systems,” *Electric Power Systems Research*, vol. 79, no. 11, pp. 1503–1510, Nov. 2009, doi: 10.1016/j.epsr.2009.05.003.

[105] U. Eminoglu and M. H. Hocaoglu, “Distribution Systems Forward/Backward Sweep-based Power Flow Algorithms: A Review and Comparison Study,” *Electric Power Components and Systems*, vol. 37, no. 1, pp. 91–110, Dec. 2008, doi: 10.1080/15325000802322046.

[106] Jen-Hao Teng, “A direct approach for distribution system load flow solutions,” *IEEE Transactions on Power Delivery*, vol. 18, no. 3, pp. 882–887, Jul. 2003, doi: 10.1109/TPWRD.2003.813818.

[107] G. Díaz, J. Gómez-Aleixandre, and J. Coto, “Direct Backward/Forward Sweep Algorithm for Solving Load Power Flows in AC Droop-Regulated Microgrids,” *IEEE Transactions on Smart Grid*, vol. 7, no. 5, pp. 2208–2217, Sep. 2016, doi: 10.1109/TSG.2015.2478278.

[108] F. Hameed, M. Al Hosani, and H. H. Zeineldin, “A Modified Backward/Forward Sweep Load Flow Method for Islanded Radial Microgrids,” *IEEE Transactions on Smart Grid*, vol. 10, no. 1, pp. 910–918, Jan. 2019, doi: 10.1109/TSG.2017.2754551.

[109] A. Kumar, B. K. Jha, D. K. Dheer, D. Singh, and R. K. Misra, “Nested backward/forward sweep algorithm for power flow analysis of droop regulated islanded microgrids,” *Transmission Distribution IET Generation*, vol. 13, no. 14, pp. 3086–3095, Jul. 2019, doi: 10.1049/iet-gtd.2019.0388.

[110] A. Elrayyah, Y. Sozer, and M. E. Elbuluk, “A Novel Load-Flow Analysis for Stable and Optimized Microgrid Operation,” *IEEE Transactions on Power Delivery*, vol. 29, no. 4, pp. 1709–1717, Aug. 2014, doi: 10.1109/TPWRD.2014.2307279.

[111] D. Liu, C. Zhang, and Z. Dong, “Stochastic Optimal Power Flow for Islanded Microgrids Considering Droop Control,” in *Proc. IEEE ISGT Asia*, Chengdu, China, 2019, pp. 3156–3161. doi: 10.1109/ISGT-Asia.2019.8881100.

[112] M. Dorigo, G. D. Caro, and L. M. Gambardella, “Ant Algorithms for Discrete Optimization,” *Artificial Life*, vol. 5, no. 2, pp. 137–172, Apr. 1999, doi: 10.1162/106454699568728.

[113] K. Socha and M. Dorigo, “Ant colony optimization for continuous domains,” *European Journal of Operational Research*, vol. 185, no. 3, pp. 1155–1173, Mar. 2008, doi: 10.1016/j.ejor.2006.06.046.

[114] M. Lopez-Ibanez and T. Stutzle, “The Automatic Design of Multiobjective Ant Colony Optimization Algorithms,” *IEEE Transactions on Evolutionary Computation*, vol. 16, no. 6, pp. 861–875, Dec. 2012, doi: 10.1109/TEVC.2011.2182651.

[115] M. Schlüter, J. A. Egea, and J. R. Banga, “Extended ant colony optimization for non-convex mixed integer nonlinear programming,” *Computers & Operations Research*, vol. 36, no. 7, pp. 2217–2229, Jul. 2009, doi: 10.1016/j.cor.2008.08.015.

[116] M. Schlüter and M. Gerdts, “The oracle penalty method,” *J Glob Optim*, vol. 47, no. 2, pp. 293–325, Jun. 2010, doi: 10.1007/s10898-009-9477-0.

[117] M. Schlueter, C. H. Yam, T. Watanabe, and A. Oyama, “Parallelization impact on many-objective optimization for space trajectory design,” *International Journal of Machine Learning and Computing*, vol. 6, no. 1, pp. 9–14, Feb. 2016, doi: 10.18178/ijmlc.2016.6.1.563.

[118] M. Schlueter, C. H. Yam, T. Watanabe, and A. Oyama, “Many-objective optimization of interplanetary space mission trajectories,” in *Proc. IEEE CEC*, Sendai, Japan, 2015, pp. 3256–3262. doi: 10.1109/CEC.2015.7257297.

[119] S. Goss, S. Aron, J. L. Deneubourg, and J. M. Pasteels, “Self-organized shortcuts in the Argentine ant,” *Naturwissenschaften*, vol. 76, no. 12, pp. 579–581, Dec. 1989, doi: 10.1007/BF00462870.

[120] M. Dorigo, V. Maniezzo, and A. Colorni, “Ant system: optimization by a colony of cooperating agents,” *IEEE Transactions on Systems, Man, and Cybernetics, Part B (Cybernetics)*, vol. 26, no. 1, pp. 29–41, Feb. 1996, doi: 10.1109/3477.484436.

[121] T. Stützle and H. H. Hoos, “MAX–MIN Ant System,” *Future Generation Computer Systems*, vol. 16, no. 8, pp. 889–914, Jun. 2000, doi: 10.1016/S0167-739X(00)00043-1.

[122] M. Dorigo and L. M. Gambardella, “Ant colony system: a cooperative learning approach to the traveling salesman problem,” *IEEE Transactions on Evolutionary Computation*, vol. 1, no. 1, pp. 53–66, Apr. 1997, doi: 10.1109/4235.585892.

[123] K. Socha, “ACO for Continuous and Mixed-Variable Optimization,” in *Proc. Ant Colony Optimization and Swarm Intelligence (ANTS 2004)*, Brussels, Belgium, 2004.

[124] M. Schlueter, “Nonlinear mixed integer based optimization technique for space applications,” PhD Thesis, School of Mathematics, Univ. of Birmingham, Birmingham, UK, 2012. Accessed: May 26, 2020. [Online]. Available: https://etheses.bham.ac.uk/id/eprint/3101/

[125] K. Socha, “ACO for Continuous and Mixed-Variable Optimization,” in *Proc. Ant Colony Optimization and Swarm Intelligence (ANTS 2004)*, Berlin, Heidelberg, 2004, pp. 25–36. doi: 10.1007/978-3-540-28646-2_3.

[126] M. Schlueter and M. Munetomo, “MIDACO solver user manual 6.0,” Hokkaido University, Sapporo, Japan, Technical Report, 2018. [Online]. Available: http://www.midaco-solver.com/data/other/MIDACO_User_Manual.pdf

[127] Ö. Yeniay, “Penalty Function Methods for Constrained Optimization with Genetic Algorithms,” *Mathematical and Computational Applications*, vol. 10, no. 1, Art. no. 1, Apr. 2005, doi: 10.3390/mca10010045.

[128] C. A. Coello Coello, “Theoretical and numerical constraint-handling techniques used with evolutionary algorithms: a survey of the state of the art,” *Computer Methods in Applied Mechanics and Engineering*, vol. 191, no. 11, pp. 1245–1287, Jan. 2002, doi: 10.1016/S0045-7825(01)00323-1.

[129] M. Schlüter, J. A. Egea, L. T. Antelo, A. A. Alonso, and J. R. Banga, “An Extended Ant Colony Optimization Algorithm for Integrated Process and Control System Design,” *Ind. Eng. Chem. Res.*, vol. 48, no. 14, pp. 6723–6738, Jul. 2009, doi: 10.1021/ie8016785.

[130] O. Exler and K. Schittkowski, “A trust region SQP algorithm for mixed-integer nonlinear programming,” *Optimization Letters*, vol. 1, no. 3, pp. 269–280, Jun. 2007, doi: 10.1007/s11590-006-0026-1.

[131] M. Schlueter and M. Munetomo, “Parallelization strategies for evolutionary algorithms for MINLP,” in *Proc. IEEE CEC*, Cancun, Mexico, 2013, pp. 635–641. doi: 10.1109/CEC.2013.6557628.

[132] M. Schlueter, “MIDACO software performance on interplanetary trajectory benchmarks,” *Advances in Space Research*, vol. 54, no. 4, pp. 744–754, Aug. 2014, doi: 10.1016/j.asr.2014.05.002.

[133] “Load representation for dynamic performance analysis (of power systems),” *IEEE Transactions on Power Systems*, vol. 8, no. 2, pp. 472–482, May 1993, doi: 10.1109/59.260837.

[134] Y. Li, H.-D. Chiang, B.-K. Choi, Y.-T. Chen, D.-H. Huang, and M. G. Lauby, “Load models for modeling dynamic behaviors of reactive loads: Evaluation and comparison,” *International Journal of Electrical Power & Energy Systems*, vol. 30, no. 9, pp. 497–503, Nov. 2008, doi: 10.1016/j.ijepes.2008.04.007.

[135] P. J. Lagace, M. H. Vuong, and I. Kamwa, “Improving power flow convergence by Newton Raphson with a Levenberg-Marquardt method,” in *Proc. IEEE PESGM - CDEE 21st Century*, Jul. 2008, pp. 1–6. doi: 10.1109/PES.2008.4596138.

[136] J. He and Y. W. Li, “An Enhanced Microgrid Load Demand Sharing Strategy,” *IEEE Transactions on Power Electronics*, vol. 27, no. 9, pp. 3984–3995, Sep. 2012, doi: 10.1109/TPEL.2012.2190099.

[137] Y. Han, H. Li, P. Shen, E. A. A. Coelho, and J. M. Guerrero, “Review of Active and Reactive Power Sharing Strategies in Hierarchical Controlled Microgrids,” *IEEE Transactions on Power Electronics*, vol. 32, no. 3, pp. 2427–2451, Mar. 2017, doi: 10.1109/TPEL.2016.2569597.

[138] Y. Zhu, F. Zhuo, and H. Shi, “Accurate power sharing strategy for complex microgrid based on droop control method,” in *Proc. IEEE ECCE Asia Downunder*, Melbourne, VIC, Australia, 2013, pp. 344–350. doi: 10.1109/ECCE-Asia.2013.6579119.

[139] A. Micallef, M. Apap, C. Spiteri-Staines, and J. M. Guerrero, “Secondary control for reactive power sharing in droop-controlled islanded microgrids,” in *Proc. IEEE International Symposium on Industrial Electronics*, Hangzhou, China, May 2012, pp. 1627–1633. doi: 10.1109/ISIE.2012.6237334.

[140] M. T. Au and J. V. Milanovic, “Development of Stochastic Aggregate Harmonic Load Model Based on Field Measurements,” *IEEE Transactions on Power Delivery*, vol. 22, no. 1, pp. 323–330, Jan. 2007, doi: 10.1109/TPWRD.2006.881455.

[141] M. Mahdavi, H. H. Alhelou, and P. Cuffe, “Test Distribution Systems: Network Parameters and Diagrams of Electrical Structural,” *IEEE Open Access Journal of Power and Energy*, vol. 8, pp. 409–420, 2021, doi: 10.1109/OAJPE.2021.3119183.

[142] Caledonian, “Medium Voltage Cable - BS/IEC/VDE Standard.” https://www.caledonian-cables.co.uk/products/medium-voltage-cable/bs-iec/index.shtml (accessed Jan. 16, 2022).

[143] S. Conti, R. Nicolosi, S. A. Rizzo, and H. H. Zeineldin, “Optimal Dispatching of Distributed Generators and Storage Systems for MV Islanded Microgrids,” *IEEE Transactions on Power Delivery*, vol. 27, no. 3, pp. 1243–1251, Jul. 2012, doi: 10.1109/TPWRD.2012.2194514.

[144] Z. Pan, J. Liu, H. Fu, T. Ding, Y. Xu, and X. Tong, “Probabilistic voltage quality evaluation of islanded droop-regulated microgrid based on non-intrusive low rank approximation method,” *International Journal of Electrical Power & Energy Systems*, vol. 117, p. 105630, May 2020, doi: 10.1016/j.ijepes.2019.105630.

[145] M. E. Baran and F. F. Wu, “Network reconfiguration in distribution systems for loss reduction and load balancing,” *IEEE Transactions on Power Delivery*, vol. 4, no. 2, pp. 1401–1407, Apr. 1989, doi: 10.1109/61.25627.

[146] M. E. Baran and F. F. Wu, “Optimal capacitor placement on radial distribution systems,” *IEEE Transactions on Power Delivery*, vol. 4, no. 1, pp. 725–734, Jan. 1989, doi: 10.1109/61.19265.

[147] A. Y. Abdelaziz, E. S. Ali, and S. M. Abd Elazim, “Optimal sizing and locations of capacitors in radial distribution systems via flower pollination optimization algorithm and power loss index,” *Engineering Science and Technology, an International Journal*, vol. 19, no. 1, pp. 610–618, Mar. 2016, doi: 10.1016/j.jestch.2015.09.002.

[148] S. Saha and V. Mukherjee, “Optimal placement and sizing of DGs in RDS using chaos embedded SOS algorithm,” *IET Generation, Transmission & Distribution*, vol. 10, no. 14, pp. 3671–3680, Jul. 2016, doi: https://doi.org/10.1049/iet-gtd.2016.0151.

[149] D. Zhang, Z. Fu, and L. Zhang, “An improved TS algorithm for loss-minimum reconfiguration in large-scale distribution systems,” *Electric Power Systems Research*, vol. 77, no. 5, pp. 685–694, Apr. 2007, doi: 10.1016/j.epsr.2006.06.005.

[150] R. Jamil Mahfoud, Y. Sun, N. Faisal Alkayem, H. Haes Alhelou, P. Siano, and M. Shafie-khah, “A Novel Combined Evolutionary Algorithm for Optimal Planning of Distributed Generators in Radial Distribution Systems,” *Applied Sciences*, vol. 9, no. 16, Art. no. 16, Jan. 2019, doi: 10.3390/app9163394.

[151] Y. Gupta, S. Doolla, K. Chatterjee, and B. C. Pal, “Optimal DG Allocation and Volt–Var Dispatch for a Droop-Based Microgrid,” *IEEE Transactions on Smart Grid*, vol. 12, no. 1, pp. 169–181, Jan. 2021, doi: 10.1109/TSG.2020.3017952.

[152] M. M. Aman, G. B. Jasmon, A. H. A. Bakar, and H. Mokhlis, “A new approach for optimum simultaneous multi-DG distributed generation Units placement and sizing based on maximization of system loadability using HPSO (hybrid particle swarm optimization) algorithm,” *Energy*, vol. 66, pp. 202–215, Mar. 2014, doi: 10.1016/j.energy.2013.12.037.

[153] Y. M. Atwa and E. F. El-Saadany, “Probabilistic approach for optimal allocation of wind-based distributed generation in distribution systems,” *IET Renewable Power Generation*, vol. 5, no. 1, pp. 79–88, Jan. 2011, doi: 10.1049/iet-rpg.2009.0011.

[154] K. Deb, *Multi-Objective Optimization using Evolutionary Algorithms*, vol. 16. Hoboken, NJ, USA: John Wiley & Sons, 2001.

[155] C. A. C. Coello, G. T. Pulido, and M. S. Lechuga, “Handling multiple objectives with particle swarm optimization,” *IEEE Transactions on Evolutionary Computation*, vol. 8, no. 3, pp. 256–279, Jun. 2004, doi: 10.1109/TEVC.2004.826067.

[156] M. R. Sierra and C. A. C. Coello, “Improving PSO-Based Multi-objective Optimization Using Crowding, Mutation and ∈-Dominance,” in *Proc. 3rd ICEMO*, Guanajuato, Mexico, 2005, pp. 505–519. doi: 10.1007/978-3-540-31880-4_35.

[157] K. Deb, A. Pratap, S. Agarwal, and T. Meyarivan, “A fast and elitist multiobjective genetic algorithm: NSGA-II,” *IEEE Transactions on Evolutionary Computation*, vol. 6, no. 2, pp. 182–197, Apr. 2002, doi: 10.1109/4235.996017.

[158] K. Deb and S. Agrawal, “A Niched-Penalty Approach for Constraint Handling in Genetic Algorithms,” in *Proc. ICANNGA*, Portorož, Slovenia, 1999, pp. 235–243. doi: 10.1007/978-3-7091-6384-9_40.

[159] Y. Zahraoui *et al.*, “Energy Management System in Microgrids: A Comprehensive Review,” *Sustainability*, vol. 13, no. 19, Art. no. 19, Jan. 2021, doi: 10.3390/su131910492.

[160] S. Mohammadi, S. Soleymani, and B. Mozafari, “Scenario-based stochastic operation management of MicroGrid including Wind, Photovoltaic, Micro-Turbine, Fuel Cell and Energy Storage Devices,” *International Journal of Electrical Power & Energy Systems*, vol. 54, pp. 525–535, Jan. 2014, doi: 10.1016/j.ijepes.2013.08.004.

[161] T. Niknam, A. Kavousifard, and J. Aghaei, “Scenario-based multiobjective distribution feeder reconfiguration considering wind power using adaptive modified particle swarm optimisation,” *IET Renewable Power Generation*, vol. 6, no. 4, pp. 236–247, Jul. 2012, doi: 10.1049/iet-rpg.2011.0256.

[162] A. Soroudi, “Possibilistic-Scenario Model for DG Impact Assessment on Distribution Networks in an Uncertain Environment,” *IEEE Transactions on Power Systems*, vol. 27, no. 3, pp. 1283–1293, Aug. 2012, doi: 10.1109/TPWRS.2011.2180933.

[163] P. M. Subcommittee, “IEEE Reliability Test System,” *IEEE Transactions on Power Apparatus and Systems*, vol. PAS-98, no. 6, pp. 2047–2054, Nov. 1979, doi: 10.1109/TPAS.1979.319398.

[164] Y. M. Atwa, E. F. El-Saadany, M. M. A. Salama, R. Seethapathy, M. Assam, and S. Conti, “Adequacy Evaluation of Distribution System Including Wind/Solar DG During Different Modes of Operation,” *IEEE Transactions on Power Systems*, vol. 26, no. 4, pp. 1945–1952, Nov. 2011, doi: 10.1109/TPWRS.2011.2112783.

[165] E. Hajipour, M. Bozorg, and M. Fotuhi-Firuzabad, “Stochastic Capacity Expansion Planning of Remote Microgrids With Wind Farms and Energy Storage,” *IEEE Transactions on Sustainable Energy*, vol. 6, no. 2, pp. 491–498, Apr. 2015, doi: 10.1109/TSTE.2014.2376356.

[166] N. Amjady, J. Aghaei, and H. A. Shayanfar, “Stochastic Multiobjective Market Clearing of Joint Energy and Reserves Auctions Ensuring Power System Security,” *IEEE Transactions on Power Systems*, vol. 24, no. 4, pp. 1841–1854, Nov. 2009, doi: 10.1109/TPWRS.2009.2030364.

[167] S. H. Jangamshetti and V. G. Rau, “Site matching of wind turbine generators: a case study,” *IEEE Transactions on Energy Conversion*, vol. 14, no. 4, pp. 1537–1543, Dec. 1999, doi: 10.1109/60.815102.

[168] C. G. Justus, *Winds and wind system performance*. Philadelphia, PA, USA: Franklin Institute Press, 1978.

[169] G. L. Johnson, *Wind energy systems*. Englewood Cliffs, NJ, USA: Prentice-Hall, Inc., 1985.

[170] R. Fajber, A. H. Monahan, and W. J. Merryfield, “At What Time of Day Do Daily Extreme Near-Surface Wind Speeds Occur?,” *Journal of Climate*, vol. 27, no. 11, pp. 4226–4244, Jun. 2014, doi: 10.1175/JCLI-D-13-00286.1.

[171] M. A. Shoeb, F. Shahnia, and G. M. Shafiullah, “A Multilayer and Event-Triggered Voltage and Frequency Management Technique for Microgrid’s Central Controller

Considering Operational and Sustainability Aspects," *IEEE Transactions on Smart Grid*, vol. 10, no. 5, pp. 5136–5151, Sep. 2019, doi: 10.1109/TSG.2018.2877999.

[172] D. Manna, S. K. Goswami, and P. K. Chattopadhyay, "Droop control for micro-grid operations including generation cost and demand side management," *CSEE Journal of Power and Energy Systems*, vol. 3, no. 3, pp. 232–242, Sep. 2017, doi: 10.17775/CSEEJPES.2016.00140.

[173] H. A. Gabbar and A. Zidan, "Optimal scheduling of interconnected micro energy grids with multiple fuel options," *Sustainable Energy, Grids and Networks*, vol. 7, pp. 80–89, Sep. 2016, doi: 10.1016/j.segan.2016.06.006.

[174] J. Ma, K. Summers, and F. Wen, "Joint energy and reserve market design with explicit consideration on frequency quality," *Energy Conversion and Economics*, vol. 2, no. 1, pp. 25–34, 2021, doi: 10.1049/enc2.12025.

[175] I. U. Nutkani, P. C. Loh, and F. Blaabjerg, "Cost-based droop scheme with lower generation costs for microgrids," *IET Power Electronics*, vol. 7, no. 5, pp. 1171–1180, May 2014, doi: 10.1049/iet-pel.2013.0243.

[176] A. Khaledian, A. Ahmadian, and M. A. Golkar, "Optimal droop gains assignment for real-time energy management in an islanding microgrid: a two-layer techno-economic approach," *Transmission Distribution IET Generation*, vol. 11, no. 9, pp. 2292–2304, Jun. 2017, doi: 10.1049/iet-gtd.2016.1718.

[177] M. Abedini and M. Abedini, "Optimizing energy management and control of distributed generation resources in islanded microgrids," *Utilities Policy*, vol. 48, pp. 32–40, Oct. 2017, doi: 10.1016/j.jup.2017.08.003.

[178] V. B. Foroutan, M. H. Moradi, and M. Abedini, "Optimal operation of autonomous microgrid including wind turbines," *Renewable Energy*, vol. 99, pp. 315–324, Dec. 2016, doi: 10.1016/j.renene.2016.07.008.

[179] A. Munawar, "Redesigning evolutionary algorithms for many core processors," PhD Thesis, Graduate School of Information Science and Technology, Hokkaido University, Hokkaido, Japan, 2012. Accessed: Jun. 01, 2021. [Online]. Available: https://ci.nii.ac.jp/naid/500000551709

[180] K. Hansen, "Decision-making based on energy costs: Comparing levelized cost of energy and energy system costs," *Energy Strategy Reviews*, vol. 24, pp. 68–82, Apr. 2019, doi: 10.1016/j.esr.2019.02.003.

[181] Z. Li, Y. Xu, X. Feng, and Q. Wu, "Optimal Stochastic Deployment of Heterogeneous Energy Storage in a Residential Multienergy Microgrid With Demand-Side Management," *IEEE Transactions on Industrial Informatics*, vol. 17, no. 2, pp. 991–1004, Feb. 2021, doi: 10.1109/TII.2020.2971227.

Appendix A: Wind and Load Percentage Powers Considering Uncertainty

A detailed summary of all load and wind levels/states considered for stochastic uncertainty modelling is presented here. The given states herein were generated using MATLAB's Mersenne twister random number generator with a randomly chosen seed. That is, with different seeds, different power levels and probabilities could be generated. Hence, better stochastic uncertainty modeling is guaranteed with increased level of randomness. The generated wind probability levels according to the wind speed PDF are given in Table A.1.

Table A.1: Wind speed and power by wind state

Wind Level	Wind Speed State (m/s)	Wind Power[a] (kW)	Probability	Wind Level	Wind Speed State (m/s)	Wind Power (kW)	Probability
1	0-1	0	0.0005	16	15-16	500	0.0454
2	1-2	0	0.0036	17	16-17	500	0.0315
3	2-3	0	0.0102	18	17-18	500	0.0203
4	3-4	0	0.0203	19	18-19	500	0.0121
5	4-5	0	0.0332	20	19-20	500	0.0067
6	5-6	83.35	0.0483	21	20-21	500	0.0034
7	6-7	166.65	0.0643	22	21-22	500	0.0016
8	7-8	250	0.0793	23	22-23	0	0.0007
9	8-9	333.35	0.0917	24	23-24	0	0.0003
10	9-10	416.65	0.0997	25	24-25	0	0.0001
11	10-11	500	0.1021	26	25-26	0	0
12	11-12	500	0.0984	27	26-27	0	0
13	12-13	500	0.0893	28	27-28	0	0
14	13-14	500	0.0761	29	28-29	0	0
15	14-15	500	0.0608	30	29-30	0	0

[a]Wind power output is based on historical high wind speed season data with average and standard deviation of 10.5473 m/s and 3.7282 m/s, respectively [167]. That corresponds to an annual average wind speed of 7.0929 m/s with 3.6193 m/s annual standard deviation [167].

From Table A.1 and for each wind level, the wind power is calculated based on wind speed and power equations (6.10 – 6.11). This is done by taking the average wind speed for each probability level (i.e., v_{st}). Moreover, the probability of occurrence for that specific level is attained integrating (6.9) over the minimum and maximum wind speeds for that specific wind speed level. Contrariwise, uncertainty modelling for load percentage from peak demand levels considering load accumulative percentage PDFs is given in Table A.2.

Table A.2: Load levels and percentage from peak demand during off-peak hours

Off-peak hour[a]	Load Level	Min % Peak Demand	Max % Peak Demand	Mean % Peak Demand[b]	Probability	Off-peak hour	Load Level	Min % Peak Demand	Max % Peak Demand	Mean % Peak Demand	Probability
1 (12-1) am	1	0.2661	0.2972	0.2817	0.0005	2 (1-2) am	1	0.2822	0.3081	0.2951	0.0005
	2	0.2972	0.3282	0.3127	0.0025		2	0.3081	0.3339	0.3210	0.0025
	3	0.3282	0.3593	0.3438	0.0093		3	0.3339	0.3597	0.3468	0.0093
	4	0.3593	0.3904	0.3748	0.0279		4	0.3597	0.3855	0.3726	0.0279
	5	0.3904	0.4214	0.4059	0.0657		5	0.3855	0.4114	0.3985	0.0657
	6	0.4214	0.4525	0.4369	0.1210		6	0.4114	0.4372	0.4243	0.1210
	7	0.4525	0.4835	0.4680	0.1747		7	0.4372	0.4630	0.4501	0.1747
	8	0.4835	0.5146	0.4991	0.1975		8	0.4630	0.4889	0.4760	0.1975
	9	0.5146	0.5456	0.5301	0.1747		9	0.4889	0.5147	0.5018	0.1747
	10	0.5456	0.5767	0.5612	0.1210		10	0.5147	0.5405	0.5276	0.1210
	11	0.5767	0.6078	0.5922	0.0657		11	0.5405	0.5664	0.5535	0.0657
	12	0.6078	0.6388	0.6233	0.0279		12	0.5664	0.5922	0.5793	0.0279
	13	0.6388	0.6699	0.6543	0.0093		13	0.5922	0.6180	0.6051	0.0093
	14	0.6699	0.7009	0.6854	0.0025		14	0.6180	0.6439	0.6310	0.0025
	15	0.7009	0.7320	0.7165	0.0005		15	0.6439	0.6697	0.6568	0.0005
3 (2-3) am	1	0.2718	0.2963	0.2840	0.0005	4 (3-4) am	1	0.2536	0.2788	0.2662	0.0005
	2	0.2963	0.3208	0.3085	0.0025		2	0.2788	0.3040	0.2914	0.0025
	3	0.3208	0.3453	0.3330	0.0093		3	0.3040	0.3292	0.3166	0.0093
	4	0.3453	0.3698	0.3575	0.0279		4	0.3292	0.3544	0.3418	0.0279
	5	0.3698	0.3943	0.3820	0.0657		5	0.3544	0.3796	0.3670	0.0657
	6	0.3943	0.4188	0.4065	0.1210		6	0.3796	0.4047	0.3921	0.1210
	7	0.4188	0.4433	0.4310	0.1747		7	0.4047	0.4299	0.4173	0.1747
	8	0.4433	0.4678	0.4555	0.1975		8	0.4299	0.4551	0.4425	0.1975
	9	0.4678	0.4923	0.4800	0.1747		9	0.4551	0.4803	0.4677	0.1747
	10	0.4923	0.5168	0.5045	0.1210		10	0.4803	0.5055	0.4929	0.1210
	11	0.5168	0.5413	0.5290	0.0657		11	0.5055	0.5307	0.5181	0.0657
	12	0.5413	0.5658	0.5535	0.0279		12	0.5307	0.5559	0.5433	0.0279
	13	0.5658	0.5903	0.5780	0.0093		13	0.5559	0.5810	0.5684	0.0093
	14	0.5903	0.6148	0.6025	0.0025		14	0.5810	0.6062	0.5936	0.0025
	15	0.6148	0.6393	0.6270	0.0005		15	0.6062	0.6314	0.6188	0.0005
5 (4-5) am	1	0.2527	0.2780	0.2654	0.0005	6 (5-6) am	1	0.2619	0.2882	0.2751	0.0005
	2	0.2780	0.3033	0.2906	0.0025		2	0.2882	0.3146	0.3014	0.0025
	3	0.3033	0.3285	0.3159	0.0093		3	0.3146	0.3410	0.3278	0.0093
	4	0.3285	0.3538	0.3412	0.0279		4	0.3410	0.3674	0.3542	0.0279
	5	0.3538	0.3791	0.3664	0.0657		5	0.3674	0.3937	0.3805	0.0657
	6	0.3791	0.4043	0.3917	0.1210		6	0.3937	0.4201	0.4069	0.1210
	7	0.4043	0.4296	0.4170	0.1747		7	0.4201	0.4465	0.4333	0.1747
	8	0.4296	0.4549	0.4422	0.1975		8	0.4465	0.4728	0.4597	0.1975
	9	0.4549	0.4801	0.4675	0.1747		9	0.4728	0.4992	0.4860	0.1747
	10	0.4801	0.5054	0.4928	0.1210		10	0.4992	0.5256	0.5124	0.121
	11	0.5054	0.5307	0.5180	0.0657		11	0.5256	0.5520	0.5388	0.0657
	12	0.5307	0.5559	0.5433	0.0279		12	0.5520	0.5783	0.5652	0.0279
	13	0.5559	0.5812	0.5686	0.0093		13	0.5783	0.6047	0.5915	0.0093
	14	0.5812	0.6065	0.5938	0.0025		14	0.6047	0.6311	0.6179	0.0025
	15	0.6065	0.6317	0.6191	0.0005		15	0.6311	0.6575	0.6443	0.0005
7 (6-7) am	1	0.1833	0.2275	0.2054	0.0005	7 (6-7) am	9	0.5365	0.5806	0.5585	0.1747
	2	0.2275	0.2716	0.2495	0.0025		10	0.5806	0.6248	0.6027	0.1210
	3	0.2716	0.3158	0.2937	0.0093		11	0.6248	0.6689	0.6468	0.0657
	4	0.3158	0.3599	0.3378	0.0279		12	0.6689	0.7131	0.6910	0.0279
	5	0.3599	0.4040	0.3820	0.0657		13	0.7131	0.7572	0.7351	0.0093
	6	0.4040	0.4482	0.4261	0.1210		14	0.7572	0.8013	0.7793	0.0025
	7	0.4482	0.4923	0.4703	0.1747		15	0.8013	0.8455	0.8234	0.0005
	8	0.4923	0.5365	0.5144	0.1975						

[a]Off-peak hour demand forecast is based on historical data of typical electricity demand at the hours between 12:00 am – 07:00 am. It is also assumed that the load demand follows the IEEE RTS load profile [163], [164]. [b]Assuming active peak system demand as 3.715 MW, 3.80 MW, and 22.71 MW for IEEE 33-, 69-, and 118-bus systems, respectively. Furthermore, the assumed reactive peak system demand was 2.3 MVAR, 2.695 MVAR, and 17.04 MVAR for IEEE 33-, 69-, and 118-bus systems, respectively [145]–[147].

According to Table A.2 and for any given load in the system, the active and reactive load random variables for each off-peak hour are modelled as PDFs. This is done by using the total average and standard deviation of the accumulative load percentage (i.e., $\mathscr{p}$) across the whole year. Likewise, the average and standard deviation for each off-peak hour, as per the assumed notion of this study, is calculated considering load's accumulative percentage. This is done to cover the hourly, daily, and weekly percentages of load peak demand as derived from the IEEE RTS load prediction [163], [164]. By considering the accumulative percentages, a 24 x 365 matrix is created for each year where each cell corresponds to an hour in that year. Subsequently, the average and standard deviation are attained for each desired off-peak hour to model the associated PDF as per equation (6.1). On the other hand, the probability of occurrence for each level for $\mathscr{p}$ is attainted by the integration of the load's PDF across the minimum and maximum percentage for that level (i.e., $\mathscr{p}_{st}^{l}$ and $\mathscr{p}_{st}^{u}$). Moreover, the effective percentage to produce the load power (i.e., $\mathscr{p}_{st}$) from the peak demand in that level is taken as the mean percentage as given in equation 6.5. In other words, as per Table A.2, the Min % Peak Demand and Max % Peak Demand correspond to $\mathscr{p}_{st}^{l}$ and $\mathscr{p}_{st}^{u}$, respectively. Likewise, the Mean % Peak Demand corresponds to the attained mean load percentage (i.e., $\mathscr{p}_{st}$)**.**